DETAILED CHEMICAL ABUNDANCES OF EXTRAGALACTIC GLOBULAR CLUSTERS USING HIGH RESOLUTION, INTEGRATED LIGHT SPECTRA

by

Janet E. Colucci

A dissertation submitted in partial fulfillment
of the requirements for the degree of
Doctor of Philosophy
(Astronomy and Astrophysics)
in The University of Michigan
2010

Doctoral Committee:

Professor Nuria P. Calvet, Co-Chair
Associate Professor Rebecca A. Bernstein, Co-Chair,
University of California
Professor August Evrard
Professor Mario L. Mateo
Associate Professor Marion S. Oey
Professor Puragra GuhaThakurta, University of California

To my mother,
Susan,
and my sisters,
Vanessa and Sara.

ACKNOWLEDGMENTS

CONTENTS

LIST OF FIGURES

LIST OF TABLES

ABSTRACT

Globular clusters (GCs) are luminous, observationally accessible objects that are good tracers of the total star formation and evolutionary history of galaxies. We present the first detailed chemical abundances for GCs in M31 using a new abundance analysis technique designed for high resolution, integrated light (IL) spectra of GCs. This technique has recently been developed using a training set of old GCS in the Milky Way (MW), and makes possible detailed chemical evolution studies of distant galaxies, where high resolution abundance analysis of individual stars are not obtainable. For the 5 M31 GCs presented here, we measure abundances of 14 elements: Mg, Al, Si, Ca, Sc, Ti, V, Cr, Mn, Fe, Co, Ni, Y, and Ba. We find the M31 GCs have ages (>10 Gyr) and chemical properties similar to MW GCs, including an enhancement in the α-elements Ca, Ti and Si of $[\alpha/\text{Fe}] \sim +0.4$.

In this thesis, we also further develop this IL abundance analysis method to include GCs of ages 10 Myr - 12 Gyrs using GCs in the Large Magellanic Cloud (LMC), which contains the necessary sample of clusters over this wide age range. This work demonstrates for the first time that this IL abundance analysis method can be used on clusters of all ages, and that ages can be constrained to within $1-2$ Gyr for clusters with ages of ~ 2 Gyr and within a few 100 Myr for clusters with ages <1 Gyr. We find that we can measure [Fe/H] in clusters with ages <12 Gyrs with similar or only slightly larger uncertainties (0.1-0.25 dex) than those obtained for old GCs; the slightly larger uncertainties are due to the rapid evolution in stellar populations at these ages.

Using the LMC clusters, we also investigate the effects of statistical fluctuations in the theoretical cluster stellar populations used in our analysis. We also develop strategies to allow for statistical variations in these stellar populations, and find

that the stability of the Fe line abundance solution can provide tight constraints on the appropriate theoretical stellar populations. Detailed chemical abundances of 22 elements are reported for six LMC clusters.

CHAPTER 1

Introduction

Globular clusters (GCs) are unique tools for probing the formation history and evolution of galaxies. As coeval populations of $10^4 - 10^6$, gravitationally bound and chemically uniform stars, they are the closest representation of true simple stellar populations (SSPs). Because the stars in a GC occupy a very small, generally spherical volume ($r_{half-light} \lesssim 10$ pc), GCs as a whole are very high surface brightness objects ($-6 \le M_V^{tot} \le -10$), and thus are observationally accessible at large distances, where individual stars are not.

Study of the Milky Way (MW) globular cluster system, which has $\sim$150 GCs (Harris, 1996), provided fundamental clues to our current picture of the formation of the MW, and by extention, other normal spiral galaxies. For example, Eggen et al. (1962) used the very small spread in age observed in the 5 best studied MW GCs as supporting evidence that the MW halo formed in a rapid, monolithic collapse. With a larger sample of 19 MW GCs, Searle & Zinn (1978) used the difference in ages, chemical abundances and stellar populations of the outer and inner halo GCs as early evidence for a more prolonged, hierarchical formation of the MW halo. Further support for a hierarchical halo formation that is still ongoing today, came from identifying the halo GCs Pal 12 and Rup 106 as tidally captured GCs by using their kinematics and chemical composition to associate them with the tidally disrupting Sagittarius dwarf spheroidal galaxy (e.g. Dinescu et al., 2000; Cohen, 2004).

Because unresolved GCs are so luminous, they are also perfect tools for studying galaxies beyond the MW, where detailed studies of individual stars are not possible, and have been used as tracers to map both luminous and dark matter distributions in distant galaxy haloes (e.g. Romanowsky et al., 2009). Extragalactic GCs have also

been used to trace metallicities in other galaxies, with the result that all galaxies that have been observed in detail show bi-modal distributions in GC metallicity, and that the peak metallicities are correlated with galaxy mass across a wide range of galaxy types (see review by Brodie & Strader, 2006). Quantitatively predicting the distribution of GC ages and metallicities and tying them to theoretical galaxy formation models is an active area of research (e.g. Schweizer, 1987; Ashman & Zepf, 1992; Forbes et al., 1997; Cote et al., 1998; Beasley et al., 2002a; Gnedin & Prieto, 2009).

1.1 Detailed Chemical Abundances

In the MW and nearby dwarf galaxies, detailed chemical abundances of stars have not only been instrumental in helping to identify past accretion events (e.g. Freeman & Bland-Hawthorn, 2002), but also in studying the star formation histories of galaxies (e.g. Venn et al., 2004; Pritzl et al., 2005; Pompéia et al., 2008; Tolstoy et al., 2009; Kirby et al., 2009). Detailed chemical abundances are powerful because different elements form in different types of events and on different timescales. The ratios of abundances of elements that formed under different circumstances therefore hold information on the relative star formation rates and nuclear processes that produced them.

Current models of chemical enrichment and stellar processing suggest that α-elements (e.g. O, Mg, Si, Ca, Mg) and r-process elements (e.g. Eu, Nd, Sm) are mostly produced in Type II supernovae, which enrich the interstellar medium on timescales of millions of years, and so are created in large amounts in very active periods of star formation (e.g. Woosley & Weaver, 1995). Fe-peak elements (e.g. Fe, Cr, Co, V) are produced in larger quantities, relative to α-elements, in Type Ia supernovae, which enrich the interstellar medium on much longer timescales, and begin to dominate chemical evolution of a galaxy on timescales of billions of years (e.g. Smecker-Hane & Wyse, 1992). Therefore, in a simple model of galaxy chemical enrichment, a high abundance of α- or r-process elements relative to Fe-peak elements,

or high $[\alpha/\text{Fe}]^1$ ratio, is a signature of enrichment dominated by Type II supernovae, which implies a period of high star formation rate. Other useful diagnostics of star formation histories are s-process elements (e.g. Y, Ba, La), which are dispersed into the interstellar medium by the stellar winds of asymptotic giant branch (AGB) stars. The yields of s-process elements in these winds are thought to be dependent on the metallicity of the progenitor AGB star, and high [Ba/Y] ratios in particular are thought to be a signature of star formation in long-lived low-metallicity environments, or low star formation rates (e.g. Busso et al., 1999).

The differences in detailed chemical abundance patterns in stars in nearby dwarf galaxies when compared to stars in the MW have emphasized how complex the star formation histories of these galaxies are and how complicated chemical evolution of galaxies can be (see reviews by Geisler et al., 2007; Tolstoy et al., 2009). However, to obtain detailed chemical abundances of $\sim$20 or more elements in order to study the star formation histories of other galaxies at the same level as can be done for the Milky Way, one requires high signal-to-noise ratio (S/N), high resolution spectra (R$\gtrsim$20,000). Unfortunately this is not feasible for stars much beyond the nearest dwarf galaxies, although new techniques using medium resolution (R$\sim$6500) spectra are making it possible to derive abundances for a handful of elements (Fe, Ca, Ti, Si and Mg) for large numbers of individual stars out to distances of $\sim$250 kpc (Kirby et al., 2008). This limitation has motivated the development of the techniques described in this thesis.

1.2 Development of an Integrated Light Abundance Analysis Method

The importance of detailed chemical abundances, and the observational and theoretical applicability of GCs as probes of galaxy formation, has motivated the development of a new technique, which enables the measurement of detailed chemical abundances

---

[1]The standard notation of abundance ratios is $[X/Y] = log(N_X/N_Y)_* - log(N_X/N_Y)_\odot$, where X and Y are the number of atoms and ions of two individual elements, and are normalized to the abundance of these elements in the Sun.

of $\sim$20 elements from the integrated light (IL) spectra of GCs. This technique results in unprecedented constraints on the chemical evolution and star formation history of galaxies beyond the MW and its nearest neighbor galaxies, where high resolution studies of individual stars are not possible.

Previous techniques for determining metallicites and estimates of $[\alpha/\text{Fe}]$ from the integrated light spectra of unresolved extragalactic GCs focused on using low resolution spectra and line index systems like the "Lick" system (e.g. Faber et al., 1985), which were originally designed for study of unresolved galaxies with high internal velocity dispersions of $100-300$ km s^{-1}(Faber & Jackson, 1976). The high velocity dispersions of galaxies mean that spectral lines of individual elements cannot be resolved, whereas GCs have very small velocity dispersions of $2-25$ km s^{-1}, and so the effect of line blending is much less severe. While high resolution spectra of the IL of extragalactic GCs have been used for some time for the measurement of velocity dispersions for derivation of dynamical mass-to-light ratios (e.g. Elson & Freeman, 1985; Peterson, 1989; Djorgovski et al., 1997; Dubath & Grillmair, 1997), there has been no method to analyze high resolution GC spectra to obtain detailed chemical abundances analogous to that which has been used on individual stars for decades.

The new IL abundance analysis technique, which was introduced in Bernstein et al. (2003) and Bernstein & McWilliam (2002, 2005), is based on standard stellar abundance analysis methods for red giant branch (RGB) stars, and like previous low resolution techniques, relies on the fact that GCs are SSPs, and thus can be easily modeled. However, unlike line index systems (see Puzia et al., 2002), this new high resolution abundance analysis method does not rely on a calibration to local MW stars, and thus there are no systematic errors due to built in assumptions on the chemical nature of the target clusters.

In brief, the power in the new IL abundance analysis technique rests in the fact that stellar evolution is reasonably well understood (e.g. Gallart et al., 2005), so that it is simple to use theoretical stellar isochrones to create arbitrary synthetic stellar populations like GCs, which are determined only by their age and metallicity. These synthetic GC populations can then be used to synthesize flux-weighted, IL spectra, for

comparison to the observed IL spectra of unresolved GCs. Like standard stellar high resolution abundance analysis methods, the IL abundance analysis method utilizes equivalent widths (EWs) of individual spectral features for derivation of abundances. Clean, unblended features with well determined transition strengths can be isolated for abundance determinations, and the self-consistency and stability of the abundance solution over many (50-150) individual transitions of Fe can be used to constrain the best-fitting synthetic GC population. This means that out of many possible combinations of age and metallicity, the most appropriate stellar population to match an unresolved GC can be identified by using constraints from the observed IL spectra alone. This best-fitting stellar population can then be used to derive abundances of $\sim$20 different chemical elements.

In McWilliam & Bernstein (2008) and Cameron (2009, PhD thesis), extensive testing on a "training set" of MW GCs of known properties was presented with the development of the IL abundance analysis method. These works focused on demonstrating the analysis method and the accuracy of the derived abundances for a set of "typical" MW GCs, which have old ages ($>$10 Gyr), span a range in metallicity from [Fe/H]~ -2 to -0.4, and have a spread in horizontal branch morphology and internal velocity dispersion (σ_V). The results of McWilliam & Bernstein (2008) and Cameron (2009), showed that the abundances measured using the IL analysis method have accuracies of $\leq$0.1 dex for nearly all species when compared to standard analysis of individual stars in the training set clusters, and the statistical uncertainties in abundances for individual element species are $\sim$0.2 dex, which is comparable to the precision in abundance measurements for other authors of $\lesssim$0.15 dex. For old GCs, the ages can be constrained to a range of 5 Gyr, which is small enough that the assumed age affects the abundance results by $<$0.1 dex, which is less than the statistical error of the measured spectral lines.

The comparison from Cameron (2009) of the derived Fe I and Fe II abundances from the IL analysis of the 7 MW training set clusters to a compilation of abundances measured in studies of individual stars is reproduced in Figure 1.1. A linear least-squares fit to these two quantities results in an offset of the derived IL Fe I abundances
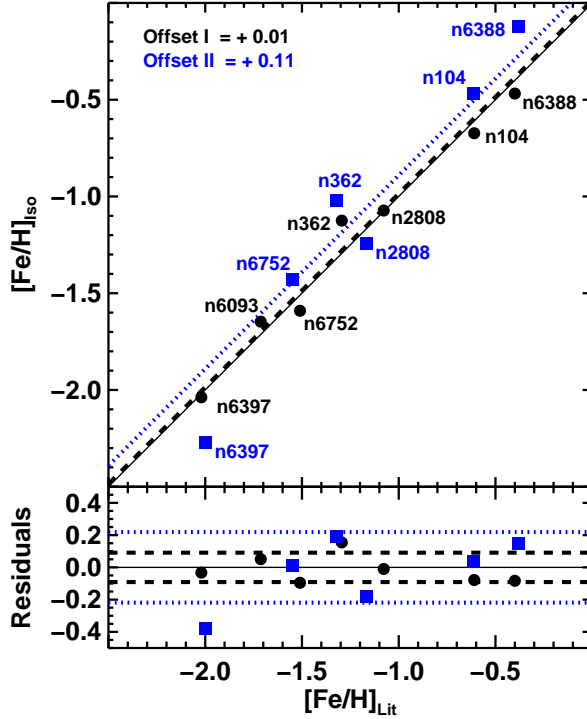
Figure 1.1. The IL [Fe/H] results for the 7 MW training set GCs are compared to the [Fe/H] for individual stars in the literature. Reproduced from Cameron (2009). The black and blue circles and squares show [Fe/H] from Fe I and Fe II lines, respectively. The solid black line marks the 1:1 line along which points would lie if there is perfect agreement between [Fe/H] from the IL analysis and from stars in the literature (references compiled in Cameron (2009)). The dashed black and dotted blue lines show fits to same-color points with the line slopes constrained to 1.0, and the y-intercepts, or systematic offsets, are labeled. The residual scatter around the fitted lines is shown in the lower panel. The horizontal black dashed and blue dotted lines mark the ±1 RMS deviation of these residuals. Note that the RMS deviations are in all cases larger than the offsets, suggesting that the systmatic agreement between the IL and stellar results is within the statistical uncertainties.

of +0.01 dex, with a statistical scatter around the fit of +0.09 dex. The offset in IL Fe II abundances is +0.11 dex, with a statistical scatter of +0.22 dex. For reference, the same comparisons for all chemical species for which individual star measurements were available are reproduced in Table 1.1. Note that the uncertainties quoted here correspond to the uncertainties in the comparison of the entire sample of MW training set GCs, and that the individual measurement uncertainty in the abundance of a given species or [X/Fe] ratio is often smaller.

Chapter 2 of this dissertation is comprised of the first application of the new IL abundance analysis method, as described in Cameron (2009), to 5 well-studied, old age GCs in M31, and was originally published as Colucci et al. (2009). As the nearest

Species	Systematic (dex)	Statistical (dex)
Fe I	$+0.01 \pm 0.09$	0.09
Fe II	$+0.11 \pm 0.08$	0.22
Fe-Peak Elements		
Cr I	$+0.01 \pm 0.05$	0.10
Mn I	$+0.12 \pm 0.13$	0.12
Ni I	$+0.08 \pm 0.10$	0.15
Sc II	$+0.30 \pm 0.11$	0.35
V I	-0.08 ± 0.24	0.31
Mean	$+0.08 \pm 0.12$	0.19 ± 0.10
α-Elements		
Ca I	$+0.05 \pm 0.10$	0.20
Mg I	-0.07 ± 0.10	0.32
Si I	$+0.12 \pm 0.09$	0.07
Ti I	-0.03 ± 0.14	0.37
Ti II	$+0.13 \pm 0.08$	0.19
Mean	$+0.04 \pm 0.09$	0.23 ± 0.12
Light Elements		
Al I	$+0.12 \pm 0.05$	0.22
Na I	$+0.10 \pm 0.26$	0.23
Mean	$+0.11 \pm 0.02$	0.22 ± 0.00
n-Capture Element		
Ba II	$+0.11 \pm 0.08$	0.23
Mean Total	$+0.07 \pm 0.10$	0.21 ± 0.10

Table 1.1. Estimated accuracy in the MW training set IL abundance analysis, based on comparison with stellar results. Reproduced from Cameron (2009). The systematic uncertainty corresponds to the mean offset, across the entire sample of 7 MW GCs, of abundances determined from the IL method from abundances determined from analysis of individual stars in each GC. The quoted statistical uncertainty represented the RMS scatter in the abundance comparisons for each GC around the mean offset for the sample of GCs.

large galaxy to the MW, and because it has more than 300 confirmed GCs, M31 is an ideal target for this IL abundance analysis technique. Moreover, even though the MW and M31 are both large spiral galaxies and one would naively expect that chemical evolution proceeded in a similar fashion under similar circumstances, there are indications from low resolution spectroscopic techniques that there may be differences in the chemical composition of MW and M31 GCs (Burstein et al., 1984; Puzia et al., 2005; Beasley et al., 2005). Our goals in this work, are both to better understand the formation of M31 and its GC system, and to demonstrate that powerful constraints on the stellar populations and accurate detailed chemical abundances of GCs can be obtained in a large galaxy other than the MW. To summarize our results, we find that the first 5 GCs we have observed in M31 show chemical properties very similar to MW GCs. We also present velocity dispersions and $E(B-V)$ constraints that can be derived using the high resolution IL spectra. Collection of a much larger, statistical sample of detailed chemical abundances of M31 GCs is ongoing, and will be used to constrain the chemical and star formation history of M31.

1.3 Extending the IL Method Using the LMC

In Chapter 3 of this dissertation, we present the IL abundance analysis of a second training set of clusters in the Large Magellanic Cloud (LMC), which we use as a tool for further refinement of the IL abundance analysis method. We also provide the first abundance results for many elements in these clusters. A second training set of clusters in the LMC was chosen primarily to evaluate whether the IL method can be successfully applied to clusters with ages <10 Gyr, which was not testable using the uniformly old GCs in the MW. The MW training set clusters are also very uniform in their chemical composition, and because previous work on the chemical abundances of RGB stars in the LMC has shown that the stars show a wide range in α, Fe-peak and neutron capture element abundances when compared to stars in the MW, the LMC potentially offers clusters with a wider range of chemical composition that we can use to test the IL method.

Another large focus of the work presented in Chapter 3, is evaluating the effect

of statistical fluctuations of the number and properties of rare, but luminous, stars on determining the stellar populations and chemical abundances of clusters using the IL analysis method. This is particularly important to address for the training set clusters, because we have only sampled a fraction (5%-60%) of the stellar populations in the clusters due to their large spatial extent on the sky, and so the mean properties of the synthetic stellar populations we use for the analysis are sensitive to small number statistics for luminous stars in rapid phases of stellar evolution. However, statistical fluctuations in the properties of distant extragalactic clusters can also be expected for both lower mass clusters, and clusters with young ages (e.g. Brocato et al., 1999, 2000), and so a specific goal of the LMC training set is to develop analysis techniques that can also be applied to young or low mass unresolved clusters.

Chapter 3 is presented in a form that will be soon be published as Colucci et al. (2010). We present the IL analysis of the LMC training set, with an emphasis on developing tests to evaluate and accomodate incomplete sampling of the stellar populations. We find that the stability and self-consistency of the Fe line abundance solutions can also be used to identify the most appropriate synthetic stellar population when the stars are allowed to vary stochastically. We find that the ages of young clusters can also be distinguished from the ages of >10 Gyr clusters using the stability of the Fe lines; with high quality data the ages of $\sim$2 Gyr LMC clusters can be constrained to a range of $1-2$ Gyr, and clusters with ages <1 Gyr can be constrained to a few hundred Myrs. In some cases the smallest spread in age we are able to constrain for young clusters is large enough that the rapidly changing stellar populations result in a higher uncertainty in [Fe/H] than we typically obtain for old clusters. While the emphasis in Chapter 3 is on determining constraints on the stellar populations and [Fe/H] of the LMC training set, we also present detailed abundances calculated for $\sim$20 different elements and discuss comparisons to previous stellar abundance work in the LMC. A thorough discussion of the implications of the abundances we derive in terms of the chemical evolution and formation history of the LMC will be presented in future work.

In Chapter 4, we summarize the main conclusions from Chapter 2 and 3, and

discuss ongoing and future work on constraining the chemical evolution and formation history of galaxies beyond the Milky Way using detailed chemical abundances of globular clusters.

CHAPTER 2

Demonstration of the Integrated Light Abundance Analysis Method on Globular Clusters in M31

2.1 Introduction

Stellar atmospheres largely retain the chemical composition of the gas from which they formed, and thus contain a record of the gas chemistry of a galaxy throughout its star formation history. The abundances relative to Fe of some key elements, α-elements in particular, can be used to identify the timescales and rates of star formation over the lifetime of a galaxy. $\alpha-$elements (C, O, Ne, Mg, Si, S, Ar, Ca, and Ti) are produced primarily in type II supernovae (SNII) (e.g. Woosley & Weaver, 1995) from massive stars and so build up quickly during active star formation epochs, while Fe-peak elements are produced in all supernovae. [α/Fe] abundance patterns are therefore particularly useful and have been central to developing our current picture of the assembly and star formation history of the Milky Way and spiral galaxies in general (see Pritzl et al., 2005, and references therein).

Bright, young stars record the current gas phase abundance in a galaxy; to probe the earliest formation times, one must target older, lower mass, fainter stars. It is only recently that individual red giant branch (RGB) stars in our nearest neighbor galaxies in the Local Group have been within reach of the high resolution spectroscopy needed for detailed chemical abundance analysis. These stars in Local Group dwarf galaxies show a much greater range of abundance ratios at all metallicities compared to stars in the Milky Way halo (Venn et al., 2004; Shetrone et al., 2001, 2003; Geisler et al., 2005; Tolstoy et al., 2009), suggesting that they have had a much more complicated star formation history than the halo's progenitor(s). Detailed abundances beyond the

Milky Way and its nearest remaining neighbors are needed to establish the broader patterns of star formation in galaxies of all masses.

Unfortunately, at ~780 kpc from the Milky Way (Holland, 1998), even M31 is distant enough that older RGB stars are too faint (V~23) to obtain the required high signal-to-noise ratio (S/N~ 60) and high spectral resolution ($\lambda/\Delta\lambda \sim 20,000$) to measure detailed abundances in individual stars. Fortunately, globular clusters (GCs) can also be targeted. Unlike single stars, high resolution spectra can be obtained of unresolved GCs out to ~ 4 Mpc with current telescopes. GCs are bright enough ($-10 < M_V < -6$ mag) and have low enough velocity dispersions ($2-20$ km s^{-1}) that even weak lines (~15 mÅ) can be detected in spectra of their integrated light. Detailed abundances have never been obtained from unresolved GCs because techniques have not existed to analyze them. We have developed a new method for analyzing high resolution integrated light (IL) spectra of single age, chemically homogeneous stellar populations to obtain detailed element abundances as described in Bernstein & McWilliam (2002, 2005) and McWilliam & Bernstein (2008), hereafter "MB08."

Our method has been developed and tested on a "training set" of Milky Way and LMC GCs with well determined properties from studies of individual stars. IL spectra of the training set GCs were obtained by scanning a 32×32 arcsec^2 region of the cluster cores in the Milky Way clusters, and a 12×12 arcsec^2 region in the LMC. Note that slit scanning is only necessary for the resolved GCs we target in our training set, not for unresolved, extragalactic GCs. The training set GCs were chosen to cover the range of metallicity, horizontal branch morphology, mass, velocity dispersion, and age available in the Milky Way and LMC systems. Using this training set, we have compared abundances determined with our IL method and abundances from the literature determined for individual RGB stars. Based on the Milky Way training set, we estimate empirically that our [Fe/H] abundances are accurate to within < 0.1 dex, and all other element ratios ([X/Fe]) accurate to within < 0.1 dex (see MB08 and S. Cameron et al. 2010, in preparation). We also derive approximate ages (>10 Gyr) for our entire Milky Way training set. Using the larger age range of

the LMC clusters, which includes clusters as young as ~10 Myr, we have found that our method can clearly distinguish clusters over a large range in age. Our accuracies at the youngest ages are described in Chapter 3 of this thesis.

In addition to the fact that GCs are among the oldest stellar populations in galaxies, there is ample evidence that GCs are a good tool for tracing both the early formation of galaxies themselves and star formation throughout their histories. The fact that the number of GCs in a galaxy scales with the total luminosity of the galaxy (e.g. Harris, 1991) suggests that the GCs trace total star formation. Additionally, young massive clusters are seen forming in regions with high star formation rates, such as mergers of gas rich galaxies (e.g. Schweizer & Seitzer, 1998; Whitmore & Schweizer, 1995), indicating that GCs form in major episodes of star formation, throughout the lifetimes of galaxies. While the old age of GCs alone suggest that they record the earliest star formation episodes in galaxies, there is additionally strong evidence that both blue (metal-poor) and red (metal-rich) sub-populations of GCs in normal galaxies correlate with the host galaxy's luminosity and overall metallicity(e.g. Brodie & Strader, 2006). This suggests that both sub-populations are a record of the formation history of the galaxy, with blue clusters possibly tracing the earliest star formation in dark matter halos and red clusters tracing the later formation after the gas is more enriched. Finally, GCs are also relatively easy spectroscopic targets to analyze because, to first order, they are simple stellar populations (SSPs), and can be approximated with a single age and single metallicity. For all of these reasons, detailed abundance analysis of GC systems is a powerful tool for understanding the formation of galaxies beyond the Milky Way.

M31 is the closest large galaxy to the Milky Way and an ideal target for galaxy formation studies using GCs. Like the Milky Way, M31 has a large system of GCs, most of which are old (≥ 10 Gyrs), and has a bimodal metallicity distribution with peaks at [Fe/H]~ -1.4 and [Fe/H]~ -0.5 and a mean of [Fe/H]~ -1.2 (Barmby et al., 2000; Perrett et al., 2002). Barmby et al. (2007) find that M31 and Milky Way GCs are structurally similar, with similar mass-to-light (M/L) ratios, and fall on a single GC fundamental plane. However, there are notable differences that have been

observed between the two galaxies. To begin with, M31's GC system is more than a factor of 2 larger than the Milky Way's (Galleti et al., 2004), has massive but diffuse GCs (Huxor et al., 2005; Mackey et al., 2006), and metal-poor and compact GCs at very large projected galactocentric radii (Martin et al., 2006; Mackey et al., 2007). There is evidence for young and/or intermediate age GCs in M31 unlike in the Milky Way (Beasley et al., 2004; Puzia et al., 2005), and a significant population of GCs of all metallicities kinematically associated with the thin disk (Morrison et al., 2004). There is also evidence for some chemical differences in M31 GCs; compared to the Milky Way, M31 GCs show enhanced CN molecular lines (e.g. Burstein et al., 1984), and the first estimates of $[\alpha/\text{Fe}]$ ratios in M31 GCs have indicated it may on average be $\sim 0.1-0.2$ dex lower than in the Milky Way (Puzia et al., 2005; Beasley et al., 2005). More detailed studies are required to understand what these similiarities and differences imply for the formation history of M31.

Much of what is known about M31 comes from low resolution spectroscopic methods like the "Lick" system (e.g. Faber et al., 1985), which have been used to target spatially unresolved GCs (e.g. Huchra et al., 1991) to obtain the constraints to date on $[\text{Fe}/\text{H}]$ and $[\alpha/\text{Fe}]$ ratios (e.g. Puzia et al., 2005; Beasley et al., 2005). These line index systems were originally developed for studying the integrated light of galaxies, which have velocity dispersions of $100-300$ km s^{-1}(Faber & Jackson, 1976). With the low velocity dispersions of GCs, individual spectral lines can be resolved with only slightly greater line blending than one finds in individual RGB stars. The accuracy of the line index systems depends on calibrations that are sensitive to abundance ratios and overall metallicity. These limitations make detailed abundance analysis from individual lines, as in our method, an important next step.

In this chapter we present the analysis of 5 GCs in M31 using high resolution spectroscopy of their integrated light. These represent the first set of clusters which we have observed as part of an ongoing project to study the GC population in M31 with the goal of constraining the stellar populations and formation history of M31. From these clusters, we derive detailed stellar abundances of old populations in M31 for the first time. We obtain results for 14 elements: Mg, Al, Si, Ca, Sc, Ti, V,

Cr, Mn, Fe, Co, Ni, Y, and Ba. We also present ages, velocity dispersions, and reddening constraints for this sample. In § 2.2, we describe our observations and data reduction. In § 2.3 we present analysis of the velocity dispersions and implications for our equivalent width abundance analysis. In § 2.4 we describe our abundance analysis method and present abundance results in § 2.5. In § 2.6 we discuss the M31 GC chemical abundances in the contexts of galaxy formation, low resolution spectra line index abundances, and overall consistency with broadband photometric colors and existing Hubble Space Telescope (HST) CMDs.

2.2 Observations and Reductions

In selecting GC targets in M31, we have focused initially on clusters which are spectroscopically confirmed, and are estimated from low resolution indexes to have abundances in the range -1.8 < [Fe/H] < -0.5 dex. At the time of selection, this was the range in which we were most confident of the accuracy of our analysis based on our previous work with the Milky Way training set clusters described above (MB08 and S. Cameron et al. 2010). The targets were further selected to be relatively well studied, reasonably isolated and well outside of M31's disk to reduce confusion and the chance of confusion from interloping sources. We also avoided the brightest, most massive GCs while still targeting GCs bright enough to get sufficient S/N in a few hours of observations, as they will have the highest velocity dispersions and thus broader, less pronounced spectral lines,. With this in mind, we have selected these GCs from the Barmby catalog (Barmby et al., 2000). This initial set of GCs has magnitudes between 15 and 16. Magnitudes and spatial information are listed for all of the GCs in Table 2.1, along with low resolution abundance estimates from the literature and horizontal branch morphologies from HST imaging when available.

For this work we obtained high resolution IL spectra of the M31 globular clusters using the HIRES spectrograph (Vogt et al., 1994) on the Keck I telescope over the dates 2006 September 10−14. We used the D3 decker, which provides a slit size of 1".7 × 7.0" and spectral resolution of $R = 24,000$. The GCs in this sample have half light radii (r_h) between ∼0.6"−1.1" (Barmby et al., 2007). We calculate

Cluster	RA (2000)	Dec (2000)	V	E(B-V)	M_V^{tot}	R_{gc} (kpc)	[Fe/H]	[α/Fe]	HBR
G108-B045	00 41 43.26	41 34 21.8	15.83	0.10	-8.95	4.87	-0.94 ± 0.27	0.22 ± 0.19	0.14
G219-B358	00 43 18.01	39 49 13.5	15.12	0.06	-9.53	19.78	-1.83 ± 0.22	0.00 ± 0.27	0.78
G315-B381	00 46 06.47	41 21 00.2	15.76	0.17a	-9.24	8.8	-1.22 ± 0.43	$\cdots$	$\cdots$
G322-B386	00 46 26.94	42 01 52.9	15.64	0.13	-9.24	14.02	-1.21 ± 0.38	0.25 ± 0.22	0.41
G351-B405	00 49 39.81	41 35 29.4	15.20	0.08	-9.52	18.2	-1.80 ± 0.31	$\cdots$	0.71

Table 2.1. M31 Clusters. *References*: Columns 1-4: Barmby et al. (2000), Column 5: Rich et al. (2005), a. Fan et al. (2008), Column 6: Reddening corrected and using a distance modulus for M31 of $(m-M)=$ 24.47 (Holland, 1998), Column 7: Perrett et al. (2002), Column 8: Low resolution spectroscopic metallicities of Huchra et al. (1991), Column 9: Low resolution [α/Fe] of Puzia et al. (2005), Column 10: Horizontal branch morphology ratios (HBR), defined as the "Mironov Index" $= B/B + R$, where B and R correspond to the number of horizontal branch stars bluer or redder than $V - I = 0.5$ in the observed CMD of Rich et al. (2005).
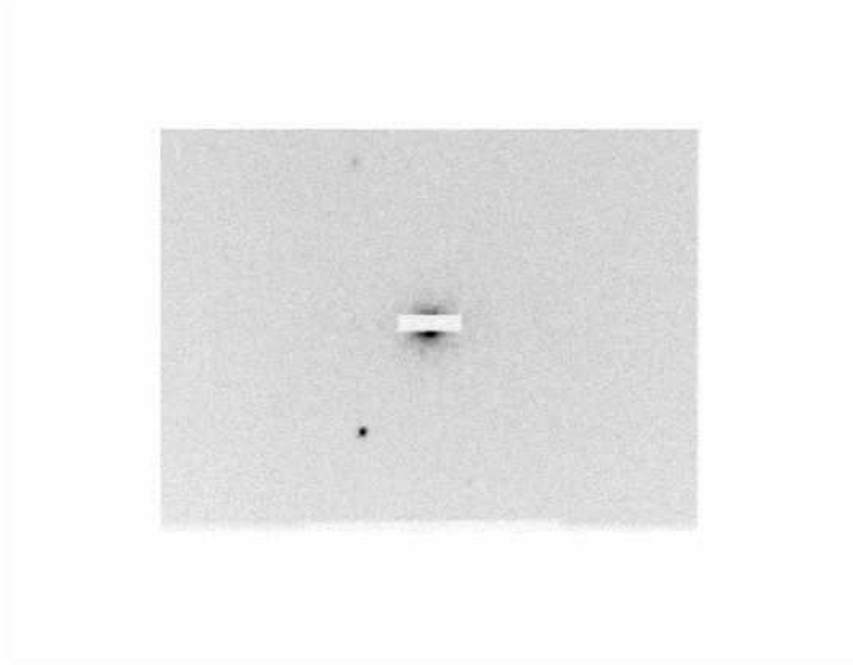
Figure 2.1. A single frame taken with the Keck I guide camera is shown here to illustrate the relative size of a GC in M31 (half-light radius $\sim$1 arcsec) relative to the 1.7×7 arcsec^2 slit. The guider images a reflection of the sky off the polished slit plate, so that the slit itself is clearly visible where no image of the sky is reflected.
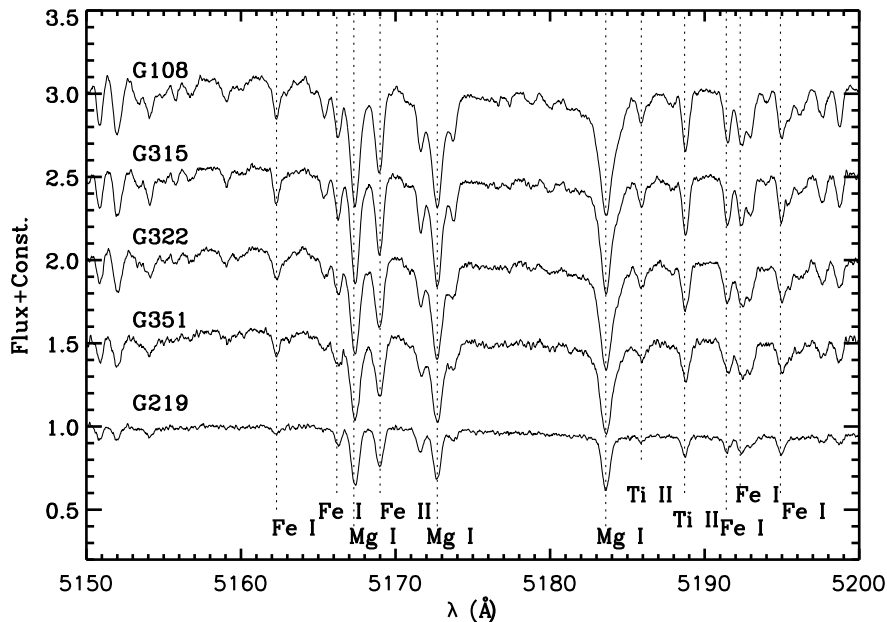
Figure 2.2. Example M31 GC spectra in Lick Mgb region shown decreasing in [Fe/H] from our analysis (top to bottom). Note that this region is dominated by saturated lines and is shown for illustration as a region familiar in low resolution spectra analyses.

from surface brightness profiles in Barmby et al. (2002, 2007) that $\sim 70-90\%$ of the light fell in the 1".7 × 7.0" slit for each cluster. An illustration of the observing setup is shown in Figure 2.1. The wavelength coverage of the HIRES spectra is approximately $3800-8300$ Å. Exposure times were between $3-4$ hours for each GC and are listed in Table 2.2 along with S/N estimates at three wavelengths, one in each HIRES CCD. Data was reduced with the MAKEE software package available from T. Barlow[1]. In analysis of more recent observing runs, we have compared data analyzed with MAKEE and with the HiRes Redux pipeline produced by J. X. Prochaska, which has many routines and strategies in common with the MIKE Redux pipeline. While HiRes Redux produces lower noise spectra overall, and often traces weak orders more accurately, the MAKEE results are accurate and sufficient for our analysis, particularly since we explicitly avoid regions with sky emission or absorption features entirely. Example spectra for the five M31 GCs are shown in

---

[1]MAKEE was developed by T. A. Barlow specifically for reduction of Keck HIRES data. It is freely available on the Web at http://spider.ipac.caltech.edu/staff/tab/makee/index.html .

Cluster	Exposure (s)	S/N (pixel^{-1})		
		4400 Å	6050 Å	7550 Å
G108-B045	16,200	40	60	80
G219-B358	10,500	40	60	70
G315-B381	14,300	30	50	60
G322-B386	12,600	30	50	60
G351-B405	10,800	40	60	80

Table 2.2. Observation Log and Estimated S/N

Figure 2.2, where it can be seen that many individual Fe I, Fe II, Mg I and Ti II lines are easily identified.

2.3 Velocity Dispersions

One of the strengths of our ILS analysis is the amount of information and the number of constraints available in the high resolution spectra. In addition to checks related to the abundance measurements themselves (see § 2.4.3), we also have overall photometric colors, magnitudes, and internal kinematics (velocity dispersions). Mass estimates from velocity dispersions can also help to constrain the basic initial mass function, contributing to the overall consistency of our understanding of the stellar population. Measurements of the velocity dispersions also tell us the spectral line resolutions we can expect for our abundance analysis. We compare these results to measurements in the literature when available.

We measure velocity dispersions from the high resolution IL spectra of the M31 GCs following the method described in Tonry & Davis (1979), which is implemented in the IRAF[2] task $fxcor$. The GC spectrum is cross correlated on an order by order basis with a suitable template star. The full width at half-maximum of the cross correlation peaks (FWHM$_{cp}$) measured by $fxcor$ is then converted to a line-of-sight velocity dispersion (σ_{obs}) using an empirical relation between the two. This relation is established by cross correlating the original template star spectrum with artificially

Cluster	σ_{obs} (km s^{-1})	RMS	N_{ord}	Error	σ_{best} (km s^{-1})	RMS	N_{best}	Error	$\sigma_{lit}{}^a$ (km s^{-1})
G108-B045	10.24	0.44	26	0.09	10.14	0.37	9	0.12	9.82 ± 0.18
G219-B358	10.99	1.00	13	0.28	10.36	0.84	5	0.38	8.11 ± 0.36
G315-B381	9.87	0.43	28	0.08	9.65	0.41	10	0.13	$< 10^b$
G322-B386	11.42	0.58	19	0.13	11.35	0.37	6	0.15	11.49 ± 0.24
G351-B405	12.29	1.06	16	0.27	12.01	0.41	7	0.15	8.57 ± 0.45

Table 2.3. Velocity Dispersion Measurements. *Notes* (a) Djorgovski et al. (1997), (b) Peterson (1989). All measured velocity dispersions are given without application of aperture corrections (see § 2.3). σ_{obs} is the mean measured from all usable orders. σ_{best} is the mean measured for higher S/N orders between $4800-5800$ Å.

broadened versions of itself that are made by convolving it with Gaussian profiles corresponding to σ_{obs} of $2-25$ km s^{-1}. RGB stars are suitable template stars for old stellar populations; in this analysis, we use a spectrum of HR 8831 (type G8 III) taken during the 2006 September run as the template.

In Table 2.3 we report σ_{obs} and the associated 1-σ errors measured for orders between $4000-6800$ Å. Only orders with high S/N and weak atmospheric absorption are used in the cross correlation. We also avoid orders that include the saturated Balmer lines. Recently, Strader et al. (2009) have found a weak trend of σ_{obs} with wavelength in a fraction of the GCs they observed. We do not find any correlations between σ_{obs} and wavelength for G108, G315, or G322. However a small correlation exists for G219 and G351. Like Strader et al. (2009), we find σ_{obs} decreasing from blue to red orders by ~ 1 km s^{-1}. It is unclear if this is due to a color/metallicity mismatch of the GCs and the template star (these two GCs are the more metal-poor ones in our sample) or other systematic effect (see Strader et al., 2009, for a larger discussion). Because of this issue, in Table 2.3 we have reported σ_{best}, which is the dispersion obtained for a subset of the highest S/N orders between $4800-5800$ Å that do not show correlations with velocity dispersion and also give the smallest RMS errors. The number of orders used in each measurement are recorded in columns 4 and 7 of Table 2.3.

Four of the GCs observed here have σ_{obs} measurements in the literature from previous observations by Djorgovski et al. (1997). The spectra used by Djorgovski et al. (1997) were taken with a slightly narrower slit (1".15 × 7.0"), which will lead to a velocity dispersion roughly 0.5 km s^{-1} larger, which is comparable to the measurement

errors. We find that our measurements for G108 and G322 agree with those in Djorgovski et al. (1997) within the quoted errors, but our observed velocity dispersions for G219 and G351 are $2 - 4$ km s^{-1} larger. It is possible that the difference between our results and those of Djorgovski et al. (1997) are due to a difference in $v\sin i$ of the template star used in the cross correlation. The template used by Djorgovski et al. (1997) has $v\sin i = 7$ km s^{-1}. We measure a mean FWHM of 8 km s^{-1} from line widths in our template star. Note that this is a combination of the intrinsic stellar line width (including $v\sin i$) and the instrumental resolution, which is FWHM $= 7.7$ km s^{-1}based on an analysis of arc lines taken through the appropriate slit. This suggests that the rotational velocity of the star is quite small (less than or equal to roughly 1 km s^{-1} when added in quadrature). The lower $v\sin i$ of our template could therefore cause the higher inferred σ_{obs} found here. Both our measurements and those of Djorgovski et al. (1997) require an additional correction of approximately $+14\%$ to convert σ_{obs} to a projected central σ_v as described in Djorgovski et al. (1997). This is the geometrical correction appropriate to obtain a systemic line of sight velocity dispersion from a velocity dispersion measured within a radius of $2 - 3 \times r_h$.

For completeness, we note that Barmby et al. (2007) have predicted aperture velocity dispersions for these same GCs by modeling surface brightness profiles. They have compared their predictions to observations of velocity dispersions in the literature to derive an empirical correction between the two. We note that our velocity dispersion measurements for G219 and G351 are more consistent with the trend derived by Barmby et al. (2007) than the measurements by Djorgovski et al. (1997). A velocity dispersion of 12.1 ± 1.3 km s^{-1} has also been measured by Strader et al. (2009), which is more consistent with the value we measure.

Finally, we report the first velocity dispersion measurement from high S/N, high spectral resolution, IL spectra for G315-B381. Our measurement of 9.65 ± 0.13 km s^{-1} is consistent with the upper limit of 10 km s^{-1} found by Peterson (1989).

Our velocity dispersions, when combined with GC r_h measurements in the literature, allow us to make order of magnitude estimates of the cluster M/L ratios. r_h for all of the GCs in this sample, with the exception of G315, can be found in

20
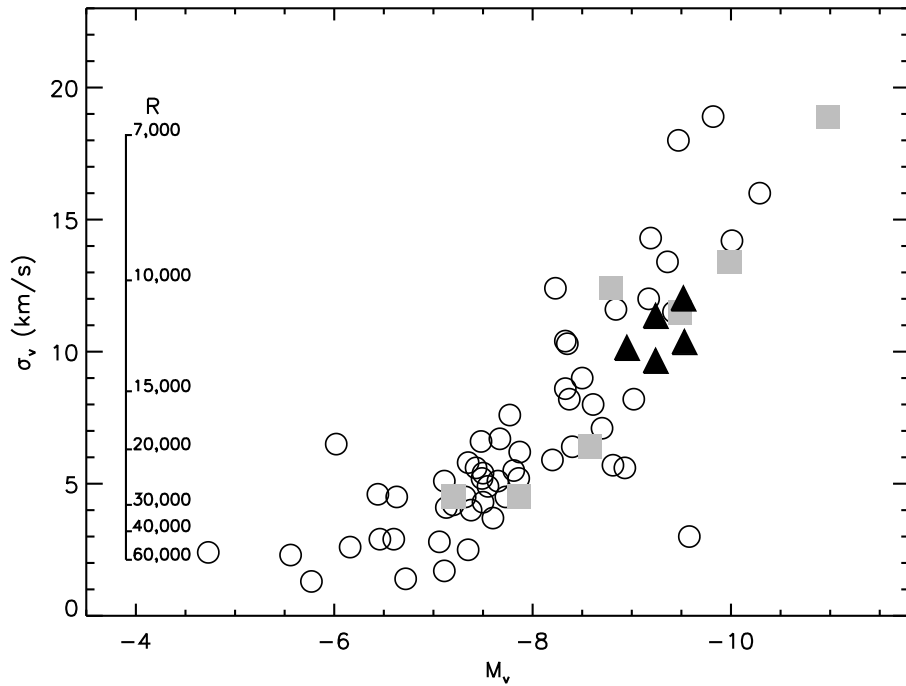
Figure 2.3. M_V-σ relation for Milky Way GCs (open circles), with data from Pryor & Meylan (1993) and Harris (1996). Training set Milky Way GCs are highlighted in gray squares and the five M31 GCs are shown as filled triangles. Training set and M31 GCs are plotted with reddening corrected V magnitudes and velocity dispersions from Pryor & Meylan (1993). The line width parameter R calculated for a range of velocity dispersions is shown on the inset axis.

Barmby et al. (2007). A simple calculation, following Spitzer (1987), assuming the virial theorem and an isotropic velocity distribution for the GCs results in dynamical M/L~1.5−2.5 for these four GCs. Here we have assumed $M = 2.5v^2r/G$, where r, the half-mass radius, is $1.3 \times r_h$, and v, the three-dimensional velocity dispersion is $\sqrt{3} \times \sigma$. We can also compare the dynamical M/L to those predicted with population synthesis models. In Percival et al. (2009), the Teramo group provides M/L ratios based on their isochrones and an appropriate IMF from Kroupa (2001). As we use the Teramo isochrones for our abundance analysis (see § 2.4.2), we can use isochrones which are self-consistent with our later analysis and well-matched to each cluster. Using our own abundance and age constraints, the most appropriate isochrones (ages and metallicities) for our clusters have a M/L~1.9−2.9 based on the Teramo group's population synthesis work. It is typical to obtain systematically different M/L from dynamical and population synthesis techniques; this difference is probably due to the inclusion of low mass stars in the population synthesis estimate, which are actually ejected in GCs due to dynamical evolution. We find a ratio between dynamical and population synthesis M/L ratios of 0.84 ± 0.27, which is consistent with the value of 0.73 ± 0.25 found by Barmby et al. (2007) for a larger sample of M31 GCs. McLaughlin & van der Marel (2005) find a similar ratio of 0.82 ± 0.07 for a sample of Milky Way and old LMC GCs. These M/L values further identify these four M31 GCs as consistent with the familiar Milky Way GC population.

The relationship described above between light and velocity dispersion is shown in Figure 2.3. The σ_{obs} for Milky Way GCs from Pryor & Meylan (1993), along with absolute magnitudes (M_V) listed by Harris (1996) are plotted as open circles. For comparison, we also plot the reddening-corrected magnitudes and velocity dispersions from Pryor & Meylan (1993) for our training set GCs as gray squares and those measured for the M31 GC sample as black triangles. From Figure 2.3 we see that the σ_{obs} measured here are consistent with what we would expect given the absolute magnitudes of this set of GCs.

The velocity dispersion that we measure above quantifies another important point about the clusters, which is the limiting resolution that we can obtain for individual

spectral lines due to velocity broadening. The velocity dispersions we measure for this set of M31 GCs of $9-12$ km s^{-1} give a line width parameter ($R = \lambda/\text{FWHM}$) $R =$ 14,000$-$10,000, from which it is clear that we are fully sampling the line profiles with the $R = 24,000$ spectral resolution provided by the slit configuration used here (the HIRES D3 decker). However, with dispersions this large we expect to have difficulty measuring equivalent widths for elements with weak lines ($\lesssim$30 mÅ), as we discuss in § 2.5.

2.4 Abundance Analysis

Our new method for obtaining detailed abundances of from their integrated light was developed and tested using a training set of Milky Way and LMC globular clusters. The basic method was described in detail in Bernstein & McWilliam (2002), Bernstein & McWilliam (2005), MB08, and the full training set is presented in S. Cameron et al. (2010) and Chapter 3 of this thesis. The method is briefly summarized below.

2.4.1 Equivalent Widths and Line Lists

We measure absorption line equivalent widths (EWs) for individual lines in the IL spectra using the semi-automated program GETJOB (McWilliam et al., 1995b), with which we fit low order polynomials to continuum regions and single Gaussian profiles to individual lines and double or triple Gaussians to line blends when necessary. Line lists and oscillator strengths were taken from McWilliam & Rich (1994), McWilliam et al. (1995a), McWilliam (1998), MB08 and Johnson et al. (2006). We measure fewer lines than in standard individual RGB star analyses, as lines in IL spectra are broader and weaker than in individual RGB stars due to the velocity dispersions of the GCs and the presence of continuum flux from warm stars. The lines and EWs included in our final analysis are listed in Table 2.4. As expected, we find fewer clean lines for the GCs with higher velocity dispersions.

Species	λ (Å)	EP (eV)	log gf	EW(mÅ) G108	EW(mÅ) G322	EW(mÅ) G315	EW(mÅ) G351	EW(mÅ) G219
Mg I	4571.102	0.000	-5.691	$\cdots$	120.0	$\cdots$	86.7	34.5
Mg I	4703.003	4.346	-0.666	$\cdots$	139.2	$\cdots$	99.8	$\cdots$
Mg I	5528.418	4.346	-0.341	$\cdots$	$\cdots$	$\cdots$	147.3	58.2
Mg I	5528.418	4.346	-0.341	$\cdots$	$\cdots$	$\cdots$	143.6	$\cdots$
Al I	3944.016	0.000	-0.638	$\cdots$	$\cdots$	$\cdots$	$\cdots$	134.9
Al I	3944.016	0.000	-0.638	$\cdots$	$\cdots$	$\cdots$	$\cdots$	140.1
Si I	7405.790	5.610	-0.660	58.4	$\cdots$	$\cdots$	$\cdots$	$\cdots$
Si I	7415.958	5.610	-0.730	66.4	$\cdots$	50.1	$\cdots$	$\cdots$
Si I	7423.509	5.620	-0.580	84.3	66.5	82.4	$\cdots$	$\cdots$
Ca I	4318.659	1.899	-0.295	$\cdots$	109.6	$\cdots$	$\cdots$	$\cdots$
Ca I	4425.444	1.879	-0.358	127.9	$\cdots$	$\cdots$	$\cdots$	46.6
Ca I	5581.979	2.523	-0.555	99.0	77.6	86.3	64.2	$\cdots$
Ca I	5588.764	2.526	0.358	$\cdots$	138.0	137.6	122.8	59.8
Ca I	5590.126	2.521	-0.571	101.4	96.6	89.6	74.2	$\cdots$
Ca I	5601.286	2.526	-0.690	112.3	91.9	89.7	53.3	21.3
Ca I	5857.459	2.933	0.240	$\cdots$	124.0	145.0	111.9	43.1
Ca I	6122.226	1.886	-0.320	$\cdots$	$\cdots$	$\cdots$	149.8	69.0
Ca I	6162.180	1.899	-0.090	$\cdots$	$\cdots$	$\cdots$	$\cdots$	89.0
Ca I	6166.440	2.520	-1.142	84.4	64.6	71.0	$\cdots$	$\cdots$
Ca I	6439.083	2.526	0.390	$\cdots$	$\cdots$	$\cdots$	147.8	57.9
Ca I	6471.662	2.526	-0.686	98.9	$\cdots$	78.8	70.0	$\cdots$
Ca I	6493.781	2.521	-0.109	$\cdots$	$\cdots$	124.8	94.3	42.7
Ca I	6572.795	0.000	-4.310	82.5	$\cdots$	$\cdots$	$\cdots$	$\cdots$
Ca I	7148.150	2.709	0.137	$\cdots$	133.5	146.4	131.3	$\cdots$
Sc II	4246.837	0.315	0.240	$\cdots$	$\cdots$	141.7	$\cdots$	78.3
Sc II	4670.413	1.357	-0.580	84.3	86.4	86.9	$\cdots$	$\cdots$
Sc II	5526.821	1.768	0.020	79.4	62.2	76.5	52.2	$\cdots$
Sc II	6604.600	1.357	-1.480	44.6	$\cdots$	$\cdots$	$\cdots$	$\cdots$
Ti I	4991.072	0.836	0.380	$\cdots$	$\cdots$	$\cdots$	134.2	$\cdots$
Ti I	4999.510	0.826	0.250	143.5	122.0	134.8	129.7	$\cdots$
Ti I	5039.964	0.021	-1.130	115.9	$\cdots$	$\cdots$	$\cdots$	$\cdots$
Ti I	5210.392	0.048	-0.884	$\cdots$	140.1	$\cdots$	$\cdots$	$\cdots$
Ti I	5401.379	0.818	-2.890	$\cdots$	$\cdots$	9.4	$\cdots$	$\cdots$
Ti I	5648.565	2.495	-0.260	17.3	$\cdots$	$\cdots$	$\cdots$	$\cdots$
Ti I	5866.451	1.067	-0.840	88.4	71.7	$\cdots$	46.3	$\cdots$
Ti I	6743.127	0.900	-1.630	53.4	$\cdots$	55.3	30.5	$\cdots$

Ti II	4395.040	1.084	-0.660	$\cdots$	$\cdots$	$\cdots$	$\cdots$	106.5
Ti II	4395.848	1.243	-2.170	98.7	$\cdots$	$\cdots$	$\cdots$	$\cdots$
Ti II	4399.778	1.237	-1.270	137.7	$\cdots$	136.6	$\cdots$	$\cdots$
Ti II	4418.342	1.237	-2.460	85.2	$\cdots$	73.6	$\cdots$	$\cdots$
Ti II	4501.278	1.116	-0.760	$\cdots$	150.1	$\cdots$	$\cdots$	$\cdots$
Ti II	4563.766	1.221	-0.960	$\cdots$	155.6	136.4	126.3	68.9
Ti II	4571.982	1.572	-0.530	$\cdots$	$\cdots$	$\cdots$	156.5	76.7
Ti II	4589.953	1.237	-1.790	82.6	91.7	77.2	$\cdots$	44.5
Ti II	5381.010	1.566	-2.080	92.0	60.6	75.3	$\cdots$	$\cdots$
V I	6039.730	1.060	-0.650	39.5	$\cdots$	$\cdots$	$\cdots$	$\cdots$
V I	6081.430	1.050	-0.580	50.6	41.8	32.2	$\cdots$	$\cdots$
V I	6274.658	0.270	-1.670	37.6	$\cdots$	$\cdots$	$\cdots$	$\cdots$
Cr I	4254.346	0.000	-0.114	$\cdots$	$\cdots$	$\cdots$	$\cdots$	83.5
Cr I	4274.806	0.000	-0.231	$\cdots$	$\cdots$	$\cdots$	$\cdots$	67.3
Cr I	4274.806	0.000	-0.231	$\cdots$	$\cdots$	$\cdots$	$\cdots$	67.1
Cr I	5206.044	0.941	0.019	$\cdots$	$\cdots$	$\cdots$	$\cdots$	84.5
Cr I	5208.432	0.941	0.158	$\cdots$	$\cdots$	$\cdots$	$\cdots$	87.2
Cr I	5208.432	0.941	0.158	$\cdots$	$\cdots$	$\cdots$	$\cdots$	93.3
Cr I	5409.799	1.030	-0.720	$\cdots$	144.7	134.0	118.7	36.8
Cr I	7400.188	2.900	-0.111	85.9	$\cdots$	76.9	$\cdots$	$\cdots$
Mn I	4754.039	2.282	-0.086	103.9	73.1	80.4	$\cdots$	$\cdots$
Mn I	6013.520	3.070	-0.250	63.7	38.1	38.7	$\cdots$	$\cdots$
Mn I	6016.620	3.070	-0.216	73.4	$\cdots$	44.7	$\cdots$	$\cdots$
Mn I	6021.820	3.070	0.034	65.1	44.5	62.5	36.6	$\cdots$
Fe I	3878.027	0.958	-0.896	$\cdots$	$\cdots$	$\cdots$	$\cdots$	85.3
Fe I	3899.719	0.087	-1.515	$\cdots$	$\cdots$	$\cdots$	$\cdots$	143.7
Fe I	4063.605	1.557	0.062	$\cdots$	$\cdots$	$\cdots$	$\cdots$	133.0
Fe I	4071.749	1.608	-0.008	$\cdots$	$\cdots$	$\cdots$	$\cdots$	120.5
Fe I	4114.451	2.831	-1.303	72.4	$\cdots$	50.7	$\cdots$	$\cdots$
Fe I	4132.067	1.608	-0.675	$\cdots$	$\cdots$	$\cdots$	$\cdots$	93.4
Fe I	4132.908	2.845	-1.005	$\cdots$	$\cdots$	$\cdots$	$\cdots$	45.3
Fe I	4147.675	1.485	-2.071	$\cdots$	109.8	$\cdots$	$\cdots$	$\cdots$
Fe I	4154.505	2.831	-0.688	$\cdots$	$\cdots$	$\cdots$	$\cdots$	33.6
Fe I	4156.806	2.831	-0.808	$\cdots$	$\cdots$	131.7	$\cdots$	$\cdots$
Fe I	4157.788	3.417	-0.403	82.9	$\cdots$	71.8	$\cdots$	$\cdots$
Fe I	4174.917	0.915	-2.938	$\cdots$	100.8	75.8	$\cdots$	45.1
Fe I	4174.917	0.915	-2.938	$\cdots$	$\cdots$	113.5	$\cdots$	$\cdots$
Fe I	4175.643	2.845	-0.827	105.6	102.9	90.2	$\cdots$	20.0
Fe I	4181.764	2.831	-0.371	$\cdots$	$\cdots$	$\cdots$	$\cdots$	50.3
Fe I	4182.387	3.017	-1.180	82.1	$\cdots$	74.0	$\cdots$	$\cdots$
Fe I	4187.047	2.449	-0.514	$\cdots$	136.1	$\cdots$	$\cdots$	56.1

Species	λ (Å)	EP	log gf					
Fe I	4191.437	2.469	-0.666	$\cdots$	$\cdots$	$\cdots$	$\cdots$	59.5
Fe I	4195.340	3.332	-0.492	$\cdots$	$\cdots$	$\cdots$	123.5	$\cdots$
Fe I	4199.105	3.047	0.156	$\cdots$	$\cdots$	135.9	$\cdots$	$\cdots$
Fe I	4202.040	1.485	-0.689	$\cdots$	$\cdots$	$\cdots$	$\cdots$	96.3
Fe I	4206.702	0.052	-3.960	140.1	$\cdots$	115.6	87.1	$\cdots$
Fe I	4216.191	0.000	-3.357	$\cdots$	$\cdots$	$\cdots$	93.3	47.6
Fe I	4222.221	2.449	-0.914	120.7	110.4	119.6	$\cdots$	50.2
Fe I	4227.440	3.332	0.266	$\cdots$	$\cdots$	$\cdots$	$\cdots$	73.7
Fe I	4233.612	2.482	-0.579	$\cdots$	$\cdots$	142.9	$\cdots$	$\cdots$
Fe I	4250.130	2.469	-0.380	$\cdots$	$\cdots$	$\cdots$	$\cdots$	69.4
Fe I	4250.797	1.557	-0.713	$\cdots$	$\cdots$	$\cdots$	$\cdots$	86.4
Fe I	4260.486	2.399	0.077	$\cdots$	$\cdots$	$\cdots$	$\cdots$	94.9
Fe I	4271.164	2.449	-0.337	$\cdots$	$\cdots$	$\cdots$	$\cdots$	78.3
Fe I	4271.774	1.485	-0.173	$\cdots$	$\cdots$	$\cdots$	$\cdots$	138.1
Fe I	4282.412	2.176	-0.779	$\cdots$	$\cdots$	$\cdots$	131.8	86.8
Fe I	4325.775	1.608	0.006	$\cdots$	$\cdots$	$\cdots$	$\cdots$	139.1
Fe I	4337.055	1.557	-1.704	$\cdots$	127.5	$\cdots$	$\cdots$	$\cdots$
Fe I	4369.779	3.047	-0.803	$\cdots$	88.9	$\cdots$	$\cdots$	$\cdots$
Fe I	4404.761	1.557	-0.147	$\cdots$	$\cdots$	$\cdots$	$\cdots$	142.2
Fe I	4415.135	1.608	-0.621	$\cdots$	$\cdots$	$\cdots$	$\cdots$	121.6
Fe I	4427.317	0.052	-2.924	$\cdots$	$\cdots$	$\cdots$	$\cdots$	96.0
Fe I	4430.622	2.223	-1.728	$\cdots$	$\cdots$	138.1	$\cdots$	$\cdots$
Fe I	4442.349	2.198	-1.228	$\cdots$	135.2	144.2	$\cdots$	$\cdots$
Fe I	4443.201	3.071	-1.043	$\cdots$	$\cdots$	$\cdots$	$\cdots$	21.7
Fe I	4447.728	2.223	-1.339	$\cdots$	114.4	119.3	$\cdots$	$\cdots$
Fe I	4466.562	0.110	-0.600	$\cdots$	128.0	139.1	$\cdots$	$\cdots$
Fe I	4494.573	2.198	-1.143	$\cdots$	141.3	$\cdots$	$\cdots$	$\cdots$
Fe I	4602.949	1.485	-2.208	142.7	105.5	113.7	97.8	45.4
Fe I	4632.918	1.608	-2.901	107.6	$\cdots$	98.3	$\cdots$	$\cdots$
Fe I	4691.420	2.990	-1.523	$\cdots$	146.1	76.1	78.6	$\cdots$
Fe I	4736.783	3.211	-0.752	106.3	107.2	113.8	$\cdots$	$\cdots$
Fe I	4871.325	2.865	-0.362	$\cdots$	157.9	$\cdots$	$\cdots$	$\cdots$
Fe I	4872.144	2.882	-0.567	$\cdots$	158.2	$\cdots$	128.7	$\cdots$
Fe I	4890.763	2.875	-0.394	$\cdots$	$\cdots$	$\cdots$	154.0	$\cdots$
Fe I	4891.502	2.851	-0.111	$\cdots$	$\cdots$	$\cdots$	141.9	$\cdots$
Fe I	4903.316	2.882	-0.926	$\cdots$	130.6	137.8	123.8	$\cdots$
Fe I	4918.998	2.865	-0.342	$\cdots$	$\cdots$	$\cdots$	141.7	60.9
Fe I	4920.514	2.832	0.068	$\cdots$	$\cdots$	$\cdots$	$\cdots$	90.6
Fe I	4966.095	3.332	-0.871	125.4	$\cdots$	113.8	84.8	78.8
Fe I	4994.138	0.915	-2.969	137.1	125.1	112.6	128.7	$\cdots$
Fe I	5001.870	3.881	0.050	102.5	$\cdots$	92.2	109.0	$\cdots$
Fe I	5014.951	3.943	-0.303	102.9	$\cdots$	81.2	$\cdots$	$\cdots$
Fe I	5049.827	2.279	-1.355	$\cdots$	157.2	134.8	111.7	$\cdots$
Fe I	5051.640	0.915	-2.764	$\cdots$	158.7	144.0	124.4	$\cdots$
Fe I	5068.771	2.940	-1.041	132.4	111.5	106.9	85.8	$\cdots$

Fe I	5074.753	4.220	-0.160	85.2	$\cdots$	87.1	$\cdots$	$\cdots$
Fe I	5083.345	0.958	-2.842	$\cdots$	131.4	122.3	109.3	$\cdots$
Fe I	5110.435	4.260	-3.758	$\cdots$	$\cdots$	$\cdots$	136.0	$\cdots$
Fe I	5123.730	1.011	-3.058	$\cdots$	$\cdots$	$\cdots$	148.4	$\cdots$
Fe I	5127.368	0.915	-3.249	$\cdots$	113.9	$\cdots$	$\cdots$	$\cdots$
Fe I	5216.283	1.608	-2.082	142.5	122.4	140.3	95.9	$\cdots$
Fe I	5225.534	0.110	-4.755	114.2	$\cdots$	$\cdots$	$\cdots$	$\cdots$
Fe I	5232.952	2.940	-0.057	$\cdots$	$\cdots$	$\cdots$	141.9	$\cdots$
Fe I	5269.550	0.859	-1.333	$\cdots$	$\cdots$	$\cdots$	$\cdots$	156.0
Fe I	5281.798	3.038	-0.833	142.6	$\cdots$	101.9	75.1	$\cdots$
Fe I	5283.629	3.241	-0.524	$\cdots$	148.2	$\cdots$	$\cdots$	$\cdots$
Fe I	5383.380	4.312	0.645	126.4	97.9	103.7	94.4	34.0
Fe I	5393.176	3.241	-0.715	117.1	103.3	91.0	74.3	$\cdots$
Fe I	5397.141	0.915	-1.982	$\cdots$	$\cdots$	$\cdots$	$\cdots$	99.8
Fe I	5405.785	0.990	-1.852	$\cdots$	$\cdots$	$\cdots$	$\cdots$	108.9
Fe I	5424.080	4.320	0.520	149.5	108.2	111.9	115.4	39.2
Fe I	5429.706	0.958	-1.881	$\cdots$	$\cdots$	$\cdots$	$\cdots$	122.5
Fe I	5434.534	1.011	-2.126	$\cdots$	$\cdots$	$\cdots$	$\cdots$	98.7
Fe I	5446.924	0.990	-3.109	$\cdots$	$\cdots$	$\cdots$	$\cdots$	103.7
Fe I	5497.526	1.011	-2.825	$\cdots$	143.7	$\cdots$	135.7	66.6
Fe I	5501.477	0.958	-3.046	147.7	134.1	122.2	97.5	$\cdots$
Fe I	5506.791	0.990	-2.789	$\cdots$	155.3	$\cdots$	136.0	65.6
Fe I	5569.631	3.417	-0.500	128.1	104.9	101.2	$\cdots$	30.3
Fe I	5572.851	3.396	-0.275	$\cdots$	141.8	141.9	$\cdots$	38.9
Fe I	5576.099	3.430	-0.900	103.6	85.3	81.3	$\cdots$	$\cdots$
Fe I	5586.771	4.260	-0.096	$\cdots$	$\cdots$	145.2	$\cdots$	57.5
Fe I	5763.002	4.209	-0.450	74.3	73.5	85.5	$\cdots$	$\cdots$
Fe I	6136.624	2.453	-1.410	$\cdots$	$\cdots$	$\cdots$	$\cdots$	67.0
Fe I	6137.702	2.588	-1.346	$\cdots$	150.5	$\cdots$	105.5	54.6
Fe I	6151.623	2.180	-3.330	51.6	$\cdots$	47.2	$\cdots$	$\cdots$
Fe I	6173.341	2.220	-2.863	71.7	61.7	60.9	54.6	$\cdots$
Fe I	6180.209	2.730	-2.628	$\cdots$	$\cdots$	50.3	26.0	$\cdots$
Fe I	6187.995	3.940	-1.673	40.7	$\cdots$	26.7	$\cdots$	$\cdots$
Fe I	6200.321	2.610	-2.386	73.8	54.5	62.1	$\cdots$	$\cdots$
Fe I	6219.287	2.200	-2.428	99.1	$\cdots$	81.9	69.4	$\cdots$
Fe I	6229.232	2.830	-2.821	40.9	$\cdots$	29.9	$\cdots$	$\cdots$
Fe I	6230.736	2.559	-1.276	$\cdots$	$\cdots$	$\cdots$	125.2	44.7
Fe I	6246.327	3.600	-0.796	101.0	$\cdots$	91.9	91.7	$\cdots$
Fe I	6252.565	2.404	-1.767	120.9	$\cdots$	104.3	107.5	44.5
Fe I	6254.253	2.280	-2.435	114.4	$\cdots$	105.7	82.6	$\cdots$
Fe I	6265.141	2.180	-2.532	96.8	$\cdots$	94.8	72.4	$\cdots$
Fe I	6270.231	2.860	-2.543	46.0	$\cdots$	43.7	22.1	$\cdots$
Fe I	6297.799	2.220	-2.669	101.4	$\cdots$	$\cdots$	$\cdots$	$\cdots$
Fe I	6335.337	2.200	-2.175	$\cdots$	$\cdots$	108.9	81.7	31.0
Fe I	6336.830	3.690	-0.667	$\cdots$	$\cdots$	89.9	69.1	$\cdots$

Fe I	6355.035	2.840	-2.328	$\cdots$	$\cdots$	75.2	51.8	$\cdots$
Fe I	6393.612	2.430	-1.505	$\cdots$	$\cdots$	129.3	134.7	47.3
Fe I	6411.658	3.650	-0.646	$\cdots$	$\cdots$	94.4	73.5	$\cdots$
Fe I	6421.360	2.280	-1.979	$\cdots$	$\cdots$	$\cdots$	83.1	$\cdots$
Fe I	6430.856	2.180	-1.954	$\cdots$	$\cdots$	117.6	86.3	$\cdots$
Fe I	6481.878	2.280	-2.985	74.3	$\cdots$	$\cdots$	$\cdots$	$\cdots$
Fe I	6494.994	2.400	-1.246	$\cdots$	$\cdots$	$\cdots$	151.1	73.8
Fe I	6498.945	0.960	-4.675	94.2	$\cdots$	$\cdots$	$\cdots$	$\cdots$
Fe I	6546.252	2.750	-1.536	128.4	$\cdots$	$\cdots$	$\cdots$	$\cdots$
Fe I	6569.224	4.730	-0.380	61.6	52.7	$\cdots$	$\cdots$	$\cdots$
Fe I	6593.874	2.430	-2.377	$\cdots$	85.1	74.7	64.5	$\cdots$
Fe I	6677.997	2.690	-1.395	$\cdots$	$\cdots$	123.1	$\cdots$	30.5
Fe I	6703.576	2.760	-3.059	42.3	$\cdots$	39.9	$\cdots$	$\cdots$
Fe I	6710.323	1.480	-4.807	44.3	$\cdots$	$\cdots$	$\cdots$	$\cdots$
Fe I	6750.164	2.420	-2.592	89.7	71.8	71.1	86.3	$\cdots$
Fe I	6806.856	2.730	-2.633	32.6	$\cdots$	$\cdots$	$\cdots$	$\cdots$
Fe I	6839.835	2.560	-3.378	28.8	$\cdots$	$\cdots$	$\cdots$	$\cdots$
Fe I	6841.341	4.610	-0.733	$\cdots$	$\cdots$	41.1	$\cdots$	$\cdots$
Fe I	7130.925	4.300	-0.708	86.9	$\cdots$	$\cdots$	$\cdots$	$\cdots$
Fe I	7411.162	4.280	-0.287	$\cdots$	83.7	72.6	$\cdots$	$\cdots$
Fe I	7445.758	4.260	0.053	104.9	92.2	98.8	$\cdots$	$\cdots$
Fe I	7461.527	2.560	-3.507	55.7	$\cdots$	45.3	$\cdots$	$\cdots$
Fe I	7491.652	4.280	-1.067	70.1	55.8	$\cdots$	$\cdots$	$\cdots$
Fe I	7531.153	4.370	-0.557	$\cdots$	$\cdots$	64.1	$\cdots$	$\cdots$
Fe II	4178.859	2.583	-2.489	$\cdots$	61.6	51.1	$\cdots$	$\cdots$
Fe II	4178.859	2.583	-2.489	$\cdots$	$\cdots$	78.5	$\cdots$	$\cdots$
Fe II	4233.169	2.583	-1.900	$\cdots$	$\cdots$	131.2	$\cdots$	$\cdots$
Fe II	4508.289	2.856	-2.318	93.1	73.2	65.4	$\cdots$	$\cdots$
Fe II	4515.343	2.844	-2.422	102.1	84.3	97.1	$\cdots$	$\cdots$
Fe II	4541.523	2.856	-3.030	$\cdots$	$\cdots$	60.3	$\cdots$	$\cdots$
Fe II	4583.839	2.807	-1.890	130.1	131.4	140.2	131.0	61.2
Fe II	4923.930	2.891	-1.307	135.5	118.8	125.8	121.8	74.7
Fe II	5018.450	2.891	-1.292	$\cdots$	147.0	$\cdots$	136.7	84.1
Fe II	5534.848	3.245	-2.790	59.6	$\cdots$	$\cdots$	$\cdots$	$\cdots$
Fe II	6456.391	3.903	-2.075	$\cdots$	$\cdots$	56.0	$\cdots$	$\cdots$
Co I	6770.970	1.880	-1.970	49.5	$\cdots$	$\cdots$	$\cdots$	$\cdots$
Co I	6814.961	1.956	-1.900	45.8	$\cdots$	$\cdots$	$\cdots$	$\cdots$
Co I	6872.440	2.010	-1.850	51.9	$\cdots$	$\cdots$	$\cdots$	$\cdots$
Ni I	6586.319	1.951	-2.810	56.2	$\cdots$	$\cdots$	$\cdots$	$\cdots$
Ni I	6643.638	1.676	-2.300	97.8	97.7	83.3	$\cdots$	$\cdots$
Ni I	6767.784	1.826	-2.170	91.4	79.3	67.5	$\cdots$	$\cdots$
Ni I	7122.206	3.542	0.040	98.6	$\cdots$	$\cdots$	$\cdots$	$\cdots$

Ni I	7393.609	3.606	-0.270	$\cdots$	$\cdots$	66.8	$\cdots$	$\cdots$
Ni I	7414.514	1.986	-2.570	101.8	$\cdots$	63.3	$\cdots$	$\cdots$
Ni I	7422.286	3.635	-0.140	$\cdots$	63.3	62.8	$\cdots$	$\cdots$
Ni I	7525.118	3.635	-0.520	$\cdots$	$\cdots$	37.1	$\cdots$	$\cdots$
Y II	4883.690	1.084	0.070	72.0	$\cdots$	73.5	$\cdots$	$\cdots$
Ba II	4554.036	0.000	0.163	$\cdots$	$\cdots$	$\cdots$	$\cdots$	85.0
Ba II	4934.095	0.000	-0.157	$\cdots$	$\cdots$	$\cdots$	$\cdots$	90.5
Ba II	5853.688	0.604	-1.010	$\cdots$	$\cdots$	87.8	86.5	$\cdots$
Ba II	6141.727	0.704	-0.076	$\cdots$	142.4	$\cdots$	112.9	67.5
Ba II	6496.908	0.604	-0.377	$\cdots$	$\cdots$	$\cdots$	141.8	59.4

Table 2.4: Line Parameters and Integrated Light Equivalent Widths for M31 GCs. *Notes*: Lines listed twice correspond to those measured in adjacent orders with overlapping wavelength coverage.

2.4.2 CMDs and EW Synthesis

In order to synthesize IL EWs to compare to our observed IL EWs, we next need to model the population using theoretical single age, single metallicity isochrones. During analyses of our training set GCs, we performed extensive testing of a variety of isochrones from the Padova[3] (Girardi et al., 2000) and Teramo[4] (Pietrinferni et al., 2004, 2006; Cordier et al., 2007) groups (see MB08). Because we require a large, self-consistent parameter space of both scaled-solar and $\alpha-$enhanced isochrones, we have chosen to use the isochrones from the Teramo group for our abundance analyses. The isochrones available cover abundances from Z=0.0001$-$0.04 for both scaled solar and $\alpha-$enhanced ratios. We choose to use the recommended canonical evolutionary tracks including an extended asymptotic giant branch (AGB) and $\alpha-$enhanced low$-$temperature opacities calculated according to Ferguson et al. (2005). We also choose isochrones with mass$-$loss parameter of η=0.2 because comparison with our training set GCs (particularly those of intermediate metallicity) show that they more accurately match the CMD of GCs; isochrones with η=0.4 over-predict the fraction of extreme blue horizontal branch (HB) stars at intermediate metallicities. Given that

[3]Padova isochrones downloadable at http://pleiadi.pd.astro.it/

[4]Teramo isochrones downloadable at http://albione.oa-teramo.inaf.it/

we find blue HB stars are less critical to accurate abundance analysis than red HB stars (see § 2.6.4), it is more important to our analysis that the isochrones accurately reproduce the red horizontal branch than that they populate the blue region of the horizontal branch when it may be present.

We apply an IMF according to the multiple−part power−law form described in Kroupa (2002), which changes index at $0.5M_\odot$ and $0.08M_\odot$. Because we only observed the core ($\sim$0.1-0.2$\times$r$_h$) regions in our training set GCs, we removed stars less massive than $\sim 0.7M_\odot$ from the IMF to match the present day core mass functions (MB08) that have experienced dynamical mass segregation and evaporation of low mass stars (e.g. Baumgardt & Makino, 2003). In this set of M31 GCs we have observed regions corresponding to $\sim$1.5-3r$_h$, well beyond the core region where significant mass segregation is expected. Although we do expect present day GCs to be stripped of stars less massive than $\sim 0.3M_\odot$ due to dynamical evaporation, the Teramo isochrones stop at $0.5M_\odot$. We do not believe that neglecting stars in the 0.3-0.5$M_\odot$ range is a problem for our analysis, as stars less massive than $0.5M_\odot$ contribute only $\sim$1-2% to the total flux of the population and <1% in absorption features. By combining the model isochrones with cluster-specific IMFs, we can create synthetic CMDs for the range of possible ages and metallicities for which we have isochrones. Each synthetic CMD is divided into $\sim$25 boxes of stars with similar properties, with every box containing $\sim$4% of the total V-band flux. The properties of a flux-weighted "average" star in each box are used for the atmospheric parameters needed in synthesizing IL flux-weighted EWs.

Flux-weighted synthesized EWs of lines are calculated using our routine ILABUNDS (see MB08) which produces an integrated light EW composed of the $\sim$25 representative stars in each CMD using spectral synthesis routines from MOOG (Sneden, 1973) and model stellar atmospheres from Kurucz (e.g. Castelli & Kurucz, 2004)[5]. The synthesized EWs of each of the $\sim$25 representative stars are averaged together, weighted by their respective contribution to the total flux of the cluster. The assumed abundance in the line synthesis is adjusted iteratively until the synthetic flux-weighted EW

---

[5]The models are available from R. L. Kurucz's Website at http://kurucz.harvard.edu/grids.html

matches the observed IL EW to 1%. Initial abundance calculations are performed using scaled−solar Teramo isochrones and Kurucz ODFNEW stellar atmospheres, and then recalculated with α-enhanced Teramo isochrones and AODFNEW atmospheres when abundance results imply enriched α−element ratios are present. All five M31 GCs analyzed here were determined to be α-enhanced, and thus the abundances we report use α-enhanced isochrones and AODFNEW atmospheres in all cases.

All abundances were calculated under the assumption of local thermodynamic equilibrium (LTE). In the case of aluminum we also discuss the non-LTE correction suggested by Baumueller & Gehren (1997) in § 2.5.3.

Our IL method as implemented here employs a fixed microturbulence law, as described in MB08. Since we do not adjust microturbulence values for individual stars in the synthetic CMDs we must be careful of line saturation. For this reason we only report abundances from lines with EW strengths less than $\sim$150 mÅ for all elements except Fe II. Our analysis indicates that abundances from Fe II lines with EWs over $\sim$100 mÅ start to deviate significantly from the linear portion of the curve of growth. To remain in the linear regime we avoid Fe II lines with EWs >100 mÅ wherever possible. In some GCs, like G351-B405, the only clean Fe II lines we measure have EWs >100 mÅ. Using these lines in those cases will result in Fe II abundances that may be slightly high. In this work we will refer to lines we do not analyze because of large EWs as "saturated" (>150 mÅ in general, or >100 mÅ for Fe II). We note that, in principle, abundance upper limits could be obtained for elements for which all lines are "saturated." However, due to the flux-weighting of EWs from stars of different types, this analysis requires special care and is not investigated further here.

We have also calculated hyperfine splitting (hfs) abundances for Al, Sc, V, Mn, Co, and Ba. For lines with EWs >20−30 mÅ, desaturation by hfs can significantly reduce the derived abundances. We use the hfs line lists given in MB08, Johnson et al. (2006), and references therein. Typical hfs abundances corrections here for Al, Sc, V, Mn, Co and Ba were -0.1, -0.01, -0.1, -0.4, -0.2, and -0.15 dex, respectively.

31

2.4.3   Finding the Best-Fitting CMD

In the course of our work with the Milky Way and LMC training set GCs, we have explored a variety of strategies for identifying the best-fitting CMD — the CMD which provides abundances that are most consistent with those obtained from the spectral analysis of individual RGB stars in those clusters. Our first efforts to identify the best-fitting CMD focused on obtaining a consistent [Fe/H] solution from the Fe I and Fe II lines. This strategy was discussed with regard to the analysis of 47 Tuc in Bernstein & McWilliam (2002, 2005), and MB08. However analysis of the full training set showed that the Fe I and Fe II lines typically give a self-consistent solution at [Fe/H] values that are frequently more metal-rich than those obtained from analysis of individual stars. There are several possible explanations for a difference in [Fe/H] from Fe I and Fe II lines, although a detailed study of this problem is beyond the scope of this thesis. We simply note here that a difference between Fe I and Fe II abundances in individual stars due to non-LTE overionization was noted by Kraft & Ivans (2003), and that inaccuracies in Fe II oscillator strengths can lead to large uncertainties in abundances (see recent discussion in Meléndez & Barbuy, 2009). These results have led us to focus on a different strategy. Using the training set spectra, we have found that the best-fitting CMD can be consistently identified by taking advantage of the fact that the metallicity dependence of RGB morphology is reasonably well understood (Gallart et al., 2005). After extensive testing, we have found that we obtain consistent, accurate abundances by requiring that the abundance used in calculating the isochrones themselves be consistent with the abundance recovered by our analysis for the Fe I lines. This is consistent with the fact that we find the RGB to have the dominant influence on the strength of the Fe I spectral lines, more so than on the Fe II lines, as discussed in MB08. To clarify our analysis methods, we describe below the procedure we follow for each GC.

For each CMD we calculate a mean [Fe/H] abundance from all available Fe I and Fe II lines. In this data set we measure $30-80$ Fe I lines and $2-10$ Fe II lines per GC. Fe abundance results for all CMDs for each GC are plotted in Figures 2.4 through 2.8. Circles and crosses correspond to Fe I and Fe II mean solutions. The horizontal
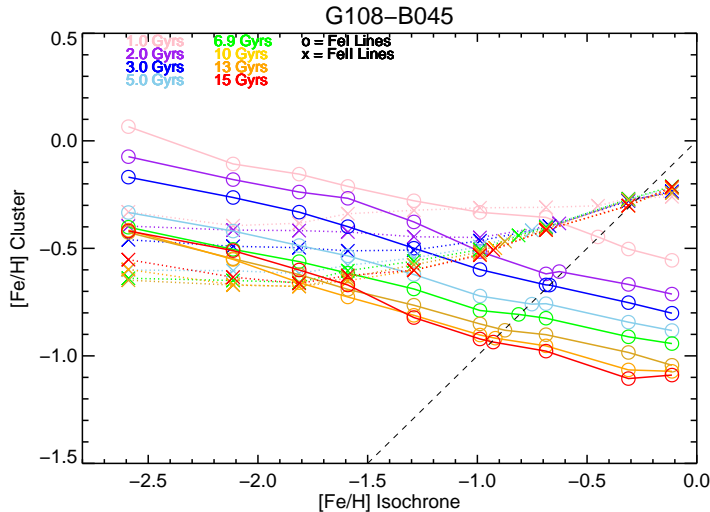
Figure 2.4. Fe I (circles) and Fe II (crosses) abundance solutions. The input [Fe/H] value of the isochrone (plotted on the x-axis) equals the output [Fe/H] value of our solution where circles lie on the dashed line.

axis shows the [Fe/H] of the $\alpha-$enhanced Teramo isochrones. CMDs of the same age are connected by colored lines. Note that $\alpha-$enrichment affects the [M/H] value of the isochrone; for clarity, the value plotted on the x-axis is the true [Fe/H] value rather than the overall metallicity [M/H] (see Pietrinferni et al., 2006).

As mentioned above, our criteria for selecting a best-fitting CMD is that the Fe abundance calculated from the Fe I lines is consistent with [Fe/H] used to produce the isochrone. This criteria is met where the solutions cross the dashed black lines in Figures 2.4 through 2.8. When the Fe I solution that crosses the dashed line for a given age (color) lies between two isochrones, we interpolate an appropriate isochrone according to the prescription recommended in Pietrinferni et al. (2006). We then have 7 possible solutions where isochrones intercept the dashed black line in Figure 2.4 — one abundance solution for each age.

We next isolate the best-fitting CMD out of these 7 using diagnostics commonly used in standard stellar abundance analyses. These diagnostics concern the stability of the [Fe/H] solutions, which should not depend on the parameters of the individual line (excitation potentials, wavelengths, or reduced EWs[6]). In principle, as in individ-

---

[6]Reduced EW $\equiv$ log(EW / wavelength)
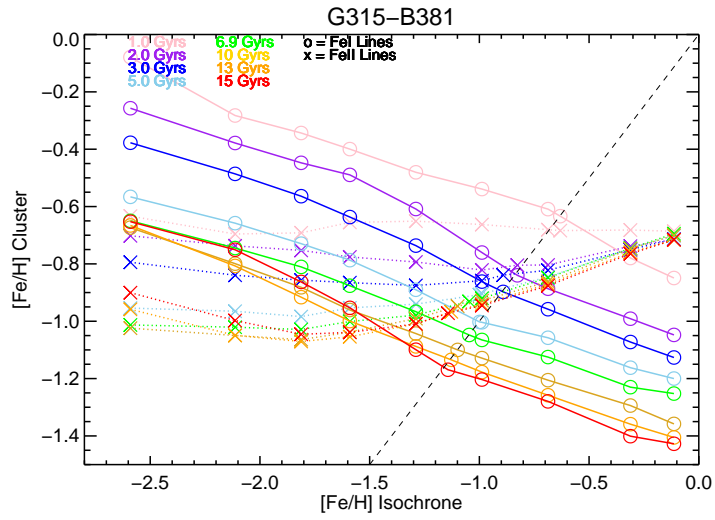
Figure 2.5. Same as Figure 2.4 for G315.
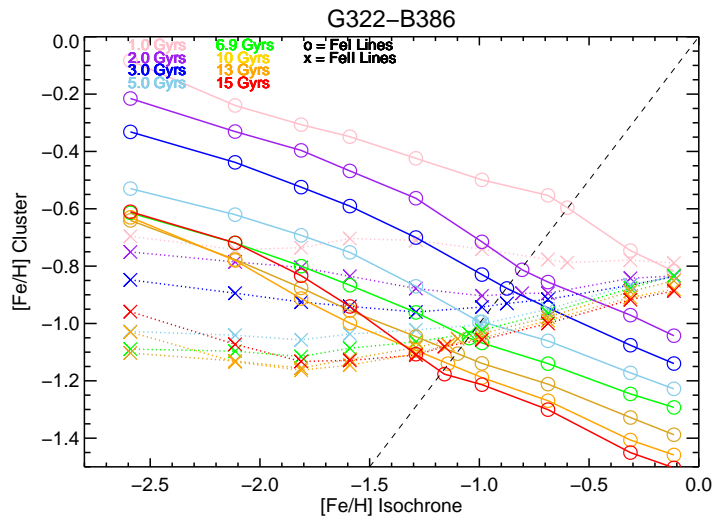
Figure 2.6. Same as Figure 2.4 for G322.
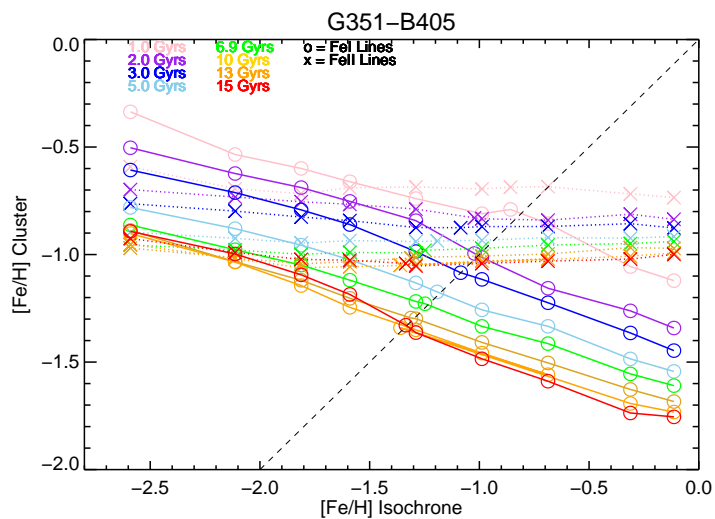
Figure 2.7. Same as Figure 2.4 for G351.
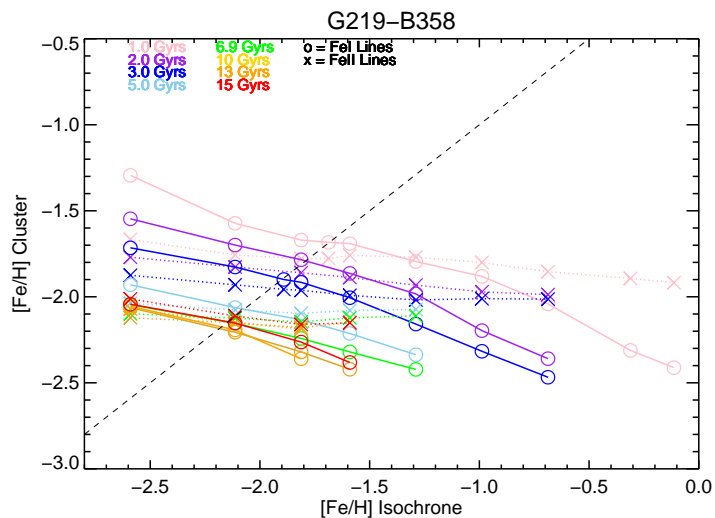
Figure 2.8. Same as Figure 2.4 for G219.

ual RGB stars, these diagnostics reflect the accuracies in the physical properties of the atmospheres used in the synthesis. The abundance versus excitation potential (EP) diagnostic is sensitive to the temperature of stars, while the abundance versus reduced EW diagnostic is sensitive to the microturbulent velocities of stars. The abundance versus wavelength diagnostic is potentially sensitive to the age of the CMD, because stars of different temperatures dominate the IL flux at different wavelengths. Unlike in RGB stars, in an IL spectrum, correlations with EP and wavelength can be caused by an inaccurate temperature distribution of stars in the CMD, which, for example, could be the result inaccurate modeling of HB morphology in the isochrones. Likewise, correlations with reduced EW can be the result of inaccurate proportions of stars of different gravities as well as a symptom of an inaccurate microturbulent velocity law. These effects are difficult to unravel without additional constraints on the CMD, and identifying these is not the primary goal of this work. We therefore take the existence of any correlations merely as an indication that a given isochrone is less representative of the true CMD then one with weaker correlations. We attempt to identify a best-fitting CMD solution by selecting an isochrone that minimizes these correlations. We use linear least squares fits between [Fe/H] and these parameters to identify and quantify the strength of any existing correlations. Plots illustrating the behavior of the Fe abundances with EP, wavelength, and reduced EW are shown in Figures 2.9 through 2.13. From these plots, we obtain 5 diagnostics: the slope of [Fe/H] with EP, wavelength and reduced EW, and the standard deviation of the [Fe/H] solution for Fe I lines and Fe II lines.

For any one of these diagnostics, there is not a statistically significant difference between the quality of the solution from CMDs within a range of ± 5 Gyrs. For example, the slope of the [Fe/H] vs. EP relationship in Figure 2.10 for G315 looks essentially the same for CMDS between ages 5 and 15 Gyrs. However, while the difference in these diagnostics may be small over a wide range in CMD age, we do find that they change monotonically, and are strongly correlated with each other. This suggests that there is clearly a preferred age and [Fe/H] range of CMD for each GC.
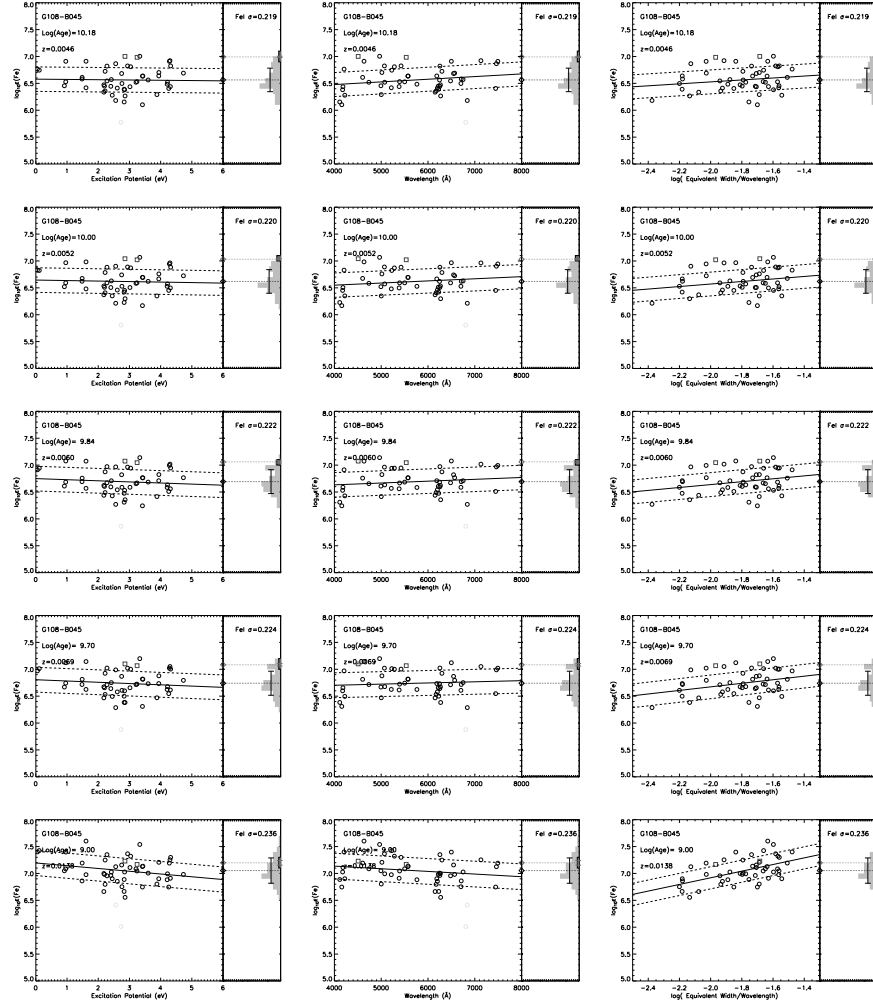
Figure 2.9. Diagnostic plots for G108-B045, for ages of 15, 10, 7, 5, and 1 Gyr (top to bottom). Oldest solutions have smallest Fe I standard deviation and smallest dependence on EP, wavelength, or or reduced equivalent width (log(EW/wavelength)) for this cluster. Fe I and Fe II lines are marked by dark circles and light squares, respectively. Gray points mark lines rejected by a sigma clipping routine when calculating the mean abundances. The solid line shows the linear fit to the Fe I lines and dashed lines show the 1 σ deviation of points around the fit. Dark and light diamonds mark the final average Fe I and Fe II abundances.
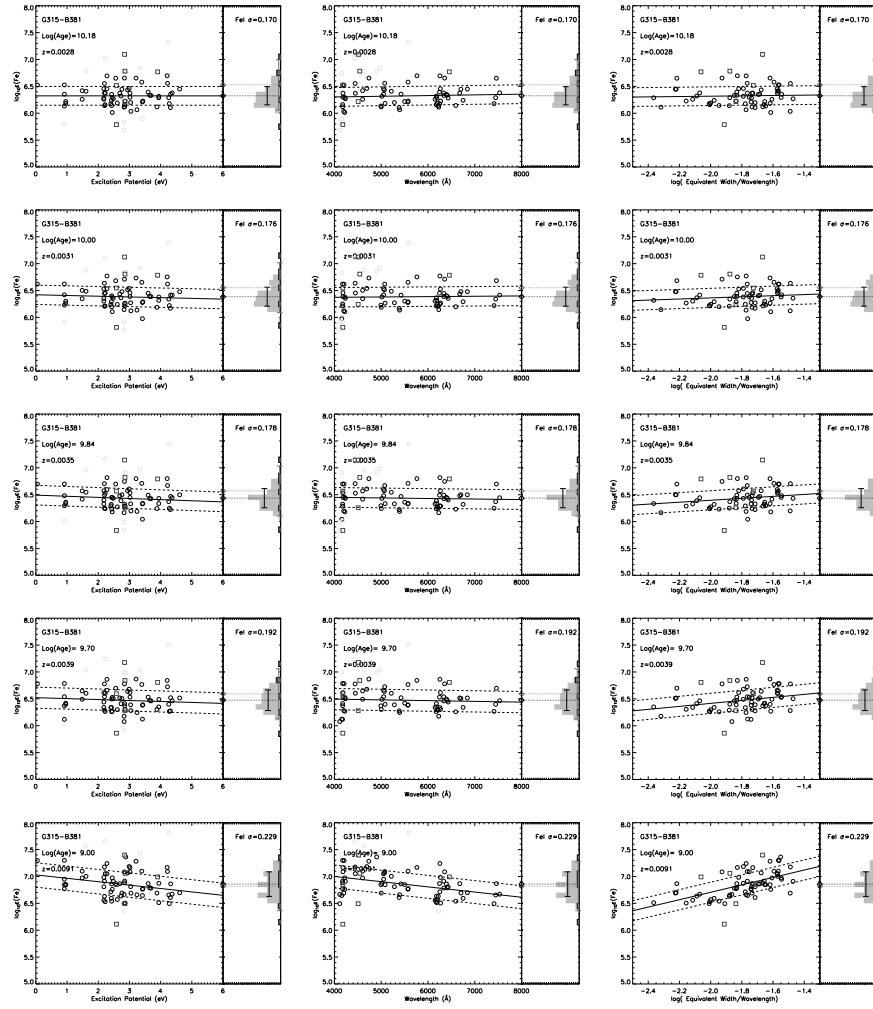
Figure 2.10. Diagnostics for G315-B381. The smallest Fe I standard deviation and smallest dependence on EP, wavelength, and observed equivalent width at ages of 10-15 Gyr. Symbols are the same as in Figure 2.9.
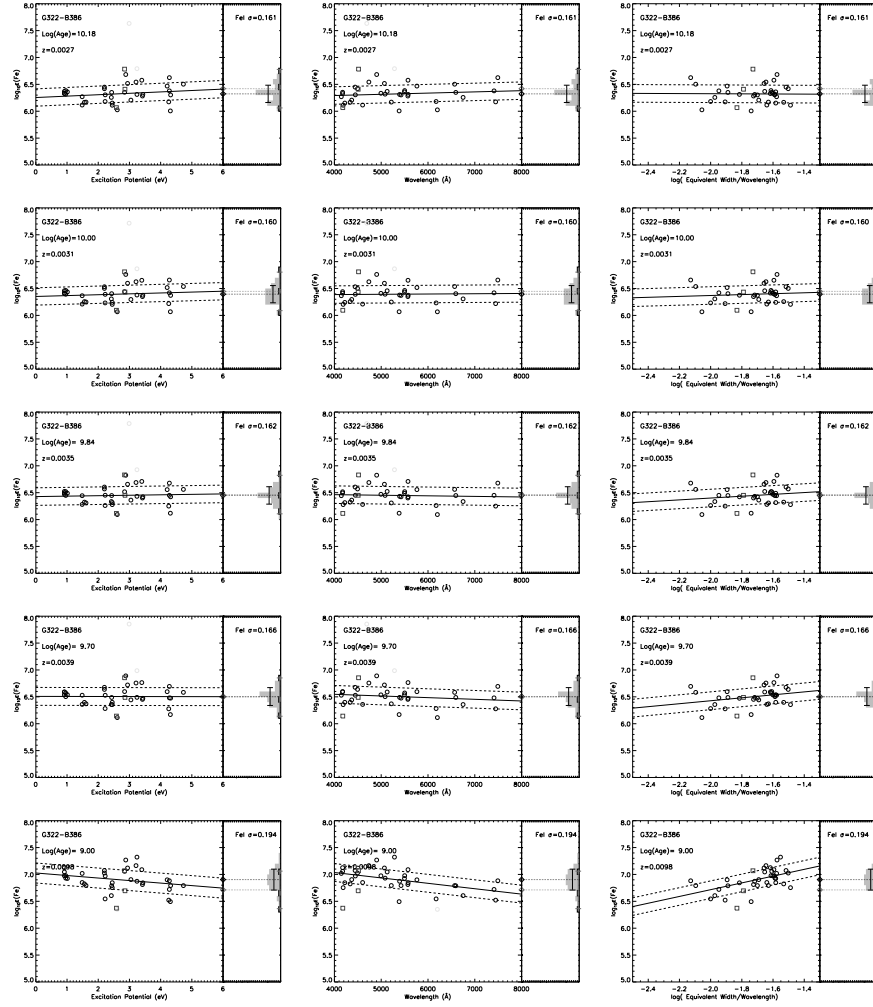
Figure 2.11. Diagnostics for G322-B386. The smallest Fe I standard deviation and smallest dependence on EP, wavelength, and observed equivalent width at ages of 7-13 Gyr. Symbols are the same as in Figure 2.9.
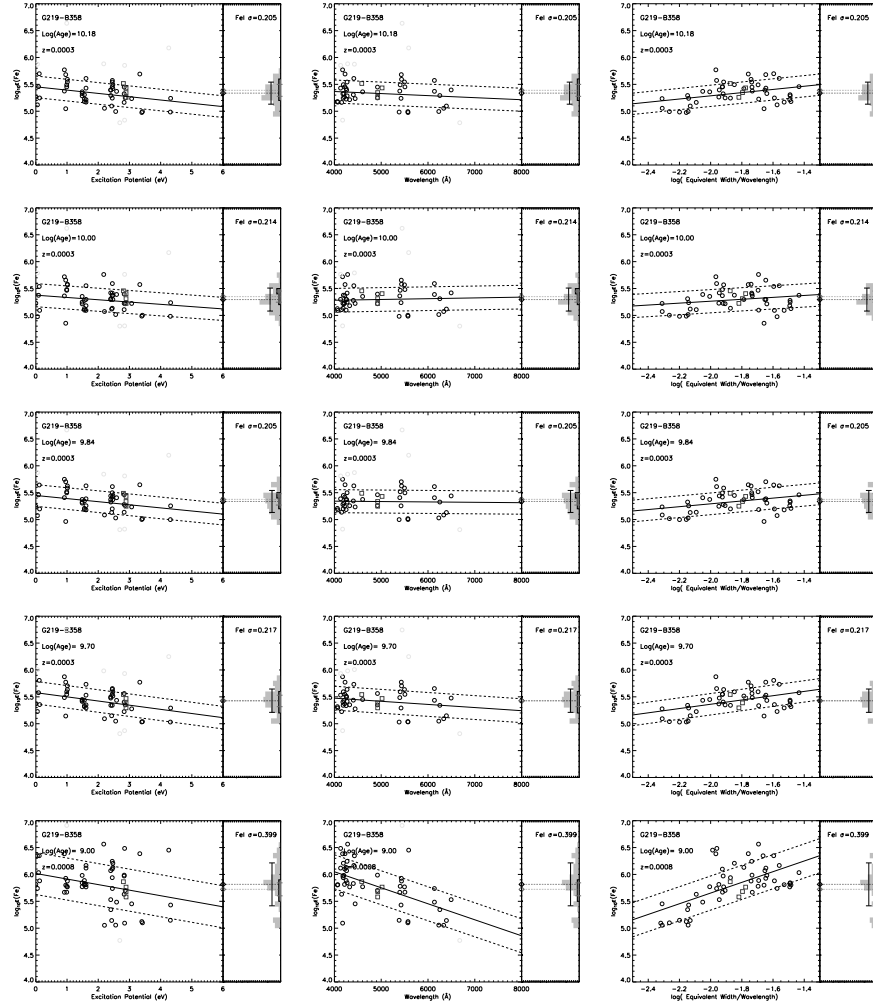
Figure 2.12. Diagnostics for G219-B358. The smallest Fe I standard deviation and smallest dependence on EP, wavelength, and observed equivalent width at ages of 7-13 Gyr. Symbols are the same as in Figure 2.9.
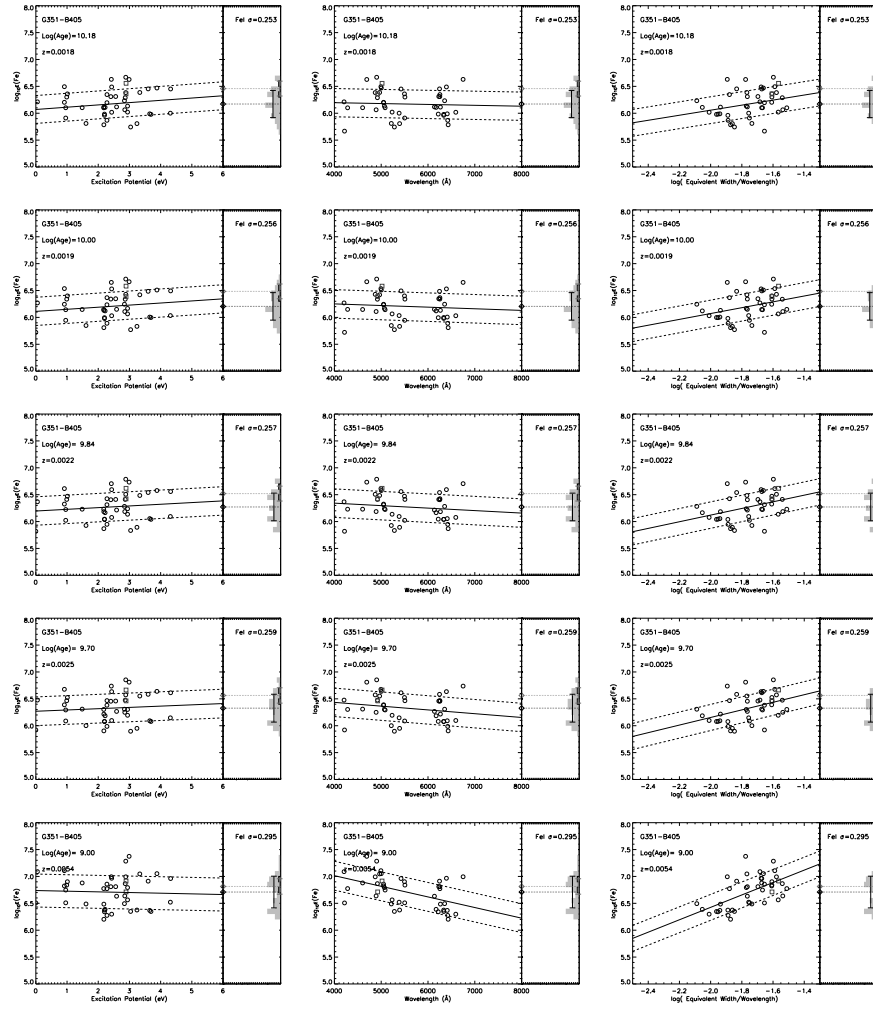
Figure 2.13. Diagnostics for G351-B405. The smallest Fe I standard deviation and smallest dependence on EP, wavelength, and observed equivalent width at ages of 10-15 Gyr. Symbols are the same as in Figure 2.9.
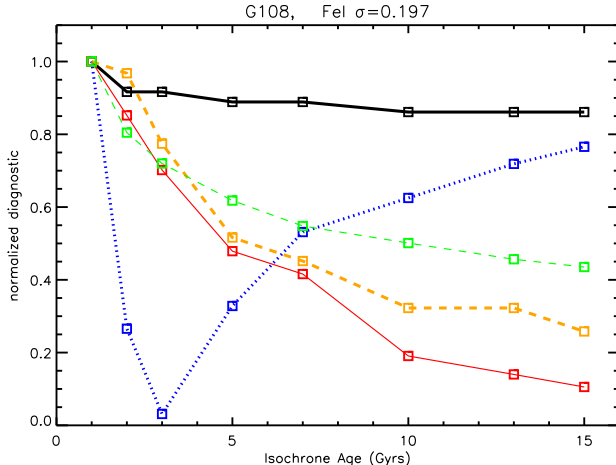
Figure 2.14. Fe line abundance diagnostics for G108. All diagnostics are normalized to their maximum values so that they can be shown on the same scale. The thick black line is Fe I σ, thick dashed orange line is Fe II σ, dotted blue line is the slope in [Fe/H] vs. λ, thin dashed green line is the slope in [Fe/H] vs. reduced EW, and the thin red solid line is the slope in [Fe/H] vs. EP.

To see this more clearly, we plot these diagnostics for the M31 sample in Figures 2.14 through 2.18. These plots show all five diagnostics as a function CMD age for the 7 CMDs that satisfy the original selection criteria (see Figures 2.4 through 2.8). From Figures 2.14 through 2.18, it is clear that for all of the GCs in our sample, all five diagnostics simultaneously imply that better solutions are obtained for CMDs with ages >7 Gyr. For these GCs, as for old Milky Way GCs analyzed as part of our training set (S. Cameron et al. 2010), we find the acceptable CMD ages typically cover a range of 5 Gyrs (e.g. 10−15 Gyrs or 7−13 Gyrs). This is not surprising because the CMDs themselves change very little over those ranges in age. We discuss these age constraints in detail in the next section.

From this range of acceptable ages, we select one CMD to use for a final analysis run of all elements for which we measure lines. For old GCs, such as the present sample, our abundance results are quite insensitive to which CMD in this age range is used. Again, this is not surprising as the CMDs in this age range are very similar. This weak dependence is quantified in Figure 2.19, in which the upper plot shows the small difference in abundance between the oldest and youngest CMDs in the acceptable age range for each GC (discussed in § 2.5.1). Nearly all elements change
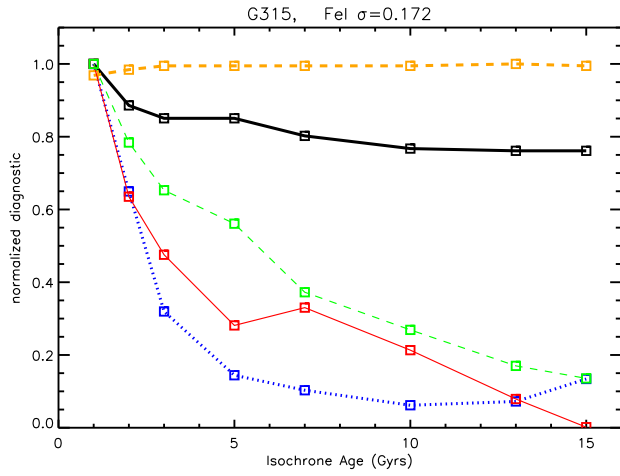
Figure 2.15. Same as Figure 2.14 for G315.
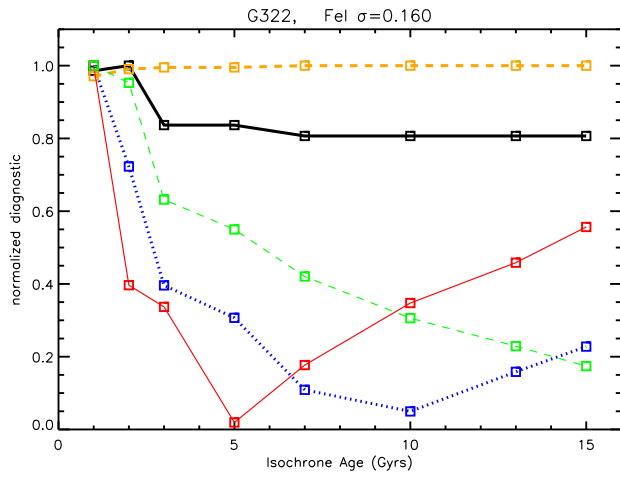
Figure 2.16. Same as Figure 2.14 for G322.
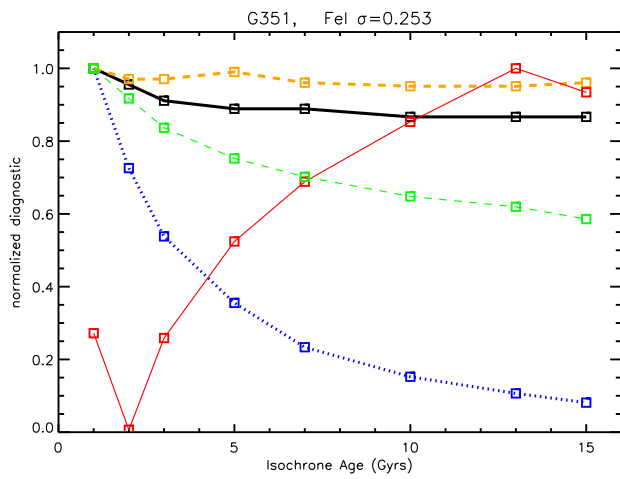
Figure 2.17. Same as Figure 2.14 for G351.
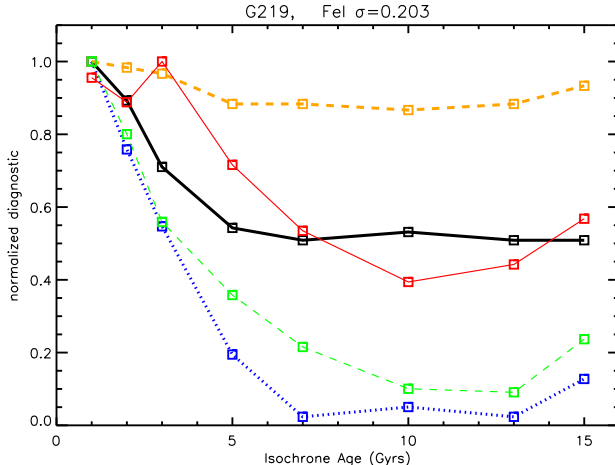
Figure 2.18. Same as Figure 2.14 for G219.

by ≤0.1 dex, and older CMD ages always give smaller abundances. The lower plot of Figure 2.19 demonstrates that the derived abundance *ratios* are even more robust. Since the change in the abundances of most elements tracks the change in Fe, the net difference in the abundance ratios is <0.05 dex in almost all cases.

2.5   Results: Chemical Abundances

We have measured abundances from the available clean lines of $\alpha-$elements, Fe and Fe$-$peak elements, and neutron capture elements for each GC. Final abundances, the number of analyzed spectral lines, line-to-line scatter, and the age of the best-fitting isochrone are reported in Tables 2.5 through 2.9. All abundance ratios relative to Fe use the solar abundance distribution of Asplund et al. (2005), with a solar $\log\epsilon$(Fe)= 7.50. Abundance ratios of Sc II, Ti II, Y II, and Ba II are reported with respect to [Fe/H]$_{\mathrm{II}}$. Figures 2.20 through 2.24 show the M31 abundance ratios (green circles) compared to our Milky Way training set IL abundances (red squares). Error bars for IL abundances in Figures 2.20 through 2.24 correspond to the statistical error of the deviation in abundances from the N$_{lines}$ available for each species, as reported in Tables 2.5 through 2.9. Note that these errors are often larger for the Milky Way training set abundances, which is a result of the smaller luminosity sampling of these GCs (5-30 % of the total flux) and, in some cases, lower S/N spectra.

44
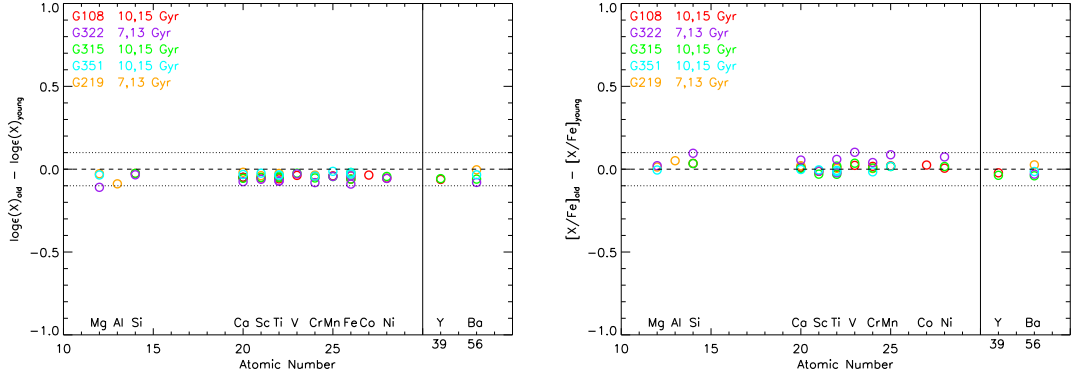
Figure 2.19. Robustness of the abundances over the ∼5 Gyr range of acceptable isochrone ages. Left plot shows the difference in the logε(X) of older and younger solutions. Right plot shows the corresponding difference in abundance ratios. Dotted lines around zero mark a change of ± 0.1 dex.

2.5.1 Iron and Ages

As in abundance analyses of individual stars, the first element we analyze is Fe because the large number of available transitions provide a wide variety of very useful diagnostics and consistency checks. As outlined in § 2.4.3, we first use the Fe lines to constrain our best CMDs. We find this sample of M31 GCs is old, with preferred ages >7 Gyrs, which is consistent with age estimates from previous photometric and low resolution spectroscopic work (Rich et al., 2005; Huchra et al., 1991). We also find this sample of GCs spans a metallicity range of [Fe/H]∼ −0.9 to −2.2, which is within the range of [Fe/H] of the Milky Way GC system. Below, we briefly discuss the best age and [Fe/H] for the individual GCs in this sample.

We find the preferred range of CMD ages for G108 to be 10-15 Gyrs. We pick a best CMD age of 15 Gyrs for our final abundance determinations. For the best solutions we find negligible trends of Fe I abundance with EP and a slight correlation remaining with wavelength and reduced EW, as shown in Figure 2.9. We note that the remaining correlation between Fe abundance and reduced EW suggests that the microturbulent velocity law we have applied is not perfect for every star in the synthetic CMD. However, while the correlation may still be present in the best solution, the overall trend in correlations over all CMDs is still very clear, and it is easy to select the most appropriate CMD. It is important to note that the scatter in microturbulence values

45

around the relation we have adopted is at least ± 0.2 km s^{-1} for studies of both dwarf and RGB stars in the Milky Way (e.g. Bensby et al., 2005; Fulbright et al., 2006). We have experimented with adjusting the microturbulence law within this range, which could potentially reduce the Fe abundance standard deviation. However, as long as the dependence of Fe abundance on reduced EW is small, this will not significantly alter the mean Fe abundance. We have not been able to find a microturbulence law that improves the overall abundance solution (i.e. improves all five diagnostics discussed in § 2.4.3). A more detailed investigation of this issue is beyond the goals of this study. To preserve the self-consistency of our solutions between GCs, we do not alter the original microturbulent velocities of the best-fitting CMD. A detailed discussion of the small (<0.1 dex) systematic error between the IL spectra abundance analysis and that for individual stars is included in S. Cameron et al. (2010). For the purposes of this work, we avoid systematic error issues by concentrating on relative comparisons between IL abundances determined in the same way for M31 and Milky Way GCs in our training set. To summarize our results, the final abundance solution for G108 is [Fe/H]$= -0.94 \pm 0.03$, where the uncertainty is the standard error in the abundances from all Fe lines ($\sigma/\sqrt{N_{lines} - 1}$).

The preferred CMD age range for G315 is also 10-15 Gyrs. Four of the five diagnostics show best solutions at the oldest ages, therefore we use the 15 Gyr solution as our best CMD. The 15 Gyr solution for G315 has negligible trends of Fe I abundance with EP, wavelength, and reduced EW, which can be seen in Figure 2.10. The final abundance for G315 is [Fe/H]$= -1.17 \pm 0.02$.

As can be seen in Figures 2.11 and 2.16, for G322 we find the EP correlation to be slightly stronger at the oldest ages, resulting in a slightly younger preferred age range of 7-13 Gyrs. We use a best CMD age of 13 Gyrs, and find a negligible correlation with wavelength and reduced EW, but a slight correlation between Fe abundance and EP for this solution. The final abundance is [Fe/H]$= -1.14 \pm 0.03$.

G219 is the only GC in this sample which appears to be slightly younger than the others. Figure 2.18 shows that four out of five Fe line diagnostics are best for ages of 7-13 Gyrs. We pick a best CMD age of 10 Gyrs, which is in the middle of this

Species	$\log_{10}\epsilon(X)$ 15 Gyrs	σ	Error	[X/Fe][1]	N_{lines}
Si I	7.15	0.17	0.12	+0.58	3
Ca I	5.64	0.17	0.07	+0.26	7
Sc II	2.54	0.26	0.18	−0.00	3
Ti I	4.10	0.21	0.10	+0.14	5
Ti II	4.86	0.34	0.17	+0.47	5
V I	2.90	0.24	0.17	−0.16	3
Cr I	4.82	⋯	⋯	+0.12	1
Mn I	4.05	0.15	0.09	−0.40	4
Fe I	6.56	0.22	0.03	−0.94	49
Fe II	6.99	0.01	0.01	−0.51	2
Co I	4.30	0.19	0.13	+0.32	3
Ni I	5.47	0.27	0.14	+0.18	5
Y II	1.45	⋯	⋯	−0.25	1

Table 2.5. G108-B045 Abundances. *Notes*: 1. For Fe this quantity is [Fe/H].

preferred age range. Figure 2.12 shows that this best solution —the 10 Gyr CMD— still shows slight correlations of Fe abundance with EP and reduced EW. We find an [Fe/H]=−2.21 ± 0.03 for G219, which makes it one of the most metal-poor GCs in the Local Group confirmed by high resolution spectra to date.

The preferred CMD age for G351 is 10-15 Gyrs. We note that G351 has a larger Fe I standard deviation than any other GC in the sample for any solution, which can be seen in Figure 2.13. We choose a best CMD age of 15 Gyrs, and note that this solution has small correlations of Fe abundance with EP and wavelength, as well as a fairly significant correlation with reduced EW. We find [Fe/H]= −1.33 ± 0.04.

2.5.2 Alpha Elements

As described in § 2.1, [α/Fe] abundance ratios are a valuable tool for studying the star formation history of a galaxy. α−elements are produced primarily in SNII that occur on timescales of 1-20 million years, which corresponds to the lifetimes of massive stars. While Fe-peak elements are produced in both type Ia (SNIa) and SNII, the SNIa contribution dominates on timescales of $\gtrsim 10^9$ years (e.g. Smecker-Hane & Wyse, 1992). Thus, at early times many α−elements are produced while total Fe abundances

Species	$\log_{10}\epsilon(\mathrm{X})$	σ	Error	$[\mathrm{X/Fe}]^1$	N_{lines}
	15 Gyrs				
Si I	7.01	0.27	0.27	+0.67	2
Ca I	5.51	0.18	0.07	+0.37	9
Sc II	2.29	0.38	0.22	+0.21	4
Ti I	4.07	0.15	0.11	+0.34	3
Ti II	4.53	0.30	0.15	+0.60	5
V I	2.72	$\cdots$	$\cdots$	-0.11	1
Cr I	4.63	0.15	0.15	+0.16	2
Mn I	3.75	0.14	0.08	-0.47	4
Fe I	6.33	0.17	0.02	-1.17	61
Fe II	6.53	0.50	0.19	-0.97	6
Ni I	4.97	0.19	0.09	-0.09	6
Y II	1.44	$\cdots$	$\cdots$	+0.20	1
Ba II	1.45	$\cdots$	$\cdots$	+0.25	1

Table 2.6. G315-B381 Abundances. *Notes* : 1. For Fe this quantity is [Fe/H].

Species	$\log_{10}\epsilon(\mathrm{X})$	σ	Error	$[\mathrm{X/Fe}]^1$	N_{lines}
	13 Gyrs				
Mg I	6.70	0.08	0.08	+0.35	2
Si I	6.70	$\cdots$	$\cdots$	+0.27[2]	1
Ca I	5.46	0.16	0.06	+0.33	8
Ti I	4.21	0.14	0.10	+0.49	3
Ti II	4.33	0.21	0.12	+0.51	4
V I	3.02	$\cdots$	$\cdots$	+0.20	1
Cr I	4.68	$\cdots$	$\cdots$	-0.04[3]	1
Mn I	3.61	0.07	0.05	-0.60	3
Fe I	6.36	0.16	0.03	-1.14	35
Fe II	6.43	0.41	0.21	-1.07	3
Ni I	5.15	0.26	0.19	+0.10	3
Ba II	1.63	$\cdots$	$\cdots$	+0.54	1

Table 2.7. G322-B386 Abundances. *Notes* : 1. For Fe this quantity is [Fe/H]. 2. A correction of -0.1 dex has been applied (see § 2.5.2) 3. A correction of -0.25 dex has been applied (see § 2.5.4)

Species	$\log_{10}\epsilon(X)$	σ	Error	$[X/Fe]^1$	N_{lines}
	10 Gyrs				
Mg I	5.42	0.14	0.14	$+0.09$	2
Al I	4.24	0.05	0.05	$+0.69^2$	2
Ca I	4.49	0.14	0.05	$+0.39$	8
Sc II	0.95	$\cdots$	$\cdots$	$+0.05$	1
Ti II	3.33	0.22	0.13	$+0.58$	4
Cr I	3.28	0.29	0.12	-0.15	7
Fe I	5.29	0.21	0.03	-2.21	47
Fe II	5.35	0.12	0.05	-2.15	4
Ba II	0.04	0.08	0.04	$+0.02$	4

Table 2.8. G219-B358 Abundances. *Notes* : 1. For Fe this quantity is [Fe/H]. 2. A non-LTE correction of $+0.6$ dex has been applied.

Species	$\log_{10}\epsilon(X)$	σ	Error	$[X/Fe]^1$	N_{lines}
	15 Gyrs				
Mg I	6.22	0.22	0.13	$+0.01$	4
Ca I	5.30	0.16	0.06	$+0.32$	9
Sc II	1.67	$\cdots$	$\cdots$	-0.34	1
Ti I	3.94	0.40	0.23	$+0.37$	4
Ti II	4.49	0.25	0.25	$+0.62$	2
Cr I	4.44	$\cdots$	$\cdots$	-0.13^2	1
Mn I	3.49	$\cdots$	$\cdots$	-0.57	1
Fe I	6.17	0.26	0.04	-1.33	42
Fe II	6.46	0.17	0.10	-1.04	2
Ni I	$\cdots$	$\cdots$	$\cdots$	-0.2^3	1
Ba II	1.39	0.29	0.20	$+0.26$	3

Table 2.9. G351-B405 Abundances *Notes* : 1. For Fe this quantity is [Fe/H]. 2. A correction of -0.25 dex has been applied (see § 2.5.4) 3. Estimate from spectral synthesis of 6767 Å (see Figure 2.26)

are low, resulting in an enhanced [α/Fe] abundance ratio at low [Fe/H]. After the onset of SNIa, the total Fe abundance increases at a faster rate than that of α−elements, decreasing the [α/Fe] ratio (Tinsley, 1979). Most GCs in the Milky Way have [α/Fe] ratios that are enhanced with respect to solar abundance ratios, similar to Milky Way halo stars at comparable [Fe/H]. This implies that Milky Way GCs formed when the ISM was dominated by enrichment by SNII. Like Milky Way GCs, we find all the GCs in our M31 sample to be enhanced in Ca, Ti and Si.

Abundances for Ca I come from 7−9 clean lines per GC, with rms scatter about the mean of 0.1−0.2 dex, which is similar to the scatter in our Fe abundances. We measure 4−10 Ti I and Ti II lines per GC, with slightly higher line-to-line scatter that may be due to weak blends. We are able to confidently measure 1−3 Si I lines in three of the GCs; lines in G219 and G351 were too noisy or badly blended to use. The one Si I line we measure in G322 is partially blended. To estimate the effect of weak blends on the Si abundance from the EW, we have used the SYNTH routine from MOOG, which we have modified to synthesize IL spectra. We estimate that at most our EW abundance measurement is ∼0.1 dex too high after visual inspection of synthesized IL spectra of different abundances.

In Milky Way field stars, the [Mg/Fe] ratios behave similarly to Ca, Ti and Si. However, in Milky Way GCs, [Mg/Fe] shows inter- and intra-cluster abundance variations (see Gratton et al., 2004) with respect to other α−elements and star-to-star differences within individual GCs. Analysis of our full training set of Milky Way GCs has revealed lower [Mg/Fe] than [Ca/Fe], [Ti/Fe], or [Si/Fe] in three out of the six GCs where it was measured (see MB08 and Cameron et al. 2010).

We have been able to measure [Mg/Fe] in three of the GCs in M31. Similar to the Milky Way training set GCs, in M31 we measure [Mg/Fe] to be lower ([Mg/Fe]< +0.1 dex) than other α−elements within individual GCs in two out of the three GCs where it was measured. In the other two clusters the Mg I lines had strengths > 150 mÅ, and were therefore not analyzed in this work.

We have performed spectral synthesis tests of the Mg I lines to see if the [Mg/Fe] depletion can be explained by line-to-line measurement error. An example of this test
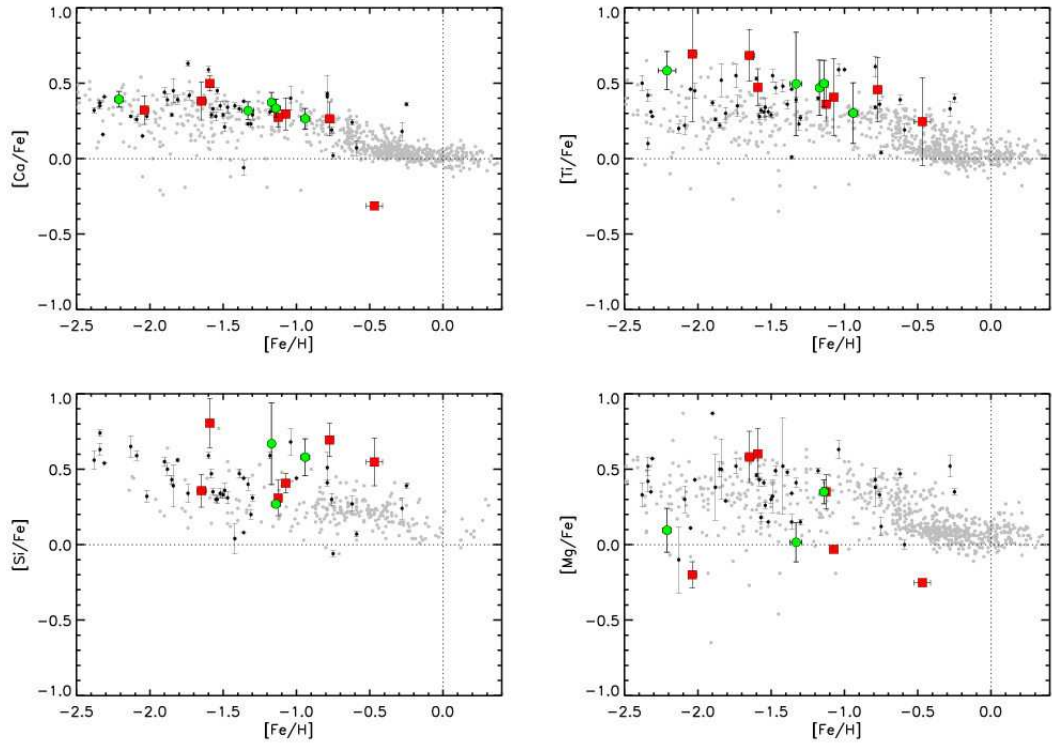
Figure 2.20. $\alpha-$element ratios. Gray points show Milky Way Stars and black points show mean Milky Way GCs abundances from single stars. Data for single stars is from Venn et al. (2004), Pritzl et al. (2005) and references therein. When possible, these abundance ratios have been adjusted to be consistent with the solar abundance distribution of Asplund et al. (2005) that was used in our analysis. Red squares show the abundances from our Milky Way training set ILS analysis and green circles show M31 ILS abundances. The average of $[Ti/Fe]_I$ and $[Ti/Fe]_{II}$ are plotted vs. $[Fe/H]_I$, where we have measured them.

	Milky Way	M31
[Ca/Fe]	$+0.35 \pm 0.08$	$+0.34 \pm 0.05$
[Ti/Fe]	$+0.46 \pm 0.15$	$+0.47 \pm 0.10$
[Si/Fe]	$+0.52 \pm 0.20$	$+0.51 \pm 0.21$
[Mg/Fe]	$+0.18 \pm 0.39$	$+0.15 \pm 0.17$
$[\alpha_{\mathrm{CaTiSiMg}}/\mathrm{Fe}]$	$+0.38 \pm 0.15$	$+0.37 \pm 0.16$
$[\alpha_{\mathrm{CaTiSi}}/\mathrm{Fe}]$	$+0.44 \pm 0.09$	$+0.44 \pm 0.09$

Table 2.10. Mean IL α Abundances for Milky Way Training Set and Current Sample of M31 GCs

is shown in Figure 2.25, for the unblended 5528 Å Mg I line in the most metal-poor GC G219. From the EW of this line, we measure an abundance of [Mg/Fe]= +0.01. Overplotted are synthesized spectra with abundances of [Mg/Fe]= $+0.3, 0.0, -0.3$. G219 is extremely metal poor, and no other elements contribute to the line EW. It is clear from Figure 2.25 that the closest matching abundance is [Mg/Fe]= 0.0, and that the line is inconsistent with the $[\alpha/\mathrm{Fe}]= +0.3$ measured for Ca and Ti, clearly showing that measurement error cannot explain the Mg deviation from the other α-element abundances in this cluster. In § 2.6.2, we further discuss light element variations in the IL of GCs, and in § 2.6.3 we discuss further implications for low resolution IL abundances.

We can address the star formation history of M31 by calculating an average $[\alpha/\mathrm{Fe}]$ ratio for each GC similar to that in Pritzl et al. (2005). While these authors use Ca, Ti, Si, and Mg in their average $[\alpha/\mathrm{Fe}]$, we note that [Mg/Fe] is probably not a good $[\alpha/\mathrm{Fe}]$ indicator in the IL of GCs, for the reasons discussed above. Therefore, for the mean $[\alpha/\mathrm{Fe}]$ for each GC discussed here, we include only Ca I, Ti I, Ti II, and Si I. The mean $[\alpha/\mathrm{Fe}]= +0.36 \pm 0.20, +0.50 \pm 0.16, +0.40 \pm 0.12, +0.44 \pm 0.16$, and $+0.49 \pm 0.13$ for G108, G315, G322, G351 and G219, respectively, which is significantly and consistently enhanced relative to solar in all five M31 GCs. We can also calculate the mean ratio for the individual $\alpha-$elements across the sample of GCs, and compare these values to similar means in our sample of Milky Way training set GCs. This comparison of abundances derived only with our IL spectra method avoids any potential sources of systematic error. The mean values for Ca, Ti, Si, and

Mg are presented in Table 2.10. In addition, we present the mean and deviation of all the $[\alpha/\text{Fe}]$ ratios including and excluding $[\text{Mg}/\text{Fe}]$. Table 2.10 shows that GCs in both the Milky Way and M31 have extremely consistent $[\alpha/\text{Fe}]$ ratios. GCs in both galaxies are also consistent with the Milky Way halo average α-enhancement of $+0.35$ (e.g. McWilliam, 1997). The obvious implication of the $[\alpha/\text{Fe}]$ abundances in this small sample of M31 GCs is that M31 was (or its now-merged components were) dominated by enrichment by SNII when these GCs formed.

2.5.3 Aluminum

Al abundances have been used to put constraints on chemical evolution models of the Milky Way because Al enrichment is particularly sensitive to the details of SNII explosions (see Gehren et al., 2006). Al abundances for Milky Way disk stars with $[\text{Fe}/\text{H}] < -2$ have some contribution from explosive burning in SNII (Andrievsky et al., 2008), so that like $[\alpha/\text{Fe}]$, Al abundances reach a plateau value of $[\text{Al}/\text{Fe}] \sim +0.3$ (e.g. Bensby et al., 2005). However, some stars in Milky Way GCs are found to be even more enriched, reaching levels as high as $[\text{Al}/\text{Fe}] \sim +1$ (Gratton et al., 2001). Also, like Mg, Al exhibits inter- and intra-cluster variations, which we discuss further in § 2.6.2, suggesting that the influences on Al abundance are more complicated in GCs than in the field.

We have only been able to make one measurement of Al I in this first sample of M31 GCs. This measurement was made from the 3944 Å Al I line in the metal-poor GC G219. We were able to make two independent measurements of this 3944 Å line because it was present at the ends of two adjacent orders. Both measurements give a consistent result of $[\text{Al}/\text{Fe}] = +0.09 \pm 0.05$. However, we note that Al I abundances derived from the 3944 Å resonance line can be problematic; McWilliam et al. (1995a) find that the line is significantly blended with CH lines in some giant stars, which causes derived abundances to be too high, and according to Baumueller & Gehren (1997) Al I abundances from this line will be underestimated by $\sim$0.6 dex due to non-LTE effects. Andrievsky et al. (2008) find that this correction may be even larger in metal-poor hot stars. We do not see evidence in the IL spectrum for contamination

of the 3944 Å line by significant CH blends. An appropriate non-LTE correction of +0.6 dex raises the abundance to [Al/Fe]= +0.69. This is higher than the [Al/Fe]~0 halo average at an [Fe/H]=−2.2, but consistent with the significantly enhanced Al I found in some individual GC stars. This enhanced [Al/Fe] is also consistent with Al abundances we derive for three Milky Way GCs in our training set.

The training set [Al/Fe] measurements provide much stronger evidence that the enhanced [Al/Fe] we measure in GC IL spectra is real because they are not measured from the potentially problematic 3944 Å Al I feature. The training set [Al/Fe] (see Figure 2.21) were measured from the 6696/6698 Å Al I doublet, which should not be contaminated by blends. In addition, Baumueller & Gehren (1997) find that non-LTE effects are much smaller for these lines. The 6696 Å feature is not detectable in G219, even though we measure an abundance as high as [Al/Fe]= +0.7 with the non-LTE correction. We performed spectral synthesis tests to check that the lower limit of [Al/Fe]= +0.7 is consistent with a 6696 Å line that would be too weak to detect in the IL spectra. We indeed find that an [Al/Fe]= +0.7 is not high enough for the feature to be seen after convolution with the velocity broadening of G219 because it results in a line depth of $< 0.01\%$ of the continuum level.

The 6696/6698 Å features were also too weak in the other M31 GC spectra to get reliable abundance measurements from EWs, with the exception of G108, in which it unfortunately falls too near the end of an order for a good measurement to be made. The 3944 Å line was saturated in all of the more metal-rich GCs.

2.5.4   Fe-peak Elements

Ni, Cr, Mn Co, Sc, and V abundances are interesting because their production generally tracks that of Fe, (e.g. Iwamoto et al., 1999), resulting in [X/Fe]~ 0. Therefore, deviations from [X/Fe]~ 0 are particularly interesting because they imply special conditions may have been present, such as variations in the mass function of supernovae, variations of mixing of supernovae ejecta into the local ISM, metallicity dependent or explosion dependent supernova yields, or contributions from special types of supernovae (e.g. McWilliam, 1997).
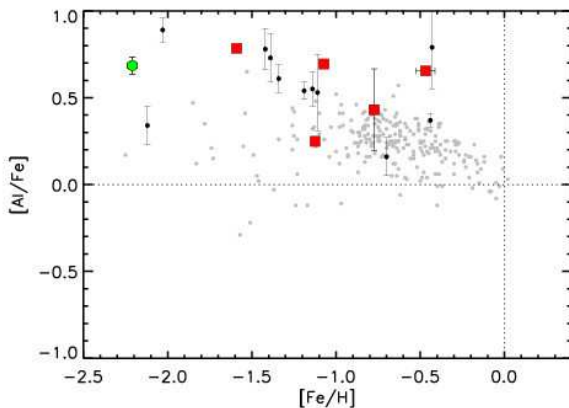
Figure 2.21. Aluminum abundances. Symbols are the same as in Figure 2.20. GC data is from references compiled in Carretta (2006). A non-LTE correction of 0.6 dex has been added to G219 abundance.

Ni abundances in Milky Way field and GC stars generally follow the expected Fe-peak element trend of [Ni/Fe]= 0 at all metallicities. We are able to measure [Ni/Fe] in three M31 GCs, and find it to be consistent with the Milky Way abundance trend. Ni was measured from 3-6 Ni I lines in G108, G315, and G322. The three GCs have a mean <[Ni/Fe]>= +0.06 ± 0.14, which is essentially identical to the mean of the Milky Way training set GCs, which have <[Ni/Fe]>= +0.05 ± 0.21.

In the most metal-poor cluster G219, all Ni I lines are too weak for EWs to be measured reliably. In G315 most Ni I lines are too weak or noisy for EW measurements, and the 7393 Å line is blended with telluric absorption lines. We estimate from spectral synthesis tests of the noisy 6767 Å line in G351, that [Ni/Fe]∼ −0.2. The spectral synthesis and spectrum are shown in Figure 2.26, where the uncertainty in abundance due to the noisy continuum can be fully appreciated.

[Cr/Fe]= 0 in Milky Way stars for [Fe/H]> −2, but [Cr/Fe]< 0 for [Fe/H]< −2. The deviation from [Cr/Fe]= 0 at low metallicity may be due to different chemical enrichment for the lowest metallicity stars in the Milky Way halo (McWilliam, 1997). We measure Cr I abundances for the four most metal-rich M31 GCs that are consistent with the solar [Cr/Fe] average in both our Milky Way training set GCs and in Milky Way stars at these metallicities. Few [Cr/Fe] measurements exist for GCs with [Fe/H]< −2. When observed, [Cr/Fe] in GCs also follows the decreasing [Cr/Fe]
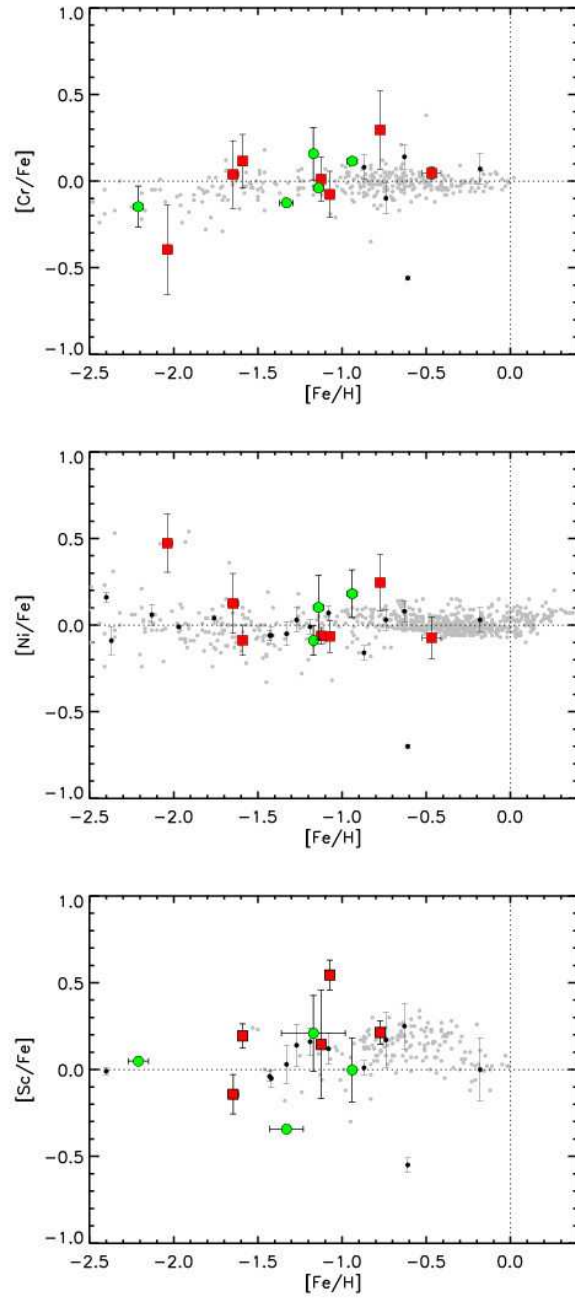
Figure 2.22. Abundances for Fe peak elements Cr, Ni and Sc. Symbols are the same as Figure 2.20. GC data from Kraft et al. (1995), Sneden et al. (1997), Cohen et al. (1999), Ivans et al. (1999), Shetrone & Keane (2000), Ivans et al. (2001), Ramírez & Cohen (2002), Lee & Carney (2002), Sneden et al. (2004), Carretta et al. (2004), Cohen (2004), Tautvaišienė et al. (2004), and Lee et al. (2005)
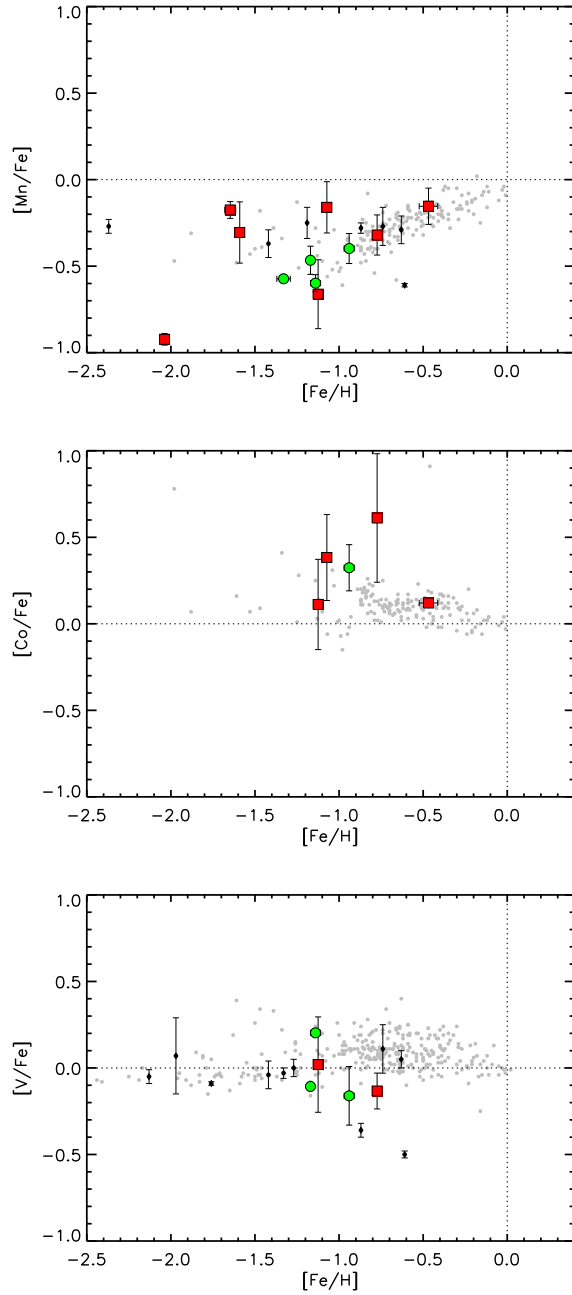
Figure 2.23. Abundances of Mn, Co and V. Symbols and references are the same as Figure 2.22.

57

abundance trend observed in Milky Way halo stars (see Shetrone et al. (2001) for M92 and NGC 2419, and Letarte et al. (2006) for M15 and Fornax GCs). We are able to measure Cr I in the low-metallicity M31 cluster G219, and find [Cr/Fe]= −0.15, which is also consistent with the decreasing halo abundance trend below [Fe/H]∼ −2. Cr abundances were calculated from one Cr I line in G108, G322 and G351, two Cr I lines in G315, and seven Cr I lines in G219. Most other Cr I lines in the more metal-rich GCs have EWs over 150 mÅ and were not analyzed. The Cr feature at 5409 Å, which is the only Cr line we measure in G322 and G351, is partially blended with weak Ti I and Fe I lines, so that the EW abundance may be slightly high. We used spectral synthesis tests of the Ti I and Fe I blends around the 5409 Å Cr I feature to estimate the effect of the blends on the derived Cr abundance. We find that the Cr I abundance derived with the original EW measurement may be approximately ∼0.25 dex too high. A correction of −0.25 dex to our EW abundances of [Cr/Fe]= +0.21 and +0.12, would result in [Cr/Fe]= −0.04, and −0.13 for G322 and G351, respectively. These [Cr/Fe] are consistent with the [Cr/Fe]∼ 0 of Milky Way GCs.

Mn is a particularly interesting Fe−peak element because unlike most Fe−peak elements the [Mn/Fe] ratio is not solar at most metallicities. From [Fe/H]= −1 to −2.5 dex, [Mn/Fe]∼ −0.4, and increases to [Mn/Fe]= 0 at [Fe/H]= 0. This trend is similar but opposite to that of α−elements (e.g. McWilliam, 1997). Possible explanations for this trend are: Mn is underproduced in SNII and overproduced in SNIa, or that SNIa Mn production is dependent on the metallicity of the progenitor star (Gratton, 1989). Recent observations of [Mn/Fe] in stars in the Sagittarius Dwarf Galaxy have shown that only the latter explanation can simultaneously reproduce the data in both the Milky Way and Sagittarius (McWilliam et al., 2003; Cescutti et al., 2008). This demonstrates the importance of obtaining abundance ratios in a variety of environments for a full understanding of chemical evolution. Because Bergemann (2008) find that Mn abundances may be underestimated due to non-LTE effects over most of this metallicity range, we focus on a relative comparison of our abundances with others calculated under similar assumption of LTE.

We find that the Mn I abundances in the M31 GCs are consistent with our training set abundances and the Milky Way [Mn/Fe] abundance trend. Our abundances for Mn are measured from 3−4 Mn I lines in each the three most metal-rich GCs, G108, G315 and G322. [Mn/Fe] is measured from the Mn I 6021 Å line only in G351. We do not see evidence for blends that would change the result by more than ∼0.1 dex.

The mean [Sc/Fe] in Milky Way stars and GCs is approximately solar. We measure a mean [Sc/Fe]∼ 0 for GCs in M31, with a larger scatter between lines for individual GCs and between the five GCs ($\sigma \sim 0.2$ dex) than we see for other, easier-to-measure Fe−peak elements ($\sigma \sim 0.1$). We find a similar mean and scatter in our training set GC abundances. We measure abundances for 1−4 Sc II lines in each of the five GCs.

Co abundances in stars and GCs in the Milky Way track that of Fe for [Fe/H]> −2, so that over this range in metallicity the [Co/Fe]∼ 0. We measure Co I from three lines for the most metal-rich GC G108. Co I features in the other four GCs are too weak to measure reliably, with the exception of the feature at 4121 Å, which we find to be significantly blended. The G108 [Co/Fe]= +0.32 ± 0.13 is in agreement with Milky Way training set abundances at this metallicity.

Milky Way stellar and GC V abundances typically track the abundance of Fe, resulting in [V/Fe]∼ 0. We measure a mean V abundance from G108, G315, and G322 of [V/Fe]= −0.02, which is consistent with our measurements of [V/Fe] in the Milky Way training set GCs. Abundances for G108 come from 3 V I lines, and abundances for G315 and G322 each come from the V I 6081 Å line. These V I lines are all weak (EWs∼30-40 mÅ), but it appears unlikely that there are any blends that would cause misleading abundance measurements.

In summary, the Fe-peak element abundances in this sample of M31 GCs are similar to those measured in Milky Way GCs, and consistent with enrichment dominated by SNII.

2.5.5 Neutron Capture Elements

The relative abundances of neutron capture elements are important because they are particularly sensitive to the details of star formation, but also because the nucle-
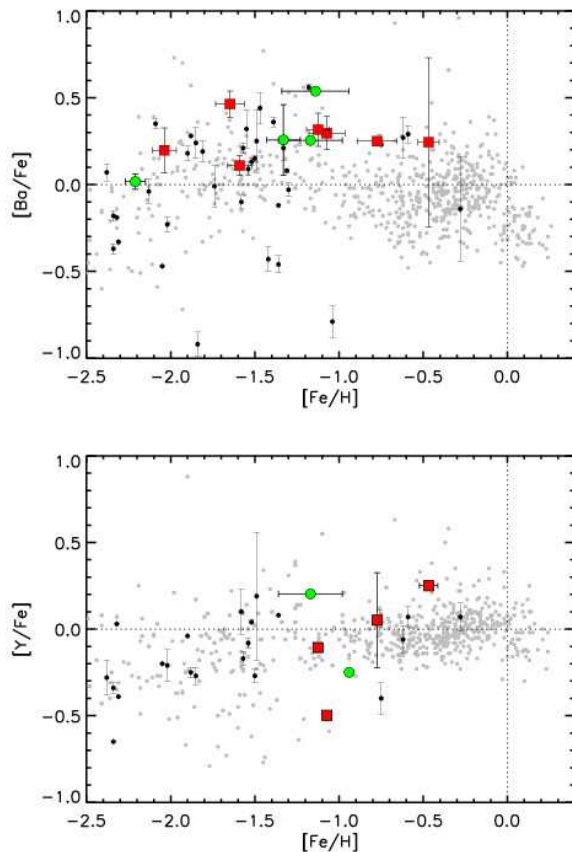
Figure 2.24. Abundances of neutron capture elements. Symbols and references are the same as in Figure 2.20.

osynthetic sources and yields of the rapid ($r-$process) and slow ($s-$process) neutron capture reactions remain uncertain (see Venn et al., 2004; McWilliam, 1997). In particular, the difference between the Ba and Y abundances for stars in the Milky Way and stars in nearby dwarf spheroidal galaxies provides strong evidence for differences between the star formation histories of large galaxies and their satellites (Shetrone et al., 2001, 2003; Geisler et al., 2005). Perhaps more interesting is that these abundance differences are at times inconsistent with simple nucleosynthetic explanations, and thus can provide new constraints on uncertain reaction sites (e.g. Venn et al., 2004).

We are able to measure abundances for the strong lines of Ba II and Y II in some of the M31 GCs. Unfortunately, we are unable to measure abundances for weaker Eu II and La II lines due to the high velocity dispersions of this sample of GCs (see
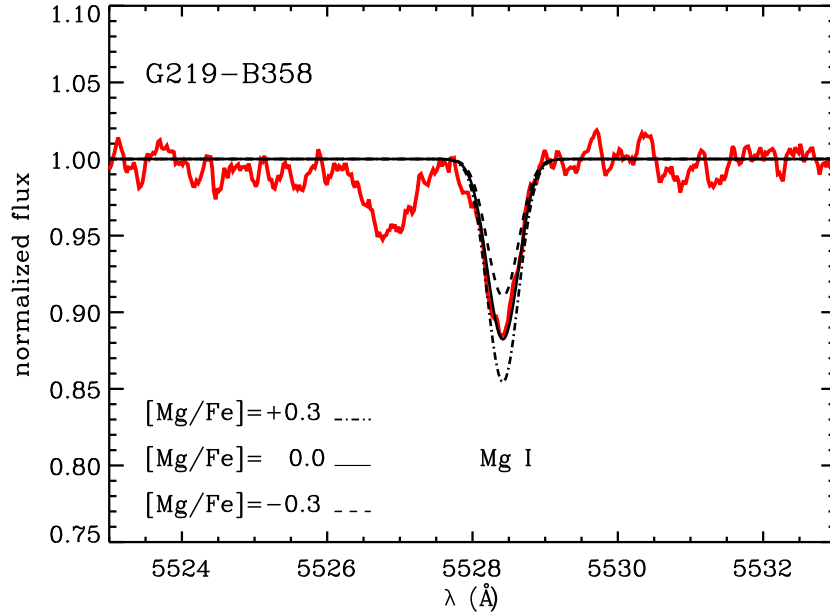
Figure 2.25. Spectrum synthesis test for Mg I 5528 Å line in G219. Smoothed data is shown in red, and overplotted synthesized spectra from top to bottom correspond to [Mg/Fe]= $-0.3, 0.0, +0.3$. The closest matching profile is for [Mg/Fe]= 0.0.

§ 2.3). Typical Ba abundances in Milky Way GC stars are between [Ba/Fe]$\sim 0 - 0.5$ for [Fe/H]> -1 and [Ba/Fe]< 0 for [Fe/H]< -1. Our Ba abundances for the M31 GCs are consistent with these trends and with what we find for our training set GCs; we also measure the lowest [Ba/Fe] for the lowest metallicity cluster G219. Ba II abundances come from 1-4 lines in each of the GCs except for the most metal-rich cluster G108, for which all line strengths were over 150 mÅ.

For [Fe/H]> -1.5, Milky Way GCs typically have [Y/Fe]~ 0. We measure a mean value of [Y/Fe]~ 0 for G108 and G315 in M31, as well, which is also consistent with what we find for the Milky Way training set. These Y abundances come from the 4883 Å Y II feature. Because the Y abundances are derived from a single line, we have performed spectral synthesis tests to confirm that the 4883 Å line is relatively unaffected by blends.
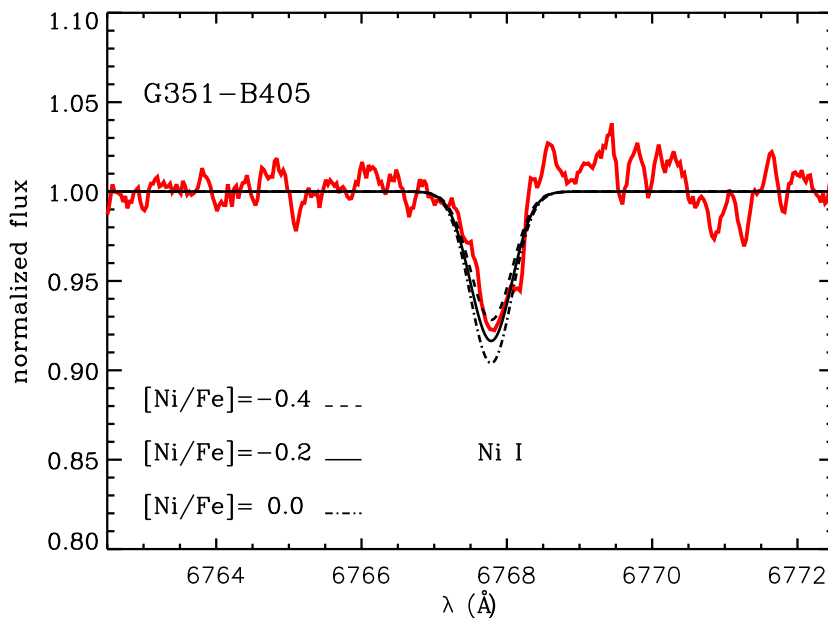
Figure 2.26. Spectrum synthesis test for Ni I 6767 Å line in G351. Smoothed data is shown in red, and overplotted synthesized spectra from top to bottom correspond to [Ni/Fe]= $-0.4, -0.2, 0.0$. The spectrum is noisy and continuum placement uncertain, but [Ni/Fe] is approximately ~ -0.2 with an uncertainty of ~ 0.2 dex.

2.6 Discussion

Although this is only the first set in a larger sample of GCs from our M31 study, we already have several interesting results. First, in § 2.6.1 we discuss the chemical enrichment history of the present sample of M31 GCs and compare it to the Milky Way and dwarf galaxy GC systems. In § 2.6.2 and § 2.6.3 we discuss the implications of our measurements for both GC formation and evolution and IL abundance work at low resolution. In the final two sections we comment on constraints that can be put on horizontal branch morphology and reddening of unresolved GCs using high resolution IL spectra.

2.6.1 Chemical History of M31 GCs

Overall, these five M31 GCs are old and have chemical properties similar to those of most Milky Way GCs. All five GCs are enhanced in the $\alpha-$elements Ca, Ti, and Si to the same extent as Milky Way GCs. Fe$-$peak element ratios are consistent

with Milky Way abundance trends. These results are consistent with existing simple Galactic chemical enrichment scenarios (e.g. Tinsley, 1979), in so far as it suggests that the gas in both the Milky Way and M31 halos was dominated by enrichment by SNII when these GCs formed. The similar levels of $\alpha-$enhancement in this small sample so far suggests that M31 and the Milky Way are likely to have had similar IMFs and star formation rates at early times. Since we do not see evidence for the low $[\alpha/\text{Fe}]$ observed in GCs in the LMC or the disrupting Sagittarius Dwarf Galaxy, it does not seem likely that any of these five GCs are associated with recent satellite accretion events.

2.6.2   Variation of Light Elements

Variations in the abundances of light elements between individual stars within GCs have been observed in all GCs studied in detail since the phenomenon was discovered in the Milky Way GCs M3 and M13 by Cohen (1978). Of the light elements, Mg and O are observed to be depleted in some GC stars, while Na and Al are over-abundant. These abundance variations are related and have since been called the Na$-$O and Mg$-$Al anticorrelations (see Gratton et al., 2004). Abundances varying in this way are predicted from high temperature $(\text{T} > 10^7)$ C$-$N$-$O cycle H$-$burning (Denisenkov & Denisenkova, 1990; Denissenkov et al., 1998). While these reaction products can in principle be brought up to the stellar surfaces during "deep mixing" on the RGB, the observation of the abundance variations even in GC main sequence stars has suggested that they are instead the result of pollution by GC intermediate$-$mass AGB stars, for example, as discussed in Ventura & D'Antona (2008), although this solution is not universally accepted (see modeling of NGC 6752 in Fenner et al. (2004)).

Star-to-star Mg variations have been more difficult to measure than those of O, Al, and Na in many Milky Way GCs (Carretta et al., 2004). Sneden et al. (2004) successfully measured [Mg/Fe] variations in a large sample of stars in the Milky Way GCs M3 and M13, with values that range from [Mg/Fe]$= -0.2$ to $+0.4$. This variation is detectable in the IL as the mean [Mg/Fe] will be lower than the mean $[\alpha/\text{Fe}]$, as

shown in § 2.5.2. We can also expect that our IL measurements correspond to a kind of average [Mg/Fe] for each GC, which is complicated by the extent of the Mg depletion present within the GC, and the flux weighting of stars of different types. As a simple consistency check, we note that our IL [Mg/Fe] measurements fall within the range [Mg/Fe]= −0.2 to +0.4 that is expected for individual stars (Sneden et al. (2004)). The scatter in IL [Mg/Fe] between GCs tends to be high in both the Milky Way and M31, and does not appear to correlate with any property of the GCs. These factors suggest that it is difficult to predict an expected value of [Mg/Fe] in the IL spectra of a GC at this time.

AGB star pollution in GCs can also affect the abundance of [Al/Fe]. Abundances in some GC stars are observed to be as high [Al/Fe]> +1, significantly higher than the abundances seen in halo field stars. We determine an abundance for G219 of [Al/Fe]= +0.69 (see § 2.5.3), which is close to the high value of [Al/Fe]∼ 1 measured in some GC stars. Three of our training set Milky Way GCs have [Al/Fe]> +0.6, which was measured from the more reliable Al 6696 Å line, so we believe that we are seeing evidence of the Mg−Al anticorrelation in IL measurements of [Al/Fe] in both the Milky Way and M31.

Unfortunately, we were unable to measure oxygen abundances in this sample of GCs. This was either due to blends with telluric absorption lines or because the lines were too weak to reliably measure from EWs with the reasonably high velocity dispersions of these GCs. Na lines were either too weak or very saturated. Future IL light abundances for GCs with smaller velocity dispersions should be more useful for investigating the Na−O anticorrelation.

2.6.3 Comparisons to Lick Indexes

Much progress has been made using low resolution Lick index systems to measure global properties of GC systems (see review by Brodie & Strader, 2006). Low resolution metallicities have helped establish the general trends in GC populations in other galaxies, and their importance for tracing galaxy formation and evolution. In this section, we compare previous measurements of Lick index metallicities for our
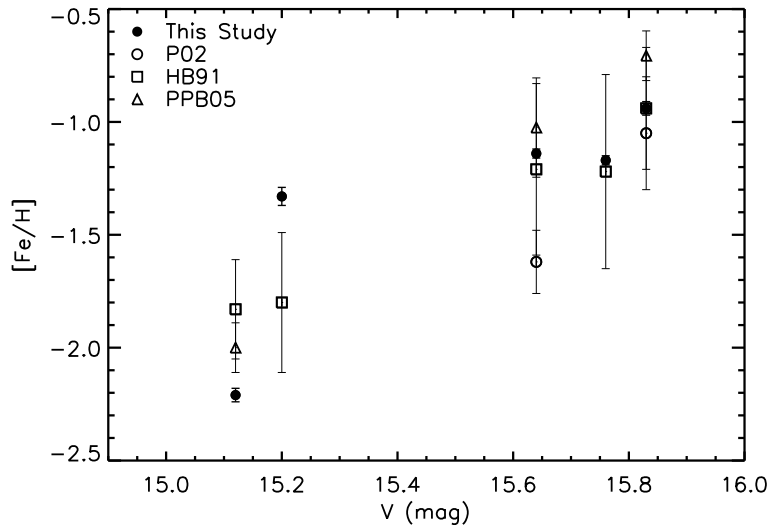
Figure 2.27. Comparison of high resolution ILS [Fe/H] with line index measurements by Perrett et al. (2002) (P02, open circles), Huchra et al. (1991) (HB91, open squares) and Puzia et al. (2005) (PPB05, open triangles) plotted as a function of V magnitude.

sample of GCs in M31 with the goal of understanding where and why abundances from low and high resolution spectra may differ. The Lick system or similar methods are critical to studying extragalactic GCs because low resolution spectra analyses will always need to be applied to systems that are so distant that high resolution analyses are impossible.

In making these comparisons we caution that the definition of [Fe/H] is slightly ambiguous. Line index metallicities are typically calibrated to the Zinn & West (1984) [Fe/H] scale as established for Milky Way GCs[7]. This metallicity scale is advantageous because it covers the metallicity range spanned by Milky Way GCs and can be easily applied to distant objects, providing a consistent IL metallicity scale for both Milky Way and extragalactic GCs. However, by definition this scale is based on blends of lines from multiple elements. This limits the information that can be reliably determined for individual element abundances, including Fe. Another difficulty in these comparisons is that the calibration is based on the Milky Way GC

---

[7]The Zinn & West (1984) scale is based on the integrated photometric parameter Q_{39} and measurements of absorption from Ca H and K, CN, Fe, and the Mgb region from low resolution integrated spectra and was calibrated to early high resolution abundance results.

Cluster	ILS [Fe/H]	1 [Fe/H]	2 [Fe/H]	3 [Fe/H]	4 [Fe/H]
G108-B045	-0.94 ± 0.03	-0.85	-0.94 ± 0.27	-1.05 ± 0.25	-0.71 ± 0.11
G219-B358	-2.21 ± 0.03	-1.92	-1.83 ± 0.22	$\cdots$	-2.00 ± 0.11
G315-B381	-1.17 ± 0.02	$\cdots$	-1.22 ± 0.43	$\cdots$	$\cdots$
G322-B386	-1.14 ± 0.02	-1.09	-1.21 ± 0.38	-1.62 ± 0.14	-1.03 ± 0.22
G351-B405	-1.33 ± 0.04	-1.77	-1.80 ± 0.31	$\cdots$	$\cdots$

Table 2.11. Metallicity Comparisons. *References* : From CMD photometry: (1.) Rich et al. (2005). From Lick index spectroscopy: (2.) Huchra et al. (1991) (3.) Perrett et al. (2002) (4.) Puzia et al. (2005), calculated from the relation in Thomas et al. (2003) : [Fe/H]=[Z/H]$-0.94[\alpha$/Fe].

system, which has a very consistent abundance pattern and HBR − [Fe/H] relation that is not necessarily the same in GCs in other galaxies. Since the calibration is based on spectral regions with blends of several elements, it may be less accurate if targets don't have Milky Way-like abundance ratios.

"[Fe/H]"

Because of the ambiguities described above, the comparison of Lick index metallicities to the high resolution [Fe/H] determined in our analysis is interesting both when the abundances agree and when they disagree. Our IL [Fe/H] results for all five GCs are summarized in Table 11, along with metallicity estimates in the literature.

A comparison of the high resolution [Fe/H] derived from our analysis and low resolution Lick index [Fe/H] estimates is shown in Figure 2.27, plotted as a function of V magnitude for convenience. High resolution [Fe/H] are plotted as solid symbols and the line index measurements of Huchra et al. (1991), Perrett et al. (2002) and Puzia et al. (2005) correspond to open squares, circles, and triangles, respectively. Figure 2.27 shows that the Lick index [Fe/H] estimates agree within the errors for the higher metallicity clusters G108, G315, and G322. However, bigger differences appear at the lowest metallicities; our measurement of [Fe/H]= -2.21 ± 0.03 for G219 is ∼ $0.2 - 0.4$ dex lower than previous estimates, and our measurement of [Fe/H]= -1.33 ± 0.04 for G351 is ∼0.5 dex higher than low resolution results (see Table 2.11).

Larger discrepancies at the lowest metallicities are expected for several reasons. First, line index strengths change little for [Fe/H]< -1.6, so calibrations to the Lick

system at low metallicity are uncertain (e.g. see Puzia et al., 2002). In the case of G219, a difference between [Fe/H]=−1.8 and [Fe/H]=−2.2 would be particularly difficult to detect at low resolution, emphasizing the importance of high resolution measurements at these lowest metallicity GCs. The discrepancy between the high resolution and Lick index abundance for G351 is a little more difficult to understand, especially since the CMD metallicity estimate of Rich et al. (2005) is similar to the Lick index result. This discrepancy stands out in our sample, however the difference is still within ∼1.3σ of the quoted error of Huchra et al. (1991), and our own rms error for this cluster is slightly larger than for others in our sample. As a simple reality check, a visual comparison of the G351 spectrum and our other 4 GC spectra (see Figure 2.2) suggest that G219 is substantially more metal poor than G351, while line index measurements put both G351 and G219 at [Fe/H]∼ −1.8.

It is possible that the Lick index analysis is complicated by a combination of factors that include both low-metallicity degeneracies and poor modeling of blue horizontal branches (see discussion of the effect of HB morphology on our results in § 2.6.4). We note G351 has been observed to have a bimodal horizontal branch (Rich et al., 2005). We also note that G351 is one of the GCs we find to have depleted [Mg/Fe], suggesting that abundance ratio calibration degeneracies may be a particular problem for this cluster in the sample.

[α/**Fe**]

Recent progress has been made in developing SSP IL spectra models with variable element ratios for comparison with Lick index absorption features (Thomas et al., 2003; Lee & Worthey, 2005; Schiavon, 2007). In particular, the models of Thomas et al. (2003) have made the [α/Fe] estimates of a portion of M31 GCs possible, including three of those studied here (Puzia et al., 2005). In this case, [α/Fe] is determined from a comparison with models of Lick indexes with Fe−dominated and Mg−dominated absorption features. A significant result of the study of (Puzia et al., 2005) is that GCs in M31 with ages >8 Gyrs have a mean [α/Fe]= +0.18±0.05 with a dispersion of 0.37 dex, which is 0.1 ∼ 0.2 dex lower than what Puzia et al. (2005)
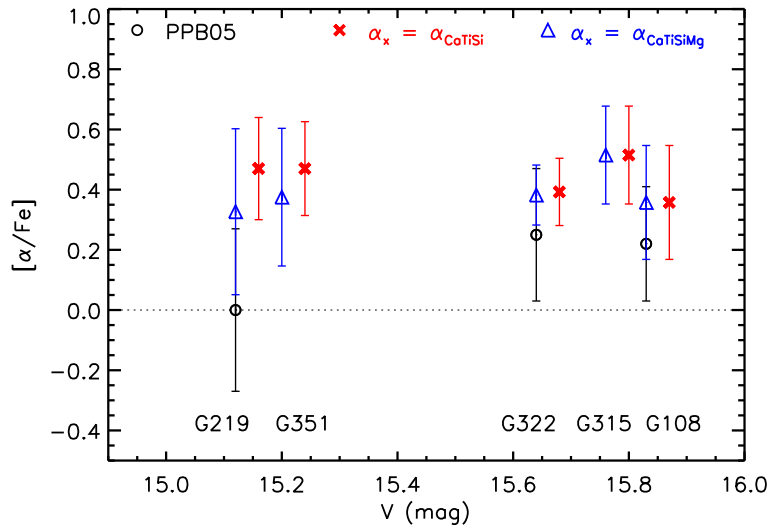
Figure 2.28. Comparison of $[\alpha/\text{Fe}]$ from high resolution ILS with line index estimates by Puzia et al. (2005) (PPB05, open circles) plotted as a function of V magnitude. Red crosses correspond to mean $[\alpha/\text{Fe}]$ measured from Ca I, Ti I, Ti II and Si I only. Crosses are plotted with a +0.05 offset in V for visibility. Blue triangles correspond to mean $[\alpha/\text{Fe}]$ from Ca I, Ti I, Ti II, Si I and Mg I.

find for Milky Way GCs. However, Beasley et al. (2005) find that the discrepancy between $[\alpha/\text{Fe}]$ in M31 and Milky Way GCs may be an SSP model−dependent result.

Since we have found that $[\text{Mg}/\text{Fe}]$ is likely to be depleted compared to other $\alpha-$elements within GCs due to AGB star self−pollution, we expect that $[\alpha/\text{Fe}]$ ratios in GCs determined from indexes with Mg−dominated absorption features could be lower than the $[\alpha/\text{Fe}]$ abundances that we determine from Ca, Si, or Ti.

To test this, we use the mean $[\alpha/\text{Fe}]$ from Ca, Si and Ti lines for each GC (discussed in § 2.5.2) and compare to the $[\alpha/\text{Fe}]$ estimated by Puzia et al. (2005) from Lick indexes in Figure 2.28. Measurements by Puzia et al. (2005) are plotted as open circles, and our mean $[\alpha/\text{Fe}]$ excluding Mg are plotted as red crosses. We measure a systematically higher value for $[\alpha/\text{Fe}]$ than Puzia et al. (2005) obtain for $[\alpha/\text{Fe}]$ in all three GCs. The largest discrepancy is for G219, for which we find $[\alpha_{\text{CaSiTi}}/\text{Fe}] = +0.47$ and Puzia et al. (2005) estimate $[\alpha/\text{Fe}] = 0.0$. We find the discrepancy for G219 is reduced, but not resolved, if we include our $[\text{Mg}/\text{Fe}] = +0.04$ measurement in the mean $[\alpha/\text{Fe}]$, which is shown by the blue triangle in Figure 2.28.

We note that, in addition to the degeneracy in the Lick indexes at low abun-

68

dances, the effect of different $[\alpha/\text{Fe}]$ ratios in SSP modeling at low abundances is also very weak, further obscuring the resolution of the Lick index measurements at low abundances, as already discussed by Maraston et al. (2003) and Puzia et al. (2005). It is likely that this is the cause of the remaining discrepancy in the $[\alpha/\text{Fe}]$ estimate from low resolution for G219.

While our present sample size of high resolution IL abundances in extragalactic GCs is still small, it already removes some of the discrepancies between M31 and Milky Way GCs from Lick indexes that have been discussed in the literature (Puzia et al., 2005; Beasley et al., 2005; Brodie & Strader, 2006). We find that for this sample of GCs the true $[\alpha/\text{Fe}]$ from Ca, Si, and Ti appear similar for the two galaxies, and that an accurate estimate of this value in GCs for interpretation of the chemical enrichment history of a galaxy must come from elements other than Mg due to the peculiarities of Mg abundances in GCs. Our results indicate that the unexpected, low $[\alpha/\text{Fe}]$ ratios in metal-poor GCs may be an artifact of the uncertainties in line index systems at low metallicities.

2.6.4 Horizontal Branch Morphology

In general, the position of a star on the HB is a function of metallicity; it is expected that metal-poor GCs will have bluer HB morphologies than GCs with higher abundances. The fact that a number of Milky Way GCs at the same metallicity are observed to have very different HB morphologies has led to the conclusion that at least one important "second−parameter" plays a role in HB morphology (see review by Gallart et al., 2005). SSP models that reproduce the HBR−[Fe/H] relationship of the Milky Way are difficult to establish because HB morphology is sensitive to a variety of factors (e.g. mass loss, age, helium abundance, and others) (e.g. Lee et al., 1994; Recio-Blanco et al., 2006). Universal SSP models will be even more difficult to establish if the HBR−[Fe/H] relationship is different in other galaxies. There is evidence that this might indeed be the case; observations of GCs in both M31 and Fornax suggest the HBR−[Fe/H] relationship is offset to lower metallicities than in Milky Way GCs (Rich et al., 2005; Smith et al., 1998).

Low resolution studies have found it important to consider the effect of HB morphology on IL spectra of unresolved GCs because the presence of old, hot stars on the blue HB can mimic light from young main sequence stars, resulting in young or intermediate age determinations for GCs that are actually old (e.g. de Freitas Pacheco & Barbuy, 1995; Beasley et al., 2002b; Schiavon et al., 2004). In the next section we discuss the effect of HB morphology on abundance and age determinations with our high resolution IL method.

Effect on Age and [Fe/H] Determinations

We have used our training set Milky Way GCs to perform tests to assess the effect of inaccurate proportions of red and blue HB stars on our results. The Teramo group has produced isochrones with two different values for mass loss during stellar post-main sequence evolution, a parameter which influences HB morphology. Of the two possible values, we have used isochrones with the less extreme mass loss parameter. This mass loss parameter produces very blue ($B - V \lesssim 0.1$) HB stars for our 13 and 15 Gyr CMDs at [Fe/H] $\lesssim -1.8$, but does not produce bimodal HBs, as is common in many intermediate metallicity GCs. Because we are using the less extreme mass loss parameter, the fear is that the HB may not be as blue as appropriate in some cases.

To test the effect of this potential error, we have added blue HB stars by hand into our synthetic CMDs to ascertain the consequences of underpredicting the number of blue HB stars with our choice of isochrones. In these tests we conserve the total number of stars and total flux of the HB. We find that even though blue HB stars can contribute $10 - 15\%$ of the total flux of the population at wavelengths below 5000 Å, most of the Fe I lines are found over the range 4500-7000 Å, which is not as strongly influenced by the blue HB stars. Empirically, the addition of these stars into the CMD changes the derived Fe I abundances by $< +0.05$ dex. This is not unexpected, because MB08 showed that the Fe I EW strengths are dominated ($\sim 80\%$) by the luminous, cooler stars on the RGB, AGB and red HB, with little effect from hot turn off or hot blue straggler stars, particularly at redder wavelengths.
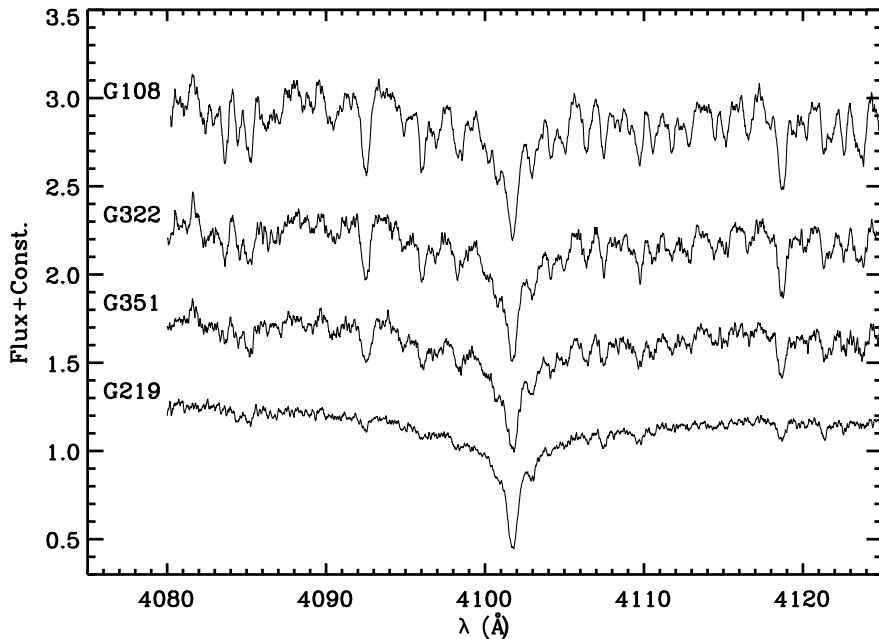
Figure 2.29. M31 GC spectra near Hδ region, shown in order of increasing HBR from top to bottom.

As an example of an extreme test case, we replaced all of the red HB stars with the same number of blue HB stars in the 10 Gyr best-fitting CMD for G219. We know from the HST CMDs of Rich et al. (2005) that G219 has both red HB stars and a large number of blue HB stars that are not entirely represented in the best-fitting CMD. Using this extreme CMD, we find that the Fe I abundance changes by <0.05 dex, the scatter in the Fe abundances increases, and the correlations of Fe abundance with EP, wavelength, and reduced EW get larger. From this extreme example, it is clear that not only do blue HB stars have little impact on the Fe I solution, but that accurate modeling of the red HB results in a much more self-consistent solution from all of the Fe I lines. Therefore, we can expect that having roughly the correct number of red HB stars in the synthetic CMDs will be more important for our abundance determinations than the correct number of blue HB stars. Given the small effect of blue HB stars on Fe I abundances, and given that our analysis only constrains the CMD age for old GCs to a 5 Gyr age range, we find that the accuracy of the blue HB morphology has a no significant (or even detectable) impact on our results.

71

We conclude that the ages and metallicities that we derive for old GCs with our abundance analysis method will not be significantly affected by synthetic CMDs that have inaccurate blue HB morphologies.

As a further consistency check, we can look for qualitative information about the temperature distribution of the preferred CMD solutions in the Fe abundance vs. EP plots discussed in § 2.4.3. A symptom of too few hot, blue HB stars in the isochrone compared to the real GC would be increasing Fe abundances for lines with larger EP. For G108, G315, and G322 we find no significant trend in Fe abundance with EP, which implies that the distribution of stellar temperatures in the CMD solutions for these GCs are very accurate.

For G219 we find decreasing Fe abundances with increasing EP, which suggests in this case that we actually do have too many hot stars in the isochrone for this metal-poor GC. However, we also find higher Fe abundances at larger reduced EWs, which implies that we may have too many dwarf (low microturbulent velocity) stars in the isochrone being used in the analysis. Since the dwarf stars have higher temperatures than the giant stars, for G219 the excess of hot dwarf stars may cause the observed trends. Note that the dependence of Fe abundance on reduced EW may be associated with a small error in the microturbulence for some stars, as discussed in § 2.5.1. However, the mean Fe solution is not strongly affected by these weak trends, and so we do not pursue this issue further.

The only GC in the sample that shows the symptom of not enough hot stars in the Fe abundance vs. EP plot is G351, although it also shows the largest positive dependence of Fe abundance on reduced EW. The diagnostics suggest that there are both too many dwarf stars and not enough hot stars in the best CMD for G351. Also, the standard deviation for [Fe/H] is larger than for the other four GCs. While the solution for this cluster shows somewhat less self-consistency than for the other 4 clusters from the diagnostics discussed above, we emphasize that the overall scatter in the solution is still quite small, suggesting that our solution has not been dramatically affected by unavoidable problems (e.g. interloping stars or internal age or abundance variations) and that the statistical uncertainty is a meaningful estimate of the overall

accuracy of the analysis. Moreover, any difficulties are not likely to be due to the HB morphology.

Consistency with Photometry

We are fortunate that the details of GC HB morphology do not have a large effect on the abundances or ages derived from high resolution IL spectra using this method. However, we can see the effect of HB stars on the temperature sensitive Balmer lines. We are still testing a method to constrain the HB morphology of unresolved GCs using the Balmer lines in high resolution IL spectra (J. Colucci et al. 2010, in preparation). For the purposes of this work, we simply check for qualitative consistency of the Balmer line profiles in the IL spectra with the HST CMDs of Rich et al. (2005). HBR ratios from Rich et al. (2005) for G108, G322, G351, and G219 are listed in Table 2.1, where a value of zero would correspond to a GC with a strongly red HB, and a value of unity would correspond to a GC with a strongly blue HB. From the IL spectra in the region of Hδ, shown in Figure 2.29, it is clear that G219 and G351 have more prominent Balmer line wings, and thus a larger contribution of flux from hot stars than G108, consistent with expectations.

Rich et al. (2005) measure an HBR$-$[Fe/H] relation from HST CMDs for 18 M31 GCs that is offset to lower metallicities than the HBR$-$[Fe/H] relation in Milky Way GCs. One explanation proposed is that the most metal-poor M31 GCs are $\sim 1-2$ Gyr younger than similar GCs in the Milky Way. We note that our lower preferred CMD age range for G219 is consistent with this, although we are unable to put strong constraints on absolute age.

2.6.5 Reddening Constraints from Broadband $B - V$ Colors

In principle, an interesting additional constraint on our potential CMD solutions can be derived by comparing total broadband $(B - V)_0$ colors with existing photometry. This comparison could help us eliminate potential CMD solutions where the integrated colors of the CMDs are inconsistent with the photometry (see MB08). In practice, however, we find that reddening estimates for GCs in M31 are too uncertain to provide constraints on CMDs of the GCs discussed here. Rather, our abundance
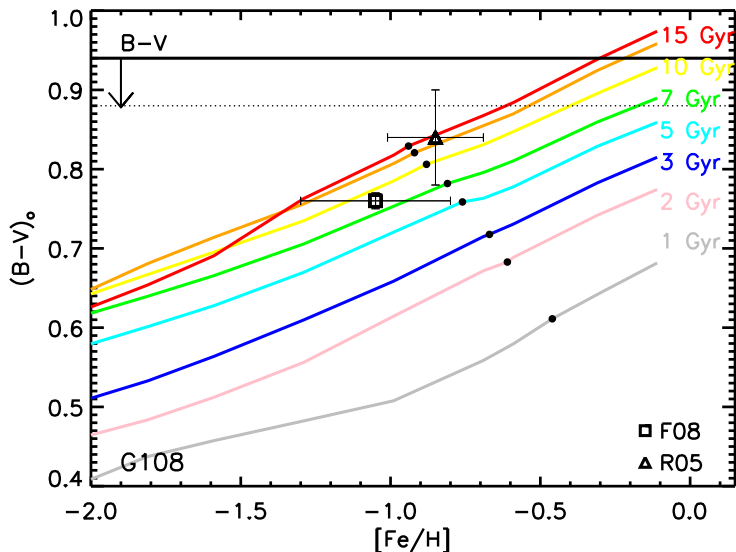
Figure 2.30. Integrated $(B - V)_0$ colors calculated from synthetic CMDs are shown as a function of [Fe/H] for each age. Black points show the [Fe/H] and age solutions determined from this analysis for G108. The horizontal solid line corresponds to the observed $B - V$ color for the GC from Galleti et al. (2004), with an arrow and dotted line to show the $E(B - V)$ correction due to Galactic reddening of Schlegel et al. (1998). $(B - V)_0$ calculated with reddening and metallicity of Fan et al. (2008) (F08) and Rich et al. (2005) (R05) are plotted as open squares and triangles, respectively.

analysis constrains the CMD with enough fidelity that we can actually put some limits on the reddening for these individual M31 GCs. We note that GCs have previously been used in this way to probe reddening in galaxies (e.g. Barmby et al., 2000).

The colors for our synthetic CMDs using Teramo isochrones are shown in Figures 2.30 through 2.34. The broadband $(B - V)_0$ colors calculated from our synthetic CMDs are plotted against the [Fe/H] adopted in the Teramo isochrones for each GC. The trend of $(B - V)_0$ with [Fe/H] for constant age is emphasized by the solid colored lines. Black points correspond to the CMD and [Fe/H] solutions for each age described in § 2.4.3 for each GC. The black solid line in each figure corresponds to the observed $B - V$ color for the GC from the Revised Bologna Catalog (Galleti et al., 2004). Black arrows show the minimum reddening for the M31 line-of-sight of $E(B - V) = 0.06$, which is due to Galactic extinction alone (Schlegel et al., 1998).

For each individual GC we show the recent reddening determination by Fan et al. (2008), who have derived these from correlations between optical and infrared colors
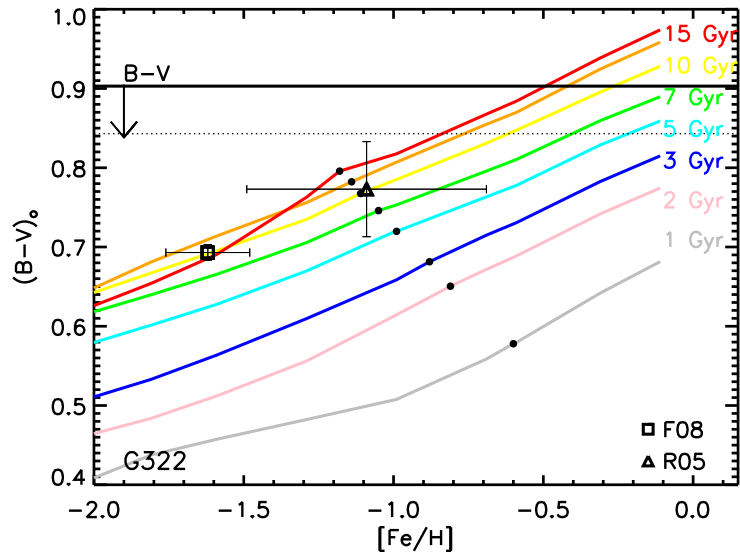
Figure 2.31. Same as Figure 2.30 for G322.
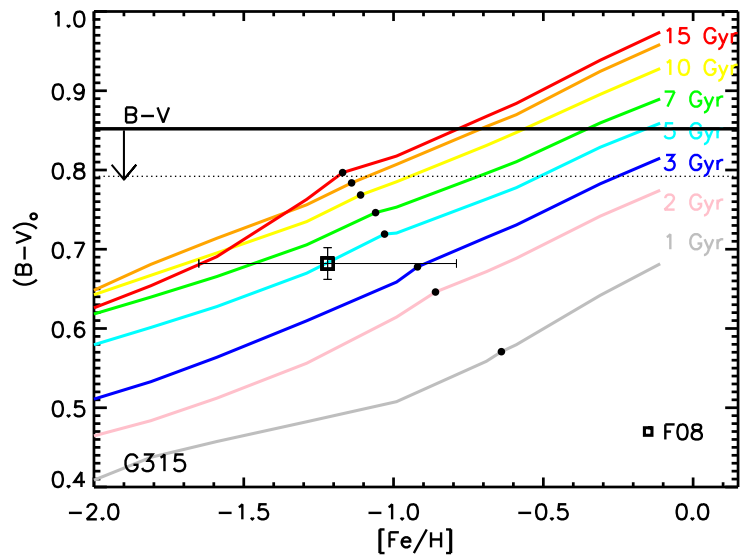
Figure 2.32. Same as Figure 2.30 for G315.
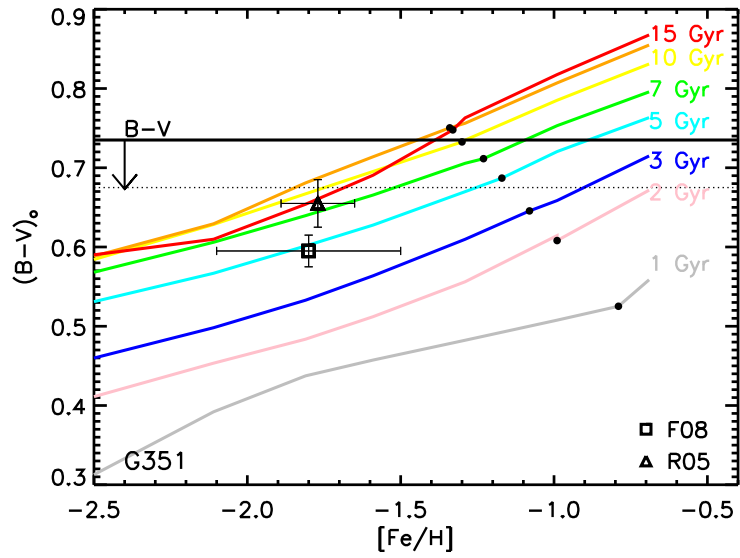
Figure 2.33. Same as Figure 2.30 for G351.
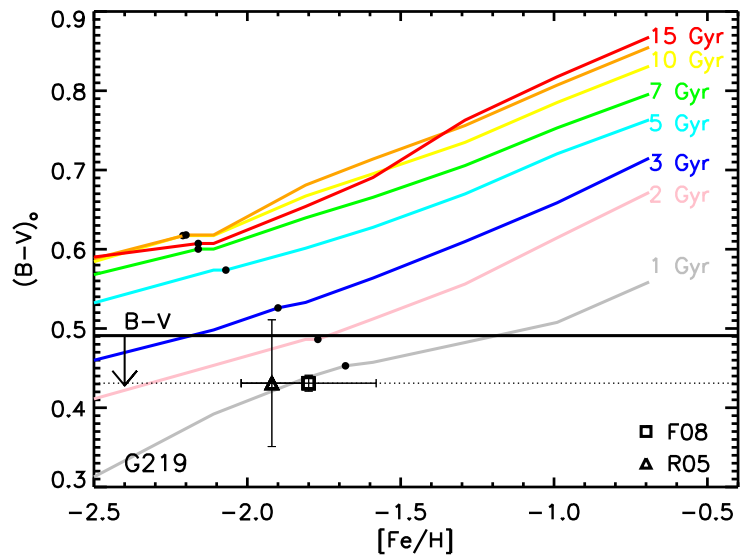
Figure 2.34. Same as Figure 2.30 for G219.

and metallicity using a large set of M31 GC low resolution spectroscopic abundances. The $(B-V)_0$ calculated with the reddenings of Fan et al. (2008) are plotted as open squares, using the low resolution spectroscopic [Fe/H] solutions for the x-axis location. For G108, G322, G351 and G219 we also show the reddening adopted by the deep HST study of Rich et al. (2005), which is an average of several previous measurements. Reddenings of Rich et al. (2005) are plotted as open triangles at the [Fe/H] determined from their HST CMDs.

For each GC we can place an upper limit on the reddening that is consistent with the preferred CMDs for each GC discussed in § 2.5.1. This limit is calculated using the $(B-V)_0$ color of the youngest CMD in the preferred age range and the $B-V$ color from Galleti et al. (2004). The limits are listed in Table 2.12 with the values of Fan et al. (2008) and Rich et al. (2005) for comparison. We note that synthetic CMDs created with the Teramo isochrones that employ a higher mass loss rate than those used here, and thus have bluer HBs overall, would result in slightly lower predicted $(B-V)_0$. For the ages relevant here, the effect HB morphology is at most $\Delta(B-V)_0 \sim -0.03$, and an indication of the uncertainty in our reddening limit.

In general, we find that our preferred CMDs and the reddenings they imply agree best with the [Fe/H] and reddenings of Rich et al. (2005), rather than with the reddenings inferred from low resolution spectroscopic metallicities. For G108, G322 and G351 the $E(B-V)$ derived by Fan et al. (2008) are higher than those adopted by Rich et al. (2005), but it is clear from Figures 2.30 through 2.34 that they are still consistent with an old (>10 Gyr) population at the metallicities applied by Fan et al. (2008).

Although G219 has been verified to be $\sim$10 Gyr or older by HST photometry, by low resolution spectral line indexes, and by high resolution spectra abundances in this work, it has $B-V$ colors substantially too blue for this age. This inconsistency has been noted in the Bologna catalog. In Table 2.12 we list the Galactic $E(B-V) = 0.06$ as the only reliable constraint. We also note that the difference between the observed and predicted $B-V$ for G219 is too large to be explained by a deficit of blue HB

Cluster	ILS Limit	$E(B-V)$	
		1	2
G108-B045	0.13	0.18	0.10
G219-B358	0.06	0.06	0.06
G315-B381	0.08	0.17	$\cdots$
G322-B386	0.15	0.21	0.13
G351-B405	0.06	0.14	0.08

Table 2.12. $E(B-V)$ Comparisons. *References*: (1.) Fan et al. (2008) (2.) Rich et al. (2005)

stars in the synthetic CMD alone, but may be reduced with some contribution from relatively rare, but luminous, post-AGB or UV-bright stars (see Moehler, 2001).

For G351, the $B-V$ of the 10 Gyr CMD is consistent with $E(B-V) = 0.0$, lower than the Galactic $E(B-V) = 0.06$, which we again list as the most reliable constraint in Table 2.12. This difference in color may be at least partially explained by missing blue HB stars in the synthetic CMD as compared to the observed HST CMD in Rich et al. (2005).

G315 is the only GC discussed here for which there are no HST constraints available. We find an $E(B-V) \leq 0.08$ is consistent with our analysis. The larger value determined by Fan et al. (2008) is hard to understand because their derived reddening implies a $(B-V)_0$ that is inconsistent with an old population, even though the high and low resolution [Fe/H] are very similar. It is possible that the discrepancy can arise from inaccurate photometry used by Fan et al. (2008) to determine the $E(B-V)$.

2.7   Summary

We have applied a new method for detailed abundance analysis of high S/N, high resolution IL spectra of unresolved GCs to a sample of five GCs in M31. From over 60-100 resolved spectral lines in each cluster we have derived abundances from EWs for Mg, Al, Si, Ca, Sc, Ti, V, Cr, Mn, Fe, Co, Ni, Y and Ba. We have used our abundance analysis to put independent constraints on the ages and reddening of these M31 GCs, and used the high resolution IL spectra to measure velocity dispersions to high precision.

We find these 5 M31 GCs to be similar to the Milky Way GCs system in several respects. First, they are >10 Gyrs old, and span a range in [Fe/H] of −2.2 to −0.9. Second, their Ca, Si, and Ti abundances are enhanced to similar levels as Milky Way GCs, and suggesting that the gas reservoirs from which they formed were dominated by products of SNII at the time of their formation. Finally, the Fe−peak and the neutron capture abundance ratios studied here also follow Milky Way abundance trends.

We have confirmed that light element abundance variations between stars within GCs can effect abundances derived from high resolution IL spectra for Mg and possibly Al. We suggest that part of the large scatter in [α/Fe] measurements of extragalactic GCs using low resolution line indexes may be due to the effects of Mg−dominated absorption features on line indexes.

We have demonstrated that a significant number of quantitative constraints on galaxy and GC formation and evolution can be made for unresolved GCs using this new abundance analysis technique. We have shown for the first time that abundance ratios fundamental to understanding galaxy formation can be obtained for other nearby, massive galaxies. While we have intentionally targeted "typical" GCs for this first sample in M31, a larger selection of GCs is crucial for a complete picture of the GC system and formation history of M31. Future work is needed to investigate other possible differences in the M31 GC system compared to the Milky Way, i.e. young GCs, high metallicity disk GCs, and enhanced nitrogen abundances.

CHAPTER 3

Refinement of the Abundance Analysis Method on Clusters in the Large Magellanic Cloud

3.1 Introduction

In this Chapter, our goal is to demonstrate and extend the integrated light (IL) abundance analysis method to clusters younger than 10 Gyr in age. Because there are few, if any, high mass, high surface brightness young star clusters in the MW, we have picked clusters in the Large Magellanic Cloud (LMC), a nearby dwarf irregular galaxy, for our second training set. As the cluster population of the LMC is not as well-studied with high resolution spectroscopy as the cluster system in the MW, this training set also provides an opportunity to measure new detailed chemical abundances for some of these clusters.

In general, the LMC cluster and field populations are well-studied photometrically and with low resolution spectra (e.g. Olszewski et al., 1996; Cioni et al., 2006; Carrera et al., 2008; Olszewski et al., 1991). These works have shown that the cluster system had a formation epic >10 Gyr ago, and another burst 2-4 Gyr when many other clusters were formed. There appears to be only one cluster that was formed in the "age-gap" between 4-10 Gyr. On the other hand, the disk field population seems to have had a nearly constant formation rate over most of the history of the LMC, with evidence of localized enhancement in star formation rate 1-4 Gyrs ago (e.g. Geha et al., 1998). The LMC also has a high surface brightness bar, which shows an underlying old population, and some evidence for a burst in star formation ~ 6 Gyr ago (Cole et al., 2000).

Despite the detailed star formation histories that can be constructed from the

resolved stellar populations in the LMC, there is still much that is unknown about the detailed chemical composition and chemical evolution of the LMC. The sample of individual stars with detailed abundances available for the LMC is much more limited than for the MW, due to the much longer integration times needed to obtain high signal-to-noise ratio (S/N), high resolution spectra. The sample of genuinely old (>10 Gyr), metal-poor LMC stars for which detailed abundances are available is limited to handfuls of stars in each of seven globular clusters (Johnson et al., 2006; Hill et al., 2000; Mucciarelli et al., 2009), and often only a handful of elements in each cluster. For younger, more metal-rich populations, Mucciarelli et al. (2008) and Hill et al. (2000) measured abundances in $\sim$2 Gyr old clusters, while Smith et al. (2002) and Pompéia et al. (2008) measured abundances for about $\sim$ 70 field RGB stars. Abundances for some elements also exist for handfuls of young main sequence or supergiant stars (e.g. Hill et al., 2000, 1995; Rolleston et al., 2002; Hunter et al., 2007)

In this paper, we refine the IL abundance analysis method on clusters in the LMC, with a focus on the accuracies of determining chemical abundances for clusters with young ages, and on determining new chemical abundances for previously unstudied clusters. In § 3.2 we discuss the properties of the LMC training set clusters and analysis goals in detail. In § 3.3 we discuss the observations and data reduction, and in § 3.4 we describe our analysis techniques. § 3.5 includes the detailed chemical abundance results and comparisons to the MW training abundances, as well as to the field stars in the LMC. In § 3.6 we compare the IL abundances for the training set clusters to previous work using high resolution spectra of individual stars, and to results from photometry and low resolution spectra. We also discuss the new chemical abundance results we have found for the LMC in this work.

3.2   Globular Cluster Training Set

Our training set includes seven MW clusters, as described in McWilliam & Bernstein (2008) (hereafter Paper I), and Cameron et al. (2010, in preparation) (hereafter Paper II), as well as nine LMC clusters (NGC 1916, NGC 2005, NGC 2019, NGC 1978, NGC

Cluster	RA (2000)	Dec (2000)	V[a]	B − V	E(B − V)	Age (Gyrs)	[Fe/H]	[α/Fe][b]	Ref.[c]
Old (> 5 Gyrs)									
NGC 1916	5 18 37.9	−69 24 23	10.38	0.78±0.02	0.13±0.02	>10	−2.08	⋯	1,13
NGC 2019	5 31 56.5	−70 09 32	10.95	0.77±0.01	0.06±0.02	>10	−1.37	+0.20	2,14
NGC 2005	5 30 10.4	−69 45 09	11.57	0.73	0.10±0.02	>10	−1.80	+0.05	2,14
Intermediate Age (1-4 Gyrs)									
NGC 1978	5 28 45.0	−66 14 14	10.74	0.78±0.04	0.09	1.9	−0.38	+0.02	3,7
							−0.96	+0.38	4
NGC 1718	4 52 25.0	−67 03 06	12.25	0.76±0.01	0.10±0.03	2.1	−0.80	⋯	5,6
Young (< 1 Gyr)									
NGC 1866	5 13 38.9	−65 27 52	9.89	0.26±0.02	0.06	0.13	−0.51	+0.08	4,15
NGC 1711	4 50 37.0	−69 59 06	10.11	0.20±0.08	0.09±0.05	0.050	−0.57	⋯	8
NGC 2002	5 30 21.0	−66 53 02	10.1	0.00	0.20	0.018	−2.2	⋯	11,12
NGC 2100	5 42 08.6	−69 12 44	9.60	0.16±0.02	0.26±0.01	0.015	−0.32	−0.06	9,10,13

Table 3.1. LMC Cluster Sample. *Notes*. a . From Pessev et al. (2008) and Bica et al. (1996) b. Mean of [Si/Fe], [Ca/Fe], and [Ti/Fe] abundances from 2, 3, and 9, and mean of [O/Fe] from 4. c. References for columns 4, 5, 6, 7 and 8: 1.Olszewski et al. (1991), 2. Johnson et al. (2006), 3. Mucciarelli et al. (2008), 4. Hill et al. (2000), 5. Grocholski et al. (2006), 6. Kerber et al. (2007), 7. Mucciarelli et al. (2007), 8. Dirsch et al. (2000), 9. Jasniewicz & Thevenin (1994), 10. Elson (1991), 11. Kumar et al. (2008), 12. Wolf et al. (2007), 13. Pessev et al. (2008), 14. Olsen et al. (1998),15. Walker et al. (2001)

1718, NGC 1866, NGC 1711, NGC 2100, and NGC 2002). The LMC training set includes clusters <10 Gyr old, which is an age range that cannot be probed using clusters in the MW alone. In addition, the LMC training set provides old clusters with a range of abundance ratios (Johnson et al., 2006). This is in contrast to MW clusters, which have very uniform abundance ratios (e.g. Pritzl et al., 2005), and reflects the difference in star formation histories between galaxies with significantly different masses.

Hereafter we separate the LMC training set into three groups according to ages previously determined using other techniques: old (>5 Gyrs), intermediate age (1-4 Gyrs) and young (< 1 Gyr). Details about the LMC training set are listed in Table 3.1.

The goals of this paper are to refine the integrated light method developed in Paper I and Paper II on clusters in the LMC, as well as measure new abundances for LMC clusters previously unstudied at high resolution. To this end, it is important to discuss potential differences between the LMC training set and the MW training

set along with the limitations of the LMC training set when compared to distant, unresolved clusters.

Overall, the LMC training set is of lower data quality (i.e. lower S/N) than the MW training set because the clusters are generally less massive, and therefore less luminous, and they lie at much greater distances (D∼50 kpc). Like the MW training set, we have only observed the core regions of the LMC clusters (discussed further in § 3.3). Because of this, and because the clusters are lower mass and lower density, incomplete sampling is a potential complication for integrated light analysis that arises from only observing a fraction of the total population of the cluster. Because our analysis method involves using theoretical color magnitude diagrams, which accurately represent the full stellar population, incomplete sampling must be explicitly included in our analysis strategy. In this paper, we refer to "sampling uncertainties" to refer to statistical fluctuations in the small numbers of bright stars, which can potentially have a significant impact on the integrated properties of the cluster due to their high luminosities. In general, the importance of sampling uncertainties scales with the total number of stars in the cluster, and therefore with the total luminosity (M_V^{tot}) of the cluster. In our training set clusters in particular, we have effectively reduced the total luminosity of the clusters by observing only a fraction of the total flux, so we can expect that sampling uncertainties will be a greater issue than they would be for integrated light analysis of distant, well populated clusters. It is also important to note that sampling uncertainties are more important for clusters of younger ages, due to the contribution of very few, but very luminous giant stars in rapid phases of stellar evolution (e.g. see Brocato et al., 1999). Therefore, it is especially important to evaluate sampling uncertainties on the younger clusters in our LMC training set, which will suffer from both greater intrinsic statistical fluctuations in the stellar populations and from fluctuations due to observing only a fraction of the total cluster population.

With this in mind, in this work we have extended the integrated light abundance analysis method developed in Paper I and Paper II to include extensive tests designed to address sampling uncertainties in the LMC training set. These tests will be

discussed further in § 3.4.

In summary, when compared to the MW training set, first we expect that the old LMC clusters will be more difficult to analyze due to lower S/N data. Second, we expect that the method strategy will be very similar to the MW training set strategy except for the addition of sampling uncertainty tests developed in this work. We will discuss the extent that these tests can improve our abundance solutions by allowing for statistical variations in the stellar populations.

For clusters <5 Gyr old, we expect that the analysis will be more challenging than for the old clusters because the stellar populations may change significantly over only a <1 Gyr age range. This age sensitivity means that it is crucial to test the IL method on younger clusters in order to assess how well the ages and abundances can be constrained, and to further develop the IL analysis strategy if needed. In addition to the greater sensitivity to smaller changes in age, we can expect that analysis of even distant, unresolved intermediate age and young clusters will be more difficult than for old clusters because of larger intrinsic statistical fluctuations in the stellar populations (e.g. Brocato et al., 1999; Fagiolini et al., 2007; Bruzual & Charlot, 2003). We aim to evaluate how the exacerbated sampling uncertainties in the young LMC training set clusters affect the constraints we can derive for the cluster ages and abundances.

Finally, we note that in this work on the LMC training set, we do not analyze the IL spectra using resolved star photometry as we did for the MW training set in Paper I and Paper II. This is mainly due to the fact that in the core regions we have observed, the quality of the available photometry is not high enough to make this analysis meaningful, with the possible exception of the deep Hubble Space Telescope (HST) photometry for NGC 1978, by Mucciarelli et al. (2007). At the distance of the LMC crowding in the cluster core regions always makes the photometry incomplete for main sequence stars. Moreover, as discussed in Paper II, even tests with the best photometry of Galactic globular clusters (GCs) (e.g. Piotto et al., 2002; Sarajedini et al., 2007) result in a higher scatter in our abundance solutions than tests performed with isochrones. Thus, for clusters in the LMC training set, we limit ourselves to

broad consistency checks with the available photometry, discussed in detail in § 3.6.2.

3.3   Observations and Data Reduction

All of the data for the LMC training set clusters, with the exception of NGC 1718, were obtained using the echelle spectrograph on the 2.5 m du Pont telescope at Las Campanas during lunar dark time in 2000 December and 2001 January. The wavelength coverage of these spectra is approximately 3700–7800 Å.

Because the LMC clusters are spatially resolved, we had to simulate integrated light spectra needed to develop this method for distant, spatially unresolved clusters. This was done by uniformly scanning the central 12×12 arcsec^2 region of NGC 1916, NGC 2005, NGC 1978, NGC 1866, NGC 2002 and NGC 2100, and the central 8×8 arcsec^2 region of NGC 2019 and NGC 1711. These spectra were reduced with standard IRAF[1] routines, combined with the scattered-light subtraction described in Paper I. The observational technique and data reduction are described in further detail in Paper II.

NGC 1718 was observed with the MIKE double echelle spectrograph (Bernstein et al., 2003) on the 6.5 m Magellan Clay telescope in 2006 November. The integrated light spectrum was obtained by scanning the central 12×12 arcsec^2 region of NGC 1718 using a modification to the telescope guiding program provided by D. Osip. The blue side wavelength coverage is 3350–5050 Å, and the red side wavelength coverage is 4800–9000 Å. We used a slit size of 1".0 × 5.0", and 3×2 pixel on-chip binning. The data were reduced using the MIKE Redux pipeline developed by S. Burles, J. X. Prochaska, and R. Bernstein[2].

Exposure times for each cluster and approximate S/N values at three regions in each spectrum are listed in Table 3.2. For all clusters we primarily use the higher S/N data > 4400 Å for our abundance analysis. Example spectra for the clusters are

---

[1]IRAF is distributed by the National Optical Astronomy Observatories, which are operated by the Association of Universities for Research in Astronomy, Inc., under cooperative agreement with the National Science Foundation.

[2]http://web.mit.edu/ burles/www/MIKE/
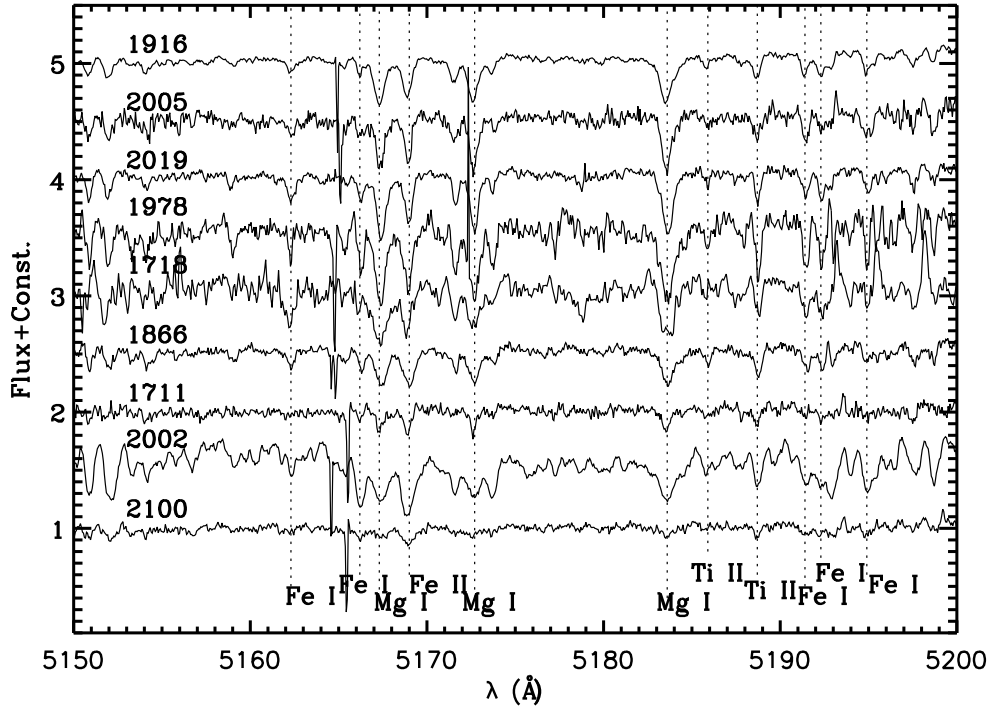
Figure 3.1. Example LMC cluster spectra in Lick Mgb region shown decreasing in age (top to bottom). Note that this region is dominated by saturated lines and is shown for illustration as a region familiar in low resolution spectra analyses.

shown in Figure 3.1.

We have calculated the total V-band flux contained in the scanned region for each cluster (with the exception of NGC 1978) using the surface brightness profiles uniformly measured by McLaughlin & van der Marel (2005). The cluster surface brightness profile parameters and core radii (Mackey & Gilmore, 2003) are listed with the calculated fraction of flux observed in Table 3.3. A surface brightness profile was unavailable for NGC 1978, so we report a rough estimate of the fraction of flux observed that is based on a comparison of the HST photometry of Mucciarelli et al. (2007) (kindly provided by A. Mucciarelli) to the other clusters in our MW and LMC training set. While the exact fraction for NGC 1978 is uncertain, it is clearly small. The S/N of our data for NGC 1978 is also lower than for most of the other clusters in the sample. The combination of lower data quality and undersampling makes analysis of NGC 1978 particularly challenging, which we discuss further in § 3.4.5.

Cluster	Exposure (s)	S/N (pixel^{-1})		
		4380 Å	6100 Å	7550 Å
NGC 2019	20,218	30	70	70
NGC 2005	22,010	20	50	60
NGC 1916	22,785	40	80	90
NGC 1978	50,150	20	50	60
NGC 1718	19,560	80	60	80
NGC 1866	41,230	50	80	70
NGC 1711	18,350	40	50	50
NGC 2100	20,800	50	70	70
NGC 2002	18,357	60	110	140

Table 3.2. Observation Log and Estimated S/N

Cluster	c[1]	R_{King}[1]	R_{core}[2]	Fraction Observed
	arcsec	arcsec	arcsec	
NGC 2019	1.68	2.56	3.61	0.45
NGC 2005	1.53	2.96	3.63	0.60
NGC 1916	1.47	3.02	3.35	0.62
NGC 1978	$\cdots$	$\cdots$	$\cdots$	0.05-0.10
NGC 1718	1.33	10.32	8.52	0.23
NGC 1866	1.65	11.97	14.15	0.14
NGC 1711	1.44	8.35	8.78	0.16
NGC 2100	1.74	4.23	5.02	0.40

Table 3.3. Cluster Structural Parameters & Fraction Observed. 1. From McLaughlin & van der Marel (2005). The concentration parameter is defined as c $\equiv \log_{10}(R_{tidal}/R_{King})$., 2. Cluster core radii from Mackey & Gilmore (2003)

3.4 Abundance Analysis

The method that we have developed for measuring detailed abundances from the integrated light spectra of GCs is extensively described in Paper I, Paper II and Colucci et al. (2009). In § 3.4.1-§ 3.4.3 we briefly review this strategy, which is the basis for the analysis described here. In § 3.4.4 we discuss the results for the old clusters of the LMC training set, as well as an additional technique that we develop here to address incomplete sampling effects. In § 3.4.5 and § 3.4.6 we present the analysis of the intermediate age and young clusters of the training set.

3.4.1 EWs and Line Lists

As in our previous work (Paper I, Paper II, Colucci et al. 2009), we use the semi-automated program GETJOB (McWilliam et al., 1995b) to measure absorption line equivalent widths (EWs) for individual lines in the IL spectra. Continuum regions for each spectral order are interactively fit with low order polynomials and line profiles are fit with single, double, or triple Gaussians. We take special care in continuum placement and attention to line blending due to the nature of IL spectra. Line lists were taken from Meléndez & Barbuy (2009), Paper II, Colucci et al. (2009), and references therein. The lines and EWs used in our final analysis for each cluster can be found in Tables 3.4 and 3.5. For the young clusters NGC 1711, NGC 2002, and NGC 2100 we report EWs measured for Fe lines only, because the abundances cannot be well constrained (see § 3.4.6).

3.4.2 Constructing CMDs and EW Synthesis

Our observed IL EWs are compared to synthesized IL EWs, which we calculate using model cluster populations (i.e. isochrones). These populations are constructed using the single age, single metallicity theoretical isochrones from the Teramo[3] group (Pietrinferni et al., 2004, 2006; Cordier et al., 2007). As in Paper II and Colucci et al. (2009), for ages older than 10 Gyr we use the canonical evolutionary tracks with extended asymptotic giant branch (AGB), $\alpha-$enhanced low$-$temperature opacities

---

[3]Teramo isochrones downloadable at http://albione.oa-teramo.inaf.it/

calculated according to Ferguson et al. (2005), and mass−loss parameter of $\eta=0.2$. However, for ages <10 Gyr we now use the non-canonical evolutionary tracks that include convective overshooting during the H-burning phase. We choose to use the non-canonical tracks for younger ages because Mucciarelli et al. (2007) found them to be a better match than the non-overshooting tracks for their high precision HST photometry of NGC 1978.

Species	λ (Å)	EP (eV)	log gf	EW(mÅ) 1916	EW(mÅ) 2005	EW(mÅ) 2019	EW(mÅ) 1978	EW(mÅ) 1718	EW(mÅ) 1866
O I	7774.180	9.146	0.223	$\cdots$	$\cdots$	$\cdots$	$\cdots$	$\cdots$	86.9
Na I	5682.650	2.100	-0.700	27.7	$\cdots$	$\cdots$	76.5	98.4	$\cdots$
Na I	5688.220	2.100	-0.460	57.4	$\cdots$	34.5	120.5	90.9	60.0
Na I	6154.230	2.100	-1.570	$\cdots$	$\cdots$	$\cdots$	$\cdots$	$\cdots$	18.6
Na I	6160.753	2.100	-1.270	$\cdots$	$\cdots$	$\cdots$	$\cdots$	70.9	39.7
Mg I	4571.102	0.000	-5.569	$\cdots$	$\cdots$	52.5	$\cdots$	$\cdots$	$\cdots$
Mg I	4703.003	4.346	-0.377	$\cdots$	$\cdots$	106.4	$\cdots$	$\cdots$	113.7
Mg I	4703.003	4.346	-0.377	$\cdots$	$\cdots$	150.7	$\cdots$	$\cdots$	113.7
Mg I	5528.418	4.346	-0.341	137.6	83.2	118.0	$\cdots$	110.9	105.1
Mg I	5711.090	4.340	-1.630	$\cdots$	$\cdots$	$\cdots$	$\cdots$	$\cdots$	46.5
Al I	6696.032	3.140	-1.481	$\cdots$	$\cdots$	$\cdots$	$\cdots$	$\cdots$	28.47
Si I	7405.790	5.610	-0.660	$\cdots$	$\cdots$	$\cdots$	$\cdots$	$\cdots$	66.7
Si I	7415.958	5.610	-0.730	$\cdots$	$\cdots$	16.3	$\cdots$	$\cdots$	$\cdots$
Ca I	4454.793	1.899	0.260	$\cdots$	$\cdots$	128.6	$\cdots$	$\cdots$	$\cdots$
Ca I	5349.469	2.709	-0.310	$\cdots$	$\cdots$	33.5	$\cdots$	$\cdots$	$\cdots$
Ca I	5581.979	2.523	-0.555	47.0	$\cdots$	$\cdots$	$\cdots$	$\cdots$	$\cdots$
Ca I	5588.764	2.526	0.358	$\cdots$	$\cdots$	72.5	129.0	84.7	113.4
Ca I	5590.126	2.521	-0.571	$\cdots$	$\cdots$	39.4	89.5	$\cdots$	63.1
Ca I	5601.286	2.526	-0.690	48.7	53.5	56.5	$\cdots$	$\cdots$	$\cdots$
Ca I	5857.459	2.933	0.240	$\cdots$	57.5	91.2	$\cdots$	$\cdots$	$\cdots$
Ca I	5867.572	2.930	-0.801	$\cdots$	$\cdots$	$\cdots$	$\cdots$	$\cdots$	41.7
Ca I	6102.727	1.879	-0.790	$\cdots$	69.2	93.7	$\cdots$	$\cdots$	$\cdots$
Ca I	6122.226	1.886	-0.320	149.5	$\cdots$	102.9	$\cdots$	$\cdots$	135.8
Ca I	6162.180	1.899	-0.090	$\cdots$	$\cdots$	136.1	$\cdots$	150.7	134.0
Ca I	6166.440	2.520	-1.142	$\cdots$	$\cdots$	26.8	$\cdots$	$\cdots$	$\cdots$
Ca I	6169.564	2.526	-0.478	$\cdots$	$\cdots$	$\cdots$	144.0	$\cdots$	$\cdots$
Ca I	6439.083	2.526	0.390	127.4	115.7	104.2	$\cdots$	151.3	123.2
Ca I	6455.605	2.523	-1.290	$\cdots$	$\cdots$	$\cdots$	95.9	$\cdots$	$\cdots$

Ca I	6462.680	2.523	0.262	$\cdots$	102.5	74.0	$\cdots$	$\cdots$	$\cdots$
Ca I	6471.668	2.526	-0.686	62.3	$\cdots$	$\cdots$	69.1	$\cdots$	$\cdots$
Ca I	6493.788	2.521	-0.109	$\cdots$	99.5	76.1	$\cdots$	$\cdots$	$\cdots$
Ca I	6572.795	0.000	-4.310	57.7	$\cdots$	$\cdots$	$\cdots$	$\cdots$	$\cdots$
Ca I	7148.150	2.709	0.137	90.5	$\cdots$	96.8	$\cdots$	$\cdots$	111.5
Sc II	4246.837	0.315	0.240	$\cdots$	$\cdots$	106.1	$\cdots$	$\cdots$	$\cdots$
Sc II	4314.091	0.618	-0.100	$\cdots$	$\cdots$	76.3	$\cdots$	$\cdots$	$\cdots$
Sc II	4670.413	1.357	-0.580	$\cdots$	$\cdots$	22.0	$\cdots$	$\cdots$	$\cdots$
Sc II	5031.024	1.357	-0.400	$\cdots$	$\cdots$	52.0	$\cdots$	$\cdots$	$\cdots$
Sc II	5526.821	1.768	0.020	59.1	62.8	48.6	59.0	66.6	$\cdots$
Sc II	5667.150	1.500	-1.360	$\cdots$	$\cdots$	27.5	83.2	$\cdots$	$\cdots$
Sc II	6245.620	1.510	-1.070	$\cdots$	$\cdots$	$\cdots$	$\cdots$	62.5	57.0
Sc II	6604.600	1.357	-1.480	23.3	$\cdots$	$\cdots$	88.6	$\cdots$	$\cdots$
Ti I	4533.249	0.848	0.476	$\cdots$	$\cdots$	$\cdots$	$\cdots$	$\cdots$	71.5
Ti I	4534.785	0.836	0.280	$\cdots$	$\cdots$	51.0	$\cdots$	$\cdots$	$\cdots$
Ti I	4981.740	0.848	0.504	$\cdots$	135.2	62.8	$\cdots$	$\cdots$	$\cdots$
Ti I	4991.072	0.836	0.380	$\cdots$	$\cdots$	69.5	$\cdots$	$\cdots$	$\cdots$
Ti I	4999.510	0.826	0.250	$\cdots$	$\cdots$	69.9	$\cdots$	122.3	$\cdots$
Ti I	5014.240	0.813	0.110	$\cdots$	74.0	66.8	$\cdots$	$\cdots$	$\cdots$
Ti I	5039.964	0.021	-1.130	$\cdots$	$\cdots$	46.8	$\cdots$	94.4	$\cdots$
Ti I	5064.658	0.048	-0.991	$\cdots$	$\cdots$	$\cdots$	77.3	$\cdots$	$\cdots$
Ti I	5173.749	0.000	-1.118	85.4	$\cdots$	51.1	$\cdots$	$\cdots$	$\cdots$
Ti I	5192.978	0.021	-1.006	$\cdots$	$\cdots$	$\cdots$	90.2	$\cdots$	$\cdots$
Ti I	5210.392	0.048	-0.884	84.1	$\cdots$	73.0	$\cdots$	$\cdots$	$\cdots$
Ti I	5866.461	1.067	-0.840	$\cdots$	$\cdots$	37.6	$\cdots$	$\cdots$	$\cdots$
Ti I	6064.600	1.050	-1.890	$\cdots$	$\cdots$	20.9	$\cdots$	$\cdots$	$\cdots$
Ti I	6126.200	1.070	-1.370	$\cdots$	$\cdots$	25.9	$\cdots$	59.6	43.8
Ti I	6554.238	1.443	-1.218	$\cdots$	$\cdots$	33.2	71.6	$\cdots$	$\cdots$
Ti I	6743.127	0.900	-1.630	$\cdots$	$\cdots$	$\cdots$	65.3	$\cdots$	$\cdots$
Ti II	4394.068	1.221	-1.590	$\cdots$	$\cdots$	58.6	$\cdots$	$\cdots$	$\cdots$
Ti II	4395.040	1.084	-0.660	$\cdots$	131.2	$\cdots$	$\cdots$	$\cdots$	$\cdots$
Ti II	4395.848	1.243	-2.170	$\cdots$	$\cdots$	51.9	$\cdots$	$\cdots$	$\cdots$
Ti II	4399.778	1.237	-1.270	$\cdots$	$\cdots$	$\cdots$	$\cdots$	$\cdots$	78.5
Ti II	4418.342	1.237	-2.460	$\cdots$	65.7	$\cdots$	$\cdots$	$\cdots$	$\cdots$
Ti II	4468.500	1.130	-0.600	$\cdots$	$\cdots$	92.2	$\cdots$	$\cdots$	$\cdots$
Ti II	4501.278	1.116	-0.750	$\cdots$	$\cdots$	81.2	$\cdots$	$\cdots$	$\cdots$
Ti II	4563.766	1.221	-0.960	110.4	72.6	61.0	$\cdots$	$\cdots$	$\cdots$
Ti II	4571.982	1.572	-0.530	137.8	130.9	81.1	$\cdots$	$\cdots$	$\cdots$
Ti II	4589.953	1.237	-1.790	102.0	66.6	$\cdots$	$\cdots$	$\cdots$	64.6
Ti II	5129.162	1.892	-1.390	102.0	$\cdots$	$\cdots$	104.4	$\cdots$	$\cdots$
Ti II	5185.908	1.893	-1.350	$\cdots$	$\cdots$	$\cdots$	92.6	$\cdots$	$\cdots$
Ti II	5188.698	1.582	-1.210	118.2	90.5	$\cdots$	$\cdots$	$\cdots$	$\cdots$

Ti II	5336.794	1.582	-1.700	57.2	42.5	39.1	$\cdots$	$\cdots$	$\cdots$
Ti II	5381.010	1.566	-2.080	$\cdots$	68.8	47.1	$\cdots$	$\cdots$	$\cdots$
V I	6090.210	1.080	-0.060	$\cdots$	$\cdots$	25.6	101.3	54.8	46.0
V I	6090.210	1.080	-0.060	$\cdots$	$\cdots$	27.1	$\cdots$	$\cdots$	$\cdots$
V I	6111.590	1.040	-0.720	$\cdots$	$\cdots$	31.5	$\cdots$	$\cdots$	$\cdots$
V I	6119.500	1.060	-0.320	$\cdots$	$\cdots$	$\cdots$	$\cdots$	63.4	$\cdots$
V I	6135.350	1.050	-0.750	$\cdots$	$\cdots$	$\cdots$	70.5	$\cdots$	$\cdots$
V I	6199.140	0.290	-1.300	$\cdots$	$\cdots$	$\cdots$	$\cdots$	84.6	$\cdots$
V I	6216.430	0.280	-0.810	$\cdots$	$\cdots$	$\cdots$	$\cdots$	$\cdots$	37.1
V I	6531.429	1.220	-0.840	$\cdots$	$\cdots$	$\cdots$	43.5	50.7	$\cdots$
Cr I	5204.470	0.940	-0.210	153.3	$\cdots$	$\cdots$	$\cdots$	$\cdots$	$\cdots$
Cr I	5206.044	0.941	0.019	$\cdots$	$\cdots$	127.8	$\cdots$	$\cdots$	$\cdots$
Cr I	5208.432	0.941	0.158	146.3	$\cdots$	164.2	$\cdots$	$\cdots$	$\cdots$
Cr I	5296.700	0.980	-1.400	$\cdots$	$\cdots$	57.7	$\cdots$	$\cdots$	$\cdots$
Cr I	5345.807	1.004	-0.980	72.3	64.8	69.3	$\cdots$	$\cdots$	$\cdots$
Cr I	5348.340	1.000	-1.290	66.8	74.4	61.0	$\cdots$	$\cdots$	$\cdots$
Cr I	5409.799	1.030	-0.720	111.3	85.0	102.9	$\cdots$	125.9	$\cdots$
Cr I	6330.096	0.941	-2.920	$\cdots$	$\cdots$	$\cdots$	$\cdots$	$\cdots$	21.0
Cr I	7400.188	2.900	-0.111	$\cdots$	$\cdots$	34.9	$\cdots$	$\cdots$	$\cdots$
Cr I	7462.342	2.914	-0.010	$\cdots$	$\cdots$	60.7	$\cdots$	$\cdots$	$\cdots$
Mn I	4754.039	2.282	-0.086	$\cdots$	$\cdots$	$\cdots$	$\cdots$	$\cdots$	45.5
Mn I	5394.670	0.000	-3.500	59.6	56.4	40.2	118.3	$\cdots$	$\cdots$
Mn I	5420.270	2.140	-1.460	$\cdots$	25.8	25.7	$\cdots$	86.7	$\cdots$
Mn I	5432.530	0.000	-3.800	$\cdots$	$\cdots$	30.6	$\cdots$	72.6	$\cdots$
Mn I	5516.670	2.180	-1.850	$\cdots$	$\cdots$	$\cdots$	94.0	$\cdots$	$\cdots$
Mn I	6013.500	3.070	-0.250	36.9	$\cdots$	101.5	$\cdots$	$\cdots$	66.7
Mn I	6016.640	3.070	-0.216	$\cdots$	$\cdots$	$\cdots$	$\cdots$	$\cdots$	60.6
Mn I	6021.800	3.070	0.034	$\cdots$	$\cdots$	$\cdots$	117.0	$\cdots$	86.4
Fe I	3787.891	1.011	-0.838	$\cdots$	$\cdots$	$\cdots$	$\cdots$	153.7	$\cdots$
Fe I	3872.501	0.990	-0.928	$\cdots$	$\cdots$	$\cdots$	$\cdots$	38.0	$\cdots$
Fe I	3927.933	2.832	-2.274	$\cdots$	$\cdots$	$\cdots$	$\cdots$	90.2	$\cdots$
Fe I	4199.105	3.047	0.156	85.1	$\cdots$	$\cdots$	$\cdots$	$\cdots$	$\cdots$
Fe I	4206.702	0.052	-3.960	65.6	$\cdots$	$\cdots$	$\cdots$	$\cdots$	$\cdots$
Fe I	4250.130	2.469	-0.380	$\cdots$	$\cdots$	145.7	$\cdots$	$\cdots$	$\cdots$
Fe I	4250.797	1.557	-0.713	133.0	$\cdots$	$\cdots$	$\cdots$	$\cdots$	$\cdots$
Fe I	4282.412	2.176	-0.779	$\cdots$	$\cdots$	96.3	$\cdots$	$\cdots$	$\cdots$
Fe I	4442.349	2.198	-1.228	$\cdots$	$\cdots$	$\cdots$	$\cdots$	$\cdots$	74.9
Fe I	4447.728	2.223	-1.339	$\cdots$	$\cdots$	$\cdots$	$\cdots$	44.0	$\cdots$
Fe I	4461.660	0.087	-3.194	$\cdots$	$\cdots$	128.6	$\cdots$	$\cdots$	$\cdots$
Fe I	4494.573	2.198	-1.143	$\cdots$	$\cdots$	90.7	$\cdots$	98.5	96.8
Fe I	4602.949	1.485	-2.208	$\cdots$	$\cdots$	84.2	157.0	53.4	78.0

Fe I	4632.918	1.608	-2.901	$\cdots$	$\cdots$	$\cdots$	$\cdots$	51.7	$\cdots$
Fe I	4654.504	1.557	-2.721	$\cdots$	$\cdots$	$\cdots$	$\cdots$	63.3	$\cdots$
Fe I	4691.420	2.990	-1.523	$\cdots$	$\cdots$	$\cdots$	$\cdots$	54.1	$\cdots$
Fe I	4736.783	3.211	-0.752	$\cdots$	$\cdots$	$\cdots$	$\cdots$	74.0	83.4
Fe I	4871.325	2.865	-0.362	$\cdots$	128.9	$\cdots$	$\cdots$	83.2	$\cdots$
Fe I	4871.325	2.865	-0.362	$\cdots$	128.9	$\cdots$	$\cdots$	83.2	$\cdots$
Fe I	4872.144	2.882	-0.567	121.0	77.7	$\cdots$	$\cdots$	107.1	$\cdots$
Fe I	4890.763	2.875	-0.394	107.8	84.9	84.8	$\cdots$	125.7	$\cdots$
Fe I	4891.502	2.851	-0.111	$\cdots$	131.6	127.6	$\cdots$	83.4	$\cdots$
Fe I	4891.502	2.851	-0.111	$\cdots$	131.6	127.6	$\cdots$	83.4	$\cdots$
Fe I	4903.316	2.882	-0.926	83.4	84.9	$\cdots$	$\cdots$	$\cdots$	62.5
Fe I	4918.998	2.865	-0.342	98.4	$\cdots$	$\cdots$	138.9	$\cdots$	$\cdots$
Fe I	4920.514	2.832	0.068	$\cdots$	$\cdots$	155.7	$\cdots$	$\cdots$	$\cdots$
Fe I	4938.820	2.875	-1.077	$\cdots$	$\cdots$	$\cdots$	152.0	64.2	$\cdots$
Fe I	4939.694	0.859	-3.252	78.9	$\cdots$	$\cdots$	$\cdots$	90.7	$\cdots$
Fe I	4966.095	3.332	-0.871	$\cdots$	$\cdots$	$\cdots$	$\cdots$	57.2	$\cdots$
Fe I	4994.138	0.915	-2.969	$\cdots$	68.4	$\cdots$	$\cdots$	46.7	77.3
Fe I	5001.870	3.881	0.050	$\cdots$	$\cdots$	$\cdots$	100.1	$\cdots$	65.1
Fe I	5006.120	2.832	-0.615	$\cdots$	108.4	$\cdots$	$\cdots$	$\cdots$	$\cdots$
Fe I	5014.951	3.943	-0.303	50.0	74.8	$\cdots$	$\cdots$	70.9	$\cdots$
Fe I	5041.763	1.485	-2.203	$\cdots$	$\cdots$	104.8	$\cdots$	$\cdots$	$\cdots$
Fe I	5049.827	2.279	-1.355	93.6	79.6	91.4	$\cdots$	121.0	$\cdots$
Fe I	5051.640	0.915	-2.764	80.3	$\cdots$	105.7	153.3	122.4	85.4
Fe I	5051.640	0.915	-2.764	103.6	$\cdots$	105.7	153.3	122.4	85.4
Fe I	5068.771	2.940	-1.041	$\cdots$	$\cdots$	$\cdots$	$\cdots$	$\cdots$	80.9
Fe I	5074.753	4.220	-0.160	57.1	$\cdots$	$\cdots$	95.4	$\cdots$	61.0
Fe I	5079.745	0.990	-3.245	$\cdots$	$\cdots$	$\cdots$	$\cdots$	84.1	$\cdots$
Fe I	5083.345	0.958	-2.842	$\cdots$	74.4	$\cdots$	$\cdots$	$\cdots$	$\cdots$
Fe I	5123.730	1.011	-3.058	$\cdots$	$\cdots$	$\cdots$	125.5	$\cdots$	$\cdots$
Fe I	5127.368	0.915	-3.249	$\cdots$	$\cdots$	73.9	$\cdots$	$\cdots$	$\cdots$
Fe I	5150.852	0.990	-3.037	$\cdots$	$\cdots$	87.4	110.2	93.2	$\cdots$
Fe I	5151.917	1.011	-3.321	$\cdots$	$\cdots$	$\cdots$	150.9	$\cdots$	$\cdots$
Fe I	5162.281	4.178	0.020	52.8	$\cdots$	$\cdots$	113.6	142.3	$\cdots$
Fe I	5166.284	0.000	-4.123	$\cdots$	$\cdots$	103.3	$\cdots$	107.0	$\cdots$
Fe I	5171.610	0.000	-1.721	$\cdots$	$\cdots$	$\cdots$	151.9	122.8	$\cdots$
Fe I	5191.465	3.038	-0.551	100.2	$\cdots$	95.3	$\cdots$	128.1	$\cdots$
Fe I	5192.353	2.998	-0.421	118.3	$\cdots$	$\cdots$	$\cdots$	133.4	$\cdots$
Fe I	5194.949	1.557	-2.021	$\cdots$	$\cdots$	$\cdots$	151.3	$\cdots$	$\cdots$
Fe I	5195.480	4.220	-0.002	$\cdots$	$\cdots$	$\cdots$	136.5	$\cdots$	$\cdots$
Fe I	5216.283	1.608	-2.082	86.3	$\cdots$	91.9	$\cdots$	69.8	$\cdots$
Fe I	5232.952	2.940	-0.057	114.3	$\cdots$	118.9	$\cdots$	149.9	$\cdots$
Fe I	5254.953	0.110	-4.764	$\cdots$	68.0	$\cdots$	127.2	$\cdots$	$\cdots$
Fe I	5266.563	2.998	-0.385	$\cdots$	96.0	106.3	$\cdots$	$\cdots$	$\cdots$
Fe I	5281.798	3.038	-0.833	$\cdots$	75.9	$\cdots$	101.2	98.1	$\cdots$
Fe I	5283.629	3.241	-0.524	110.5	$\cdots$	$\cdots$	152.9	97.4	$\cdots$

Fe I	5302.307	3.283	-0.720	$\cdots$	$\cdots$	69.5	$\cdots$	124.3	$\cdots$
Fe I	5307.369	1.608	-2.912	62.2	$\cdots$	57.8	90.4	72.5	53.0
Fe I	5324.191	3.211	-0.103	110.2	119.4	102.6	$\cdots$	$\cdots$	85.0
Fe I	5339.937	3.266	-0.720	$\cdots$	69.2	63.8	145.0	61.3	90.7
Fe I	5367.476	4.415	0.443	$\cdots$	$\cdots$	$\cdots$	102.6	45.8	$\cdots$
Fe I	5367.476	4.415	0.443	$\cdots$	$\cdots$	$\cdots$	123.2	45.8	$\cdots$
Fe I	5369.974	4.371	0.536	$\cdots$	$\cdots$	$\cdots$	124.8	101.8	$\cdots$
Fe I	5369.974	4.371	0.536	$\cdots$	$\cdots$	$\cdots$	136.5	101.8	$\cdots$
Fe I	5371.501	0.958	-1.644	$\cdots$	$\cdots$	168.6	$\cdots$	150.7	$\cdots$
Fe I	5383.380	4.312	0.645	70.6	97.1	87.2	$\cdots$	93.6	$\cdots$
Fe I	5389.486	4.415	-0.410	34.9	$\cdots$	$\cdots$	85.7	$\cdots$	$\cdots$
Fe I	5393.176	3.241	-0.715	82.3	63.5	71.6	133.2	114.9	$\cdots$
Fe I	5397.141	0.915	-1.982	$\cdots$	$\cdots$	136.7	$\cdots$	153.7	$\cdots$
Fe I	5405.785	0.990	-1.852	$\cdots$	$\cdots$	139.0	$\cdots$	$\cdots$	$\cdots$
Fe I	5424.080	4.320	0.520	76.8	$\cdots$	$\cdots$	145.2	$\cdots$	$\cdots$
Fe I	5434.534	1.011	-2.126	$\cdots$	69.0	121.2	$\cdots$	116.2	$\cdots$
Fe I	5446.924	0.990	-3.109	$\cdots$	155.9	$\cdots$	$\cdots$	$\cdots$	$\cdots$
Fe I	5455.624	0.000	-2.091	$\cdots$	$\cdots$	155.9	$\cdots$	146.2	$\cdots$
Fe I	5455.624	0.000	-2.091	$\cdots$	$\cdots$	169.5	$\cdots$	146.2	$\cdots$
Fe I	5497.526	1.011	-2.825	$\cdots$	93.0	102.4	119.2	123.7	$\cdots$
Fe I	5501.477	0.958	-3.046	109.8	$\cdots$	116.9	118.6	89.9	85.9
Fe I	5506.791	0.990	-2.789	142.4	108.7	112.3	$\cdots$	83.7	103.6
Fe I	5569.631	3.417	-0.500	75.9	$\cdots$	65.8	$\cdots$	123.0	$\cdots$
Fe I	5572.851	3.396	-0.275	$\cdots$	$\cdots$	$\cdots$	$\cdots$	$\cdots$	106.5
Fe I	5576.099	3.430	-0.900	$\cdots$	$\cdots$	46.6	$\cdots$	$\cdots$	72.7
Fe I	5586.771	4.260	-0.096	$\cdots$	$\cdots$	$\cdots$	$\cdots$	155.3	$\cdots$
Fe I	5586.771	4.260	-0.096	$\cdots$	$\cdots$	$\cdots$	$\cdots$	127.1	$\cdots$
Fe I	5763.002	4.209	-0.450	$\cdots$	$\cdots$	57.9	87.1	81.1	$\cdots$
Fe I	6136.624	2.453	-1.410	129.1	106.6	$\cdots$	129.7	$\cdots$	$\cdots$
Fe I	6137.702	2.588	-1.346	108.7	$\cdots$	85.9	126.3	$\cdots$	$\cdots$
Fe I	6173.341	2.220	-2.863	40.0	$\cdots$	$\cdots$	$\cdots$	62.5	49.1
Fe I	6180.209	2.730	-2.628	$\cdots$	$\cdots$	$\cdots$	$\cdots$	61.2	47.8
Fe I	6187.995	3.940	-1.673	$\cdots$	$\cdots$	$\cdots$	$\cdots$	$\cdots$	33.1
Fe I	6200.321	2.610	-2.386	56.2	52.3	$\cdots$	$\cdots$	72.3	49.1
Fe I	6213.437	2.220	-2.490	$\cdots$	54.7	$\cdots$	$\cdots$	89.2	$\cdots$
Fe I	6219.287	2.200	-2.428	76.6	56.5	$\cdots$	126.3	73.5	64.3
Fe I	6229.232	2.830	-2.821	31.5	$\cdots$	$\cdots$	$\cdots$	$\cdots$	$\cdots$
Fe I	6230.736	2.559	-1.276	101.3	$\cdots$	$\cdots$	$\cdots$	$\cdots$	75.6
Fe I	6240.653	2.220	-3.212	$\cdots$	$\cdots$	$\cdots$	$\cdots$	96.7	$\cdots$
Fe I	6246.327	3.600	-0.796	$\cdots$	$\cdots$	$\cdots$	141.4	65.0	59.6
Fe I	6252.565	2.404	-1.767	71.9	$\cdots$	$\cdots$	132.1	116.5	101.5
Fe I	6254.253	2.280	-2.435	55.6	$\cdots$	60.5	96.3	72.3	$\cdots$
Fe I	6265.141	2.180	-2.532	$\cdots$	$\cdots$	$\cdots$	$\cdots$	86.3	$\cdots$
Fe I	6311.504	2.830	-3.153	$\cdots$	$\cdots$	$\cdots$	$\cdots$	52.2	$\cdots$
Fe I	6322.694	2.590	-2.438	$\cdots$	36.3	47.7	128.7	$\cdots$	58.9

Fe I	6330.852	4.730	-1.640	$\cdots$	$\cdots$	$\cdots$	$\cdots$	43.5	23.7
Fe I	6335.337	2.200	-2.175	74.2	58.6	67.4	135.6	74.1	67.3
Fe I	6336.830	3.690	-0.667	59.5	$\cdots$	$\cdots$	134.6	65.8	68.7
Fe I	6355.035	2.840	-2.328	60.7	$\cdots$	49.6	$\cdots$	68.0	46.5
Fe I	6392.538	2.280	-3.957	$\cdots$	$\cdots$	$\cdots$	$\cdots$	66.5	$\cdots$
Fe I	6392.538	2.280	-3.957	$\cdots$	$\cdots$	$\cdots$	$\cdots$	30.2	$\cdots$
Fe I	6393.612	2.430	-1.505	95.0	$\cdots$	91.7	$\cdots$	129.9	93.9
Fe I	6400.009	3.602	-0.290	$\cdots$	$\cdots$	$\cdots$	$\cdots$	143.3	$\cdots$
Fe I	6411.658	3.650	-0.646	73.2	79.8	67.9	100.4	64.5	78.9
Fe I	6419.956	4.730	-0.183	$\cdots$	$\cdots$	$\cdots$	$\cdots$	$\cdots$	56.0
Fe I	6421.360	2.280	-1.979	83.9	90.2	88.0	142.5	92.0	80.7
Fe I	6430.856	2.180	-1.954	$\cdots$	74.3	76.7	$\cdots$	118.9	$\cdots$
Fe I	6475.632	2.560	-2.929	$\cdots$	$\cdots$	36.7	97.9	40.9	$\cdots$
Fe I	6481.878	2.280	-2.985	$\cdots$	$\cdots$	$\cdots$	100.1	113.3	$\cdots$
Fe I	6494.994	2.400	-1.246	103.3	87.8	124.5	$\cdots$	143.7	$\cdots$
Fe I	6498.945	0.960	-4.675	$\cdots$	$\cdots$	$\cdots$	86.0	$\cdots$	$\cdots$
Fe I	6533.940	4.540	-1.360	$\cdots$	$\cdots$	$\cdots$	58.3	$\cdots$	$\cdots$
Fe I	6546.252	2.750	-1.536	$\cdots$	$\cdots$	$\cdots$	$\cdots$	143.1	$\cdots$
Fe I	6593.874	2.430	-2.377	$\cdots$	58.4	$\cdots$	$\cdots$	$\cdots$	$\cdots$
Fe I	6608.044	2.270	-3.939	$\cdots$	$\cdots$	$\cdots$	$\cdots$	44.9	$\cdots$
Fe I	6625.039	1.010	-5.277	$\cdots$	$\cdots$	$\cdots$	$\cdots$	68.2	$\cdots$
Fe I	6677.997	2.690	-1.395	93.9	$\cdots$	91.4	$\cdots$	103.3	111.0
Fe I	6703.576	2.760	-3.059	31.5	$\cdots$	23.6	79.0	40.1	37.6
Fe I	6705.105	4.610	-1.060	$\cdots$	$\cdots$	$\cdots$	$\cdots$	34.0	35.7
Fe I	6739.524	1.560	-4.801	$\cdots$	$\cdots$	$\cdots$	67.4	44.9	$\cdots$
Fe I	6750.164	2.420	-2.592	$\cdots$	$\cdots$	$\cdots$	$\cdots$	66.0	44.8
Fe I	6806.856	2.730	-2.633	27.1	$\cdots$	$\cdots$	$\cdots$	38.7	48.8
Fe I	6828.596	4.640	-0.843	$\cdots$	$\cdots$	$\cdots$	$\cdots$	$\cdots$	47.9
Fe I	6839.835	2.560	-3.378	$\cdots$	$\cdots$	$\cdots$	77.4	56.5	33.3
Fe I	6841.341	4.610	-0.733	39.3	$\cdots$	$\cdots$	$\cdots$	72.7	50.5
Fe I	6842.689	4.640	-1.224	$\cdots$	$\cdots$	$\cdots$	$\cdots$	$\cdots$	32.4
Fe I	6851.652	1.600	-5.247	$\cdots$	$\cdots$	$\cdots$	$\cdots$	58.4	$\cdots$
Fe I	7024.644	4.540	-1.106	$\cdots$	$\cdots$	$\cdots$	$\cdots$	71.4	$\cdots$
Fe I	7038.220	4.220	-1.214	$\cdots$	$\cdots$	$\cdots$	$\cdots$	65.5	$\cdots$
Fe I	7068.423	4.070	-1.319	$\cdots$	$\cdots$	26.3	$\cdots$	$\cdots$	$\cdots$
Fe I	7130.925	4.300	-0.708	$\cdots$	$\cdots$	$\cdots$	$\cdots$	91.7	70.5
Fe I	7132.985	4.060	-1.635	$\cdots$	$\cdots$	$\cdots$	$\cdots$	64.0	39.1
Fe I	7145.312	4.610	-1.240	$\cdots$	$\cdots$	$\cdots$	$\cdots$	41.5	$\cdots$
Fe I	7151.464	2.480	-3.657	$\cdots$	$\cdots$	$\cdots$	$\cdots$	$\cdots$	45.6
Fe I	7411.162	4.280	-0.287	73.6	$\cdots$	$\cdots$	$\cdots$	$\cdots$	100.7
Fe I	7445.758	4.260	0.053	82.3	69.4	$\cdots$	$\cdots$	99.8	115.1
Fe I	7461.527	2.560	-3.507	$\cdots$	$\cdots$	$\cdots$	$\cdots$	$\cdots$	62.3
Fe I	7491.652	4.280	-1.067	$\cdots$	$\cdots$	$\cdots$	$\cdots$	89.4	$\cdots$
Fe I	7507.273	4.410	-1.107	$\cdots$	$\cdots$	$\cdots$	$\cdots$	49.7	64.7
Fe I	7531.153	4.370	-0.557	$\cdots$	$\cdots$	$\cdots$	$\cdots$	86.6	$\cdots$

Fe I	7540.444	2.730	-3.777	$\cdots$	$\cdots$	$\cdots$	60.2	$\cdots$	$\cdots$
Fe I	7583.790	3.018	-1.885	$\cdots$	$\cdots$	57.2	$\cdots$	$\cdots$	$\cdots$
Fe II	4178.859	2.583	-2.489	$\cdots$	$\cdots$	53.8	$\cdots$	$\cdots$	$\cdots$
Fe II	4416.828	2.778	-2.580	$\cdots$	$\cdots$	46.3	$\cdots$	$\cdots$	$\cdots$
Fe II	4491.405	2.856	-2.710	66.9	$\cdots$	$\cdots$	$\cdots$	$\cdots$	43.9
Fe II	4582.835	2.844	-3.180	$\cdots$	$\cdots$	$\cdots$	82.8	$\cdots$	$\cdots$
Fe II	4583.837	2.807	-1.930	$\cdots$	$\cdots$	$\cdots$	148.4	$\cdots$	102.0
Fe II	4620.521	2.828	-3.210	$\cdots$	$\cdots$	$\cdots$	$\cdots$	$\cdots$	46.3
Fe II	4923.927	2.891	-1.260	112.0	131.4	$\cdots$	$\cdots$	$\cdots$	$\cdots$
Fe II	4923.930	2.891	-1.307	$\cdots$	$\cdots$	114.2	$\cdots$	83.8	$\cdots$
Fe II	5018.440	2.891	-1.100	125.2	124.1	$\cdots$	$\cdots$	$\cdots$	$\cdots$
Fe II	5018.450	2.891	-1.292	$\cdots$	$\cdots$	146.0	$\cdots$	$\cdots$	$\cdots$
Fe II	5197.576	3.230	-2.167	$\cdots$	$\cdots$	47.3	$\cdots$	81.5	$\cdots$
Fe II	5197.577	3.230	-2.220	64.1	$\cdots$	$\cdots$	$\cdots$	$\cdots$	$\cdots$
Fe II	5234.625	3.221	-2.180	87.4	65.8	$\cdots$	87.2	$\cdots$	$\cdots$
Fe II	5234.630	3.221	-2.268	$\cdots$	$\cdots$	60.6	$\cdots$	66.0	$\cdots$
Fe II	5256.938	2.891	-4.060	$\cdots$	$\cdots$	$\cdots$	50.2	$\cdots$	$\cdots$
Fe II	5316.615	3.153	-1.870	117.4	$\cdots$	$\cdots$	145.8	$\cdots$	$\cdots$
Fe II	5316.620	3.153	-1.889	$\cdots$	$\cdots$	111.2	$\cdots$	153.1	$\cdots$
Fe II	5325.553	3.221	-3.160	$\cdots$	30.5	$\cdots$	68.5	$\cdots$	34.2
Fe II	5362.869	3.199	-2.570	$\cdots$	45.7	$\cdots$	$\cdots$	$\cdots$	72.1
Fe II	5425.257	3.199	-3.220	$\cdots$	27.5	$\cdots$	74.9	104.4	$\cdots$
Fe II	5432.967	3.267	-3.380	$\cdots$	$\cdots$	$\cdots$	61.8	$\cdots$	$\cdots$
Fe II	5534.847	3.245	-2.750	$\cdots$	$\cdots$	$\cdots$	$\cdots$	$\cdots$	90.6
Fe II	5534.847	3.245	-2.750	$\cdots$	$\cdots$	$\cdots$	$\cdots$	$\cdots$	47.6
Fe II	5991.376	3.153	-3.540	$\cdots$	$\cdots$	$\cdots$	$\cdots$	$\cdots$	39.9
Fe II	6416.928	3.890	-2.740	$\cdots$	$\cdots$	$\cdots$	$\cdots$	37.8	$\cdots$
Fe II	6432.680	2.891	-3.570	$\cdots$	$\cdots$	$\cdots$	$\cdots$	$\cdots$	54.7
Fe II	6456.391	3.903	-2.075	$\cdots$	$\cdots$	35.4	$\cdots$	104.9	$\cdots$
Fe II	7449.338	3.890	-3.200	$\cdots$	$\cdots$	$\cdots$	$\cdots$	43.0	$\cdots$
Co I	5483.350	1.710	-1.410	$\cdots$	$\cdots$	34.8	$\cdots$	$\cdots$	$\cdots$
Co I	7052.870	1.956	-1.620	$\cdots$	$\cdots$	22.7	$\cdots$	$\cdots$	$\cdots$
Ni I	5084.100	3.680	0.030	39.2	49.7	$\cdots$	89.2	$\cdots$	$\cdots$
Ni I	5115.400	3.830	-0.110	$\cdots$	$\cdots$	$\cdots$	79.5	$\cdots$	$\cdots$
Ni I	5435.880	1.990	-2.590	$\cdots$	$\cdots$	16.5	$\cdots$	$\cdots$	$\cdots$
Ni I	6108.100	1.680	-2.450	$\cdots$	$\cdots$	33.9	$\cdots$	50.1	50.5
Ni I	6108.100	1.680	-2.450	$\cdots$	$\cdots$	39.9	$\cdots$	50.1	50.5
Ni I	6128.900	1.680	-3.330	$\cdots$	$\cdots$	$\cdots$	71.2	$\cdots$	$\cdots$
Ni I	6314.650	1.940	-1.770	$\cdots$	$\cdots$	33.4	$\cdots$	$\cdots$	$\cdots$
Ni I	6327.604	1.676	-3.150	33.5	98.6	21.3	$\cdots$	49.7	31.9
Ni I	6482.809	1.935	-2.630	$\cdots$	$\cdots$	28.3	$\cdots$	$\cdots$	$\cdots$
Ni I	6586.319	1.951	-2.810	$\cdots$	$\cdots$	39.2	$\cdots$	$\cdots$	$\cdots$

Ni I	6643.638	1.676	-2.300	63.0	53.1	58.9	$\cdots$	87.2	74.9
Ni I	6767.784	1.826	-2.170	51.2	51.2	61.6	$\cdots$	$\cdots$	55.2
Ni I	7110.905	1.935	-2.980	$\cdots$	$\cdots$	24.0	$\cdots$	$\cdots$	$\cdots$
Ni I	7122.206	3.542	0.040	61.2	$\cdots$	71.0	$\cdots$	$\cdots$	70.7
Ni I	7393.609	3.606	-0.270	44.1	$\cdots$	51.8	$\cdots$	$\cdots$	$\cdots$
Ni I	7414.514	1.986	-2.570	$\cdots$	$\cdots$	46.1	$\cdots$	$\cdots$	$\cdots$
Ni I	7522.778	3.660	-0.400	$\cdots$	$\cdots$	56.3	$\cdots$	$\cdots$	$\cdots$
Ni I	7525.118	3.635	-0.520	$\cdots$	$\cdots$	41.8	$\cdots$	$\cdots$	52.7
Ni I	7555.607	3.850	0.110	68.2	$\cdots$	42.3	$\cdots$	$\cdots$	74.9
Cu I	5782.050	1.640	-2.920	$\cdots$	$\cdots$	$\cdots$	116.6	$\cdots$	$\cdots$
Sr II	4215.539	0.000	-0.170	112.9	$\cdots$	$\cdots$	$\cdots$	$\cdots$	$\cdots$
Y II	4883.685	1.084	0.070	46.0	$\cdots$	$\cdots$	103.8	$\cdots$	54.6
Y II	5087.420	1.080	-0.170	$\cdots$	$\cdots$	$\cdots$	78.2	$\cdots$	$\cdots$
Zr I	6127.480	0.150	-1.060	$\cdots$	$\cdots$	$\cdots$	$\cdots$	$\cdots$	22.3
Ba II	4554.036	0.000	0.163	118.7	$\cdots$	127.4	$\cdots$	$\cdots$	$\cdots$
Ba II	5853.688	0.604	-1.010	56.0	$\cdots$	48.4	$\cdots$	$\cdots$	118.4
Ba II	6141.727	0.704	-0.077	102.1	108.8	101.2	$\cdots$	$\cdots$	151.6
Ba II	6496.908	0.604	-0.377	79.4	$\cdots$	106.0	$\cdots$	121.4	$\cdots$
La II	5114.510	0.240	-1.030	$\cdots$	$\cdots$	$\cdots$	47.0	$\cdots$	$\cdots$
La II	6390.480	0.321	-1.520	$\cdots$	$\cdots$	$\cdots$	$\cdots$	$\cdots$	33.9
La II	6774.260	0.126	-1.810	$\cdots$	$\cdots$	14.8	$\cdots$	$\cdots$	$\cdots$
Nd II	5249.590	0.976	0.217	$\cdots$	$\cdots$	20.5	53.0	$\cdots$	$\cdots$
Nd II	5293.180	0.820	0.100	$\cdots$	$\cdots$	32.9	$\cdots$	$\cdots$	$\cdots$
Nd II	5319.820	0.550	-0.194	$\cdots$	$\cdots$	36.1	$\cdots$	$\cdots$	$\cdots$
Sm II	4537.954	0.485	-0.230	$\cdots$	$\cdots$	$\cdots$	$\cdots$	$\cdots$	25.9
Eu II	6645.127	1.380	0.204	$\cdots$	$\cdots$	$\cdots$	$\cdots$	$\cdots$	29.9

Table 3.4: Line Parameters and Integrated Light Equivalent Widths for LMC GCs. *Notes*: Lines listed twice correspond to those measured in adjacent orders with overlapping wavelength coverage.

Species	λ	EP	log gf	EW(mÅ)	EW(mÅ)	EW(mÅ)
	(Å)	(eV)		1711	2100	2002
Fe I	4005.254	1.557	-0.583	78.6	$\cdots$	$\cdots$
Fe I	4076.637	3.211	-0.528	41.8	$\cdots$	$\cdots$
Fe I	4132.067	1.608	-0.675	76.8	$\cdots$	$\cdots$
Fe I	4187.047	2.449	-0.514	48.7	$\cdots$	$\cdots$
Fe I	4447.728	2.223	-1.339	61.1	$\cdots$	$\cdots$
Fe I	4736.783	3.211	-0.752	$\cdots$	$\cdots$	107.8
Fe I	4903.316	2.882	-0.926	$\cdots$	$\cdots$	128.4
Fe I	4939.694	0.859	-3.252	$\cdots$	68.9	$\cdots$
Fe I	4966.095	3.332	-0.871	$\cdots$	$\cdots$	136.4
Fe I	5049.827	2.279	-1.355	$\cdots$	$\cdots$	140.6
Fe I	5051.640	0.915	-2.764	$\cdots$	89.7	$\cdots$
Fe I	5074.753	4.220	-0.160	$\cdots$	$\cdots$	73.7
Fe I	5127.368	0.915	-3.249	47.7	$\cdots$	$\cdots$
Fe I	5194.949	1.557	-2.021	61.8	94.9	$\cdots$
Fe I	5254.953	0.110	-4.764	55.2	$\cdots$	$\cdots$
Fe I	5281.798	3.038	-0.833	43.0	$\cdots$	$\cdots$
Fe I	5367.476	4.415	0.443	$\cdots$	$\cdots$	104.7
Fe I	5369.974	4.371	0.536	57.2	$\cdots$	$\cdots$
Fe I	5371.501	0.958	-1.644	73.7	$\cdots$	$\cdots$
Fe I	5371.501	0.958	-1.644	80.6	$\cdots$	$\cdots$
Fe I	5383.380	4.312	0.645	43.2	105.0	135.8
Fe I	5393.176	3.241	-0.715	$\cdots$	106.3	$\cdots$
Fe I	5397.141	0.915	-1.982	45.6	$\cdots$	$\cdots$
Fe I	5446.924	0.990	-3.109	67.4	$\cdots$	$\cdots$
Fe I	5446.924	0.990	-3.109	44.6	$\cdots$	$\cdots$
Fe I	5501.477	0.958	-3.046	$\cdots$	112.1	$\cdots$
Fe I	5569.631	3.417	-0.500	$\cdots$	$\cdots$	155.3
Fe I	5576.099	3.430	-0.900	$\cdots$	$\cdots$	125.3
Fe I	5586.771	4.260	-0.096	$\cdots$	$\cdots$	157.4
Fe I	5763.002	4.209	-0.450	$\cdots$	$\cdots$	122.2
Fe I	6137.702	2.588	-1.346	71.6	$\cdots$	$\cdots$
Fe I	6151.623	2.180	-3.330	$\cdots$	$\cdots$	112.7
Fe I	6200.321	2.610	-2.386	$\cdots$	88.4	105.4
Fe I	6219.287	2.200	-2.428	$\cdots$	$\cdots$	152.4
Fe I	6229.232	2.830	-2.821	$\cdots$	$\cdots$	82.9
Fe I	6265.141	2.180	-2.532	$\cdots$	87.5	$\cdots$
Fe I	6311.504	2.830	-3.153	$\cdots$	54.7	$\cdots$
Fe I	6322.694	2.590	-2.438	47.4	63.4	$\cdots$
Fe I	6330.852	4.730	-1.640	$\cdots$	$\cdots$	33.0
Fe I	6335.337	2.200	-2.175	53.5	106.1	$\cdots$
Fe I	6336.830	3.690	-0.667	40.4	$\cdots$	$\cdots$
Fe I	6353.849	0.910	-6.360	$\cdots$	$\cdots$	86.5

Fe I	6393.612	2.430	-1.505	$\cdots$	135.3	$\cdots$
Fe I	6400.009	3.602	-0.290	69.3	$\cdots$	$\cdots$
Fe I	6411.658	3.650	-0.646	$\cdots$	139.4	158.7
Fe I	6498.945	0.960	-4.675	$\cdots$	127.9	134.0
Fe I	6518.373	2.830	-2.397	$\cdots$	$\cdots$	132.9
Fe I	6533.940	4.540	-1.360	$\cdots$	48.1	36.4
Fe I	6597.571	4.770	-0.970	$\cdots$	$\cdots$	37.5
Fe I	6646.966	2.600	-3.917	$\cdots$	54.1	52.3
Fe I	6648.121	1.010	-5.730	$\cdots$	77.8	107.0
Fe I	6703.576	2.760	-3.059	$\cdots$	57.4	$\cdots$
Fe I	6710.323	1.480	-4.807	$\cdots$	88.7	$\cdots$
Fe I	6725.364	4.100	-2.227	$\cdots$	$\cdots$	60.7
Fe I	6750.164	2.420	-2.592	$\cdots$	90.2	151.1
Fe I	6750.164	2.420	-2.592	$\cdots$	95.2	151.1
Fe I	6806.856	2.730	-2.633	$\cdots$	70.5	91.3
Fe I	6810.267	4.590	-0.992	$\cdots$	64.3	67.6
Fe I	6828.596	4.640	-0.843	$\cdots$	$\cdots$	82.3
Fe I	6839.835	2.560	-3.378	$\cdots$	58.3	100.0
Fe I	6841.341	4.610	-0.733	$\cdots$	53.5	83.7
Fe I	6842.689	4.640	-1.224	$\cdots$	$\cdots$	50.2
Fe I	6843.655	3.650	-0.863	51.6	$\cdots$	52.6
Fe I	6851.652	1.600	-5.247	$\cdots$	51.0	73.4
Fe I	6916.686	4.150	-1.359	$\cdots$	$\cdots$	133.7
Fe I	6960.330	4.570	-1.907	$\cdots$	$\cdots$	37.8
Fe I	7007.976	4.180	-1.929	$\cdots$	$\cdots$	105.2
Fe I	7022.957	4.190	-1.148	$\cdots$	$\cdots$	134.8
Fe I	7038.220	4.220	-1.214	$\cdots$	$\cdots$	139.6
Fe I	7068.423	4.070	-1.319	48.7	$\cdots$	143.1
Fe I	7071.866	4.610	-1.627	$\cdots$	$\cdots$	34.9
Fe I	7072.800	4.070	-2.767	$\cdots$	$\cdots$	23.0
Fe I	7090.390	4.230	-1.109	$\cdots$	$\cdots$	135.1
Fe I	7127.573	4.990	-1.177	$\cdots$	$\cdots$	55.7
Fe I	7130.925	4.300	-0.708	$\cdots$	$\cdots$	146.2
Fe I	7132.985	4.060	-1.635	$\cdots$	$\cdots$	94.2
Fe I	7142.517	4.930	-1.017	$\cdots$	$\cdots$	41.7
Fe I	7145.312	4.610	-1.240	$\cdots$	$\cdots$	80.1
Fe I	7151.464	2.480	-3.657	$\cdots$	$\cdots$	123.0
Fe I	7155.634	4.990	-1.017	$\cdots$	$\cdots$	81.4
Fe I	7445.758	4.260	0.053	89.5	$\cdots$	$\cdots$
Fe I	7454.004	4.190	-2.337	$\cdots$	$\cdots$	47.1
Fe I	7531.153	4.370	-0.557	71.4	147.8	$\cdots$
Fe I	7540.444	2.730	-3.777	$\cdots$	$\cdots$	124.2
Fe I	7583.790	3.018	-1.885	58.8	$\cdots$	$\cdots$
Fe II	4416.828	2.778	-2.580	43.6	$\cdots$	$\cdots$

Fe II	4520.229	2.807	-2.590	47.0	$\cdots$	$\cdots$
Fe II	4666.754	2.828	-3.310	34.8	$\cdots$	$\cdots$
Fe II	4923.930	2.891	-1.307	92.9	$\cdots$	$\cdots$
Fe II	5197.577	3.230	-2.220	$\cdots$	35.0	$\cdots$
Fe II	5234.625	3.221	-2.180	$\cdots$	45.2	$\cdots$
Fe II	5276.002	3.199	-1.963	88.7	$\cdots$	$\cdots$
Fe II	5316.620	3.153	-1.889	106.6	$\cdots$	$\cdots$
Fe II	6317.983	5.511	-1.960	$\cdots$	107.3	$\cdots$
Fe II	6416.919	4.795	-2.640	$\cdots$	51.1	$\cdots$
Fe II	6416.928	3.890	-2.740	$\cdots$	$\cdots$	53.8
Fe II	6516.080	2.891	-3.310	$\cdots$	34.7	$\cdots$

Table 3.5: Line Parameters and Integrated Light Equivalent Widths for young LMC GCs. *Notes*: Lines listed twice correspond to those measured in adjacent orders with overlapping wavelength coverage.

Synthetic color magnitude diagrams (CMDs) are created by combining the model isochrones with an IMF of the form in Kroupa (2002). Unlike in Paper I and Paper II, for the old clusters we do not make a correction for mass segregation in the LMC cluster cores because we have observed a larger fraction of the cluster population than we did for the MW training set. For the younger clusters, for which we have observed a smaller fraction of the population, we do not expect mass segregation due to dynamical evolution to be as significant an effect; as the timescales for central and half-mass relaxation time are several hundred Myr and $\sim$3 Gyr, respectively (e.g. Fischer et al., 1992). For simplicity and self-consistency, in this analysis we ignore the possibility of primordial mass segregation (Vesperini et al., 2009).

Synthetic CMDs are created for the available range of age and metallicity of the Teramo isochrones. Each CMD is divided into $\sim$25 equal flux boxes containing stars of similar properties. The properties of a flux-weighted "average" star for each box are used in the IL EW synthesis, which we perform with ILABUNDS (Paper I). ILABUNDS employs the spectral synthesis code MOOG (Sneden, 1973). We use the (A)ODFNEW model stellar atmospheres of Kurucz[4] (e.g. Castelli & Kurucz, 2004) for all abundance analysis.

As in our previous work, all abundances are calculated under the assumption of

---

[4]The models are available from R. L. Kurucz's Website at http://kurucz.harvard.edu/grids.html

local thermodynamic equilibrium (LTE). To avoid line saturation problems, we only include lines with EWs<150 mÅ in general, or <100 mÅ for Fe II (see Paper II).

3.4.3 Determining the Best-Fitting CMD

Our abundance analysis technique allows us to calculate [Fe/H] solutions for any synthetic CMD, without a priori knowledge of the true cluster population. We draw synthetic CMDs from the library of Teramo isochrones, spanning a range in age and metallicity. To begin the analysis of any cluster, we calculate a mean [Fe/H] abundance from all available Fe I and Fe II lines for a large grid of synthetic CMDs. Then, we are able to use the quality of the Fe abundance solution to constrain the best-fitting age and abundance for each cluster.

The first step in this procedure is to determine one synthetic CMD for each age that has the best-fitting metallicity. Our analysis of the MW training set (Paper II) has shown that the best strategy for consistently identifying the best-fitting CMD for each age is to require that the abundance used in constructing the isochrones be consistent with the abundance recovered by our analysis (see also Colucci et al., 2009). This is essentially taking advantage of the fact that the dependence of the red giant branch (RGB) on metallicity is well understood (e.g. Gallart et al., 2005), and that RGB stars have an important influence on Fe I line strengths in IL spectra. Hereafter, we refer to the solutions where $[\text{Fe/H}]_{\text{iso}} = [\text{Fe/H}]_{\text{cluster}}$ as "self-consistent" Fe abundance solutions. Often, it is clear that the self-consistent solution lies at a metallicity in between two synthetic CMDs in our grid. When this occurs, we calculate an isochrone with the appropriate metallicity according to the interpolation scheme recommended by Pietrinferni et al. (2006).

After constraining the best-fitting synthetic CMD properties from an initial grid of $\sim$70 possibilities to a single [Fe/H] for each age, we are able to isolate the most appropriate age(s) out of these 8 solutions using Fe line diagnostics. These diagnostics, which are commonly used in standard stellar abundance analyses, relate to the quality of the [Fe/H] solutions. In particular, a stable [Fe/H] solution should not depend on the parameters of individual lines (excitation potentials, wavelengths, or

reduced EWs[5]), and the standard deviation of the [Fe/H] solution for Fe I and Fe II lines should be small. Correlations of [Fe/H] with EP, wavelength, and reduced EW are indicative of improper distributions of stellar temperatures, gravities, etc, in the synthetic CMDs as compared to the actual clusters. In general, these effects are difficult if not impossible to disentangle without additional constraints; although we will discuss them in the context of incomplete sampling in § 3.4.4. For the purposes of constraining the best-fitting CMD, we consider synthetic CMDs that minimize these correlations to be most representative of the cluster stellar population. To that end, for each sythetic CMD solution, we perform a linear least-squares fit to [Fe/H] versus EP, wavelength, reduced EW. We then use the magnitude of the slope in these fits for our Fe line diagnostics, along with the standard deviation of the mean [Fe/H] of the Fe I and Fe II lines. We find that these 5 diagnostics are usually strongly correlated with each other, which provides a means to identify the most appropriate synthetic CMD using Fe lines alone.

3.4.4 Old Clusters

In the following sections we describe how we determine the best-fitting synthetic CMD for the old clusters in the LMC training set. We first use the analysis of NGC 2019 to review the basic analysis method developed in Paper I and Paper II, and to introduce the technique we develop here to evaluate sampling uncertainties for each cluster. We then summarize the best-fitting CMD results for NGC 2005 and NGC 1916, respectively.

NGC 2019

We start by outlining the basic analysis strategy for NGC 2019, which is an old, moderately metal-poor cluster with a total luminosity of $M_V^{\rm tot} \sim -8$ (Olsen et al., 1998; Pessev et al., 2008). NGC 2019 is a useful test case for demonstrating the need for accounting for sampling uncertainties in an integrated light analysis. We calculate that we have observed $\sim 45\%$ of the total flux of NGC 2019, which means that this

---

[5]Reduced EW $\equiv$ log(EW / wavelength)
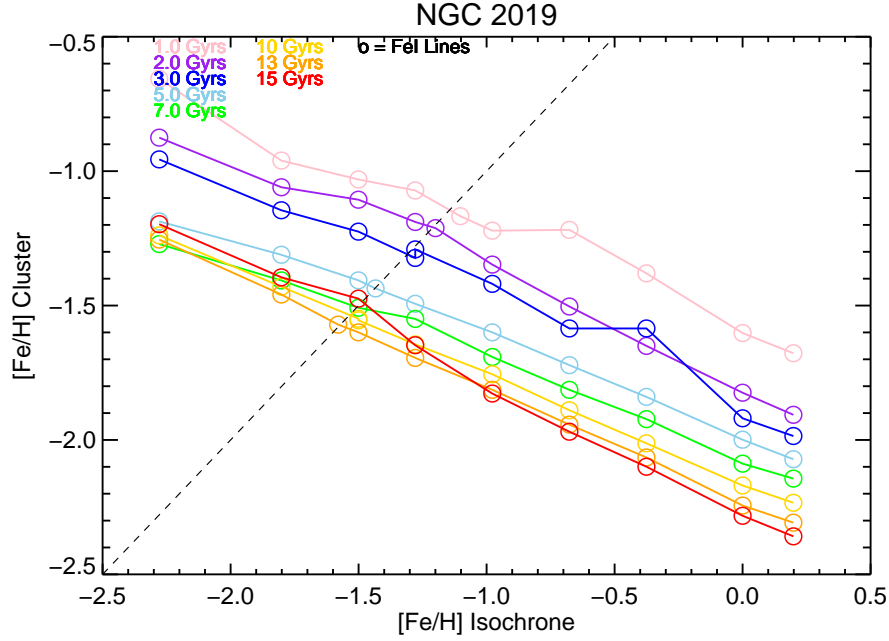
Figure 3.2. Abundance solutions for Fe I lines for NGC 2019. Colors correspond to CMDs of different ages, as labeled. Self-consistent solutions are found where the output [Fe/H]$_{cluster}$ solution equals the input [Fe/H]$_{iso}$ abundance of the isochrone. These solutions fall on the dashed black 1:1 line.

cluster has the most sampling incompleteness of the old clusters in the LMC training set because it has the fewest number of stars in each synthetic CMD.

Before we describe the technique we have applied to NGC 2019 for evaluating sampling uncertainties, we describe our initial strategy for determining a best-fitting CMD and [Fe/H] solution. In Figure 3.2, we show the [Fe/H] solutions for the grid of synthetic CMDs described in § 3.4.2, which span a range in age of 1-15 Gyr, and range in metallicity of $-2.6 \leq$[Fe/H]$\leq +0.2$. The CMDs with self-consistent [Fe/H] solutions (i.e. [Fe/H]$_{iso}$=[Fe/H]$_{cluster}$), lie on the dashed line in Figure 3.2. By requiring self-consistency in the [Fe/H] solution, we have narrowed down the grid of synthetic CMDs to one acceptable CMD for each age. To determine which of the 8 self-consistent CMDs is the best match to the stellar population of NGC 2019, we next compare the Fe line diagnostics. These diagnostics are shown in Figure 3.3. Each diagnostic has been normalized to its worst value in order to show all 5 diagnostics on the same scale. The diagnostics in Figure 3.3 show similarities to the diagnostics found for other old clusters in the MW training set in Paper II and for old clusters
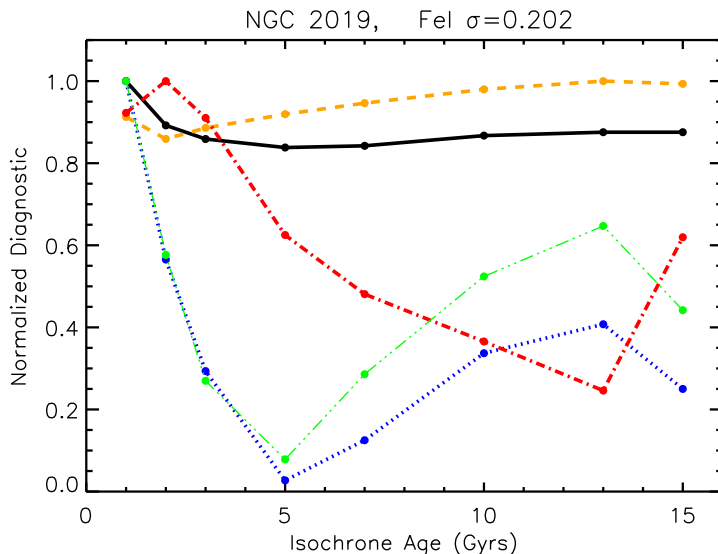
Figure 3.3. Fe abundance diagnostics for self-consistent solutions for NGC 2019. Each diagnostic has been normalized to its maximum, or worst, value in order to show all diagnostics on the same scale. Solid black line shows Fe I σ, orange dashed line is Fe II σ, dotted blue line is the slope in [Fe/H] vs. λ, red dash-dot line is the slope in [Fe/H] vs. EP, and the green dash-triple dot line is the slope in [Fe/H] vs. reduced EW (log(EW/wavelength)). The best solutions are found for ages > 5 Gyr.

in M31 (Colucci et al., 2009). All of the diagnostics are poorest for ages of 1-3 Gyr, which implies that the preferred age for NGC 2019 is ≥5 Gyr. While 5-15 Gyr is a large range in age, it can be seen in Figure 3.2 that the difference in [Fe/H] between the 5 and 15 Gyr synthetic CMDs is only ∼0.15 dex, which means that the metallicity of NGC 2019 is already very well constrained.

We next investigate the effect of incomplete sampling on the age and abundance solutions for NGC 2019. We note that for old clusters, the most important sampling uncertainties will be fluctuations in the number and type of evolved stars; particularly luminous AGB stars and RGB stars (Brocato et al., 2000). Here we will explore tests to improve upon our solution by accounting for statistical fluctuations in luminous stars in NGC 2019, which has the poorest sampling out of the three old clusters in the LMC training set. Although these tests are probably unnecessary for the analysis of more distant and thus better sampled extragalactic clusters, they can be applied with no a priori knowledge of the CMD, and therefore can be easily generalized for the analysis of any cluster.

In order to allow the synthetic CMD stellar populations to vary in a meaningful way, we use a Monte Carlo technique to randomly populate the cluster IMF with discrete numbers of stars. The total number of stars in each synthetic CMD is normalized so that the total flux in the CMD is consistent with the observed M_V^{tot} of the cluster, modulated by the observed flux fraction. We have assumed that stars of different masses are evenly distributed throughout the cluster when reducing the total flux of the cluster to be consistent with the observed region. An important difference between generating the synthetic CMDs using a Monte Carlo method versus the technique used for the original analysis method developed in Paper I and Paper II, is that the Monte Carlo method creates averaged CMD boxes with integer numbers of stars, whereas the original method creates averaged CMD boxes with non-integer numbers of stars (with the constraint that the number of stars in each box must be ≥ 1.0). To illustrate this point, in Table 3.6 we compare the synthetic CMD created using the original method for a 10 Gyr, Z=0.0006 isochrone, to a synthetic CMD created using the Monte Carlo technique. As expected, the significant differences between the two CMDs occur for the luminous ($M_V \leq 0$) boxes representing the upper RGB and AGB stars. Most of these boxes were created by averaging the properties of 10 stars or less, and thus are particularly sensitive to small number statistics. In the example comparison in Table 3.6, the CMD created using the Monte-Carlo technique has one less box than the CMD created using the original technique, due to the redistribution of the luminous stars in boxes 17 through 28.

To approximately assess the impact of sampling uncertainties we have decided to create 100 synthetic CMDs for each isochrone of interest using the Monte-Carlo technique. We will refer to these CMDs created using the Monte-Carlo technique as "CMD realizations." For clarity, we will refer to synthetic CMDs created using the original technique as "averaged CMDs."

One way to assess the effect of under-sampling the population for a given isochrone is to compare the level of statistical fluctuations in the integrated $(B - V)_\text{o}$ color for the CMD realizations (e.g. Brocato et al., 1999, 2000). In Figure 3.4 we show a histogram of the $(B - V)_\text{o}$ for the 100 CMD realizations for a 15 Gyr, [Fe/H]=-1.5

	Averaged			Monte Carlo		
Box	M_V	$B - V$	N_{stars}	M_V	$B - V$	N_{stars}
1	7.178	0.865	19033.70	7.188	0.868	18867
2	6.211	0.640	7343.58	6.215	0.641	7439
3	5.640	0.520	4460.14	5.651	0.521	4325
4	5.208	0.455	2913.89	5.231	0.458	3025
5	4.836	0.414	2185.18	4.863	0.417	2169
6	4.488	0.384	1596.35	4.520	0.386	1596
7	4.165	0.360	1234.24	4.200	0.363	1212
8	3.875	0.346	853.19	3.901	0.347	867
9	3.592	0.349	661.95	3.616	0.348	665
10	3.290	0.404	492.02	3.333	0.389	508
11	2.876	0.593	340.62	2.977	0.567	370
12	2.056	0.674	160.46	2.231	0.665	187
13	1.310	0.719	81.82	1.478	0.708	99
14	0.653	0.771	44.14	0.888	0.750	55
15	0.101	0.830	26.12	0.319	0.805	33
16	−0.235	0.871	19.25	−0.104	0.854	22
17	−0.743	0.948	12.11	−0.453	0.902	16
18	−1.204	1.033	7.90	−0.897	0.975	11
19	−1.623	1.124	5.35	−1.289	1.051	8
20	−2.009	1.225	3.82	−1.815	1.173	5
21	−2.344	1.339	2.80	−2.455	1.387	3
22	−2.606	1.448	1.88	0.442	0.569	36
23	0.185	0.629	31.98	0.430	0.532	35
24	0.430	0.530	35.19	0.400	0.531	34
25	0.404	0.528	34.44	−0.231	0.732	23
26	0.071	0.653	26.34	−1.552	1.048	6
27	−1.258	0.981	7.93	−2.676	1.514	3
28	−2.583	1.520	2.28	. . .	. . .	. . .

Table 3.6. Example Synthetic CMD Comparison

isochrone, which is one of the self-consistent age and abundance solutions for NGC 2019. The 100 CMD realizations for this isochrone show a spread in $(B-V)_{\rm o}$ of ~0.13 mag. Note that the number of stars in these CMDs were normalized to correspond to 45% of the flux of a $M_V^{\rm tot} \sim -8$ cluster, which corresponds to the observed flux of NGC 2019. To evaluate the spread in $(B-V)_{\rm o}$ that is a result of our observed flux fraction, in Figure 3.4 we also show the histogram for the 100 realizations of a CMD normalized to 100% of a $M_V^{\rm tot} \sim -8$ cluster. The spread in $(B-V)_{\rm o}$ of the more luminous CMD realizations is ~0.8 mag, which, as expected, is less than that for the less luminous CMD realizations. For comparison, we also mark the $(B-V)_{\rm o}$ of the averaged CMD created using the original technique with a dotted line in Figure 3.4. The $(B-V)_{\rm o} = 0.69$ of this synthetic CMD is consistent with the $(B-V)_{\rm o}$ of the peak in both CMD realization histograms, which we would expect because this CMD represents an average population for the isochrone.

After creating CMD realizations for a given isochrone, an appropriate subset of CMD solutions can be identified by applying other observable constraints. As a first constraint, we can eliminate any CMD realization that has an integrated $(B-V)_{\rm o}$ that is inconsistent with the observed, reddening-corrected $B-V$ of the cluster. For example, the CMD realizations for NGC 2019 that have a $(B-V)_{\rm o}$ consistent with the observed color from the catalog of Pessev et al. (2008), and the $E(B-V)$ determined by Olsen et al. (1998) are shown by the shaded the region of the histogram in Figure 3.4. In this case, we note that the $(B-V)_{\rm o}$ of the averaged CMD is also consistent with the observed $B-V$ of NGC 2019, which is a hint that the averaged CMD may already be a reasonable match.

With this subset of CMD realizations, we can now calculate new [Fe/H] abundance solutions. These solutions are shown in Figure 3.5, which also shows the averaged CMD solutions from Figure 3.2 for reference. We find that the redistribution of luminous, cool giants in the CMD realizations results in a spread in the derived output [Fe/H]. This result is not unexpected, because cool giants have a strong influence on the flux-weighted Fe I EWs, which was discussed in Paper I. To clarify this point in the context of sampling uncertainties, in Figure 3.6 we show the contribution of
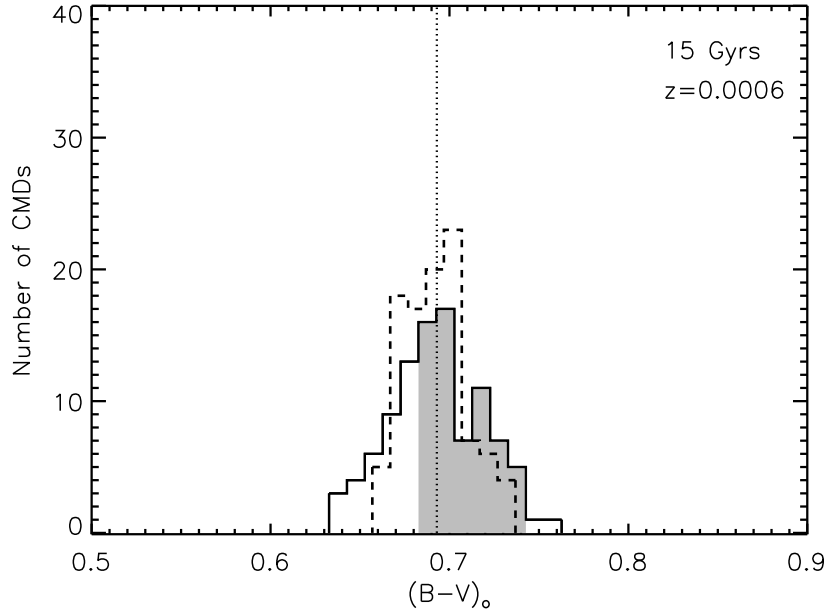
Figure 3.4. Histogram of integrated $(B-V)_\mathrm{o}$ color for 100 CMD realizations of a 15 Gyr, z=0.0006, ([Fe/H]=−1.5) isochrone. Solid black line shows the histogram for a population where the total flux in stars has been normalized to 45% of a $M_V^\mathrm{tot}=-8$ cluster, which is appropriate for our integrated light spectrum of NGC 2019. Dashed black line shows the histogram for a population normalized to 100% of a $M_V^\mathrm{tot}=-8$ cluster. CMDs with $(B-V)_\mathrm{o}$ color consistent with the observed, reddening-corrected $B-V$ of NGC 2019 are shaded in gray. The $(B-V)_\mathrm{o}$ of the averaged CMD is marked by the dotted line, and is consistent with the peak in both histograms for the CMD realizations, as it represents an average population.
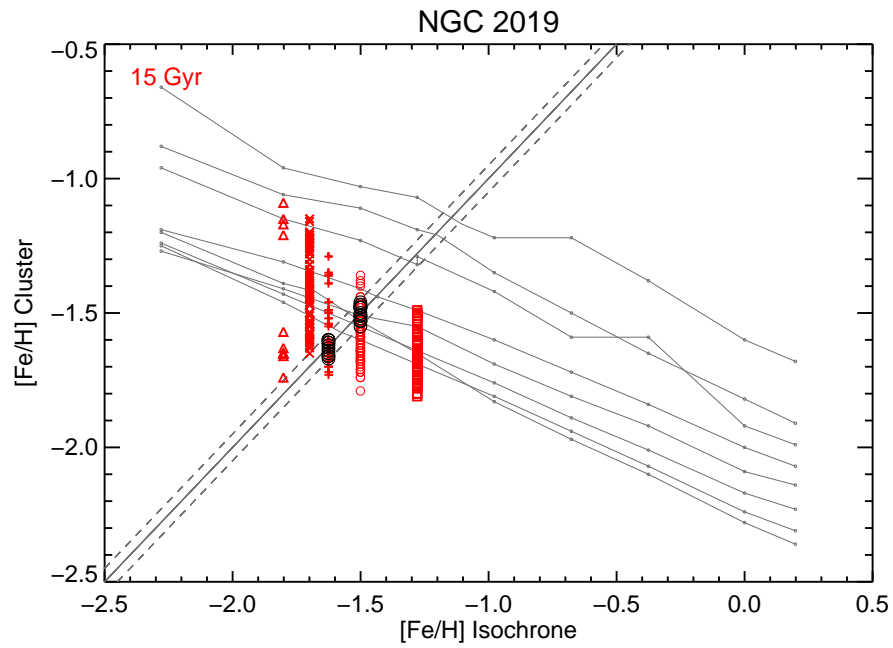
Figure 3.5. Same as Figure 3.2, with the addition of the Fe I abundance results for the CMD realizations of NGC 2019. Red points correspond to 15 Gyr CMD realizations. Only CMD realizations consistent with the observed $B-V$ color of NGC 2019 are shown. Black circles on the solid black 1:1 line denote CMD realizations that satisfy the self-consistent criterion $[Fe/H]_{iso}=[Fe/H]_{cluster}$, and are therefore possible solutions for the population of NGC 2019.

each box in some example synthetic CMDs to the flux-weighted Fe I EWs. The left panels in Figure 3.6 show the EW fraction for two Fe I lines with significantly different EPs, but similar wavelengths, as well as two Fe I lines with similar EPs but a large difference in wavelength. These line comparisons are chosen to emphasize how redistributions of luminous, cool giants can affect the [Fe/H] vs. EP and [Fe/H] vs. wavelength diagnostics. In general, Figure 3.6 demonstrates that the RGB and AGB CMD boxes dominate ($\sim$80%) the Fe I EWs. More subtle is the fact that high EP and bluer wavelength Fe I lines are slightly less sensitive to AGB and RGB boxes than low EP and redder wavelength lines. The high EP and bluer wavelength lines are more sensitive to the main sequence (MS) and horizontal branch (HB) boxes than the low EP and redder wavelenth lines, because they have stars at hotter temperatures. The sensitivity of the Fe I line abundances to small redistributions of flux between the AGB, RGB and HB means that different CMD realizations result in a spread in mean [Fe/H], but also that the Fe line diagnostics are in principle sensitive to whether a statistically rare CMD realization results in an improvement in the overall stability of the [Fe/H] solution.

A consequence of the spread in output [Fe/H] seen in Figure 3.5 for the CMD realizations is that many of the CMD realizations are not self-consistent, which is a violation of one of our first criteria for a good solution. Therefore we eliminate CMD realizations that do not result in a [Fe/H]$_{\mathrm{cluster}}$ that is within ± 0.05 dex of the [Fe/H]$_{\mathrm{iso}}$. For this example, we have marked the CMD realizations that meet this requirement as black circles in Figure 3.5.

It is clear from this exercise that there may be self-consistent CMD realizations that exist at different [Fe/H] than our original solution. It is therefore necessary to follow the procedure outlined above for a range of isochrone metallicity (and ages if warranted). In the case of NGC 2019, we have done this for isochrones with [Fe/H]=-1.8 to -1.3 and for ages between $5-15$ Gyr, which can be seen in Figure 3.5. We note that the original averaged CMD solutions at ages of 5 and 7 Gyr have integrated $(B - V)_{\mathrm{o}}$ colors that are inconsistent with the observed $B - V$ of NGC 2019. This is apparent in Figure 3.7, where it can be seen that the averaged 5 and
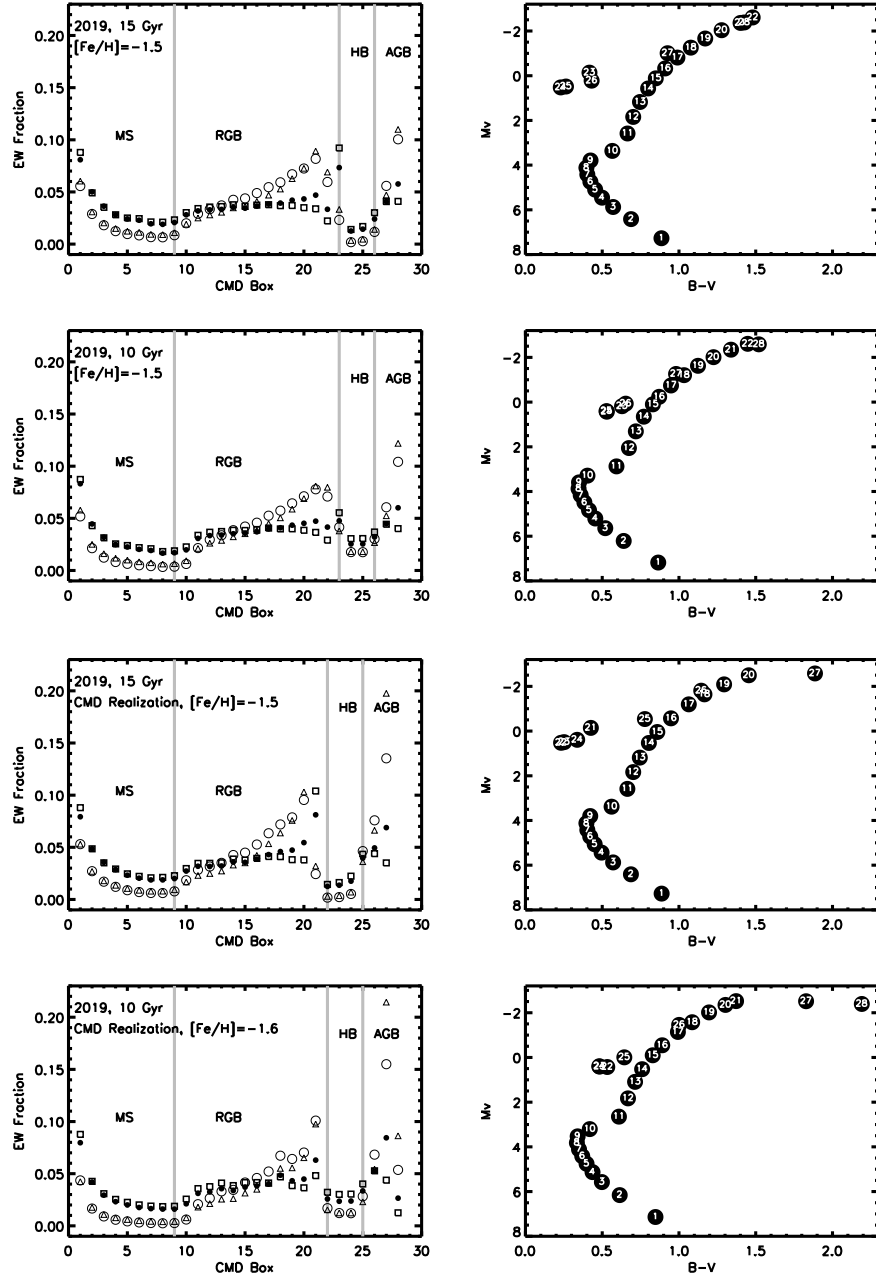
Figure 3.6. Fe I EW strength for synthetic CMD boxes. Left panels show the contribution of each synthetic CMD box to the total EW fraction of an Fe I line, and right panels show the associated synthetic CMDs, with the box numbers labeled. Top two rows correspond to the averaged CMDs with ages of 15 and 10 Gyr, respectively, and [Fe/H]=−1.5. Third row corresponds to the best-fitting CMD realization for NGC 2019 with an age of 15 Gyr and [Fe/H]=−1.5, and the bottom row corresponds to the best-fitting CMD realization with an age of 10 Gyr and [FeH]=−1.6. In the left panels, for an EP comparison, the 5307 Å Fe I line (EP=1.60 eV), and 5383 Å Fe I line (EP=4.3eV), are shown by open and filled circles respectively. For a wavelength comparison, the 4494 Å Fe I line (EP=2.20 eV), and 6677 Å Fe I line (EP=2.70) are shown by open squares and open triangles, respectively. The RGB and AGB CMD boxes dominate the contribution to the Fe I line EWs.
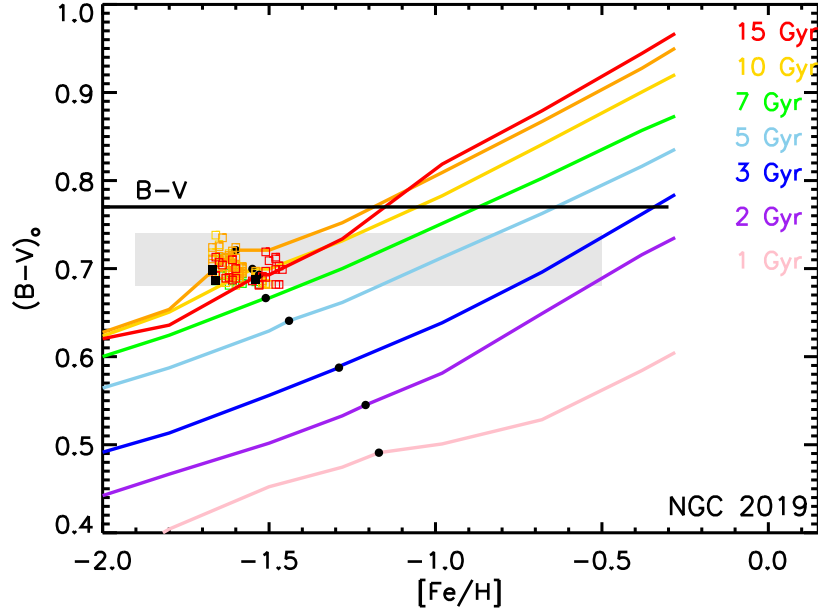
Figure 3.7. Integrated $(B-V)_o$ colors calculated from the grid of synthetic CMDs for NGC 2019, shown as a function of $[Fe/H]_{iso}$ for each age. Colors denote CMDs with the same ages as in Figure 3.2. Black circles show the $[Fe/H]_{cluster}$ and age solutions determed for the averaged CMD analysis. Solid horizontal line corresponds to the observed $B-V$ of NGC 2019 from Table 3.1. Gray shaded region corresponds to the region in $(B-V)_o$ that is consistent with the reddening corrected $B-V$, with photometric uncertainties. Colored square points correspond to the $(B-V)_o$ and $[Fe/H]_{cluster}$ of self-consistent CMD realizations for NGC 2019, while black solid squares correspond to the best-fitting CMD realization for each age.

7 Gyr solutions, which are marked as filled black circles, are outside the shaded gray region corresponding to the observed $B-V$ of NGC 2019. However, there are some CMD realizations for an age of 7 Gyr that satisfy the $(B-V)_o$ requirement, but in general there are many fewer acceptable 7 Gyr CMD realizations than there are for ages >10 Gyr.

We find 120 CMD realizations for isochrones with ages of $7-15$ Gyr and $[Fe/H]_{iso} = -1.6$ to -1.5 that are consistent with the observed $(B-V)_o$ of NGC 2019 and also result in a self-consistent $[Fe/H]$ solution. We next identify the best-fitting CMD(s) for each age using the Fe diagnostics introduced in § 3.4.3. In Figure 3.8 we show the normalized Fe I diagnostics for the 120 CMD realizations, which we have designated CMDs 0 through 119. As was the case for the original 8 averaged CMD solutions, the most stable CMD realizations are those that minimize all of the diagnostics si-
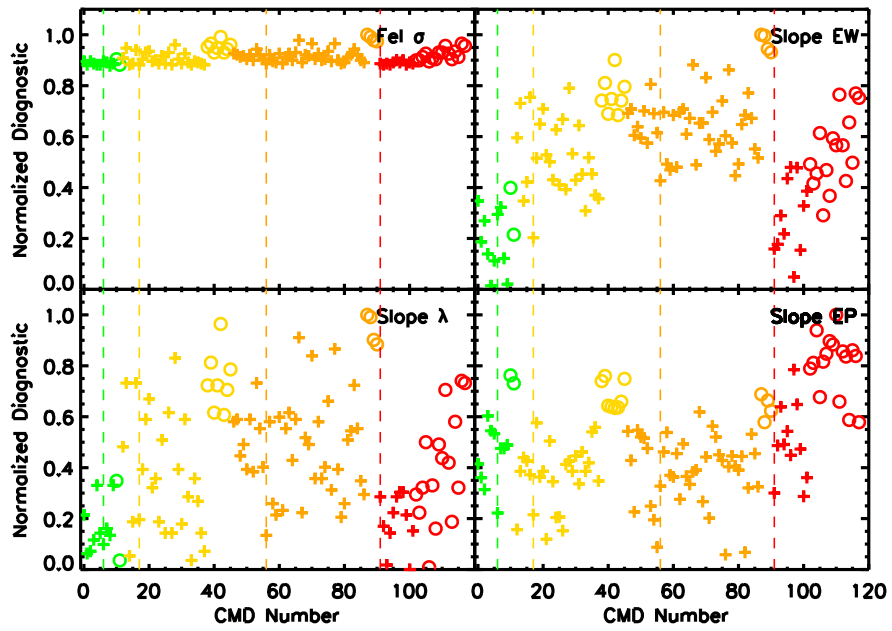
Figure 3.8. Normalized diagnostics for NGC 2019 CMD realizations that satisfy color and Fe I self-consistency criteria. Symbols and colors are the same as in Figure 3.5. CMDs are arranged by increasing age, and then by increasing [Fe/H]$_{iso}$ for each age. The best solution for each age is shown by a dashed line, and corresponds to the solution that best minimizes all four diagnostics at once. For NGC 2019, the best solution overall is for an age of 10 Gyr, and [Fe/H]= -1.6.

multaneously. We highlight the best-fitting, most stable solution for each age with dashed lines in Figure 3.8. In the case of NGC 2019 we find that for ages of 7, 10 and 15 Gyrs the best-fitting CMD realization has an input $[\mathrm{Fe/H}]_{\mathrm{iso}} = -1.6$, which is 0.1 dex lower than the $[\mathrm{Fe/H}]_{\mathrm{iso}}$ of the best-fitting averaged CMD solutions. For an age of 13 Gyrs the best-fitting solution has an input $[\mathrm{Fe/H}]_{\mathrm{iso}} = -1.5$, which is the same as for the original averaged CMD solution.

After identifying a best-fitting CMD realization for each age, we can compare the normalized diagnostics in order to identify the best-fitting age(s) for NGC 2019, similar to what we did for the averaged CMD solutions at the beginning of this section. Figure 3.9 shows the diagnostics for the original $1-5$ Gyr solutions compared to the diagnostics for the best-fitting CMD realizations at ages of $7-15$ Gyr. The main differences between Figure 3.3 and Figure 3.9 are that the diagnostics for ages of $7-15$ Gyrs are clearly much more strongly correlated with each other, and that the CMDs with ages of 7, 10 and 15 Gyrs result in more stable $[\mathrm{Fe/H}]$ solutions than the original averaged CMD solutions. For reference, in Figure 3.10 we show the $[\mathrm{Fe/H}]$ solutions as a function of EP, wavelength and reduced EW for the original averaged 15 Gyr solution, as well as the best-fitting 10 Gyr CMD realization. It is visually apparent in Figure 3.10 that for the 10 Gyr CMD realization the Fe I σ is reduced and the dependence of $[\mathrm{Fe/H}]$ on EP, wavelength and reduced EW is significantly smaller. Therefore, we choose to use the 10 Gyr CMD realization as our best-fitting CMD for calculating the abundances of all other elements.

To understand why the 10 Gyr CMD realization results in a much more stable solution than the original averaged 15 Gyr solution, it is helpful to revisit Figure 3.6. The right panels of Figure 3.6 show the synthetic CMDs for the original 15 and 10 Gyr solutions, as well as a 15 Gyr CMD realization at the same $[\mathrm{Fe/H}]$ of the original solutions and the best-fitting 10 Gyr CMD realization, which has a lower $[\mathrm{Fe/H}]$ by ~ 0.1 dex. The original 10 and 15 Gyr solutions are very similar except for the position of the HB boxes, and therefore there are only subtle differences in the Fe I EW fractions in the left panels. However, for both the 15 Gyr and 10 Gyr CMD realizations there are very red, very luminous, and very cool average star boxes on

113
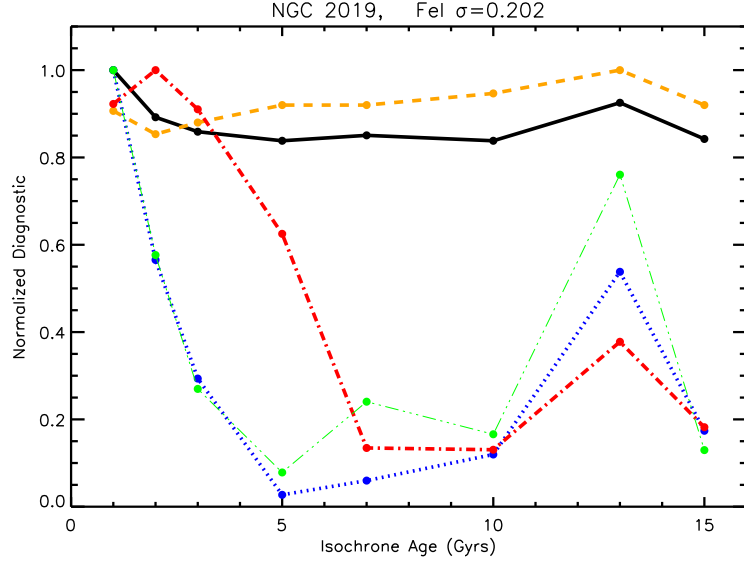
Figure 3.9. Same as Figure 3.3, except the solutions shown for ages of 7 to 15 Gyr correspond to the solutions for the best-fitting CMD realizations. The diagnostics for these ages are more correlated with each other than for the averaged CMD solutions, and the best solutions are found for 7−15 Gyrs.

the AGB that are not present in either of the original CMDs. AGB stars at these types of luminosities and temperatures are relatively rare, so for less massive clusters, boxes at these positions in the CMD do not appear for the "averaged" CMDs that we construct using our original technique. It is evident from Figure 3.6 that not only do the AGB stars in the very luminous and very cool boxes contribute significantly to the Fe I EWs, but they contribute especially to the low EP and redder wavelength Fe I line EWs. This means that in principle, we can evaluate whether allowing for very cool and luminous AGB stars does or does not improve the stability of the [Fe/H] solution with EP and wavelength. In the case of NGC 2019, for the original averaged CMD solutions we found higher [Fe/H] at redder wavelengths, as well as higher [Fe/H] at lower EP. The addition of significant line strength in very red and very cool stars in the synthesized EWs means that lower Fe abundances are required to match the observed EWs for the redder wavelength and lower EP lines. Therefore the result of adding significant cool AGB flux is a decrease in the dependence of [Fe/H] on EP and wavelength.

In conclusion, we have calculated age and abundance solutions for synthetic CMDs
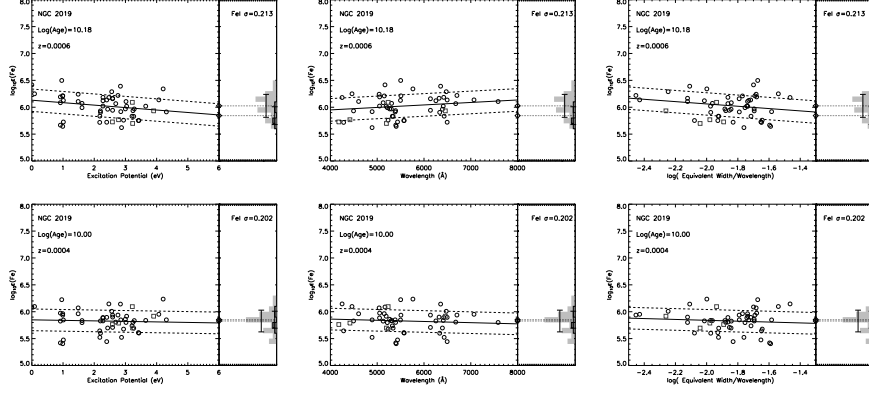
Figure 3.10. Individual diagnostic plots for NGC 2019, where Fe I and Fe II lines are marked by dark circles and light squares, respectively. The solid line shows the linear fit to the Fe I lines and dashed lines show the 1 σ deviation of points around the fit. Dark and light diamonds mark the average Fe I and Fe II abundances. The original averaged CMD solution using a 15 Gyr, [Fe/H]-1.5 isochrone is shown in the top panels. The final solution for a best-fitting CMD realization using a 10 Gyr, [Fe/H]$=-1.6$ CMD isochrone is shown in the bottom panels. The final solution has a smaller Fe I σ and smaller dependence on EP, wavelength, or reduced EW than the original solution.

with a range of age and [Fe/H] for NGC 2019, and found that a stellar population that is 5$-$15 Gyr in age, and has [Fe/H]$= -1.5$ provides the most self-consistent solution using our original technique. In this section we have described a supplementary technique to evaluate the level of sampling incompleteness for our observations, and performed tests to assess whether the [Fe/H] solutions can be improved by allowing for statistical fluctuations in the stellar population. In the case of NGC 2019, we find that these tests allow us to improve our constraint on the age to 7$-$15 Gyr, as well as determine that a CMD realization with [Fe/H]$=-1.6$ that includes rare and cool AGB stars is a more appropriate match to the stellar population.

NGC 2005

The next LMC training set cluster we analyze is NGC 2005. We summarize the results for the best-fitting CMD solutions, which are determined following the procedure outlined for NGC 2019 above.

The diagnostics for the 8 self-consistent averaged CMD solutions for NGC 2005 are shown in Figure 3.11. Like NGC 2019, the diagnostics for the 1$-$3 Gyr CMDs for NGC 2005 show that the [Fe/H] solutions for these ages are worse than those with ages $>$5 Gyr. There is very little difference in the quality of the solutions between
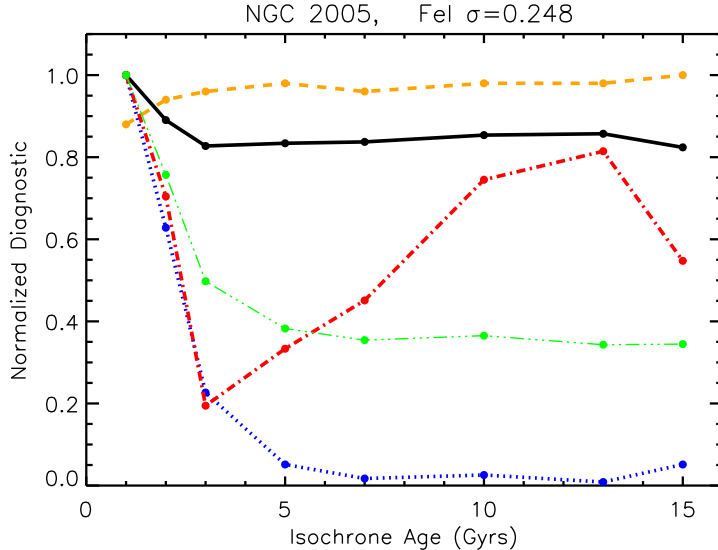
Figure 3.11. Same as Figure 3.3 for NGC 2005. Best solutions are found for ages >5 Gyr.

$5-15$ Gyr. It is likely that we cannot constrain the age further because the line-to-line scatter of the best abundance solutions is $\sigma \sim 0.25$ dex, which is higher than what we typically obtained for clusters in the MW training set. As discussed in § 3.2, this is probably a consequence of the lower S/N of the LMC training set. The $10-15$ Gyr averaged CMD solutions result in [Fe/H]~ -1.6, and the individual diagnostics for the 15 Gyr averaged CMD solution show a small dependence of [Fe/H] with wavelength, as well as a more significant dependence of [Fe/H] with EP and reduced EW.

NGC 2005 is less luminous than NGC 2019 by ~ 0.5 V mag, and we calculate that we have observed 60% of the total flux. Although NGC 2005 is better sampled than NGC 2019, the 15 Gyr synthetic CMDs have a comparable number of stars ($\sim$40,000) to those of NGC 2019 because it is less luminous overall. We next use the strategy demonstrated for NGC 2019 to test for sampling uncertainties, and to search for CMD realizations that improve the Fe abundance solution.

For the subset of CMD realizations that we use to calculate Fe abundances, we determine the appropriate $(B-V)_o$ color range to search using the $B-V$=0.73 and $E(B-V)$=0.1 of Pessev et al. (2008), and Olsen et al. (1998), respectively. The resulting $(B-V)_o$ range allowed for the CMD realizations is shown by the shaded gray area in Figure 3.12. Although we derive comparable [Fe/H] for both clusters,
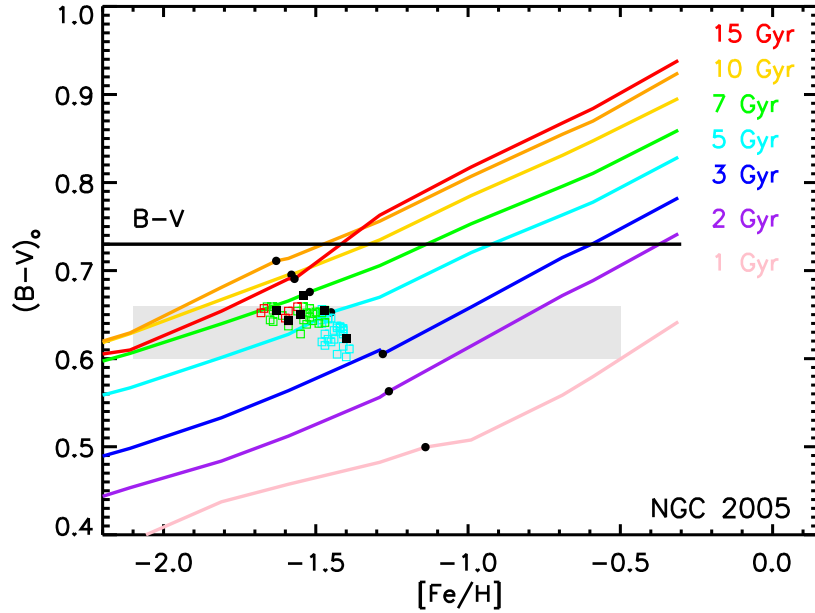
Figure 3.12. Same as Figure 3.7 for NGC 2005.

the reddening corrected $B - V$ for NGC 2005 is bluer than that of NGC 2019, which means that the $10-15$ Gyr averaged CMD solutions are actually inconsistent with the observed, reddening-corrected color. While this might imply a younger age for NGC 2005, we note that the age of NGC 2005 has been confirmed to be >10 Gyr by the deep HST imaging of Olsen et al. (1998). The color disagreement is not likely due to a large error in the $E(B - V)$ of Olsen et al. (1998), because the $E(B - V)$ was determined from the HST CMD. Instead, it is more likely that the blue color of NGC 2005 is due to a large number of blue HB stars, which are not reproduced by the set of isochrones we have chosen for our analysis. Our previous tests in Colucci et al. (2009) on M31 clusters have shown that it is possible for blue HB stars to change the synthetic CMD $(B - V)_o$ by -0.1 mag, which is more than the change in $(B - V)_o$ needed for the $10-15$ Gyr synthetic CMDs to match the observed color of NGC 2005. However, our tests with blue HB stars have also shown that the derived abundances are not very sensitive to the addition of blue HB stars, but are more sensitive to a lack of cooler, redder HB stars. As discussed previously, this is because hot stars contribute very little to the total Fe I EW fraction, while the cooler, redder

117

stars contribute a significant fraction of the Fe I EWs. Because the blue HB stars don't contribute significantly to the Fe I EWs, they typically do not improve the diagnostics. Thus, we expect that if the blue color of NGC 2005 is due to HB stars, it will be difficult to improve the diagnostics for the averaged CMD solutions while requiring the CMD realizations to match observed $B - V$ of NGC 2005.

To explore this further, we first calculate abundance solutions for CMD realizations that match the observed $B - V$ of NGC 2005. We use CMD realizations created from isochrones with [Fe/H]= -2.1 to -1.5 and ages of $5-15$ Gyr. We find that only a handful of CMD realizations with ages of $10-15$ Gyr result in self-consistent [Fe/H] solutions. Moreover, none of these solutions significantly improve the Fe line diagnostics over the diagnostics for the averaged CMD solutions. However, the range in [Fe/H] of the possible solutions still remains small, and consistently around [Fe/H]= -1.6. This means that the [Fe/H] for NGC 2005 is well constrained.

We find many more CMD realizations that result in self-consistent [Fe/H] solutions for ages of 5 and 7 Gyrs, which is expected because many more of these realizations satisfy the original $(B - V)_o$ color constraint. However, the best of these solutions offer only a marginal improvement over the averaged CMD solutions. This implies that a $5-7$ Gyr age for NGC 2005 is not preferred over a $10-15$ Gyr age.

Because we cannot significantly improve the abundance solution with younger ages or with $10-15$ Gyr CMD realizations that match the observed $B - V$, it seems likely that the observed $B - V$ of NGC 2005 is bluer than the $(B - V)_o$ of the synthetic CMDs because of a significant number of blue HB stars. This also means that the requirement for the CMD realizations to match the reddening corrected $B - V$ may not be meaningful in this case. For NGC 2005, this requirement effectively means that we eliminate CMD realizations with significant flux in red AGB stars, which we found improved the [Fe/H] solutions for NGC 2019. Therefore, to allow for redder CMD realizations, for our next test we relax the constraint that the CMD realizations must have $(B - V)_o < 0.66$, and instead require that the CMD realizations have $(B - V)_o < 0.73$, which corresponds to the observed $B - V$ of NGC 2005, uncorrected for reddening. Many more CMD realizations result in self-consistent solutions in this
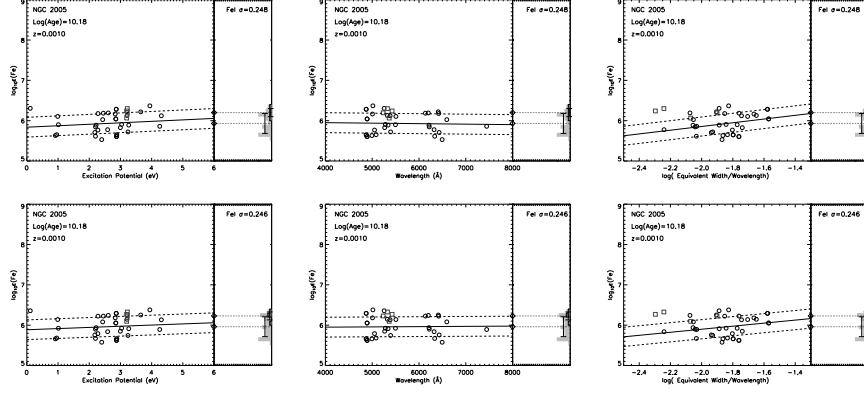
Figure 3.13. Same as Figure 3.10 for NGC 2005. The top panels correspond to the solution for the self-consistent averaged CMD solution for a 15 Gyr, [Fe/H]= −1.5 isochrone, and the bottom panels correspond to the solution for the best-fitting CMD realization from a 15 Gyr, [Fe/H]=−1.5 isochrone. The solution shown in the bottom panels has a smaller Fe I σ, and reduced [Fe/H] dependence on wavelength, EP, and reduced EW than the original solution.

case, and the best-fitting CMD realizations have [Fe/H]∼-1.6, which is the same as the [Fe/H] found from the averaged CMDs. However, we find that the best-fitting CMD realization has $(B-V)_o$= 0.672, which is only slightly redder than our original constraint of $(B-V)_o$=0.66, and is actually bluer than the color of the 15 Gyr averaged CMD, which had $(B-V)_o$=0.69. This implies that CMD realizations with significant flux in very red AGB stars are not preferred solutions for NGC 2005.

In conclusion, the final best-fitting CMD we use for NGC 2005 has an age of 15 Gyr, and [Fe/H]= −1.6, although in general we find that we can only constrain the age of NGC 2005 to a 5−15 Gyr range. We show the individual Fe line diagnostics for the best-fitting 15 Gyr CMD realization in the bottom panels of Figure 3.13, so that they can be visually compared to the 15 Gyr averaged CMD solutions in the top panels. When compared to the averaged CMD solution, we find that the best-fitting CMD realization has a slightly reduced Fe I σ, and the dependence of [Fe/H] on wavelength has disappeared. The dependence of [Fe/H] on EP and reduced EW has decreased, but still remains. It is impossible to tell whether the remaining dependency of [Fe/H] on EP and reduced EW is due to a more insiduous sampling incompletness, interloping stars, or simply a result of the lower S/N of the data.

It is apparent from the analysis of NGC 2005 that it is important to be aware of
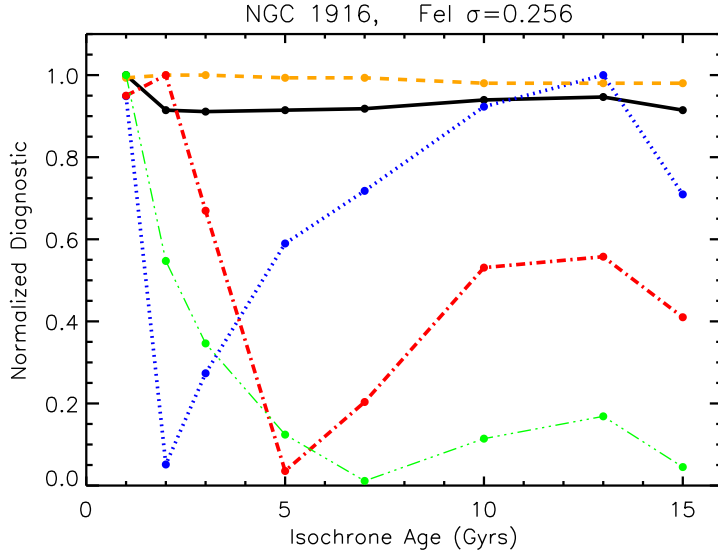
Figure 3.14. Same as Figure 3.3 for NGC 1916. Best solutions are found for ages >5 Gyrs.

the impact of blue HB stars on the integrated $B-V$ of a cluster when comparing it to the $(B-V)_o$ of the synthetic CMDs. However, while blue HB stars may be important for matching the $B-V$, cooler and redder stars continue to be more important for deriving self-consistent, stable [Fe/H] solutions. Moreover, our tests for sampling uncertainties are adequate to determine whether significant flux from cool AGB stars is necessary for a stable [Fe/H] solution. Despite the issues discussed for NGC 2005, we find that the [Fe/H] is well determined and is within ~ 0.15 dex of [Fe/H]=-1.6 over the $5-15$ age range found for the best-fitting CMD solutions.

NGC 1916

NGC 1916 is the most massive old cluster in the LMC training set ($M_V^{\rm tot}= -8.96$), and we have observed $\sim 60\%$ of the total flux. The 15 Gyr synthetic CMDs we create for NGC 1916 contain $\sim$170,000 stars, so we do not expect that sampling uncertainties will have a large impact on our solution, but we follow the same analysis procedure as for NGC 2019 as an example of how the sampling uncertainty technique might be applied to distant, well-sampled, extragalactic clusters.

In Figure 3.14 we show the normalized Fe line diagnostics for the self-consistent averaged CMD solutions. Like NGC 2019 and NGC 2005, we find that the diagnostics
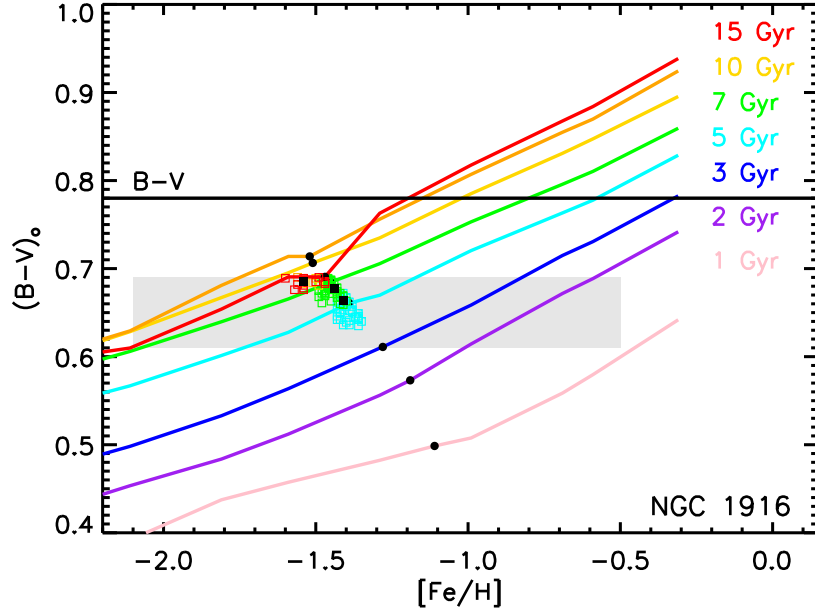
Figure 3.15. Same as Figure 3.7 for NGC 1916.

for NGC 1916 are generally best for ages between 5 and 15 Gyrs. The Fe I lines result in solutions of [Fe/H]~ -1.5, with a best Fe I σ=0.259, which is comparable to the result for NGC 2005, but higher than that for NGC 2019. The 15 Gyr solution shows a fairly significant dependence of [Fe/H] with wavelength, a small dependence of [Fe/H] with reduced EW, and negligible dependence of [Fe/H] with EP.

We next investigate how sensitive the age and abundance solutions are to sampling uncertainties. In Figure 3.15 we show the $(B-V)_\mathrm{o}$ of the original synthetic CMDs for NGC 1916. The shaded region corresponds to the range of $(B-V)_\mathrm{o}$ that is consistent with the known $B-V$ and $E(B-V)$ of NGC 1916, which we have taken from the catalog of Pessev et al. (2008). We note that like NGC 2005, the reddening corrected $B-V$ color of NGC 1916 is inconsistent with the color of the 10 and 13 Gyr averaged CMD solutions.

The CMD realizations we create that match the reddening corrected $B-V$ of NGC 1916 and have self-consistent [Fe/H] solutions, show marginal improvement in the diagnostics for CMDs with ages of 5, 7 and 15 Gyrs. The most stable solutions have the same [Fe/H] as the averaged CMD solutions. We cannot find CMD realizations for
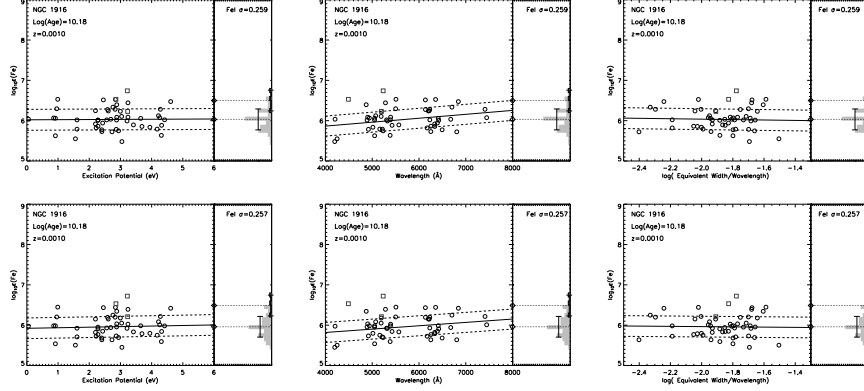
Figure 3.16. Same as Figure 3.10 for NGC 1916. The top panels correspond to the solution for the self-consistent averaged CMD solution for a 15 Gyr, [Fe/H]= −1.5 isochrone, and the bottom panels correspond to the solution for the best-fitting CMD realization from a 15 Gyr, [Fe/H]=−1.5 isochrone. The solution in the bottom panels has a smaller Fe I σ than the original solution.

ages of 10 and 13 Gyr that improve the diagnostics and satisfy the $B-V$ requirement. However, we note that Olsen et al. (1998) find that NGC 1916 is both likely to be affected by differential reddening, and to have a significant number of blue HB stars. Therefore, as with NGC 2005, we next relax the $(B-V)_o$ constraint and search for better solutions from additional CMD realizations with $0.69 < (B-V)_o < 0.78$, in order to allow for more flux from cool AGB stars. We find many more ≥ 10 Gyr CMD realizations result in self-consistent [Fe/H] solutions in the redder $B-V$ color range. However, in the case of NGC 1916, we do not find a better solution from CMDs with redder colors. Therefore, we use the best 15 Gyr CMD realization in the $0.61 < (B-V)_o < 0.70$ range that we originally searched as our best-fitting solution. In Figure 3.16 we show the original 15 Gyr averaged CMD solution, as well as the best-fitting solution from the 15 Gyr CMD realizations. The latter shows a slightly smaller Fe I σ, and slightly smaller dependence of [Fe/H] with wavelength and reduced EW than the original solution. We find $(B-V)_o$=0.685 for the best solution, which is very close to the original synthetic CMD solution, which had $(B-V)_o$=0.690, and slightly redder than the observed $(B-V)_o$=0.65 from the catalog of Pessev et al. (2008).

In summary, we find the best-fitting solutions for NGC 1916 have ages of 5-15 Gyrs, and a well-constrainted [Fe/H]~ -1.5. The fact that we cannot substantially

improve the diagnostics by allowing for statistical fluctuations and a large range in $(B - V)_o$ suggests that either the mean $E(B - V)$ is smaller than that in Pessev et al. (2008) or that as in the case of NGC 2005, the synthetic CMD $(B - V)_o$ is not blue enough due to a deficit of blue HB stars in the isochrones. In either case, both the preferred CMD population and the metallicity of NGC 1916 are well determined from our analysis. This is an important demonstration of the utility of our method for determining the properties of GCs affected by differential reddening, which are otherwise difficult to study using other means.

3.4.5   Intermediate Age Clusters

We have tested our analysis method on two LMC clusters with ages of ~1-2 Gyr. For these clusters we refine the initial grid of synthetic CMD ages we test between 0.5 Gyr and 5 Gyr because significant changes in the CMD stellar populations can occur on much shorter timescales (0.5-1 Gyr) than they do for old, >5 Gyr CMDs. For the intitial synthetic CMD grid, we use isochrones with ages of 0.5, 0.7, 1.0, 1.25, 1.5, 1.75, 2.0, 2.5, 3.0, 3.5, 5.0, 7.0, and 10 Gyr. We discuss the determination of the best-fit CMDs below.

NGC 1718

NGC 1718 is the least massive cluster in the training set ($M_V^{\mathrm{tot}} \sim -6.5$), and has an age of ~2 Gyr (Kerber et al., 2007). The mean [Fe/H] solutions we derive for the grid of synthetic CMDs are shown in Figure 3.17, and the diagnostics for the self-consistent CMDs for each age are shown in Figure 3.18. The best Fe I σ=0.324, which is significantly larger than the Fe I σ we obtain for any of the old clusters in the sample. However, even though the Fe I σ is large, it can clearly be seen in Figure 3.18 that all of the diagnostics are consistently better for the younger ages than they are for the older ages. This is the best demonstration to date that in using our abundance analysis method, the Fe I lines alone can successfully distinguish clusters of different ages.

We next investigate the limits we can place on the age of the cluster using this method, and whether we can successfully identify an age that is consistent with the

123
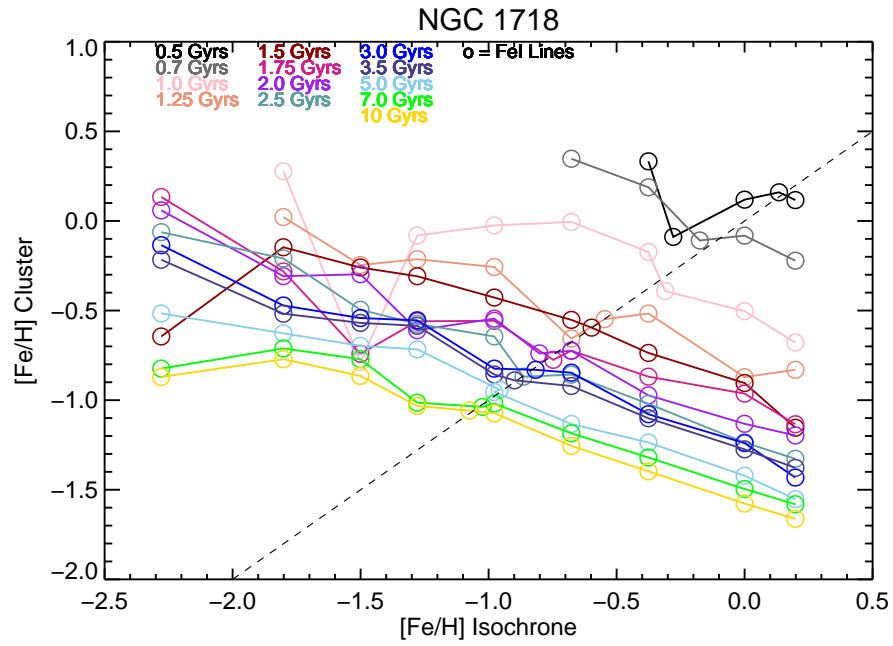
Figure 3.17. Same as Figure 3.2 for NGC 1718. Additional ages for the grid of synthetic CMDs for intermediate age clusters are shown by the labeled colors.
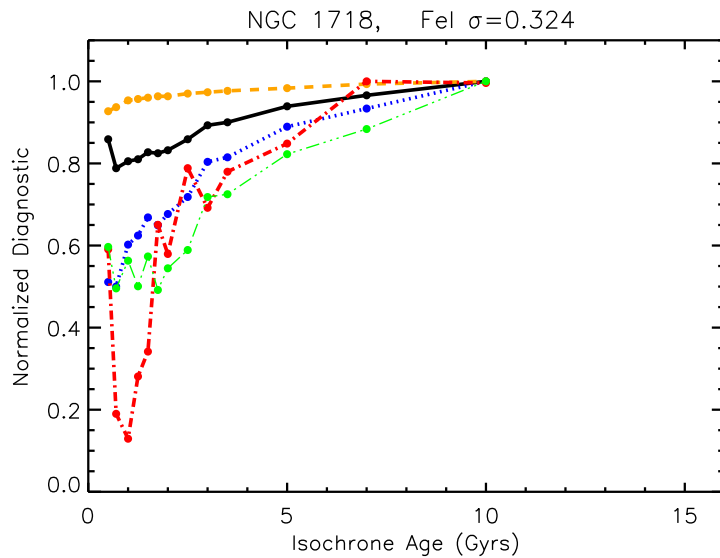
Figure 3.18. Same as Figure 3.3 for NGC 1718. The best solutions are found for ages of 0.7−1.25 Gyrs.

age determined from resolved star photometry. Figure 3.18 shows that the minimum in Fe I σ occurs at 0.7-1.25 Gyrs, and there is a corresponding minimum in the Fe I slope with EP and some indication of a minimum in Fe I slope with EW at these ages. However, while there is some indication of a preferred solution in the appropriate age range around 1 Gyr, it is not conclusive that the 0.5 and 0.7 Gyr solutions are worse than the 1-1.25 Gyr solutions. We find that the 1 Gyr solution results in [Fe/H]~ -0.4, and has a small dependence of [Fe/H] with EP, but a fairly significant dependence of [Fe/H] with both wavelength and reduced EW. This suggests that the synthetic CMD populations that we are using at this stage in the analysis are not a sufficiently accurate match to the true CMD of the cluster. To improve the analysis, we next explore how incomplete sampling of the cluster affects our analysis and whether a more appropriate population can be found by allowing for statistical variations in the population of the CMD.

It is especially important to evaluate the effect that sampling uncertainties can have on the age and abundance solutions for NGC 1718, both because it is ~ 2 Gyr in age, and therefore rapidly evolving, and because it is the least luminous, least massive, cluster in both the LMC and MW training sets, and therefore the most likely to suffer from statistical fluctuations in a small number of luminous stars. In Figure 3.19 we show the histogram of $(B-V)_{\mathrm{o}}$ for 100 CMD realizations of a $M_V^{\mathrm{tot}}=-6.5$ cluster, which corresponds to the total flux of NGC 1718 (Kerber et al., 2007). Also shown is the histogram for CMD realizations for 23% of a $M_V^{\mathrm{tot}}=-6.5$ cluster, which corresponds to the fraction of NGC 1718 we have observed. The larger spread in $(B-V)_{\mathrm{o}}$ of the CMD realizations in Figure 3.19 when compared to that for NGC 2019 in Figure 3.4 demonstrates that statistical stellar population fluctuations are a greater issue for NGC 1718. It is also clear from the comparison of the two histograms for NGC 1718 in Figure 3.19 that the sampling uncertainties are significantly exacerbated due to the incomplete sampling of our observations. It is particularly worrisome that the peak is hard to distinguish for the less luminous CMD realizations.

In the case of NGC 1718, the large spread in $(B-V)_{\mathrm{o}}$ is primarily due to the
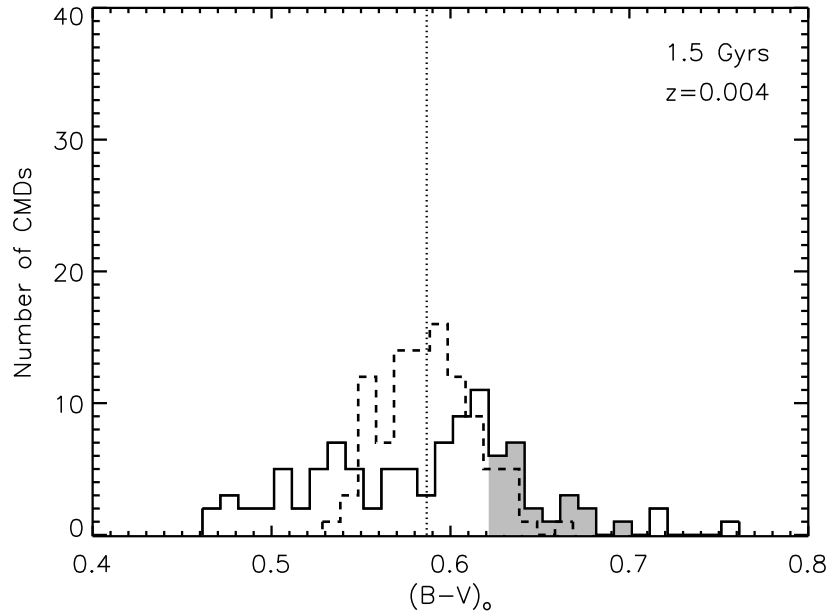
Figure 3.19. Histogram of integrated $(B-V)_{\mathrm{o}}$ color for 100 CMD realizations of a 1.5 Gyr, z=0.004 ([Fe/H]=-0.66) isochrone. Solid black line shows the histogram for a population where the total flux in stars has been normalized to 23% of a $M_V^{\mathrm{tot}}= -6.5$ cluster, which is appropriate for our integrated light spectrum of NGC 1718. Dashed black line shows the histogram for a population normalized to 100% of a $M_V^{\mathrm{tot}}= -6.5$ cluster. CMDs with $(B-V)_{\mathrm{o}}$ color consistent with the observed, reddening-corrected $B-V$ of NGC 1718 are shaded in gray. The large spread of $(B-V)_{\mathrm{o}}$ in the solid line histogram is an indication that our observations of NGC 1718 are significantly affected by sampling incompleteness.
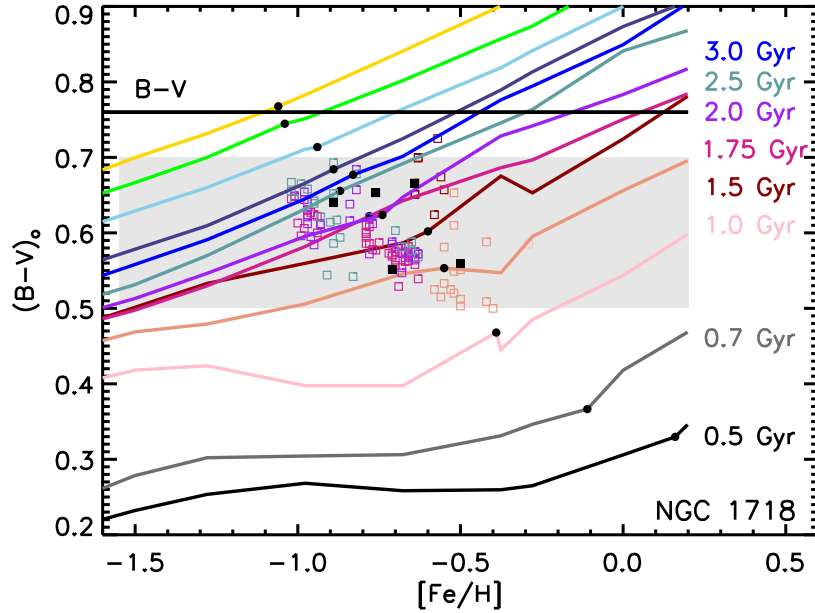
Figure 3.20. Same as Figure 3.7 for NGC 1718. Colors are the same as in Figure 3.17. Shaded gray region corresponds to the range in $(B - V)_o$ allowed for the subset of CMD realizations used for abundance analysis.

significantly smaller luminosity of NGC 1718 combined with the incomplete sampling of the observations. However, it is important to note that we would expect that its younger age would also result in a larger spread in $(B - V)_o$ for the CMD realizations even if it had the same total luminosity as NGC 2019. This is because at a fixed total luminosity a 1 Gyr cluster will have fewer stars than a 10 Gyr cluster due to the higher masses and luminosities of the stars (e.g., see Brocato et al., 1999). In general, Brocato et al. (1999) find that it is difficult to determine the properties (i.e. age, metallicity) of clusters using integrated colors when the stellar population has <30,000 stars. The CMDs corresponding to the observed flux of NGC 1718 have ∼2500 stars, while the CMDs for a fully sampled $M_V^{tot}=-6.5$ cluster have ∼11,000 stars, which means that NGC 1718 is in the regime where sampling uncertainties can have a significant impact on the analysis.

With this difficulty in mind, we create CMD realizations for NGC 1718 with ages and [Fe/H] in the range 1−2.5 Gyr and −0.98 to −0.26, and include isochrones at the interpolated [Fe/H] solutions from the averaged CMDs. We include CMD

realizations with 0.5< $(B-V)_o$< 0.7 for abundance analysis, which is highlighted by the shaded gray region in Figure 3.20. The upper limit of this range corresponds with the observed, reddening corrected $B-V$ of NGC 1718. However, we extend the lower limit of the $(B-V)_o$ range to include more CMD realizations with ages of 1 to 1.5 Gyr, which have bluer colors, to search a wider parameter space because of the significant trends in the original [Fe/H] solutions, and because Figure 3.18 suggests that the diagnostics at these ages are generally better. We note that even with a lower limit of $(B-V)_o$=0.5, it is pretty clear from Figure 3.20 that CMDs with ages <1.0 Gyr can be ruled out based on the observed $B-V$.

We find that the large subset (∼1200) of CMD realizations that meet the $(B-V)_o$ requirement result in a wide range of [Fe/H] abundance solutions, ranging from [Fe/H]∼ −2 to [Fe/H]∼ 0. This is a result of fairly drastic fluctuations in luminous giant stars, which both cause the large scatter in $(B-V)_o$ seen in Figure 3.19 and have a large impact on the Fe I EWs. Fortunately, this means that it is easier to use the Fe lines to identify CMD realizations that are viable solutions. For NGC 1718 we are able to narrow down the possible CMD realizations from ∼1200 to ∼120 by applying our usual requirement that the solutions be self-consistent with the abundance assumed in the calculation of the stellar evolutionary tracks (i.e. [Fe/H]$_{iso}$=[Fe/H]$_{cluster}$).

In Figure 3.21 we show the Fe I diagnostics for the CMD realizations that have self-consistent [Fe/H] solutions, ordered first by increasing age and then by increasing [Fe/H] for each age. This figure shows that the Fe I σ tends to get larger with increasing age, as was found for the averaged CMDs in Figure 3.18, which implies that the younger ages are generally better solutions. We pick the solution that best minimizes all of the diagnostics for each age, while no one solution ideally minimizes all diagnostics at once. We find that the best-fitting CMD realization at each age has the same [Fe/H] as the original averaged CMD solution, which implies that in this case incomplete sampling is not adding significant uncertainty to the best-fitting [Fe/H], despite the sampling concerns discussed above.

After narrowing down the possible solutions from ∼120 self-consistent CMD realizations to 5 solutions, one for each age, we compare these 5 solutions to the 7
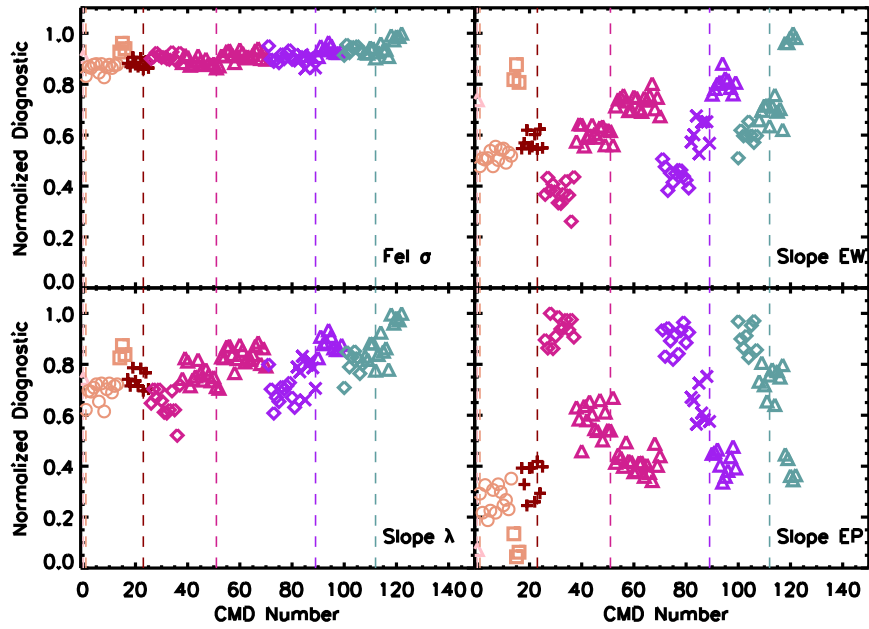
Figure 3.21. Same as Figure 3.8 for NGC 1718. Colors are the same as in Figure 3.17. Younger ages are overall better solutions.
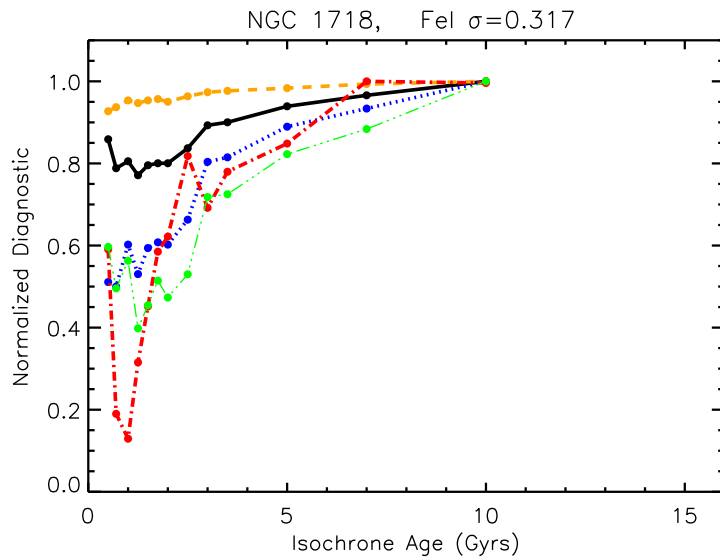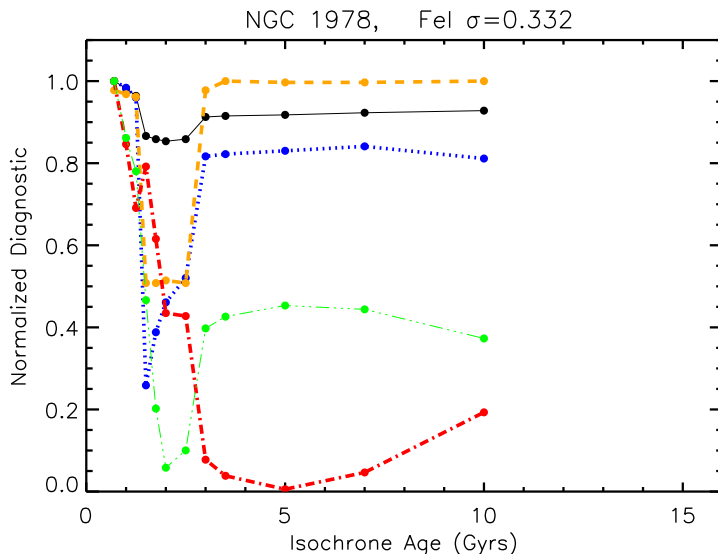

Figure 3.22. Same as Figure 3.18, except the 1.25-2.5 Gyr solutions have been replaced by the solutions for the best-fitting CMD realization at these ages. The best solutions are found for ages of $1-2.5$ Gyr.
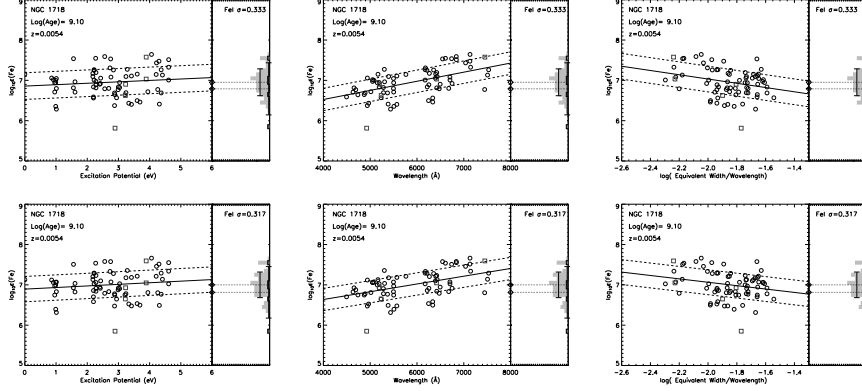
Figure 3.23. Same as Figure 3.10 for NGC 1718. The top panels correspond to the averaged CMD solution using a 1.25 Gyr, [Fe/H]=−0.55 isochrone, and the bottom panels correspond to the best-fitting CMD realization using a 1.25 Gyr, [Fe/H]=−0.55 isochrone. The solution in the bottom panels has a smaller Fe I σ and slightly smaller [Fe/H] dependence on EP, wavelength, and reduced EW.

averaged CMD solutions for the other ages in the grid. The diagnostics for these final 12 solutions are shown in Figure 3.22. We find that the case for an age of ∼1 Gyr is a little stronger than it was from Figure 3.18, due to an improvement in the Fe I σ, and that the other diagnostics are more closely correlated with this improvement. However, while the 1−1.25 Gyr solutions are the most stable overall, the differences between the solutions with ages between 1−2.5 Gyr are still small. Therefore, our final age constraint for NGC 1718 is 1−2.5 Gyr. This is a narrower range in age than we are generally able to constrain for old clusters, but because NGC 1718 is young, the stellar population changes considerably over this 2.5 Gyr timescale. The consequence of this is that we cannot constrain the [Fe/H] of NGC 1718 with the same power as we could for older clusters in the training set. We find that the 1.0 Gyr solution has [Fe/H]=−0.39, while the 2.5 Gyr solution has [Fe/H]=−0.89. To convey this range of possible solutions in age and corresponding abundance, we average the two [Fe/H] results and quote an uncertainty of ±0.25 dex.

To give a more qualitative impression of the difference between the original solution and the final solutions given above, in Figure 3.23 we compare the individual diagnostics for the averaged CMD solution with an age of 1.25 Gyr, compared to the best-fitting CMD realization with an age of 1.25 Gyr. The most significant improvement in the bottom panels when compared to the top panels is a reduced Fe I σ.

130

Because there is still a significant dependence of [Fe/H] with EP, wavelength, and reduced EW, it is clear that our best-fitting stellar population is still not an ideal match to the true population of the cluster.

In summary, the analysis of NGC 1718 demonstrates that we are able to distinguish between clusters that are $\sim$1 Gyr in age and clusters that are $>$5 Gyr in age using our abundance analysis method. We are able to confidently constrain the age of NGC 1718 to a range of 1−2.5 Gyr using the stability of the [Fe/H] solution and the observed integrated color. The resulting constraint on the abundance is [Fe/H]=-0.64 ± 0.25 dex, which is a larger error than we typically obtain for the analysis of older clusters, but it is possible that this could be refined with higher quality data and more complete sampling. We find that while sampling uncertainties can cause a large spread in $(B - V)_o$, we are able to constrain a small subset of solutions by requiring self-consistency in the [Fe/H] solution. In the case of NGC 1718, we don't find that this adds uncertainty in the [Fe/H] we derive for each age, but we are able to slightly improve on the stability of the [Fe/H] solution by allowing for sampling uncertainties.

NGC 1978

The second intermediate age cluster in the LMC training set, NGC 1978, has an age of $\sim$2 Gyr and is more massive ($M_V^{\rm tot} \sim -7.7$) than NGC 1718. Similar to NGC 2005, the S/N of the NGC 1978 spectrum is lower than for most of the other clusters in our MW and LMC training sets. We measure EWs for only 36 clean, reasonably unblended Fe I lines, and 4 Fe II lines, whereas we typically measure 50−100 Fe I lines for clusters with high S/N data. The best solution has Fe I $\sigma = 0.351$, which is larger than the Fe I σ for NGC 1718, as well as the Fe I σ for the old clusters in the LMC training set. The large line-to-line scatter for Fe I makes NGC 1978 particularly difficult to analyze.

We calculate the [Fe/H] solutions for the same grid of isochrones as NGC 1718, but note that the averaged CMDs with ages of 0.5 Gyrs result in solutions with [Fe/H] $> +0.5$, which is outside the range of isochrones and stellar atmospheres used in our
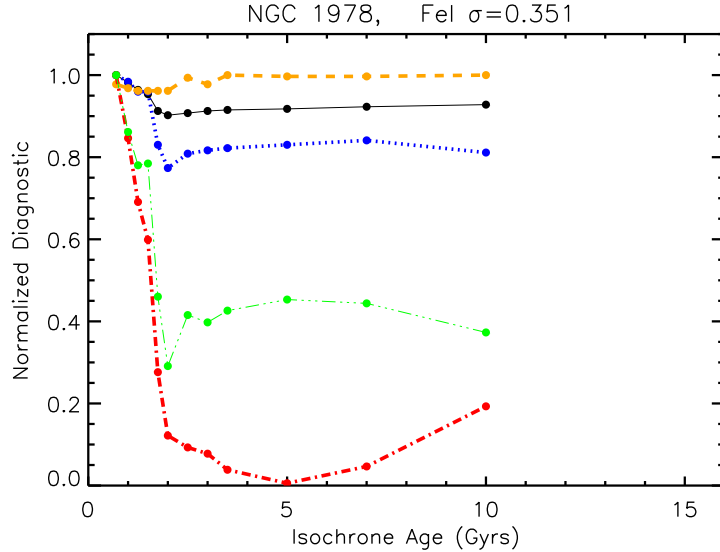
Figure 3.24. Same as Figure 3.3 for NGC 1978. Best solutions are found for ages >1.5 Gyr.

analysis and so are not considered further here. We show the normalized diagnostics for the self-consistent, averaged CMDs of the other 7 ages in Figure 3.24. In the case of NGC 1978, we find that the diagnostics show that the worst solutions have ages between 0.7−1.25 Gyrs. The solutions with ages >1.5 Gyr are of comparable quality, although there is some indication from the EP diagnostic that solutions with ages >7 Gyr are also unfavorable. The solutions with ages of 1.5−7 Gyr show a moderate dependence of [Fe/H] with both EP and reduced EW, and a significant dependence of [Fe/H] with wavelength. As was discussed for NGC 1718, the poor diagnostics for NGC 1978 imply that the stellar populations in the averaged CMDs are not ideal.

We estimate that we have only observed 5−10% of the total flux of NGC 1978 in the scanned region, which means that incomplete sampling is a big concern. The synthetic CMDs for NGC 1978 have ~4,000 stars, whereas a cluster with $M_V^{\mathrm{tot}} \sim$ −7.7 would have ~76,000 stars in the synthetic CMDs if we had observed 100% of the total flux. As in the case of NGC 1718, the synthetic CMDs for NGC 1978 have significantly less than 30,000 stars, so it is important that we evaluate how the sampling uncertainties affect our age and abundance solutions.

We create CMD realizations for ages of 1.5−3 Gyr and [Fe/H]= −1.5 to [Fe/H]= 0 to see if we can find a population that results in a more stable [Fe/H] solution. We
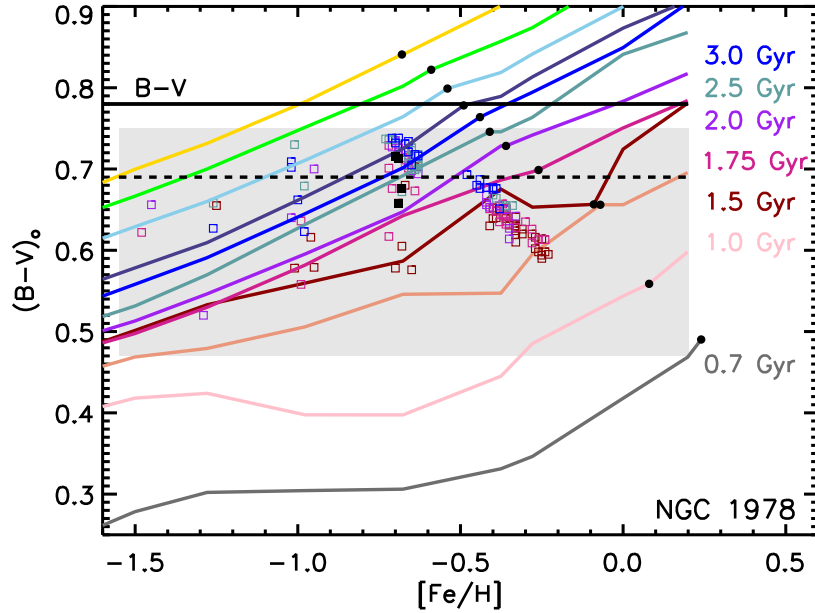
Figure 3.25. Same as Figure 3.7 for NGC 1978. Colors are the same as in Figure 3.17. The shaded gray region corresponds to the range in $(B-V)_o$ allowed for the subset of CMD realizations used for abundance analysis.

calculate abundances for a subset of CMD realizations that satisfy the requirement $0.47 < (B-V)_o < 0.75$. This is a fairly large range in $(B-V)_o$, and is chosen to include both the $E(B-V)=0.09$ of Mucciarelli et al. (2007) and the significantly larger value of $E(B-V)=0.25$ from the catalog of Pessev et al. (2008). This $(B-V)_o$ requirement is highlighted by the shaded gray area in Figure 3.25, where it can be seen that the averaged CMD solutions with ages >3 Gyr have $(B-V)_o$ colors inconsistent with this requirement. Moreover, from Figure 3.25 there is some justification for eliminating the averaged CMDs with ages >5 Gyr from consideration for a best-fitting solution because they have redder colors than the observed $B-V$.

Like NGC 1718, for NGC 1978 we find that we are able to eliminate the majority of the possible CMD realizations using the self-consistency of the Fe lines. Out of the ~2200 CMD realizations that satisfy the $(B-V)_o$ requirement, we find only ~150 that have self-consistent [Fe/H] solutions. We show the diagnostics for these ~150 self-consistent solutions in Figure 3.26, where it can be seen that all four Fe diagnostics show similar, correlated behavior with age and metallicity. We pick one
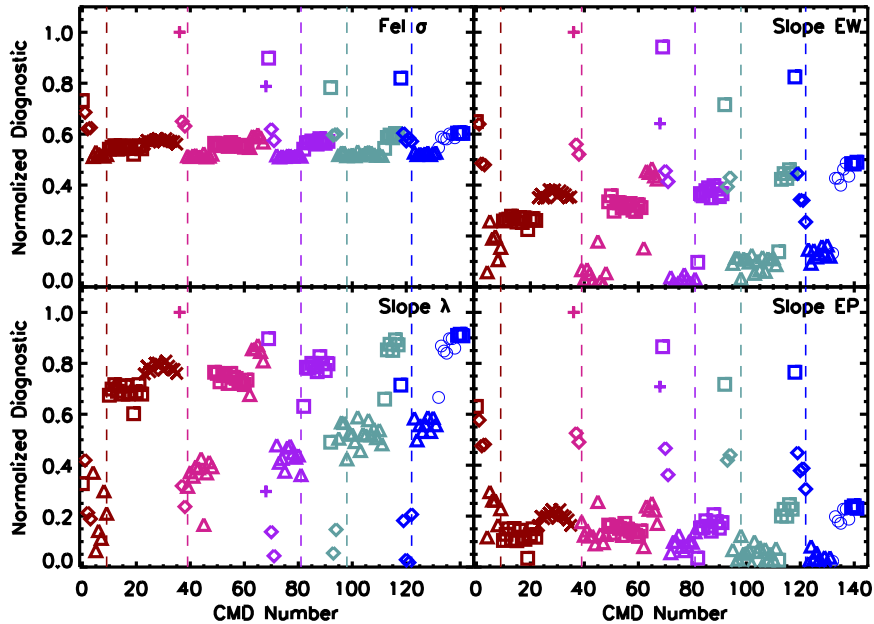
Figure 3.26. Same as Figure 3.21 for NGC 1978. Colors are the same as in Figure 3.17. Diagnostics are strongly correlated with both age and metallicity.

best-fitting solution for each age (5 total) from the ∼150 CMD realizations, and compare the normalized diagnostics to the solutions for the other ages in Figure 3.27. From Figure 3.27 it appears clearer that there is a preferred age for NGC 1978 between 1.5−2.5 Gyr. There is significant improvement in the Fe I σ, and a much smaller dependence of [Fe/H] on wavelength and reduced EW when compared to the averaged CMD solutions in Figure 3.24, although a dependence of [Fe/H] on EP and wavelength is still present. The difference between the best-fitting 2.5 Gyr CMD realization and the original averaged 2.5 Gyr CMD can be seen most clearly in Figure 3.28, where we compare the individual diagnostics.

Interestingly, we find that all of best-fitting CMD realizations for NGC 1978 have [Fe/H]∼ −0.7, regardless of the age. The solution for NGC 1978 is therefore much better constrained than for NGC 1718. Note that this is also much more metal-poor than the solution obtained from the averaged CMDs. Comparing with the original solution, we find that the main difference is that the CMD realizations that allowed for partial sampling of the CMD have flux in much cooler AGB stars than the original solutions. This is further evidence that we are able to tell whether

Figure 3.27. Same as Figure 3.24, except the solutions at ages of $1.5-2.5$ Gyr have been replaced by the solutions for the best-fitting CMD realization at these ages. The best solutions are found for ages of $1.5-2.5$ Gyr.

significant flux in cool AGB stars is needed in the syntehtic CMDs by using the Fe I diagnostics. We also find that the best-fitting CMD realizations have $(B-V)_\mathrm{o}{\sim}0.66$-0.72, which corresponds to $E(B-V){\sim}0.07-0.12$. This range is very consistent with the $E(B-V)$=0.09 derived by Mucciarelli et al. (2007) from their very deep HST CMD, and supports the use of this method to provide independent constraints on the $E(B-V)$ of unresolved clusters as done in Colucci et al. (2009).

In summary, the mean solution for NGC 1978 using the best-fitting CMD realizations with ages of $1.5-2.5$ Gyr is [Fe/H]=-0.74 ± 0.07. Although the line-to-line scatter for the Fe abundance is high, it is likely that it can be explained by the low S/N of the data. Like NGC 1718, we find that the best-fitting solutions for NGC 1978 show pretty significant dependence of [Fe/H] on EP and wavelength. However, unlike the case of NGC 1718, for NGC 1978 we find the [Fe/H] has only a weak dependence on age within the preferred age range, despite the low quality of the data and large standard deviation of the Fe lines.

Given the data quality and that we only have two clusters in the intermediate age range, it is impossible to determine if the difficulties we encounter in finding an accurate stellar population match for these clusters is due to broader, generic
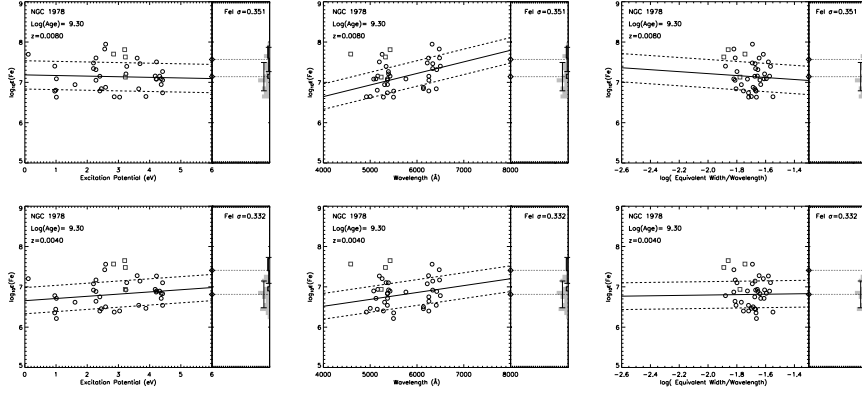
Figure 3.28. Same as Figure 3.10 for NGC 1978. The top panels correspond to the averaged CMD solution using a 2 Gyr, [Fe/H]=−0.38 isochrone, and the bottom panels correspond to the best-fitting CMD realization using a 2 Gyr, [Fe/H]=−0.66 isochrone. The solution in the bottom panels has a smaller Fe I σ, and smaller [Fe/H] dependence on wavelength and reduced EW.

problems in the isochrones at these ages. Along those lines, we note that there is still some debate over the presence or degree of convective overshooting needed in the input physics of the isochrones in order to match the observed CMDs of young clusters (e.g. Pietrinferni et al., 2004; Mucciarelli et al., 2007). There are also many open questions as to the modeling of AGB star evolution and mass loss on the RGB, both of which can have a particularly significant effect on the integrated properties of clusters in this age range (e.g. Cordier et al., 2007; Girardi et al., 2000; Gallart et al., 2005). A more extensive training set of high quality integrated light spectra of clusters in this age range is clearly needed to begin to address these questions.

3.4.6 Young Clusters

There are four young clusters in the LMC training set, which have ages < 1 Gyr. To analyze these clusters, we add synthetic CMDs with ages between 30−300 Myr to the grid used for the intermediate age clusters.

In the following sections we present the analysis for NGC 1866 and NGC 1711. The remaining two clusters, NGC 2100 and NGC 2002 have ages of ∼18 Myrs and ∼15 Myrs, respectively (Kumar et al., 2008; Elson, 1991). Because the youngest age in the grid of isochrones we currently employ for our analysis is 30 Myr, these clusters appear to be too young for this abundance analysis method. We find that while we
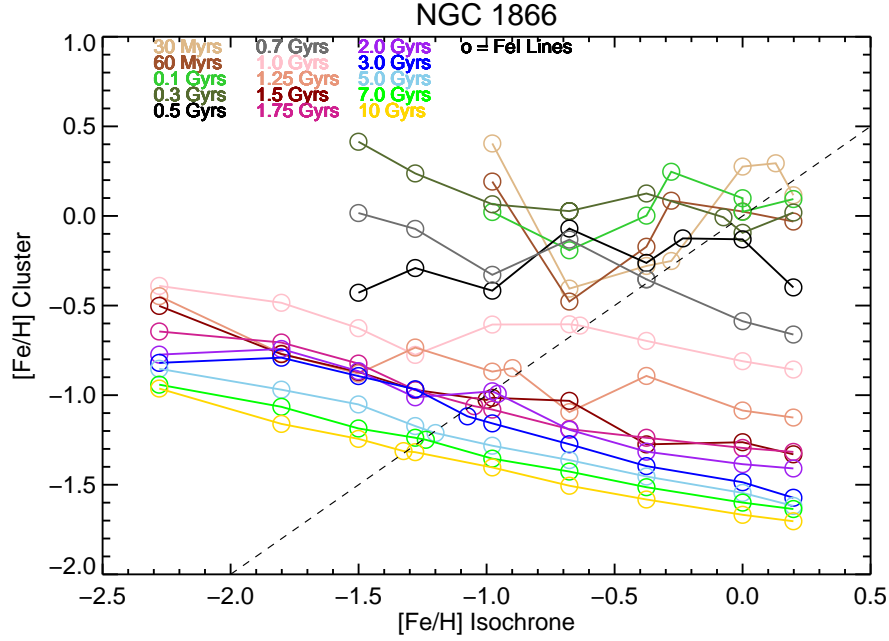
Figure 3.29. Same as Figure 3.2 for NGC 1866. Additional CMDs with ages <0.5 Gyr are shown by the labeled colors.

are able to measure EWs for NGC 2100 and NGC 2002 (as reported in Table 3.5), the solutions for synthetic CMDs with ages between 30 Myrs and 1 Gyr do not converge at self-consistent values of [Fe/H]. This implies that these clusters are indeed too young to analyze using this grid of isochrones, and so we do not discuss NGC 2100 and NGC 2002 further in this work.

NGC 1866

NGC 1866 is a relatively massive ($M_V^{tot} \sim -9$), well-studied cluster, with an age of $100-200$ Myr (e.g. Testa et al., 1999; Brocato et al., 2003). From the reasonably high S/N spectra for NGC 1866 we are able to measure 49 Fe I lines and 8 Fe II lines. We find a line-to-line scatter for the Fe I abundance that is comparable to that of the old clusters ($\sigma \sim 0.244$), and significantly smaller than that of the intermediate age clusters, which makes NGC 1866 an important test case for our abundance analysis method.

We derive a mean [Fe/H] for the full grid of synthetic CMDs, which are shown in Figure 3.29. We find that the [Fe/H]$_{cluster}$ solutions for synthetic CMDs with ages
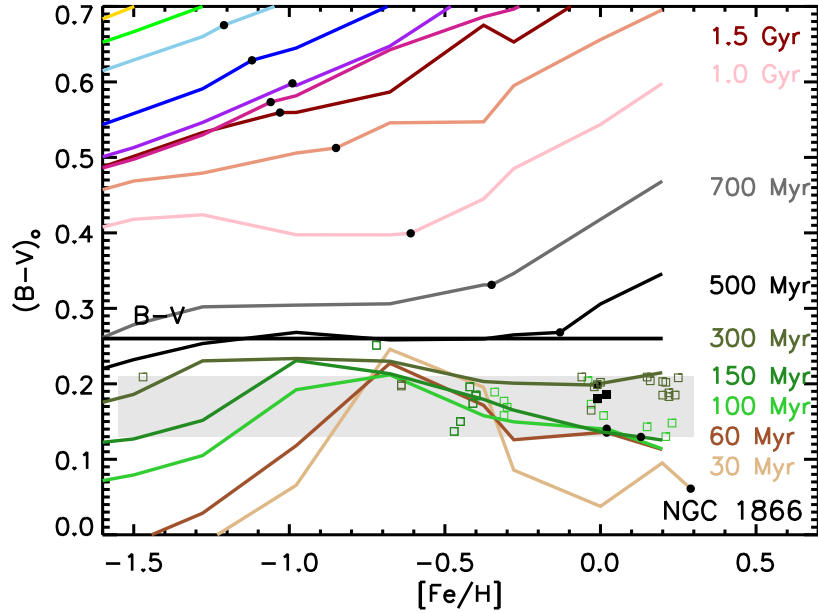
Figure 3.30. Same as Figure 3.7 for NGC 1866. Colors are the same as in Figure 3.29.

younger than 150 Myr deviate from the behavior of the $[Fe/H]_{cluster}$ of the older CMDs, which generally result in monotonically decreasing output $[Fe/H]_{cluster}$ with increasing input $[Fe/H]_{iso}$. This behavior is due to the stellar atmospheres over-compensating the Fe abundance to match the observed Fe EWs when the input $[Fe/H]_{iso}$ is lower than the real abundance, or under-compensating when the input $[Fe/H]_{iso}$ is too high. For synthetic CMDs with old ages, the stellar populations generally change slowly and smoothly with increasing metallicity, which leads to the smooth change in derived $[Fe/H]_{cluster}$. For synthetic CMDs with ages <150 Myr, the temperatures of core He-burning, luminous supergiants not only vary significantly on short timescales, but are also very sensitive to metallicity (e.g. Chiosi et al., 1992; Brocato & Castellani, 1993; Brocato et al., 1999). For this grid of isochrones, the averaged, synthetic CMDs with ages <150 Myr and $[Fe/H]=-1$ to -0.3 contain supergiants at cooler temperatures than CMDs at other metallicities at the same age. Because the cooler supergiants have stronger Fe I features, the derived $[Fe/H]$ tend to be lower, which is seen in Figure 3.29.

The temperature of the luminous supergiants also significantly affects the inte-
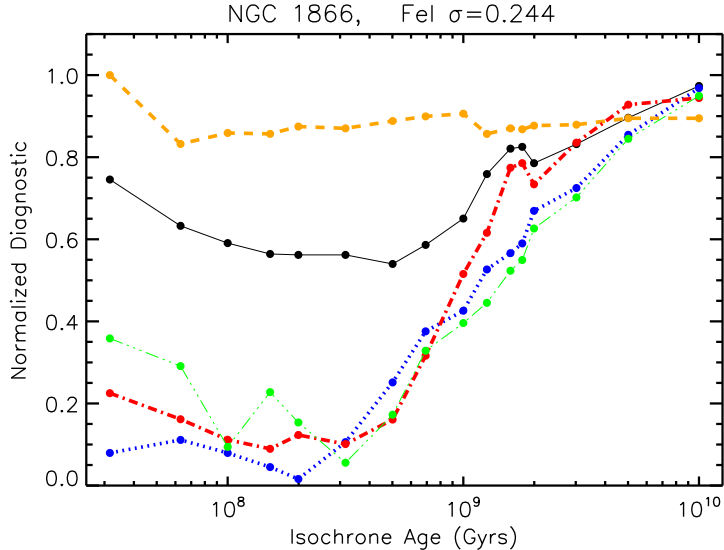
Figure 3.31. Same as Figure 3.3 for NGC 1866. Best solutions are for ages of 100−300 Myr.

grated colors of the synthetic CMDs. In Figure 3.30, we show the behavior of the integrated $(B-V)_\mathrm{o}$ for the grid of isochrones as a function of $[\mathrm{Fe/H}]_\mathrm{iso}$. As expected, the youngest synthetic CMDs with $[\mathrm{Fe/H}]=-1$ to -0.3 have redder $(B-V)_\mathrm{o}$ colors than CMDs at other metallicities (note the "bump" in $(B-V)_\mathrm{o}$ at $-0.7 <[\mathrm{Fe/H}]< -0.5$ for the $30-100$ Myr age isochrones). A more subtle point that can be seen in Figure 3.30 is that there is a complicated $(B-V)_\mathrm{o}$-metallicity-age degeneracy for synthetic CMDs with ages <150 Myr, which we will discuss further at the conclusion of this section.

The complex behavior of the $[\mathrm{Fe/H}]_\mathrm{cluster}$ solutions in Figure 3.29 hints that constraining the $[\mathrm{Fe/H}]$ of clusters with ages <1 Gyr may be difficult. However, in the case of NGC 1866, we find that the self-consistent $[\mathrm{Fe/H}]$ solutions follow the same pattern seen for old and intermediate age clusters, in the sense that the self-consistent synthetic CMDs with younger ages tend to have more metal-rich $[\mathrm{Fe/H}]$ solutions. In Figure 3.31 we show the diagnostics for the 14 self-consistent CMD solutions for the initial grid. We find that it is very clear from the Fe I line diagnostics alone that a young age for NGC 1866 is preferred. Specifically, we find that the most stable $[\mathrm{Fe/H}]$ solutions for NGC 1866 are found at ages of $100-500$ Myrs. We note that this independent age constraint using our abundance analysis method is consistent with the observed $B-V=0.26$ from Pessev et al. (2008). Figure 3.30 shows that in
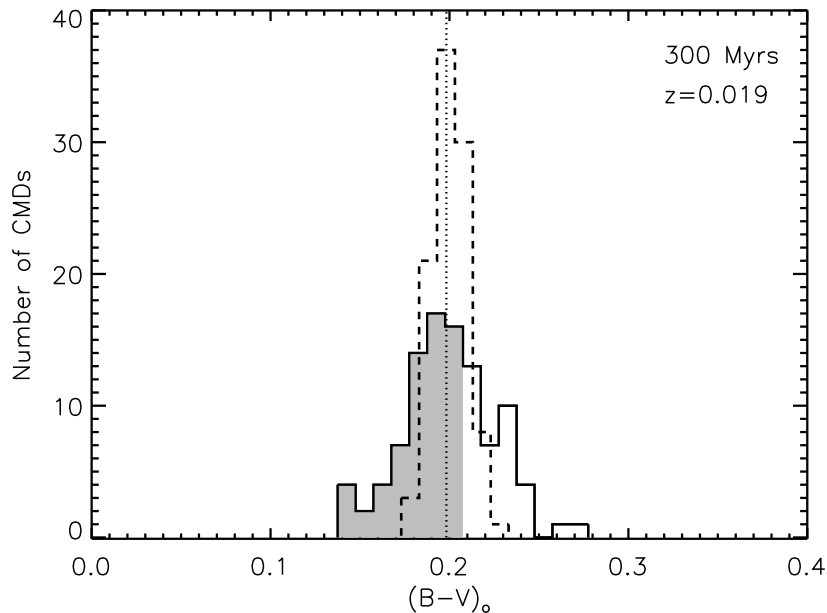
Figure 3.32. Histogram of integrated $(B - V)_o$ color for 100 CMD realizations of a 300 Myr, z=0.019 ([Fe/H]=0) isochrone. Solid black line shows the histogram for a population where the total flux in stars has been normalized to 14% of a $M_V^{tot} = -9$ cluster, which is appropriate for our integrated light spectrum of NGC 1866. Dashed black line shows the histogram for a population normalized to 100% of a $M_V^{tot} = -9$ cluster. CMDs with $(B-V)_o$ color consistent with the observed, reddening-corrected $B - V$ of NGC 1866 are shaded in gray.

particular, the $(B - V)_o$ of the synthetic CMDs for ages of $\sim$500 Myr or less are consistent with the observed $B - V$, which can be thought of as an upper limit to the $(B - V)_o$ of NGC 1866.

In view of the earlier discussion of the importance of luminous supergiants for clusters in this age regime, it is important to evaluate if sampling uncertainties can significantly change the derived [Fe/H] and age for NGC 1866. However, in the case of NGC 1866, we find that the original averaged CMD solutions for ages of $100-300$ Myr are very stable, and show only a very slight dependence of [Fe/H] with EP and wavelength. Because these solutions are very stable already, we can expect it will be difficult to find CMD realizations that are better solutions. Regardless, we investigate the impact of sampling uncertainties at young ages. To that end, the dashed line in Figure 3.32 shows a histogram of the integrated $(B - V)_o$ of 100 CMD realizations created for an isochrone with an age of 300 Myr, and [Fe/H]=0, which is consistent

with the properties we derive for NGC 1866. The CMD realizations that make up the dashed line histogram have been normalized to the total flux of a $M_V^{\mathrm{tot}} \sim -9$ cluster. It can be seen in Figure 3.32 that a cluster with $M_V^{\mathrm{tot}} \sim -9$ is massive enough that the range of $(B-V)_{\mathrm{o}}$ is small (~ 0.5 mag) because the CMDs are not significantly impacted by statistical fluctuations in the number and properties of the supergiant stars. Similarly, even though we estimate that we have only observed 14% of the total flux of NGC 1866, we find that CMD realizations normalized to 14% of the flux of a $M_V^{\mathrm{tot}} \sim -9$ cluster are still so well-populated that the spread in $(B-V)_{\mathrm{o}}$ is only a little larger (~ 0.1 mag), and comparable to that for the better sampled old clusters in the training set. The histogram for 100 CMD realizations normalized to the observed region of NGC 1866 is shown by the solid line in Figure 3.32.

However, we note that fluctuations in $(B-V)_{\mathrm{o}}$ tend to be larger at lower metallicities (see Figure 3.30), especially for clusters with young ages, so it is important to establish if acceptable CMD realizations exist at other metallicities and whether they result in more stable [Fe/H] solutions.

In determining a range in $(B-V)_{\mathrm{o}}$ for the first subset of CMD realizations, we note that NGC 1866 is well-studied and there are several estimates of the $E(B-V)$ that are consistently in the range of 0.06 to 0.13. The $(B-V)_{\mathrm{o}}$ requirement that we use includes this range of $E(B-V)$, as shown by the shaded gray region in Figure 3.30. We include CMD realizations with ages of $100-300$ Myr, and [Fe/H]$=-1.5$ to $+0.2$.

As we found for the intermediate age clusters, for NGC 1866 we find that the spread in $(B-V)_{\mathrm{o}}$ leads to a large spread in [Fe/H]$_{\mathrm{cluster}}$. The solutions range from [Fe/H]$=-1.7$ to $> +0.5$. We show the results for the CMD realizations with ages of 100, 150, and 300 Myr in Figure 3.33; compared to the original averaged CMD solutions for reference. Out of the ~ 600 CMD realizations that satisfy the $(B-V)_{\mathrm{o}}$ requirement, only ~ 50 result in self-consistent solutions (see those falling on the diagonal line in Figure 3.33). Because so many of the possible CMD realizations do not satisfy the [Fe/H] self-consistency requirement, we can conclude that for young clusters our analysis method is very successful in picking out a small range of viable CMD realizations from a large set of CMD possibilities, just as discussed for the
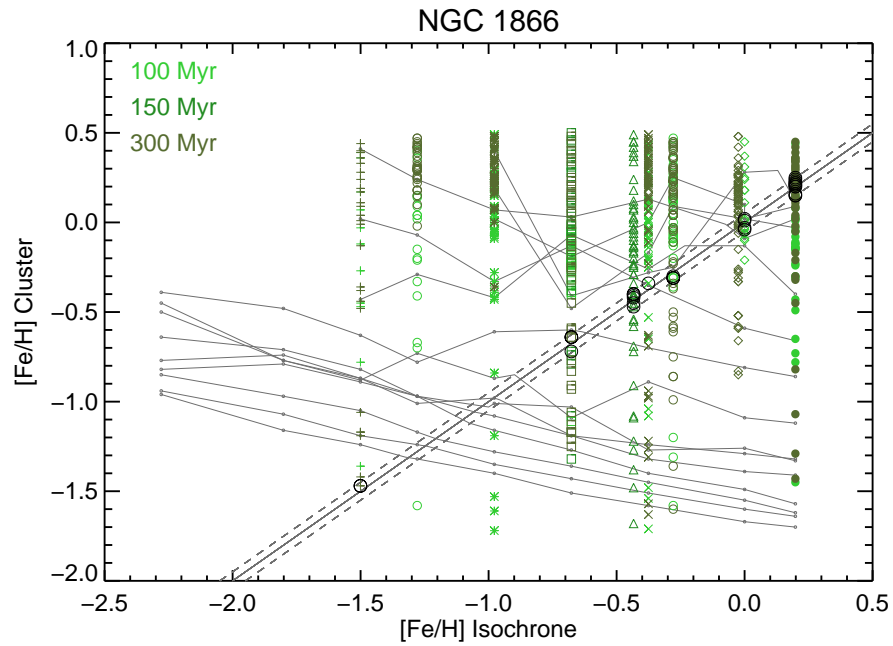
Figure 3.33. Same as Figure 3.29, with the addition of the Fe I abundance results for the CMD realizations of NGC 1866. Colors of the points denote the same ages as Figure 3.29. Only CMD realizations consistent with the observed $B-V$ color of NGC 1866 are shown. Black circles on the solid black line denote CMD realizations that satisfy the self-consistent criterion $[Fe/H]_{iso}=[Fe/H]_{cluster}$. Only a small number of the possible CMD realizations have self-consistent $[Fe/H]$ solutions.
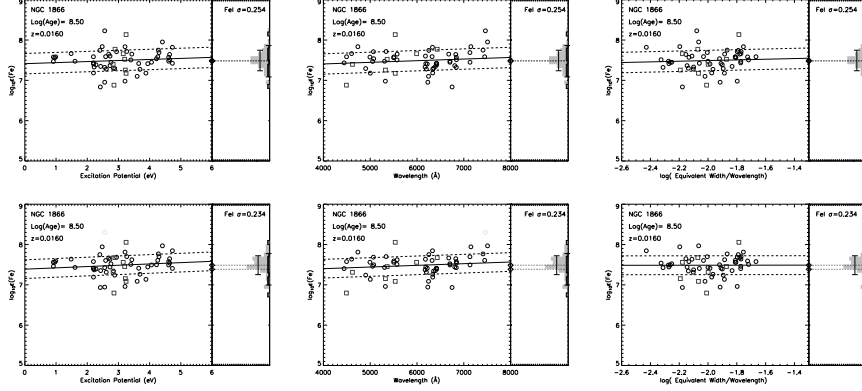
Figure 3.34. Same as Figure 3.10 for NGC 1866. The top panels correspond to the averaged CMD solution using a 300 Myr, [Fe/H]=0 isochrone, and the bottom panels correspond to the best-fitting CMD realization using a 300 Gyr, [Fe/H]=0 isochrone. The solution in the bottom panels has a smaller Fe I σ.

intermediate age clusters in § 3.4.5. This is due to the sensitivity of the Fe line EWs to the temperature of the luminous supergiants.

From the ∼50 possible self-consistent CMD realizations, we pick one best-fitting CMD realization for each age by minimizing the Fe I line diagnostics. We find that solutions with [Fe/H]∼0 are the most stable solutions overall, just as was found from the original averaged CMD solutions. These solutions have a smaller Fe I σ than the original averaged CMD solutions, and small improvements in the EP, wavelength, and reduced EW diagnostics. A comparison of the individual diagnostics for the 300 Myr averaged CMD solution and the best-fitting 300 Myr CMD realization is shown for reference in Figure 3.34. In Figure 3.35 we show the normalized diagnostics for the solutions with ages of 100−500 Myr compared to the averaged CMD solutions at other ages. From Figure 3.35 we derive a final age constraint for NGC 1866 of 100−300 Myr. The range of [Fe/H] for the 100−300 Myr solutions results in a mean of [Fe/H]=+0.05 ± 0.06, which is comparable to the standard error in the mean of the Fe I abundance.

In summary, the analysis of NGC 1866 demonstrates that using our abundance analysis method, we can obtain very tight constraints on the age and abundance of massive clusters with ages of ∼100-500 Myr. We see evidence for the significant impact of luminous supergiants on both the integrated $(B-V)_{\mathrm{o}}$ colors and the
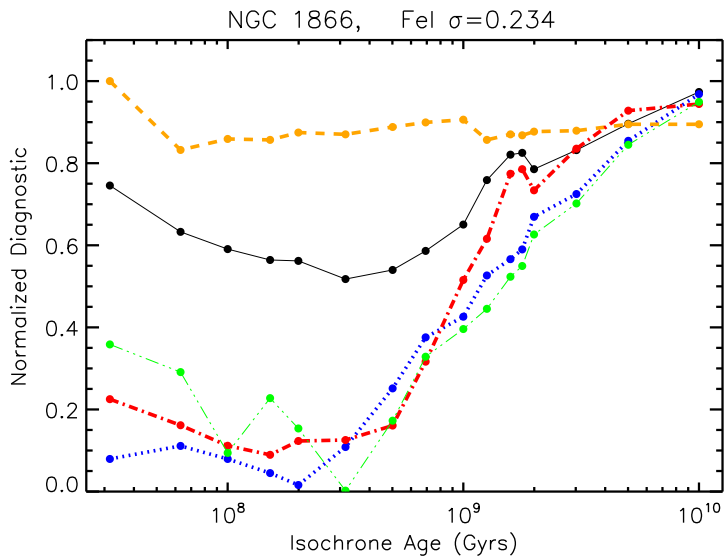
Figure 3.35. Same as Figure 3.31, except the solutions at ages of $100-300$ Myr have been replaced by the solutions for the best-fitting CMD realization at these ages. Best solutions are for ages of 100-300 Myr.

derived [Fe/H] abundances. As was the case for the intermediate age clusters, for NGC 1866 it is the sensitivity of the [Fe/H] solution to luminous, cool stars that facilitates strong constraints on age and metallicity from high resolution integrated light spectra. By allowing for statistical fluctuations in the synthetic CMDs, we are able to reduce the Fe I σ of the original solutions and improve the [Fe/H] stability with EP, wavelength, and reduced EW. Moreover, we find that with high quality data, the self-consistency and stability of the [Fe/H] solution can break the $(B-V)_{\rm o}$-metallicity degeneracy seen in Figure 3.30. Possible systematic offsets from using IL analysis are discussed in § 3.6.1.

NGC 1711

NGC 1711 is estimated to have an age of 50 Myr, and is less massive than NGC 1866 with $M_V^{\rm tot}-8.3$. Our analysis of NGC 1711 is hampered by low S/N spectra and poor sampling ($\sim$16%). We are only able to measure $\sim$25 reasonably clean Fe I lines, and find a very high line-to-line scatter of Fe I σ $\sim$0.45. These difficulties mean that the constraints we can make from our abundance analysis are limited, but we find the general trends are consistent with those of NGC 1866.
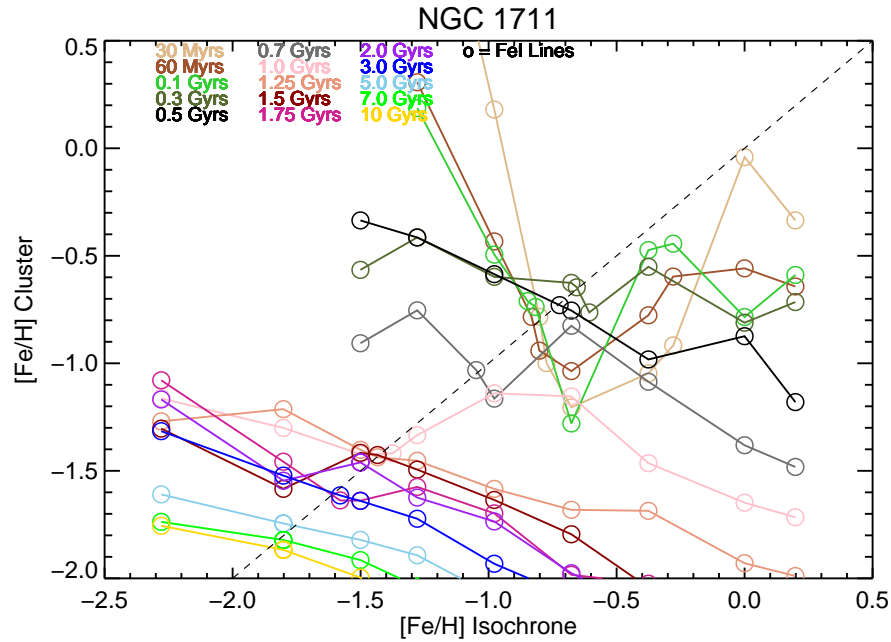
Figure 3.36. Same as Figure 3.2 for NGC 1711.

We find that the self-consistent [Fe/H] solutions appear at [Fe/H]~ -0.8 for synthetic CMDs with ages <300 Myrs, as shown in Figure 3.36. These solutions fall into the region of $(B-V)_o$-metallicity space that is very sensitive to the evolution of cool supergiants, as discussed in the previous section. These solutions also imply that NGC 1711 is very metal-poor for its young age, although the high scatter in the Fe I abundance solution must be kept in mind. However, there is also some indication from Figure 3.36 that the 30 Myr CMD solutions near solar metallicity are also close to a self-consistent [Fe/H]. The large jumps in output [Fe/H] indicate that sampling uncertainties are having an impact on the synthetic CMDs and the [Fe/H] solution, as well.

Although the [Fe/H] solutions are not ideal in terms of absolute quality, we are still able to evaluate the relative quality of the solutions for different ages. We find that, like NGC 1866, the normalized diagnostics for the self-consistent solutions for each age clearly suggest the best solutions are at the youngest ages, as seen in Figure 3.37. For NGC 1711, we find that the solutions imply an age <300 Myr. This is further evidence that the Fe lines are powerful diagnostics for determining ages of young
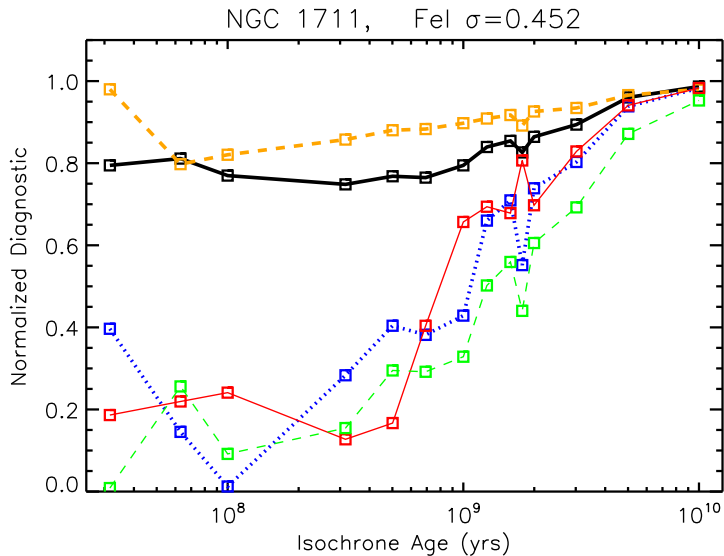
Figure 3.37. Same as Figure 3.3 for NGC 1711. Best solutions are for ages of <300 Myr.

clusters, and it suggests that with high quality data our abundance analysis method could be used to put tight constraints on age and [Fe/H] of ∼50 Myr clusters that are sufficiently massive and well-sampled.

We repeat the exercise of creating CMD realizations covering the range of interest in age and [Fe/H], primarily to evaluate if we can see evidence for better solutions at more metal-rich abundances. For a comparison to the older clusters in the training set, we show the $(B-V)_\circ$ histogram of 100 CMD realizations created for a $M_V^{\text{tot}}-8.3$, 60 Myr cluster, like NGC 1711, by the dashed lines in Figure 3.38. We note that the $(B-V)_\circ$ scale in Figure 3.38 is bigger than for the histograms shown for other clusters in this work, because the range in $(B-V)_\circ$ for the CMD realizations is larger. This is most apparent from the solid line histogram, which is made from CMD realizations normalized to the total flux of 16% of a $M_V^{\text{tot}}-8.3$ cluster, which corresponds to the fraction of NGC 1711 we have observed. The range of $(B-V)_\circ$ for the CMD realizations in this histogram is ∼0.6 mag, significantly higher than the ∼0.1 mag discussed for NGC 1866. Figure 3.38 underscores the fact that it is crucial that young clusters are very luminous and well-sampled when observed for integrated light analyses (e.g. Brocato et al., 1999).

We next explore the range of solutions that can be obtained from the CMD real-
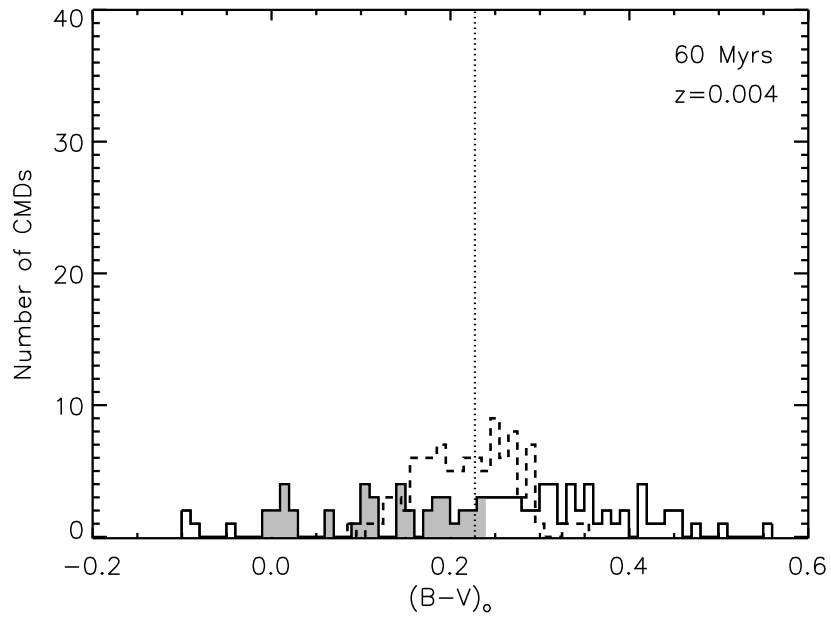
Figure 3.38. Histogram of integrated $(B-V)_o$ color for 100 CMD realizations of a 60 Myr, z=0.004 ([Fe/H]=−0.66) isochrone. Solid black line shows the histogram for a population where the total flux in stars has been normalized to 16% of a M_V^{tot}= −8.3 cluster, which is appropriate for our integrated light spectrum of NGC 1711. Dashed black line shows the histogram for a population normalized to 100% of a M_V^{tot}= −8.3 cluster. CMDs with $(B-V)_o$ color consistent with the observed, reddening-corrected $B-V$ of NGC 1711 are shaded in gray. The range in $(B-V)_o$ for the CMD realizations is very large, demonstrating that sampling uncertainties are a big concern.

izations for NGC 1711. We allow the subset of CMD realizations used for abundance analysis to have a wide range in color ($0.0 < (B-V)_o < 0.3$), due to large uncertainties in the observed $B - V$ and $E(B - V)$ of Pessev et al. (2008) and Dirsch et al. (2000). While in general we do not find that the self-consistent CMD realizations offer significant improvements over the averaged CMD solutions, we do find that there are two more groups of self-consistent solutions with comparable diagnostics at [Fe/H]~ -0.3 and [Fe/H]~ 0. However, it is impossible to tell if this is purely a consequence of the large Fe I σ making it difficult to distinguish between different CMD realizations, or if the solution is really degenerate in [Fe/H]. It is possible that with higher quality data and better sampling the best-fitting solution would be more apparent, as in the case of NGC 1866.

In conclusion, the limited constraints for the properties of NGC 1711 that can be derived from our abundance analysis method are an age <300 Myrs, and $-0.7 <$ [Fe/H] < 0.0. Although these constraints are large, we find that the general trends from the analysis are very similar to that of NGC 1866, which means that it may be possible to obtain better constraints for $\sim$50 Myr clusters that are more massive and better sampled.

3.5 Results : Chemical Abundances

We have been able to constrain the ages and determine precise metallicities for six clusters in the LMC training set: NGC 2019, 2005, 1916, 1718, 1978, and 1866. For these clusters, we also report abundances measured for the available clean lines of α-elements, light elements, Fe-peak elements and neutron capture elements. For the other young cluster we were able to analyze, NGC 1711, we find that the large uncertainties due to the age and large Fe I σ do not allow us to obtain meaningful constraints on the abundances of other elements. The remaining two young clusters, NGC 2100 and NGC 2002, were found to be too young for our abundance analysis and so we cannot report abundances for any elements.

In the following sections we present abundance results for over 20 individual elements in the LMC in the context of previous results from detailed chemical abundance

studies of individual stars in the LMC and the MW. Many of these results are the first measurements for certain clusters, and will be discussed further in §3.6.3. We have demonstrated in Paper II and this work that our ability to obtain precise measurements of chemical abundances is largely determined by the empirical quality of the Fe I abundance solution, in that solutions with larger Fe I σ are more uncertain than those with well-constrained [Fe/H]. We have found in §3.4 that for the LMC training set, the quality of our solutions are most limited for clusters with low S/N data or large sampling uncertainties. In particular, the intermediate age clusters NGC 1718 and NGC 1978 have the most uncertain [Fe/H] solutions and so this must be kept in mind for interpretation of the results for other elements.

For the six LMC clusters we are able to analyze, we show the final abundances, number of available spectral lines, line-to-line scatter (σ), and standard error, or uncertainty, ($\sigma/\sqrt{(N_{lines} - 1)}$) for each species in Tables 3.7 through 3.12. For NGC 1718, NGC 1978, and NGC 1866 we also report the uncertainty in the [X/Fe] ratios that is due to the age range we derive for the cluster (σ_{age}), as well as the mean abundance over that range that we adopt for our final solution. We note that for the old clusters in the training set, the uncertainty associated with the age of the cluster is small—usually <0.05 dex for [X/Fe]— and so is not included for the individual species. All abundances relative to Fe in Tables 3.7 through 3.12 use the solar abundance distribution of Asplund et al. (2005), with a solar logϵ(Fe)=7.50. The abundances ratios for ionized species (Ti II, Sc II, La II, Ba II, Nd II, Sr II, Sm II, Y II, Eu II) are reported with respect to [Fe/H]$_{II}$. We have calculated abundances with hyperfine splitting (hfs) of energy levels taken into account for the elements Sc, V, Mn, Cu, Ba, and Eu. The hyperfine splitting abundance corrections vary depending on the EW of the line, and can be large (several tenths of a dex) for V, Mn, Ba and Cu, but are generally <0.1 dex for Sc and Eu.

In Figures 3.39 through 3.44, we show the LMC cluster abundances from our analysis (red squares) compared to the MW training set abundances from Paper II (gray squares). For reference, we also show a compilation of abundances measured for individual stars in the LMC as small red points and for the MW as small gray points.

Species	$\log_{10}\epsilon(X)$ 10 Gyrs	σ	Uncertainty	[X/Fe][1]	N_{lines}
Na I	4.74	$\cdots$	$\cdots$	+0.24	1
Mg I	6.03	0.29	0.17	+0.17	4
Si I	5.93	$\cdots$	$\cdots$	+0.09	1
Ca I	4.85	0.21	0.05	+0.21	16
Sc II	1.48	0.25	0.13	+0.08	5
Ti I	3.38	0.29	0.09	+0.15	12
Ti II	3.36	0.37	0.14	+0.13	8
V I	2.35	0.35	0.24	+0.02	3
Cr I	4.03	0.19	0.07	+0.06	8
Mn I	3.29	0.20	0.14	−0.43	3
Fe I	5.83	0.20	0.03	−1.67	49
Fe II	5.85	0.07	0.04	−1.65	5
Co I	3.39	0.30	0.30	+0.14	2
Ni I	4.50	0.28	0.07	−0.06	16
Ba II	0.57	0.18	0.09	+0.05	5
La II	-0.13	$\cdots$	$\cdots$	+0.41	1
Nd II	0.38	0.23	0.16	+0.60	3

Table 3.7. NGC 2019 Abundances *Notes*: 1. For Fe this quantity is [Fe/H].

Species	$\log_{10}\epsilon(X)$ 15 Gyrs	σ	Uncertainty	[X/Fe][1]	N_{lines}
Mg I	5.61	$\cdots$	$\cdots$	−0.38	1
Ca I	5.04	0.22	0.08	+0.27	8
Sc II	1.93	$\cdots$	$\cdots$	+0.15	1
Ti I	4.08	0.47	0.47	+0.72	2
Ti II	3.99	0.48	0.18	+0.36	8
Cr I	4.19	0.26	0.18	+0.09	3
Mn I	3.77	0.09	0.09	−0.08	2
Fe I	5.96	0.25	0.04	−1.54	34
Fe II	6.23	0.05	0.03	−1.27	4
Ni I	4.80	0.14	0.10	+0.11	3
Ba II	1.10	$\cdots$	$\cdots$	+0.20	1

Table 3.8. NGC 2005 Abundances *Notes*: 1. For Fe this quantity is [Fe/H].

Species	$\log_{10}\epsilon(X)$ 15 Gyrs	σ	Uncertainty	$[X/Fe]^1$	N_{lines}
Na I	4.98	0.24	0.24	+0.35	2
Mg I	6.31	$\cdots$	$\cdots$	+0.32	1
Ca I	5.15	0.24	0.10	+0.38	7
Sc II	1.70	0.08	0.08	−0.34	2
Ti I	3.91	0.16	0.16	+0.55	2
Ti II	4.34	0.42	0.19	+0.45	6
Cr I	4.20	0.24	0.12	+0.10	5
Mn I	3.67	0.09	0.09	−0.18	2
Fe I	5.96	0.26	0.04	−1.54	50
Fe II	6.49	0.15	0.11	−1.01	3
Ni I	4.69	0.17	0.07	+0.00	7
Sr II	0.84	$\cdots$	$\cdots$	−1.12	1
Y II	0.73	$\cdots$	$\cdots$	−0.47	1
Ba II	0.58	0.18	0.10	−0.58	4

Table 3.9. NGC 1916 Abundances *Notes*: 1. For Fe this quantity is [Fe/H].

Species	$\log_{10}\epsilon(X)$ 1-2.5 Gyrs	σ	Uncertainty	σ_{age}	$[X/Fe]^1$	N_{lines}
Na I	6.21	0.24	0.17	0.15	+0.68	3
Mg I	6.25	$\cdots$	$\cdots$	0.15	−0.64	1
Ca I	5.47	0.37	0.26	0.10	−0.20	3
Sc II	2.46	$\cdots$	$\cdots$	0.13	+0.13	1
Ti I	5.00	0.18	0.13	0.07	+0.74	3
V I	4.08	0.29	0.17	0.11	+0.72	4
Cr I	5.19	$\cdots$	$\cdots$	0.00	+0.19	1
Mn I	4.78	0.10	0.10	0.07	+0.03	2
Fe I	7.11	0.33	0.04	0.25	−0.64	69
Fe II	6.89	0.29	0.14	0.29	−0.72	5
Ni I	5.76	0.35	0.25	0.10	+0.17	3
Ba II	1.79	$\cdots$	$\cdots$	0.33	+0.34	1

Table 3.10. NGC 1718 Abundances *Notes*: 1. For Fe this quantity is [Fe/H].

Species	$\log_{10}\epsilon(X)$ 1.5-2.5 Gyrs	σ	Uncertainty	σ_{age}	$[X/Fe]^1$	N_{lines}
Na I	5.87	0.35	0.35	0.04	+0.44	2
Ca I	5.69	0.52	0.26	0.06	+0.12	5
Ti I	3.88	0.45	0.26	0.13	−0.28	4
Ti II	4.83	0.22	0.22	0.03	+0.02	2
V I	3.39	0.39	0.27	0.11	+0.13	3
Mn I	4.79	0.33	0.23	0.03	+0.14	3
Fe I	6.76	0.34	0.06	0.07	−0.74	36
Fe II	7.40	0.16	0.09	0.08	−0.10	4
Ni I	5.95	0.04	0.03	0.01	+0.46	3
Cu I	3.67	$\cdots$	$\cdots$	0.02	+0.20	1
Y II	2.11	0.33	0.33	0.02	−0.00	2
La II	1.15	$\cdots$	$\cdots$	0.01	+0.11	1
Nd II	1.42	$\cdots$	$\cdots$	0.01	+0.06	1

Table 3.11. NGC 1978 Abundances *Notes*: 1. For Fe this quantity is [Fe/H].

References for individual star abundances are located in the captions of Figures 3.39 through 3.44. The error bars on the abundances for the LMC training set clusters in Figures 3.39 through 3.44 correspond to the standard error in the mean of the lines for each species by default, and points without error bars correspond to species where only one clean line was available. However, in the case of the intermediate age and young clusters, if the uncertainty due to the age is larger, that value is used in place of the standard error.

3.5.1 Alpha Elements

The ratio of α-elements to Fe is a powerful tool for studying galaxy evolution. This is because while both α-elements and Fe-peak elements are produced in large quantities in the supernovae of massive stars on short timescales, Fe-peak elements are also produced in large quanities in type Ia supernovae on much longer timescales. Thus the ratio of the two groups of elements holds information on the rates and durations of different types of supernovae, and is sensitive to the star formation history of a galaxy.

In the LMC, observations of individual stars have shown a larger range in $[\alpha/Fe]$

Species	$\log_{10}\epsilon(X)$ 100-300 Myrs	σ	Uncertainty	σ_{age}	$[X/Fe]^1$	N_{lines}
O I	8.80	$\cdots$	$\cdots$	0.07	+0.13	1
Na I	6.04	0.20	0.14	0.15	−0.13	3
Mg I	7.15	0.30	0.22	0.21	−0.38	3
Al I	6.23	$\cdots$	$\cdots$	0.17	−0.15	1
Si I	7.61	$\cdots$	$\cdots$	0.06	+0.10	1
Ca I	6.30	0.12	0.05	0.12	−0.02	7
Sc II	3.34	$\cdots$	$\cdots$	0.25	+0.43	1
Ti I	5.21	0.16	0.16	0.28	+0.31	2
Ti II	5.21	0.12	0.12	0.15	+0.45	2
V I	3.79	0.46	0.46	0.46	−0.22	2
Cr I	5.52	0.25	0.25	0.25	−0.12	2
Mn I	5.12	0.39	0.22	0.22	−0.28	4
Fe I	7.55	0.27	0.07	0.06	+0.05[2]	50
Fe II	7.35	0.38	0.15	0.05	−0.15	8
Ni I	6.02	0.21	0.09	0.22	−0.22	7
Y II	2.47	$\cdots$	$\cdots$	0.14	+0.41	1
Zr I	2.97	$\cdots$	$\cdots$	0.49	+0.37	1
Ba II	3.15	0.11	0.11	0.17	+1.12	2
La II	2.03	$\cdots$	$\cdots$	0.30	+1.04	1
Sm II	1.78	$\cdots$	$\cdots$	0.34	+0.91	1
Eu II	0.99	$\cdots$	$\cdots$	0.22	+0.61	1

Table 3.12. NGC 1866 Abundances *Notes*: 1. For Fe this quantity is [Fe/H]. 2. An opacity correction results in [Fe/H]=−0.2, as discussed in § 3.6.1.
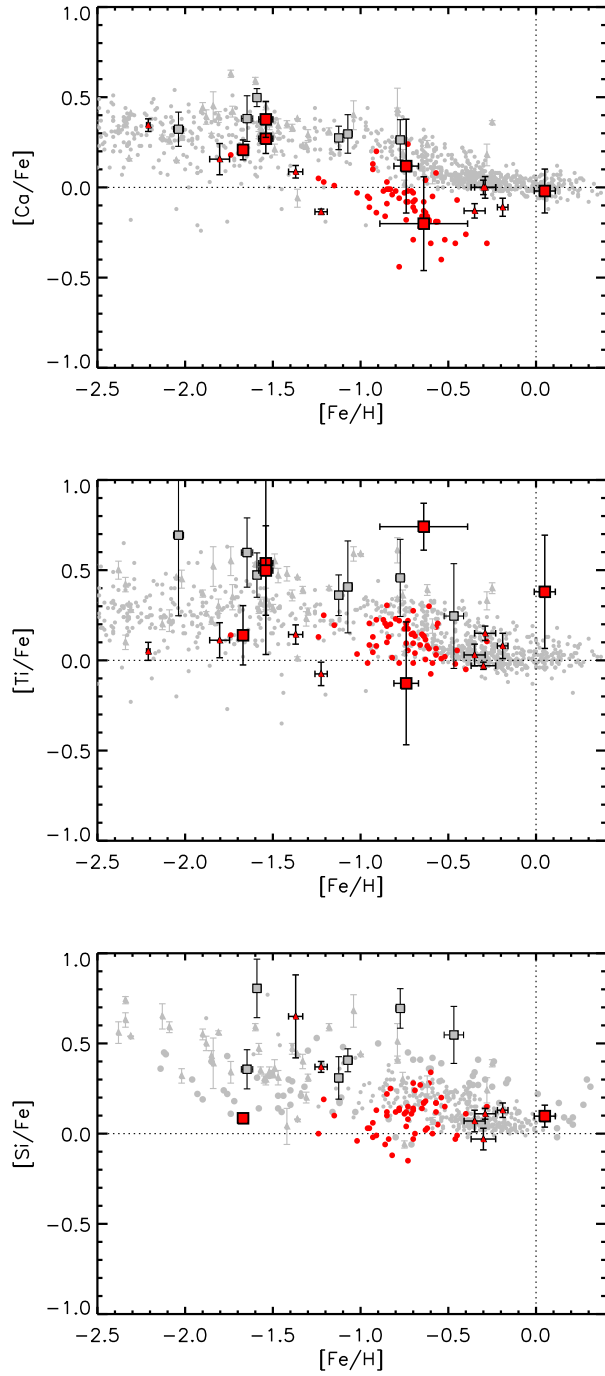
Figure 3.39. α-element ratios. Large red squares show the LMC IL abundances, and large grey squares show the MW training set abundances. Small grey points show MW stellar abundances, and small red points show LMC stellar abundances. Data for single stars in the MW are from Venn et al. (2004), Pritzl et al. (2005) and references therein. Data for LMC single stars are from Johnson et al. (2006), Mucciarelli et al. (2008), and Pompéia et al. (2008). When possible the abundance ratios have been adjusted to be consistent with the solar abundance distribution of Asplund et al. (2005) that was used in our analysis. The average of [Ti/Fe]$_I$ and [Ti/Fe]$_{II}$ are plotted vs [Fe/H]$_I$ where we have measured them.

abundances than is seen in studies of stars in the MW (e.g. Venn et al., 2004; Pritzl et al., 2005; Pompéia et al., 2008; Smith et al., 2002), and reflects the different star formation history of the LMC. The abundance information available for the LMC is also more limited than for the MW. There are α-element abundances for only a handful of unambiguously old stars, primarily in the sample of globular cluster stars of Johnson et al. (2006), who found [Mg/Fe] and [Si/Fe] were comparable to abundances in MW globular clusters, but that [Ca/Fe] and [Ti/Fe] were significantly lower. These results are interesting, because while in a simple model, low [α/Fe] ratios can be explained by a higher contribution of Type Ia supernovae in the LMC when compared to the MW, the fact that not all of the α-elements are low means a different explanation is needed for the chemical enrichment in the LMC.

For more metal-rich field stars, Pompéia et al. (2008) found that [Ca/Fe], [Ti/Fe], and [Si/Fe] were lower than for MW stars at similar [Fe/H], and the authors favored an explanation of a slower star formation history for the LMC than for the MW. For younger clusters, Mucciarelli et al. (2008) found that stars in 4 LMC clusters with ages of $\sim$2 Gyr had solar [α/Fe] at metallicities of [Fe/H]~ -0.4, and overlap with the [α/Fe] in MW stars more so than older, lower metallicity LMC stars. Observations of young O, B, and F type stars in the LMC have shown abundances of O, Mg, and Si that may be slightly underabundant when compared to MW stars at similar metallicities, but are generally still consistent with MW O and B type stars (Russell & Bessell, 1989; Luck & Lambert, 1992; Rolleston et al., 2002; Hunter et al., 2007). Hill et al. (1995) found that young LMC cluster supergiants with [Fe/H]~ -0.3 have slightly enhanced Si, S, Ca and Ti abundances with respect to solar, but subsolar [Mg/Fe]. This wide range in [α/Fe] implies that the star formation history of the LMC is very complex.

In our sample of LMC clusters, we have measured abundances for Ca I, Ti I, Ti II, Si I, Mg I, and O I in one or more clusters in the LMC training set, including the first measurements of Ca, Ti, and Si in NGC 1866, and the first measurements of any α-elements in NGC 1916 and NGC 1718. Like other light elements, O and Mg often show star-to-star abundance variations in GCs, so we defer discussion of

	Milky Way	LMC (>10 Gyr)
[Ca/Fe]	+0.35 ± 0.08	+0.29 ± 0.09
[Ti/Fe]	+0.46 ± 0.15	+0.39 ± 0.23
[Si/Fe]	+0.52 ± 0.20	+0.09
[Mg/Fe]	+0.18 ± 0.39	+0.04 ± 0.37
$[\alpha_{\mathrm{CaTiSiMg}}/\mathrm{Fe}]$	+0.38 ± 0.15	+0.20 ± 0.17
$[\alpha_{\mathrm{CaTiSi}}/\mathrm{Fe}]$	+0.44 ± 0.09	+0.26 ± 0.15

Table 3.13. Mean IL α Abundances for Milky Way Training Set and Old LMC GCs

these elements to § 3.5.2. For Ca, Ti, and Si, we find that the integrated light $[\alpha/\mathrm{Fe}]$ measurements show more scatter at a given [Fe/H] than we saw for the MW training set clusters in Paper II, or than is seen in the stellar abundances of MW GCs in general. [Ti/Fe] generally shows both a larger line-to-line scatter and scatter between clusters than [Ca/Fe] or [Si/Fe], which is similar to what was found for the MW clusters and for integrated light analysis of GCs in M31 (Colucci et al., 2009). However in this case the scatter is larger, and likely due to the poorer data quality of the LMC training set. The [Ca/Fe] and [Si/Fe] we find for the LMC clusters falls within the range of LMC stellar abundances discussed above, as can be seen in Figure 3.39.

We also find that although there is considerable scatter, the mean $[\alpha/\mathrm{Fe}]$ for each individual element is lower than that in the MW, and that the mean of all Ca I, Ti I, Ti II, and Si I abundances is $\sim$0.2 dex lower than what we find for the MW training set clusters. For reference, we have tabulated the mean $[\alpha/\mathrm{Fe}]$ for the old (>10 Gyr) LMC training set clusters in Table 3.13, as well as the mean IL $[\alpha/\mathrm{Fe}]$ for the MW training set clusters, for comparison. The comparison of the IL Ca I abundance is the most statistically sound; we are able to measure 3−8 clean, unblended Ca I lines for each cluster, which usually have small line-to-line scatter. Conversely, Ti I and Ti II lines are often affected by line blending and have high line-to-line scatter, while Si I only has a few useful transitions, most of which are often affected by blends or atmospheric absorption/emission. Moreover, Ti cannot be considered a "pure" α-element because it is also produced in Type Ia supernovae, although it is often observed to have α-like

behavior (Gratton et al., 2004). Thus, [Ca/Fe] can be thought of as the most accurate and consistent α-element, although in practice a mean α of Ca, Ti and Si abundances is also useful for comparisons to other authors and other abundance analysis methods. Based on this, the [α/Fe] for the old LMC clusters is $\sim$0.06 dex lower than for the MW training set GCs, and within the statistical uncertainty.

We do not include the intermediate age or young clusters in the [α/Fe] comparison, as there are no clusters with comparable ages in the MW training set, and because some evolution with time in [α/Fe] is expected in simple chemical evolution models. Consistent with this expectation, we find that the mean Ca I abundance for the young and intermediate age cluster sample is [Ca/Fe]$=-0.03 \pm 0.16$, much lower than the mean for the old LMC training set clusters of [Ca/Fe]$=+0.29 \pm 0.09$ and similar to the result of Hill et al. (1995) for supergiants in young LMC clusters.

3.5.2 Light Elements

It is well known that MW GCs exhibit star-to-star abundance variations for light elements involved in proton-capture nucleosynthesis (e.g. Gratton et al., 2004). Recently, Mucciarelli et al. (2009) confirmed that abundance variations for O, Na, Mg, and Al are also present in three old, metal-poor GCs in the LMC. When these variations are present, a fraction of stars in the cluster can exhibit any of the following to varying degrees: depleted O due to the ON-cycle, enriched Na due to the NeNa-cycle, and depleted magnesium and/or enriched Al due to the MgAl-cycle. We saw evidence for abundance variations in the IL analysis of MW training set clusters in both Paper I and Paper II, and further evidence in the M31 GCs analyzed in Colucci et al. (2009). Specifically, in our IL analysis, the large scatter in [Mg/Fe] when compared to other α-elements, combined with a lower mean [Mg/Fe] and elevated [Al/Fe] and [Na/Fe] suggests that a fraction of stars in certain clusters have depleted Mg and enhanced Al and/or Na.

In the LMC training set, we are able to measure Na and Mg in 5 clusters, and Al and O in the young cluster NGC 1866. Unfortunately, the weak lines of Al and O are more difficult to measure with EWs in more metal-poor clusters like the old
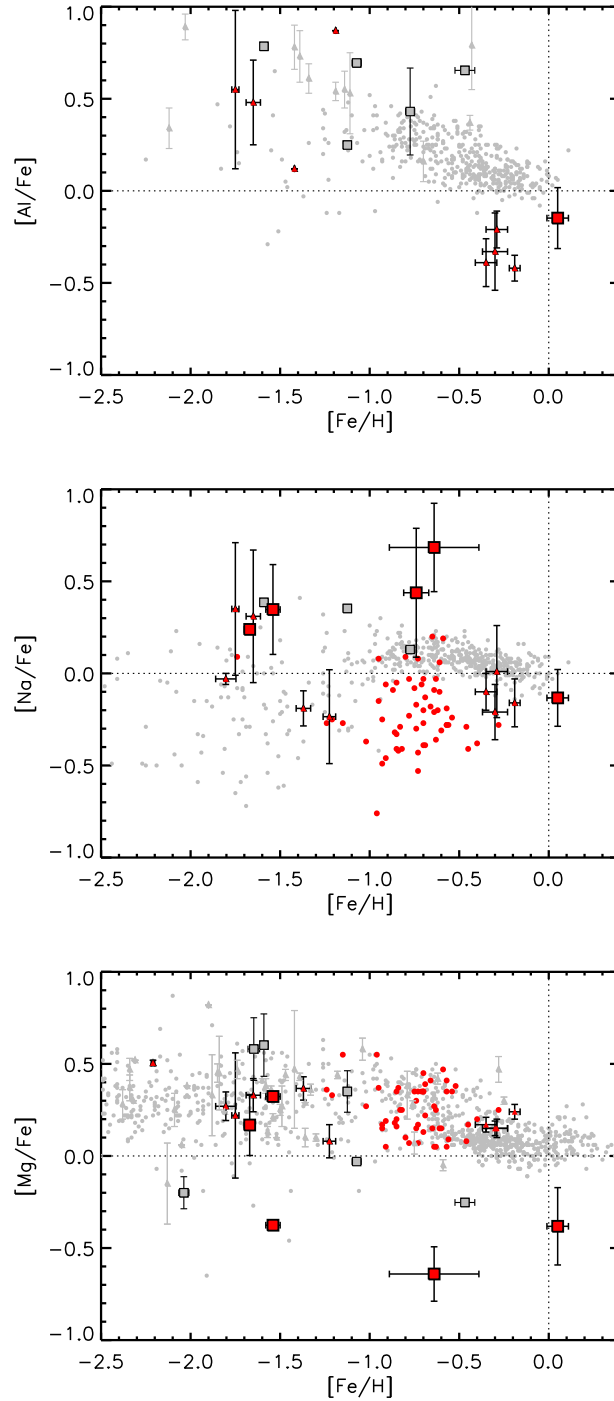
Figure 3.40. Light element abundances. Additional LMC individual star data are from Mucciarelli et al. (2009). Additional MW GC individual star data are from references compiled in Carretta (2006). Symbols are the same as in Figure 3.39.

clusters in the training set, and for the intermediate age clusters the S/N for these features was too low for accurate measurements to be made. In the LMC training set, we find a large scatter in [Mg/Fe], including very depleted [Mg/Fe] over the entire range in [Fe/H]. The mean [Na/Fe] for the old and intermediate age clusters is super-solar ([Na/Fe]$\sim$ +0.5), which is similar to the value for the MW training set clusters, as well the individual stars in old LMC GCs analyzed by Mucciarelli et al. (2009). These results for [Mg/Fe] and [Na/Fe] are consistent with stars in these clusters being affected by abundance variations, while individual field stars are not. As shown in Figure 3.40, the cluster [Na/Fe] is significantly different than the subsolar [Na/Fe] observed in LMC field stars by Pompéia et al. (2008) and Smith et al. (2002). These are the first measurements supporting star-to-star abundance variations in the old clusters NGC 2019, NGC 2005 and NGC 1916, as we will discuss in § 3.6.3. We also find that both the intermediate age clusters in our sample have enhanced [Na/Fe] and NGC 1718 additionally has depleted [Mg/Fe]. This is very interesting, and the first indication of star-to-star abundance variations in clusters with ages of $\sim$2 Gyr. We note that Mucciarelli et al. (2008) do not find that their sample of clusters in this age range show evidence for abundance variations. However, the clusters in the sample of Mucciarelli et al. (2008) have higher metallicities, and there is evidence that the star-to-star variations are less pronounced at high [Fe/H]. Detailed comparisons with stars will be discussed further in § 3.6.1 for NGC 1978, which is a cluster common to both our training set and the sample of Mucciarelli et al. (2008).

For NGC 1866 we find [Na/Fe] and [Al/Fe] to be sub-solar and [O/Fe] to be approximately solar, which is in good agreement with the LMC field stars analyzed by Pompéia et al. (2008) and the stars in $\sim$2 Gyr LMC clusters analyzed by Mucciarelli et al. (2008). This suggests that NGC 1866 is not affected by star-to-star abundance variations, which is in agreement with the findings of Hill et al. (2000) (discussed further in § 3.6.1). This behavior is expected if the explanation for abundance variations in star clusters is self-pollution by $3-8\ M_\odot$ AGB stars, because a cluster with an age of only $\sim$100 Myr is too young to be affected. We note that abundance variations are not found in young MW open clusters either.

3.5.3 Fe-peak Elements

Fe peak elements are well-studied in individual stars in the MW. In general, the abundances of Ni, Cr, Sc, V, and Co tend to scale with that of Fe, so that the [X/Fe] ratios for these elements are approximately solar for [Fe/H]> -2.0. The abundance of Mn however, decreases from solar at [Fe/H]$=0$ to a plateau value of [Mn/Fe]~ -0.4 at [Fe/H]$=-1.0$, as seen in Figure 3.41.

In the LMC, observations of individual RGB stars from Pompéia et al. (2008) have shown subsolar Ni, Cr, and Co, while Hill et al. (1995) finds approximately solar ratios in young supergiants. Johnson et al. (2006) also finds subsolar V in LMC globular cluster stars. The explanation or mechanism for low Fe-peak abundances in the LMC is still unclear, so abundances of these elements in both field stars and clusters are very interesting.

We have been able to measure abundances for Ni, Cr, Mn, Sc, and V in most clusters in the LMC training set, as well as Co in NGC 2019 and Cu in NGC 1978. For Ni, Cr, and Co we generally find that the LMC cluster abundances are consistent with solar rather than subsolar, and the uncertainties in some cases can be large, as seen in Figures 3.41 and 3.42. We find [Sc/Fe] and [V/Fe] to be consistent with solar as well, although there is a large scatter in [Sc/Fe] between clusters as was found for the IL MW abundances in Paper II.

We do find that the abundances of Ni, Cr, and Mn for NGC 1866 appear to be sub-solar; again there are significant uncertainties in this case, due to the assumed age. A similar sub-solar abundance of Mn was found in young LMC clusters by Hill et al. (1995). The [Mn/Fe] for the LMC clusters appears to follow the general trend exhibited by MW field stars, with increasing [Mn/Fe] from [Fe/H]$=-1.5$ to -0.5. However there is some indication of an offset of this trend to slightly higher [Mn/Fe] for the LMC clusters at a given [Fe/H]. In Paper II, [Mn/Fe] IL abundances were found to be systematically higher than stellar [Mn/Fe] by $\sim +0.1$ dex, but Figure 3.42 shows that the LMC clusters still have systematically higher [Mn/Fe] than the MW training set clusters. This result is very interesting (as discussed further in § 3.6.3), because there is very little Mn abundance information available for LMC
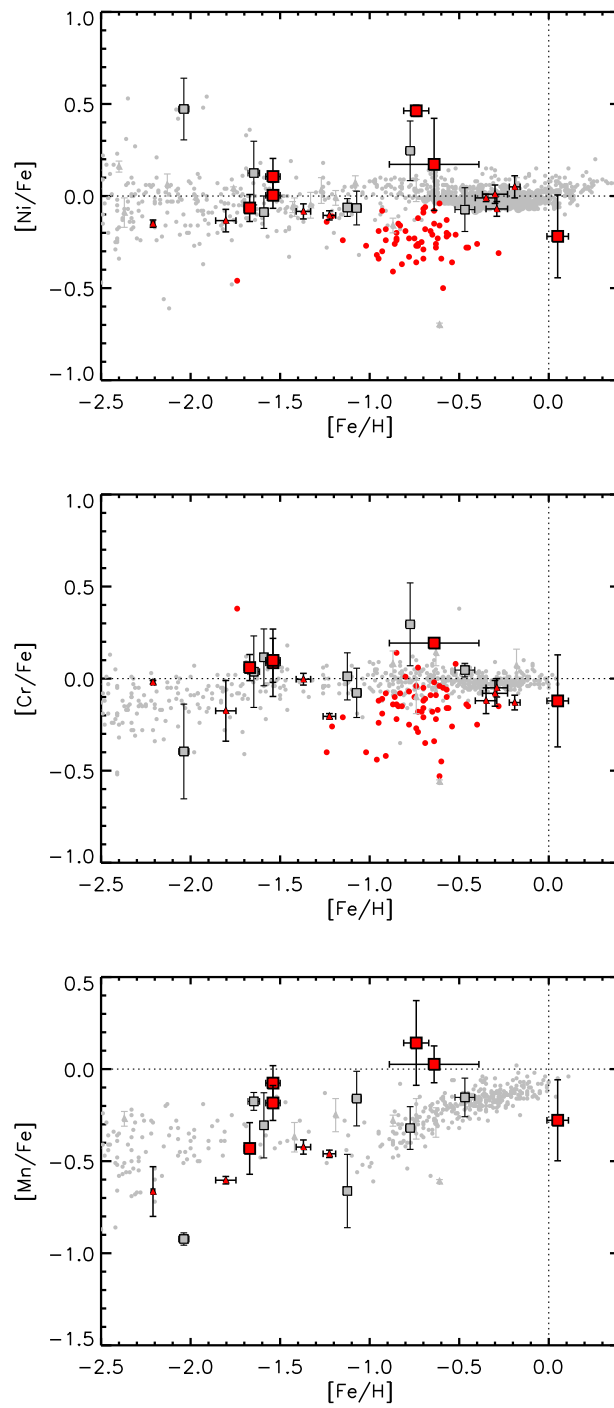
Figure 3.41. Abundances for Fe-peak elements Ni, Cr, and Mn. Symbols are the same as in Figure 3.39.
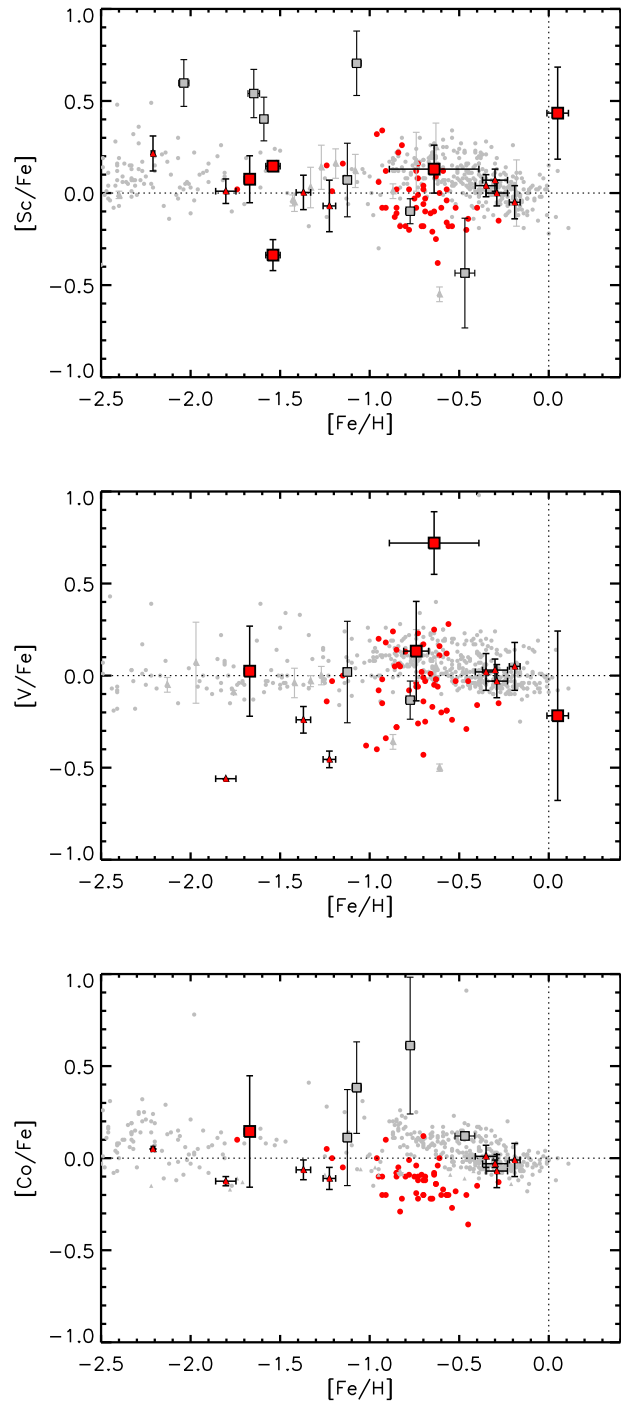
Figure 3.42. Abundances for Fe-peak elements Sc, V, and Co. Symbols are the same as in Figure 3.39.

stars except for the globular cluster stars of Johnson et al. (2006).

3.5.4   Neutron Capture Elements

Neutron capture elements are divided into two categories based on their formation mechanisms: rapid and slow, or r- and s-process, respectively. The elements we measure that are primarily r-process are Eu, Nd, and Sm, while the elements primarily formed in the s-process include Y, Ba, La, Zr, and Sr. The abundances of these elements in different environments are particularly useful for constraining chemical evolution models, especially the contribution of AGB stars to the interstellar medium. These elements have been observed to be critically sensitive to the star formation history of a galaxy and, like α-elements, show different patterns in dwarf galaxies than in the MW. A high [Ba/Y] ratio in particular is thought to be a signature of low star formation rates, as seen in nearby dwarf spheroidal galaxies, because it can indicate a higher contribution to the ISM by low-metallicity AGB stars (e.g. Venn et al., 2004).

Because of line broadening due to the velocity dispersion of the clusters, neutron capture elements tend have weak lines in IL spectra, with the exception of Ba, which has several strong transitions in the optical wavelength range. We have been able to measure Ba in most of the LMC clusters but can only measure Zr, Y, Eu, La, Nd, Sm, and Sr in $1-3$ clusters each.

With the exception of NGC 1916, we find the LMC [Ba/Fe] to be supersolar as is found for LMC individual stars. However we also measured supersolar [Ba/Fe] using identical techniques in the MW training set clusters, so there is no clear difference in [Ba/Fe] between the MW and LMC in general. However, the young cluster in the sample, NGC 1866 has significantly higher [Ba/Fe] than the other clusters, as well as high [Zr/Fe], [Y/Fe], [Eu/Fe], [La/Fe], and [Sm/Fe]. These consistently high neutron-capture abundances are intriguing, as discussed further in § 3.6.3. Hill et al. (1995) found that in young LMC cluster supergiants the heavier neutron capture elements La, Ce, Nd, and Eu to be enhanced to $\sim +0.3$ dex over solar ratios, while the lighter neutron capture elements Y, and Zr are approximately solar, although the star to
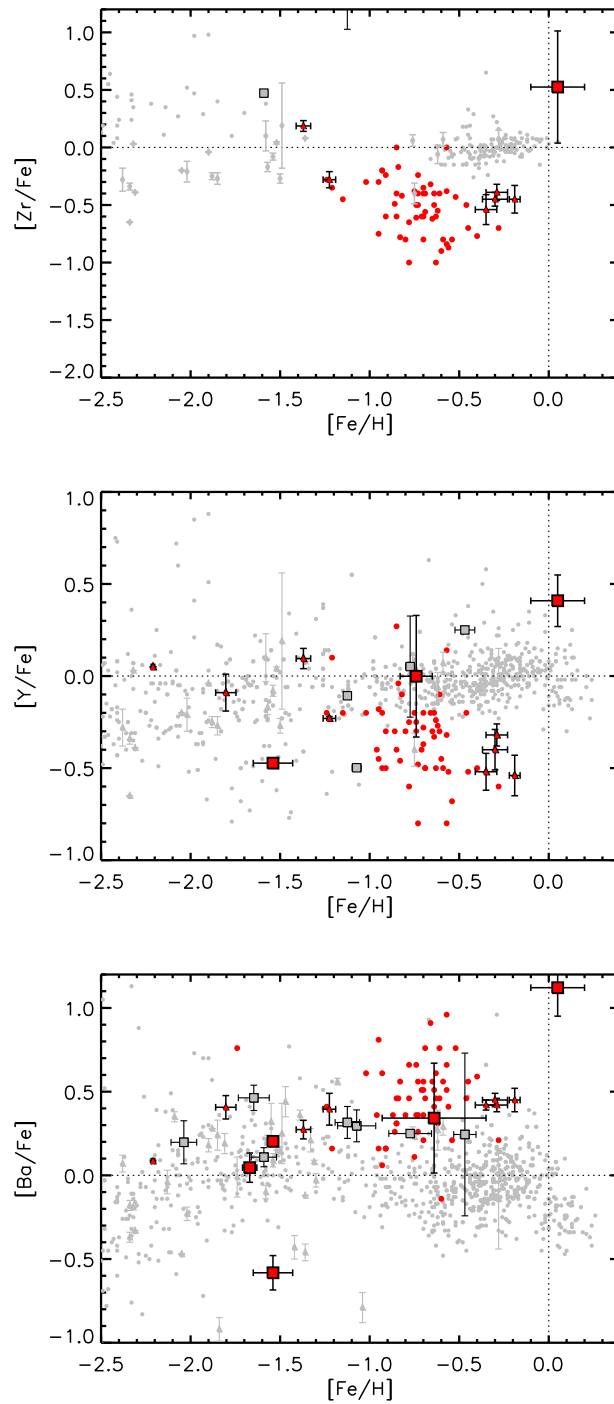
Figure 3.43. Abundances of neutron-capture elements Zr, Y, and Ba. Symbols are the same as in Figure 3.39.
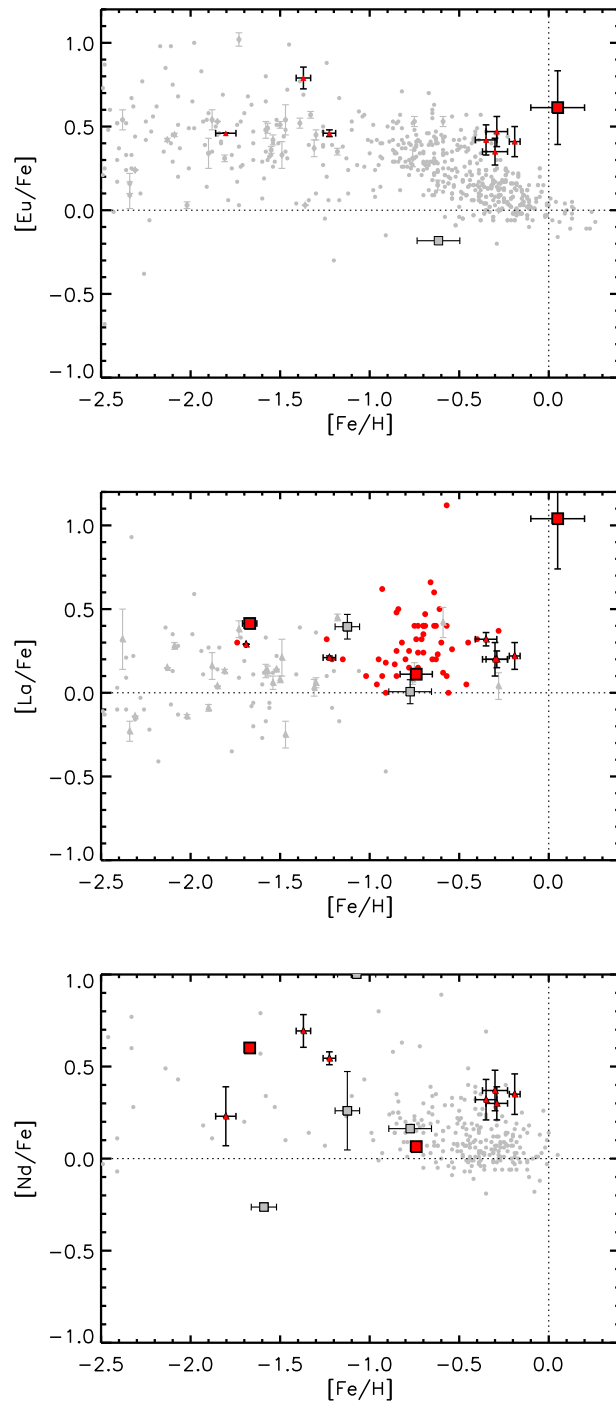
Figure 3.44. Abundances of neutron-capture elements Eu, La, and Nd. Symbols are the same as in Figure 3.39.

star scatter is large. Qualitatively similar results were found by Spite et al. (1993) for Ba, La and Eu in one LMC supergiant and by Russell & Bessell (1989) for Nd and Sm in a sample of 8 F-type LMC supergiants.

Like [Ba/Fe] we find that [Y/Fe], [La/Fe], and [Nd/Fe] are broadly consistent with observations of individual stars in the LMC and that statistically significant differences between the LMC training set abundances and MW training set abundances are not seen with this data set. However, we have demonstrated with the LMC training set that many neutron-capture elements can be analyzed in a high resolution IL spectra, and that this analysis method holds promise for stronger constraints on these elements for extragalactic clusters with high quality data.

3.6 Discussion

In the first part of this section, we focus on the utility of the LMC clusters as a training set, for which the results of the IL spectra analysis method can be compared to properties determined from studies of individual stars with other methods. In § 3.6.1 we compare the abundances we measure to detailed chemical abundances obtained from high resolution analysis of individual stars by different authors in the literature. These comparisons can only be made for a subset of clusters in the training set: NGC 2019, NGC 2005, NGC 1978, and NGC 1866, and for some elements in each cluster there are no comparisons from the literature available. We discuss the extent to which meaningful comparisons to analyses of individual stars can be made for each cluster individually, below. In § 3.6.2, we discuss how estimates of the LMC cluster properties from resolved photometric and low resolution spectra abundance analyses compare to the properties revealed with high resolution abundance analysis in this work. Finally, in § 3.6.3, we summarize the new results for the chemical properties of the LMC clusters found from our IL abundance analysis.

3.6.1 Detailed Abundance Comparisons to Individual Cluster Stars

When comparing chemical abundances from different authors, it is important to keep in mind that many systematic uncertainties can arise due to choice of analysis meth-

ods. In particular, offsets can result from different line lists and line parameters, stellar atmospheres, line synthesis codes, methods for determining stellar parameters like T_{eff}, surface gravity, or microturbulence, and different solar reference abundance distributions, to name a few. This means that there is no well-defined, standard abundance scale, and that detailed abundances determined by different authors typically do not agree to better than ±0.1 dex (see discussions in Gratton et al., 2004; Kraft & Ivans, 2003). In that respect, it is only meaningful to either compare abundances determined using identical methods, or to compare a given analysis to the mean results from many different authors so that an idea of systematic uncertainties can be obtained. The latter was the approach used for evaluation of the MW training set cluster abundances in Paper I and Paper II, because stars in MW GCs have been well-studied by a variety of authors.

As mentioned previously in the text, there are very few detailed chemical abundance analyses available in the literature for individual stars in LMC clusters. We are able to compare abundances for most elements in the old and intermediate age clusters NGC 2005, NGC 2019, and NGC 1978, as well as limited abundance comparisons for the young cluster NGC 1866. In almost all of these cases, we are comparing our results to one reference set of abundances, so we primarily aim to evaluate general consistencies while keeping in mind the possibility of the systematic uncertainties described above.

NGC 2019 and NGC 2005

The first comprehensive study of the detailed chemical composition in old LMC cluster stars was presented in Johnson et al. (2006). This work included three RGB stars in NGC 2019 and three in NGC 2005. These clusters are particularly interesting targets, as the metallicities derived from CMDs and low resolution Ca T spectroscopy are significantly different, as discussed in § 3.6.2. Using high resolution spectroscopy, Johnson et al. (2006) found higher values for [Fe/H] in NGC 2019 and NGC 2005 than Olszewski et al. (1991) determined from low resolution spectroscopy. The [Fe/H] values we determine are also higher than the low resolution results, but we find that
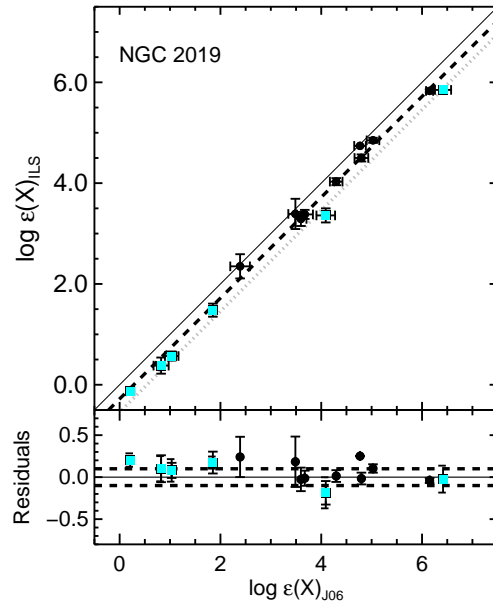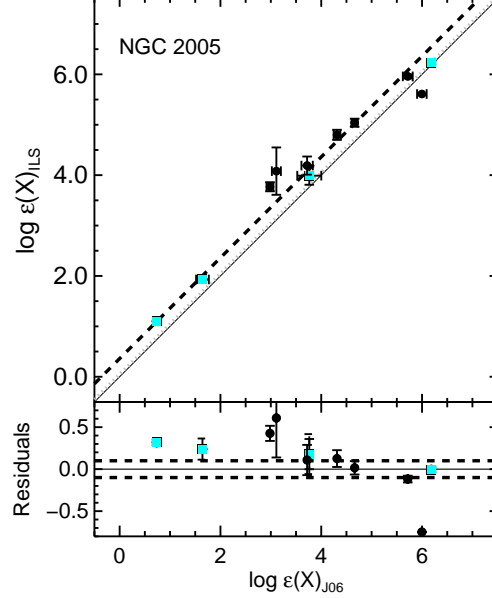
Figure 3.45. Comparison of abundances from IL and stellar analysis for NGC 2019. Stellar abundances are from Johnson et al. (2006). Black and cyan points show abundances for neutral and ionized species, respectively. Solid line shows the 1:1 line where points would lie if there were perfect agreement between IL and stellar results. Dashed line and dotted line show linear fits to neutral and ionized species respectively, with slopes constrained to one. Bottom panel shows the residuals for abundances from the linear fit, and dashed line corresponds to residuals of ± 0.1 dex.
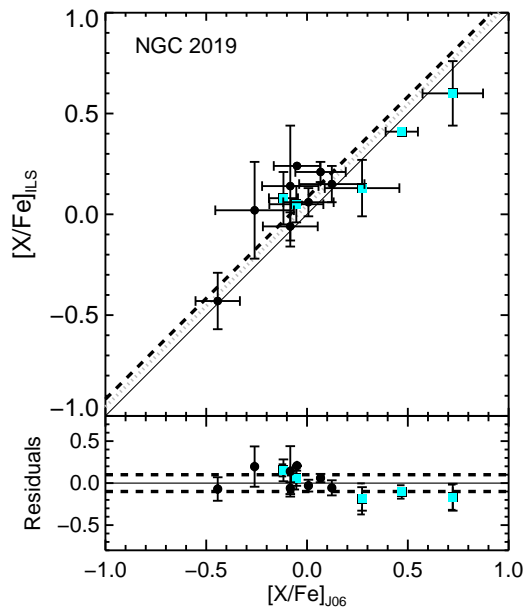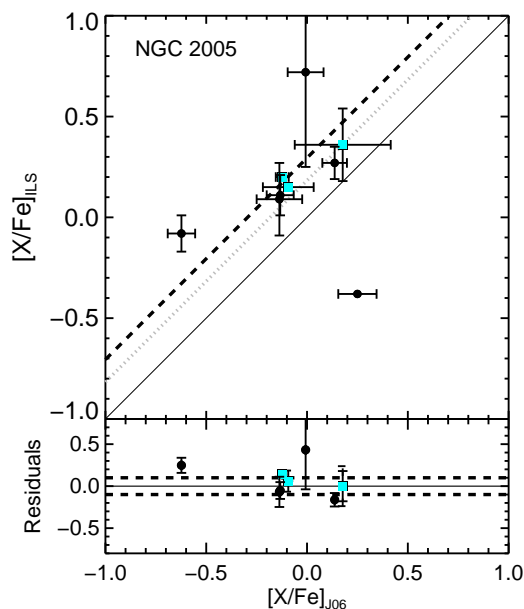

Figure 3.46. Comparison of abundance ratios from IL and stellar analysis for NGC 2019. Stellar abundances are from Johnson et al. (2006). Symbols and lines are the same as in Figure 3.45.

our abundance for NGC 2019 is lower than that of Johnson et al. (2006) by $\sim$0.3 dex, and higher for NGC 2005 by $\sim$0.25 dex.

The offsets between our [Fe/H] and that of Johnson et al. (2006) could be due to differences in analysis methods or line parameters. It is interesting to compare the similarities and differences for all the elements in common for our analysis and Johnson et al. (2006). In Figures 3.45 and 3.46 we show the comparison between the $\log\epsilon(X)$ abundance values and the [X/Fe] ratios for NGC 2019, and in Figures 3.47 and 3.48 for NGC 2005. In these comparisons, perfect agreement corresponds to the solid black 1:1 line in each panel. As in Paper II, we compare the results for all elements using a simple linear least-squares fit to $\log\epsilon(X)_{Lit}$ vs. $\log\epsilon(X)_{ILS}$ while constraining the slope of the fit to unity. In this way, the intercept of the fit corresponds to a systematic offset, and the dispersion around the best fit line can be evaluated. Because the data obtained for this training set has lower S/N than the MW, there are generally fewer clean spectral lines for each element, and the line-to-line scatter is larger than for MW GCs in Paper II. The uncertainties are shown by the vertical error bars, which corresponds to the standard error of the abundance of each element $(\sigma/\sqrt{N_{lines}-1})$. Note also that, the abundances from the literature in these cases correspond to 3 stars analyzed by one author for each cluster, which themselves have higher scatter than MW GC studies due to the difficulty in obtaining high S/N spectra in the LMC. The points in Figures 3.45 through 3.48 therefore have horizontal error bars corresponding to the star-to-star scatter in abundance for each species from Johnson et al. (2006).

From the dashed line in the top panel of Figure 3.45, we see that for NGC 2019 the neutral species are offset to lower abundances, and that the offset is roughly constant at -0.28 dex over the range in $\log\epsilon(X)$. For the ionized species, the offset is larger (-0.54 dex), with the highest difference for Ti II and Fe II. However, it is worth noting that Johnson et al. (2006) finds a $\sim$0.3 dex difference between Fe I and Fe II abundances, while we find better agreement between the two in our analysis of NGC 2019. In any case, the constant offsets imply that the overall abundance distribution pattern derived for NGC 2019 is very similar for the two analyses. This is clearer from
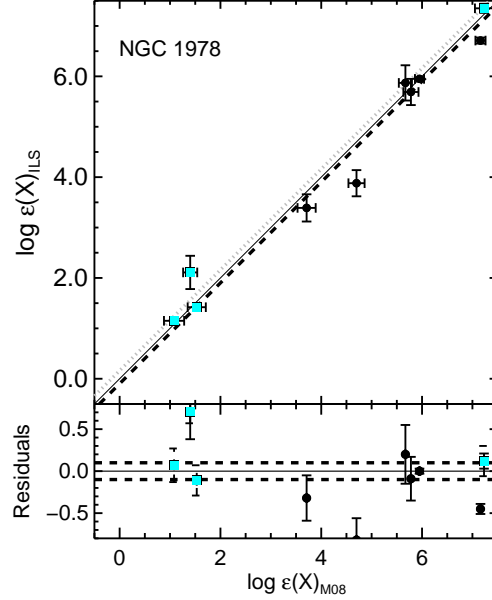
Figure 3.47. Comparison of abundances from IL and stellar analysis for NGC 2005. Stellar abundances are from Johnson et al. (2006). Symbols and lines are the same as in Figure 3.45.

Figure 3.46, where the [X/Fe] abundances are shown. This figure illustrates the virtue in comparing abundance ratios instead of raw abundances, because systematic offsets will cancel out. For NGC 2019, we find that all of the element ratios are consistent within the uncertainties to ≤0.1 dex, with the exception of [Si/Fe]. However, we note that the dispersion in Si between the 2 stars of Johnson et al. (2006) is large, and we only measure one Si I feature in our IL spectrum. The Si abundance in NGC 2019 is by no means well-determined. The formal offset for neutral species in [X/Fe] is +0.07 dex, while the offset for ionized species is +0.05 dex, which is smaller than the typical line-to-line scatter for NGC 2019.

Due to lower S/N ratio spectra for NGC 2005 relative to NGC 2019, we were only able to measure abundances for 9 elements other than Fe in the IL spectrum of NGC 2005. The comparison to the results for stars from Johnson et al. (2006) is therefore more limited for this cluster. Figure 3.47 shows a positive offset for the neutral species of +0.36 dex, while the ionized species have a small positive offset of +0.05 dex. The only element that doesn't follow this general behavior is Mg I, which is under-abundant in our analysis by ∼0.4 dex when compared to Johnson et al.

170

Figure 3.48. Comparison of abundance ratios from IL and stellar analysis for NGC 2005. Stellar abundances are from Johnson et al. (2006). Symbols and lines are the same as in Figure 3.45.

(2006). However, this is likely due to Mg depletion in the IL spectra as discussed in § 3.5.2. While Johnson et al. (2006) do not find evidence for star-to-star light element abundance variations for NGC 2005, variations cannot yet be ruled out due to the small sample size. If we exclude [Mg/Fe], we find that the [X/Fe] ratios for the two analyses presented in Figure 3.47 mostly agree to ≤0.15 dex, within the quoted uncertainties. The exceptions include $[Ti/Fe]_I$, for which we only measure two lines with high dispersion, and [Mn/Fe], which is elevated with respect to the MW [Mn/Fe] abundance pattern for most clusters in the training set (see § 3.5.3). The formal offset in [X/Fe] for NGC 2005 is +0.29 dex in neutral species and +0.18 in ionized species, but the larger abundance uncertainties in this case must be kept in mind.

NGC 1978

The intermediate age cluster NGC 1978 has been the subject of much recent work by Mucciarelli et al. (2008) and Ferraro et al. (2006), who presented the abundances of ∼20 different elements for a sample of 11 stars. We compare $\log\epsilon(X)$ and [X/Fe] in Figures 3.49 and 3.50 to the sample of Mucciarelli et al. (2008). Hill et al. (2000)
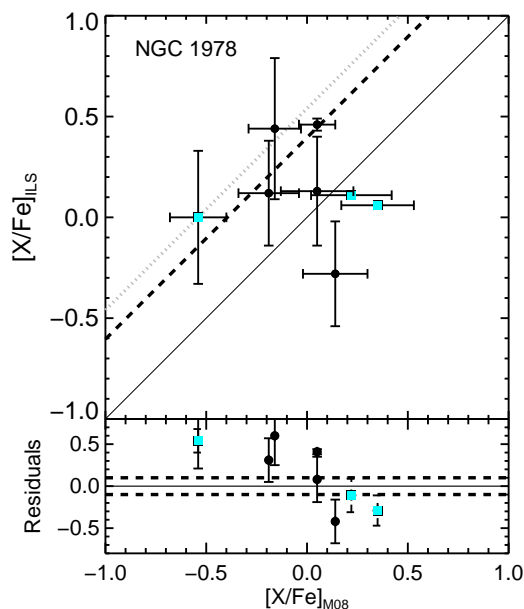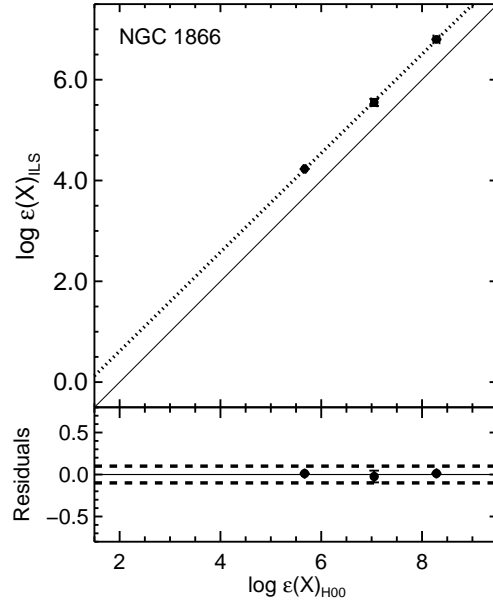
Figure 3.49. Comparison of abundances from IL and stellar analysis for NGC 1978. Stellar abundances are from Mucciarelli et al. (2008). Symbols and lines are the same as in Figure 3.45.

determined abundances for Fe, O and Al in 2 stars. Unfortunately, due to low S/N, we were not able to determine accurate abundances for O or Al,

We find the offset in $\log\epsilon(X)$ for neutral species to be -0.09 dex, and $+0.16$ for ionized species, although the dispersion is large $\sim$0.4. Interestingly, we find that the overall agreement is worse for the [X/Fe] ratios. The offset significantly increases for both species to $+0.40$ and $+0.54$ for neutral and ionized, respectively. However, in most cases, the error bars are large enough to be consistent with the 1:1 line on the $\sim$0.2 dex level. The reason that the offsets get worse in the [X/Fe] seems to be that we find pretty good agreement for most elements in $\log\epsilon(X)$, with the notable exceptions of Fe I and Fe II. While Mucciarelli et al. (2008) find [Fe/H]$=-0.4$, we find a more metal-poor value of [Fe/H]$=-0.74$ after allowing for sampling uncertainties. This is interesting because Hill et al. (2000) also find NGC 1978 to be significantly more metal-poor than Mucciarelli et al. (2008), with a mean of [Fe/H]$=-0.96 \pm 0.2$ from 2 stars. Mucciarelli et al. (2008) conclude that the difference in [Fe/H] from different analysis is mostly due to different methods for determining the stellar microturbulence values, which is a very extreme example of systematic error due to different analysis

Figure 3.50. Comparison of abundance ratios from IL and stellar analysis for NGC 1978. Stellar abundances are from Mucciarelli et al. (2008). Symbols and lines are the same as in Figure 3.45.

methods of different authors.

NGC 1866

The only detailed chemical abundance information for NGC 1866 from the analysis of individual stars using high resolution spectra is from Hill et al. (2000). These authors determined [Fe/H], [O/Fe] and [Al/Fe] for three stars. Using IL spectra, we were able to measure abundances for these 3 elements, as well as 17 additional elements that have never been measured before in NGC 1866.

In Figures 3.51 and 3.52 we show the abundance comparison for $\log\epsilon(X)$ and [X/Fe] to the stars of Hill et al. (2000). Figure 3.51 shows that the IL spectra abundances have a constant offset of $\sim +0.5$ from Hill et al. (2000), which means that the [X/Fe] ratios in Figure 3.52 for O and Al are consistent between the two analyses to <0.1 dex. Therefore, the main difference between the IL analysis and that of Hill et al. (2000) is the [Fe/H] measurement, where we have obtained [Fe/H]=+0.05±0.07 for NGC 1866 and Hill et al. (2000) measured [Fe/H]=−0.45 ± 0.06.

In the case of NGC 1866, it is interesting to investigate whether the difference in

Figure 3.51. Comparison of abundances from IL and stellar analysis for NGC 1866. Stellar abundances are from Hill et al. (2000). Symbols and lines are the same as in Figure 3.45.
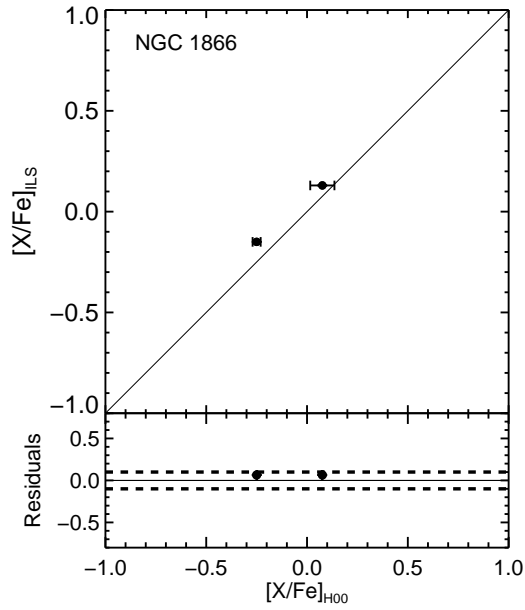
Figure 3.52. Comparison of abundance ratios from IL and stellar analysis for NGC 1866. Stellar abundances are from Hill et al. (2000). Symbols and lines are the same as in Figure 3.45.

174

[Fe/H] could be due to a systematic uncertainty in the IL analysis method itself at ages of ∼100 Myr. One possibility is that unavoidable inaccuracies for young ages in the isochrones used to construct the synthetic CMDs are affecting the derived [Fe/H]. For example, if the predictions for the core He-burning supergiants are systematically too blue, we would expect to derive a more metal-rich abundance. However, this does not seem likely because the [Fe/H] solution we derive is very stable, and we would expect that if the stellar population wasn't accurately represented that we would have a large Fe I σ and more significant dependence of [Fe/H] with wavelength and EP. We would also expect that the tests we performed with a wide range of CMD realizations to evaluate statistical variations would have shown some indication of a preference for CMDs with redder supergiants, but we found that the most self-consistent solutions were always at approximately solar [Fe/H]. We can also qualitatively evaluate the appropriateness of the best-fitting CMD realizations by comparing to the available CMD photometry. This is shown In Figure 3.53, where the average star CMD boxes for the best-fitting 100 Myr and 300 Myr solutions are shown in red and black, respectively. The gray points in Figure 3.53 correspond to the photometry of Testa et al. (1999), which have been reddening corrected using $E(B-V)$=0.06, and adjusted using a distance modulus of $(m - M)_o = 18.5$. We find that the CMDs with ages of 100 Myr and 300 Myr seem to bracket the stellar population of NGC 1866, including the supergiants at $M_V \sim -0.3$. Note that the assumed distance modulus in this case seems to favor an age closer to 100 Myr, which is what was found by Testa et al. (1999). An interesting feature of the NGC 1866 photometric CMD is a clump of intermediate age field RGB stars at $M_V \sim 0$, which, if included in the synthetic CMD could lower the derived [Fe/H]. However, we would expect that in the high surface brightness core of NGC 1866 that we observed, there would not be a significant population of field stars and they would not dominate the flux. Regardless, we can test to see the effect on the derived [Fe/H] solution of adding this field population to the best-fitting CMD. Note that the intermediate age field population should have an [Fe/H]∼ −0.5 (Carrera et al., 2008), similar to the [Fe/H] of NGC 1866 that Hill et al. (2000) derive. We find that adding a field RGB population to the 100 Myr
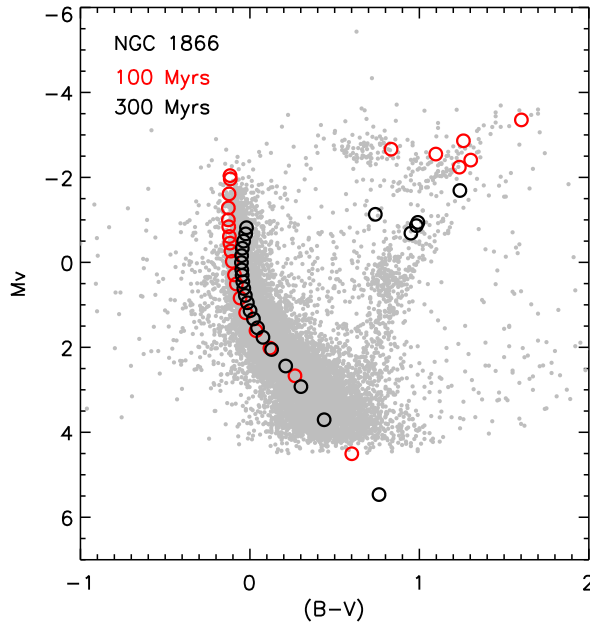
Figure 3.53. Comparison of photometric CMD of NGC 1866 to best-fitting synthetic CMDs from our analysis. Photometry is from Testa et al. (1999) and has been reddening corrected using $E(B-V)$=0.06 and converted into absolute magnitudes using $(m-M)_o = 18.5$. The best-fitting CMD realizations using a 100 Myr isochrone ([Fe/H]=0), and 300 Myr isochrone ([Fe/H]=0) are shown in red and black, respectively.

synthetic CMD can lower the derived [Fe/H], but only by $\sim$0.1 dex, which means that the derived [Fe/H] from IL is still more metal-rich than measured by Hill et al. (2000). The stability of the solution is also worse overall: the dependence of [Fe/H] on EP and wavelength is stronger. Thus, adjusting the synthetic CMD to account for field stars does not lead to a solution that is more consistent with the [Fe/H] for NGC 1866 that is derived by Hill et al. (2000).

A more troubling concern regarding our current results for young clusters, is that our analysis presently uses a version of MOOG that does not include atmospheric opacity due to electron scattering, which can be significant for hot stars. To estimate the impact of this effect, we have used the most recent version of MOOG (2008), which does include electron scattering opacity, to develop the IL spectral synthesis code. In this way we can estimate the offset due to different opacity calculations by comparing the observed spectrum of NGC 1866 with spectral synthesis of a [Fe/H]=0 cluster. In Figure 3.54 we show two regions of the NGC 1866 spectrum with several
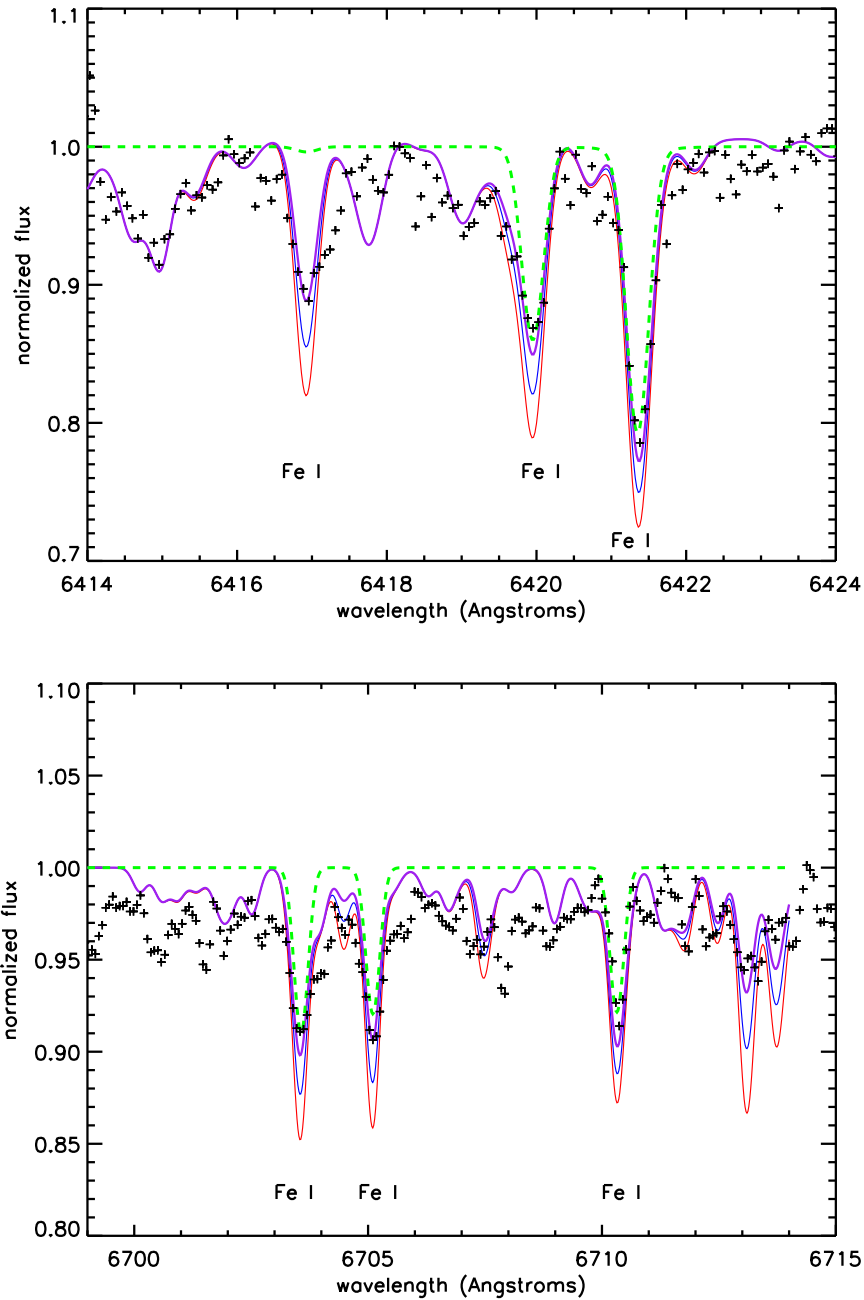
Figure 3.54. Comparison of IL spectra of NGC 1866 to synthesized IL spectra, which have electron scattering opacities included. Data for NGC 1866 are shown by black crosses. Synthesized spectra with an age 100 Myr, and [Fe/H]=+0.3, [Fe/H]=0.0, and [Fe/H]=−0.3, are shown by red, blue, and purple lines respectively. Dashed green line shows spectra with [Fe/H]=−0.3 and Fe transitions only, in order to evaluate the effect of line blending. Strong Fe I transitions are marked. An estimate of the appropriate abundance for NGC 1866 is [Fe/H]∼ −0.2.

Fe transitions. Including electron scattering opacity, a synthesis with [Fe/H]=−0.3 is generally a better match than a spectrum synthesized with [Fe/H]=0.0, which is what we derive with the old version of MOOG. Note that for reference we also show a synthesis with [Fe/H]=−0.3 and only Fe transitions in order to estimate the effect of line blending of other elements as well. We find that the difference due to blends is small, reasonably estimated by the line-to-line scatter we measure for the Fe EWs, and therefore cannot account for the difference between the [Fe/H]=0.0 and [Fe/H]=−0.3 synthesized spectra. Therefore, with the line blending taken into account, it seems possible that missing electron scattering opacity can account for a $\sim 0.2 - 0.3$ dex offset to more metal-rich abundances using the old version of MOOG.

A correction of −0.25 dex to the IL abundance for NGC 1866 would result in [Fe/H]= −0.2, and because the abundances of other elements generally scale with Fe, the [X/Fe] ratios should be reasonably well constrained. This [Fe/H] is still more metal-rich than the analysis of NGC 1866 stars by Hill et al. (2000), but it is possible that the remaining difference can be due to choice of stellar atmospheres or line lists. As discussed for NGC 1978, the results of Hill et al. (2000) appear to be systematically lower than the analysis of NGC 1978 stars by Mucciarelli et al. (2008) due to a systematic difference in analysis technique. Follow-up, detailed abundance analysis of stars in NGC 1866 using the same stellar abundance methods as employed in ILABUNDS is necessary to determine if a true systematic uncertainty for IL analysis of young clusters exists. We have collected high resolution spectra for 3 stars in NGC 1866 to address this question in the future.

3.6.2 Estimates of Cluster Properties from Photometry and Low Resolution Spectra

All of the LMC training set clusters have CMDs of variable depth and photometric quality available for reference in the literature. These CMDs have been used to constrain ages and estimate metallicities for the clusters, just as is done for clusters in the MW. In addition, metallicity estimates from low resolution Ca II triplet (Ca T) spectroscopy or line index methods exist for most of the clusters. In this section

we summarize the previous estimates for ages and metallicities of the training set clusters in the context of what we measure with high resolution abundance analysis.

NGC 2019. The precise metallicity we measure using high resolution IL spectra is [Fe/H]=-1.67 ± 0.03, along with an age of >7 Gyr. Olsen et al. (1998) also derive an age of >12 Gyr by comparison of an HST CMD to MW clusters and the location of the HB. Olsen et al. (1998) estimate [Fe/H]=-1.23 ± 0.15 from the HST CMD, which is significantly more metal-rich than what we find. Using low resolution Ca T spectroscopy of individual stars, Olszewski et al. (1991) estimate [Fe/H]=-1.8 ± 0.2, which is consistent with our result, while Grocholski et al. (2006) find a more metal-rich [Fe/H]=-1.31. We also note that Beasley et al. (2002b) find [Fe/H]=-1.43 ± 0.2 for NGC 2019 using low resolution IL spectra, which is consistent with our results given the large uncertainties in line index metallicity measurements.

NGC 2005. We measure [Fe/H]= -1.54 ± 0.04, with an age constraint of > 5 Gyr. Olsen et al. (1998) find an age of >12 Gyr for NGC 2005, similar to that of NGC 2019. They also find [Fe/H]=-1.35 ± 0.16 using the HST CMD, which is reasonably consistent with our result given their uncertainties. The metallicity estimate of Olszewski et al. (1991) from low resolution Ca T spectroscopy is more metal-poor than the CMD estimate, at [Fe/H]=-1.92 ± 0.2. The line index metallicity estimate for NGC 2005 is [Fe/H]=-1.45 ± 0.2, which is in good agreement with our measurement (Beasley et al., 2002b).

NGC 1916. With high resolution spectroscopy, we are able to constrain the age of NGC 1916 to >5 Gyr, and obtain a precise measurement of the metallicity of [Fe/H]=-1.54 ± 0.04. While an HST CMD for NGC 1916 exists in Olsen et al. (1998), no detailed analysis of cluster properties was performed due to differential reddening. However, Olsen et al. (1998) note there is a blue horizontal branch present in the CMD, indicating that NGC 1916 is old >10 Gyr. Olszewski et al. (1991) measured an abundance of [Fe/H]=-2.08 ± 0.2 using Ca T spectroscopy, which is more metal-poor than we find with high resolution. Beasley et al. (2002b) estimate [Fe/H]=-1.8 to -2.1 using various line indexes, which highlights the importance of high resolution abundances for GCs with moderate to low metallicities.

179

NGC 1718. We constrain the age of NGC 1718 to 1−2.5 Gyr, and find [Fe/H]= −0.64 ± 0.25. Kerber et al. (2007) use a HST CMD to derive an age of 2±0.15 Gyr, and [Fe/H]=−0.40 ± 0.10. Using Ca T spectroscopy, Grocholski et al. (2006) find [Fe/H]=−0.80, and Beasley et al. (2002b) find [Fe/H]= −0.98 to −1.12 using line indexes, which are both consistent with our result that NGC 1718 is a relatively metal-poor intermediate age cluster.

NGC 1978. Our result using high resolution IL spectra is [Fe/H]=−0.74 ± 0.07, with an age constraint of 1.5−2.5 Gyr. Mucciarelli et al. (2007) present a very deep HST CMD of NGC 1978, and derive a best fit age of 1.9 ± 0.1 Gyr, but with an assumption about the metallicity based on high resolution spectroscopy of individual stars. Using low resolution Ca T, Olszewski et al. (1991) determine [Fe/H]=−0.42 ± 0.2, which is consistent with our result within the uncertainties.

NGC 1866. Our measurement for NGC 1866, including a correction for missing opacity, is [Fe/H]=−0.2. Testa et al. (1999) find an age of 100−200 Myr for NGC 1866 from a deep, ground-based CMD, while from a HST CMD, Brocato et al. (2003) derive an age of 140−250 Myr depending on assumptions about binary fractions and convective overshooting. Our age estimate of 100−300 Myrs is consistent with this result, and also only slightly larger than the best constraint that can be made using deep HST photometry. Using Stromgren photometry, Hilker et al. (1995) derive a metallicity for NGC 1866 of [Fe/H]=−0.43±0.18, with the caveat that the calibration assumes that MW and LMC clusters have similar metallicities, which is not generally the case.

3.6.3   New Chemical Abundance Results for the LMC

In § 3.5, we presented the detailed chemical abundance results for 6 of the LMC training set GCs, and in this section we summarize the new results found in this work. Three of the clusters in our sample have little or no chemical abundance information available. We have measured the first detailed chemical abundances for 12 elements in the old cluster NGC 1916, for 11 elements in the intermediate age cluster NGC 1718, and for 17 elements in the young cluster NGC 1866. Our results for the intermediate

age clusters NGC 1718 and NGC 1978, point to a more metal-poor [Fe/H] for these clusters than the mean metallicity of [Fe/H]~ -0.4 found for many other clusters in this age range (Olszewski et al., 1991; Mucciarelli et al., 2008). Our result for the young cluster NGC 1866 is a more metal-rich abundance than recent estimates, and consistent with the mean metallicity of young OB-type LMC stars (Rolleston et al., 2002; Hunter et al., 2007).

With our sample of clusters, we are able to probe both a wide range in metallicity ($-1.5 <$[Fe/H]< -0.2) and age (100 Myr-12 Gyr) for the LMC for many elements, which can be used to model the chemical evolution history of the LMC in future work. We find that the old cluster NGC 1916 has α-enhancement comparable to that in MW GCs, which is higher than the α-enhancement found for NGC 2019. These clusters are both old and have a similar metallicity, so the spread in α-enhancement we find between them could mean that the ISM in the LMC was not well-mixed at the time these clusters formed. We find that the young cluster NGC 1866 has solar, or slightly super-solar, α-enhancement, which shows that the $[\alpha/\text{Fe}]$ in the LMC cluster population has evolved with time as one would expect from a simple model of chemical enrichment for a closed system.

We have also measured depleted Mg and enhanced Na in the IL spectra for the old clusters and intermediate age clusters in our training set. These results imply that these clusters have star-to-star abundance variations in the light elements that are sensitive to proton-capture nucleosynthesis. For two of these clusters, NGC 2019 and NGC 2005, star-to-star abundance variations were not found in the analysis of individual stars (Johnson et al., 2006), but this is likely because the sample of 3 stars analyzed in each cluster was too small. Our results show that high resolution IL spectra are useful as a tool to look for the presence of star-to-star abundance variations for resolved clusters for which it is difficult to observe a large number of individual stars. For the intermediate age cluster NGC 1978, we also find evidence for star-to-star abundance variations while Mucciarelli et al. (2008) did not find such evidence in a sample of 11 stars. It is possible that the effect we see in the IL is due to AGB stars with peculiar chemical composition dominating the EWs; we note that

Lederer et al. (2009) find that some AGB stars in NGC 1978 show a complex dredge-up pattern from evolution on the RGB and AGB. For the young cluster NGC 1866, we do not see evidence for star-to-star abundance variations. This result supports the theory that star-to-star abundance variations in clusters are due to pollution by AGB stars (e.g. Ventura & D'Antona, 2008). A larger sample of young and intermediate age clusters would be very interesting to study the occurence of star-to-star abundance variations further.

We also find that abundances of the Fe-peak element Mn are systematically higher at a given [Fe/H] in the LMC clusters than in MW GCs, with the exception of the young cluster NGC 1866. This is especially interesting because there have been no other measurements of Mn abundances for old or intermediate age LMC clusters with [Fe/H]> -1.2. For [Fe/H]< -1.2, the only Mn abundance measurements are for the GC stars in (Johnson et al., 2006), which overlap with our results. The behavior of [Mn/Fe] in the Sagittarius Dwarf Galaxy has led to the theory that Mn production in supernovae is dependent on the metallicity of the progenitor star (McWilliam et al., 2003). More sophisticated models for Mn production and evolution must be also be able to reproduce the [Mn/Fe] we find in LMC clusters.

Finally, we have measured the first abundances for the neutron capture elements Ba, Zr, Y, Eu, La, and Sm for the young cluster NGC 1866. We find all of these neutron capture elements to be significantly enhanced, even with a large uncertainty due to the assumed age of NGC 1866. While enhanced neutron capture element abundances have been found in young LMC stars for many years (Russell & Bessell, 1989; Luck & Lambert, 1992; Spite et al., 1993), this is the first indication from an identical analysis of clusters spanning a wide age range that the neutron-capture abundance ratios are significantly higher in young LMC stars than in the intermediate or old LMC populations.

3.7 Summary

In summary, we have analyzed a training set of clusters in the LMC using the high resolution IL abundance analysis method originally developed and tested on MW

clusters in Paper I and Paper II. In this work we have tested the method on clusters with ages <10 Gyr for the first time, and developed a strategy to accomodate the effect of incomplete statistical sampling of CMD stellar populations. While this strategy is motivated by incomplete sampling in the training set clusters in particular, for which we have only observed a fraction of the stellar population due to the large spatial extent of the clusters on the sky, it is applicable without any a priori knowledge of a cluster's resolved stellar populations and can also be applied to distant extragalactic clusters. This is primarily important for low luminosity and young clusters, as their integrated properties are more sensitive to statistical fluctuations in the number of stars in short-lived, cool, luminous stages of stellar evolution.

Our IL abundance analysis of clusters with ages of $1-5$ Gyr and <1 Gyr has demonstrated that clusters of these ages can be distinguished from old clusters using constraints derived from the Fe lines in the high resolution spectra alone. For intermediate age clusters we find that we can constrain ages to a ≤ 2.5 Gyr range, but that this range can result in a larger error on the derived abundances than typically found for old clusters. For the two intermediate age clusters in the training set we have found abundance solutions with higher scatter and less stability in [Fe/H] than generally found in the analysis of old clusters. This is likely due to low S/N data and poor statistical sampling, but it is possible that it is a systematic problem in the synthetic CMD populations at these ages. For the young clusters in the training set we have found that we can constrain ages to a 200 Myr range for a well sampled cluster with high S/N spectra. Using NGC 1866, we have found evidence that IL abundance analyses of young clusters are sensitive to the opacities used in the spectral synthesis, and that precise abundance measurements for young clusters should include opacity due to electron scattering. This software is available in MOOG (2008) and being implemented in future analysis.

The IL abundance analysis of > 10 Gyr LMC clusters has shown that the number of element abundances that can be measured is fewer and the line-to-line scatter is larger than that obtained for MW clusters when the S/N of the data is poor. The analysis of NGC 1916 has shown that ages and abundances for many elements can be

obtained for clusters with significant differential reddening, and that the precision of these measurements is the same as for clusters with little or no differential reddening.

We present detailed abundances for ∼20 individual elements in the LMC clusters, many of which are the first such measurements of these elements in some clusters using any high resolution abundance analysis method. Like other authors, we find that the α-element abundances are consistent with being lower at a given [Fe/H] than stars in the MW, although the scatter for Ti in particular, is high. We also see evidence in the old and intermediate age cluster populations for the light element variations observed in MW and some LMC clusters, which is consistent with pollution by intermediate mass AGB stars. We find Fe-peak element abundances are generally similar to MW Fe-peak abundances. We find most neutron capture elements to have super-solar [X/Fe] ratios. We cannot place tight constraints on similarities or differences in these abundance ratios between MW and LMC clusters from the current data.

In conclusion, we have demonstrated the utility of the new high resolution IL spectra abundance analysis method to obtain tight age, abundance, and stellar population constraints on clusters spanning a large range in age from ∼100 Myrs to >10 Gyrs. This method makes it possible to study the chemical enrichment history of distant galaxies in unprecedented detail by using stellar clusters of varying ages.

CHAPTER 4

Conclusions

In this thesis, we have presented two main results. In Chapter 2, we presented the first accurate detailed chemical abundances of globular clusters (GCs) in M31. This is the first application of a new integrated-light (IL) abundance analysis method using high resolution (R>20,000) spectra. This method, developed for old (∼12 Gyr) GCs, has allowed us to obtain abundances for 14 different elements in M31, including α, Fe-peak, neutron capture and light elements. The abundances in M31 of most of these elements have not been determined using any other technique because individual stars at the distance of M31 (∼780 kpc) are too faint for high resolution abundance analysis.

The first set of 5 M31 GCs presented in this thesis are part of an ongoing program. These 5 GCs show a chemical abundance pattern very similar to GCs in the Milky Way (MW), and provide evidence that M31's early chemical enrichment was dominated by Type II supernovae. We find that the α-elements Ca, Ti and Si are enriched to [α/Fe]∼ +0.4 dex, which is nearly identical to what we observe for GCs in the MW. Our results therefore do not support the conclusions of previous work using low resolution spectra that M31 GCs have systematically lower [α/Fe] than MW GCs by ∼ 0.1 − 0.2 dex (Puzia et al., 2005; Beasley et al., 2005). We believe that the underestimation of [α/Fe] using low resolution spectra is from a combination of degeneracies in line index strengths at low [Fe/H], and unpredictability of Mg line strengths in GCs, which we find show evidence of inter- and intra-cluster abundance variations. This work demonstrates that it is particularly crucial in the case of unresolved GCs to have abundance constraints from high resolution spectroscopy, especially in the low metallicity regime. Our IL abundance analysis can also provide

independent constraints on the $E(B - V)$ toward the M31 GCs, and high precision internal velocity dispersions for the GCs.

The second result presented in this thesis is a refinement of our IL abundance analysis method that is developed using a training set of clusters in the Large Magellanic Cloud (LMC). This training set was chosen to include clusters with a wide range of ages (10 Myr -12 Gyr), and is an important demonstration that the IL analysis method can be applied to clusters with ages of <12 Gyr. In doing so, we have developed a strategy for evaluating the effect of incomplete sampling of the training set stellar populations. To do this, we have presented methods to accommodate for statistical fluctuations in stellar populations due to luminous stars in rapid phases of stellar evolution. We find that when allowing for statistical variations in the synthetic stellar populations we use for our IL abundance analysis, suitable stellar populations for each cluster can be identified using the same strategies we have previously used to constrain the age of clusters; i.e. by requiring that the Fe I abundance solution for an appopriate stellar population be stable and self-consistent. The strategy we have developed using the LMC training set requires no a priori knowledge of a clusters' properties except for readily observable quantities such as the visual magnitude. While incomplete sampling is generally not an issue for massive, distant clusters, the strategy we have developed can be easily generalized. For extragalactic clusters, we can expect that this strategy will be most important for analysis of less massive or young cluster populations (e.g. Brocato et al., 1999).

Our analysis of the LMC training set clusters shows that clusters of different ages can be successfully distinguished by using the the stability of the Fe line solution. For clusters with ages of ~2 Gyr, we find that we can constrain the age using the IL analysis method to a range of $1-2$ Gyr, and that it may be possible to obtain tighter constraints with high quality data of well-sampled clusters. We find that the resulting uncertainties in the derived [Fe/H] (0.1-0.25 dex) are similar to or only slightly greater than the uncertainties we derive for old clusters (<0.1 dex). The greater uncertainties are due to rapidly changing stellar populations at these ages, which can have a significant impact on the [Fe/H] solution, and the uncertainties can

186

be determined from the empirical stability of the Fe line solution. We find that for clusters with ages <1 Gyr, we are able to constrain the age from the IL abundance analysis to a range of 100-300 Myr. We find evidence that the IL abundances of the youngest clusters are sensitive to the inclusion of electron scattering opacities in the spectral synthesis, which we will employ for future abundance work and in our final analysis of these LMC clusters (Colucci et al., 2010, in preparation).

We also present detailed abundances for $\sim$20 individual elements in the LMC training set clusters, many of which are the first detailed abundances ever published for some of these clusters. We have briefly summarized the results and discuss consistencies or inconsistencies of the IL abundances with abundances measured from individual stars in the LMC. Like other authors, we find that [α/Fe] in the old population of LMC training set clusters shows a larger spread between clusters, and has a lower mean when compared to both MW and M31 GCs of similar ages and metallicities. The difference in [α/Fe] between the large galaxies, the MW and M31, and the dwarf galaxy, the LMC are a reflection of the very different star formation and evolutionary histories of galaxies of different masses. The MW and M31 show evidence of a prolonged period of high star formation rate and homogeneous ISM. On the other hand, the LMC shows evidence for a more complex history; possibly a lower star formation rate, a bursty history, inhomogeneous ISM mixing, or sensitivity to gas inflow/outflow.

Our analysis of the IL spectra of extragalactic GCs demonstrates that many quantitative constraints on the GC stellar populations and on the chemical and formation history of galaxies in general can be made with this new IL abundance analysis technique. We have presented many new detailed chemical abundances for GCs in M31 and the LMC, but much is also left for future work. We have an ongoing project to collect a statistical sample of high resolution, IL spectra of GCs in M31, so that we can expand the number of clusters with detailed abundance measurements as well as the number of individual elements measured to include more neutron capture and light elements. With a statistical sample of clusters, we can begin to discuss the evolution of the M31 halo in a larger context, and make detailed comparisons to pub-

lished and upcoming works on the photometric and medium resolution spectroscopic measurements of individual stars in M31 (e.g. Kalirai et al., 2006; Chapman et al., 2006).

In the LMC, we have measured a variety of different elements for clusters spanning a wide range in age. Future work includes a more comprehensive analysis of the chemical evolution and age-metallicity relation of the LMC using constraints from the IL analysis of clusters presented in this thesis, in combination with abundances for individual field and cluster stars in the literature (e.g. Johnson et al., 2006; Pompéia et al., 2008; Hunter et al., 2007). We have also collected a small sample of high resolution spectra of stars in the young cluster NGC 1866, with the goals of comparing abundances measured for the individual stars to the IL abundances presented here, as well as demonstrating the power of analyzing young clusters with IL spectra.

In conclusion, the LMC and M31 are only the first of many galaxies in the Local Group that can be probed with this technique. Detailed chemical abundances of GCs hold the promise to provide unprecedented constraints on galaxy formation and evolution beyond the Milky Way.

BIBLIOGRAPHY

Andrievsky, S. M., Spite, M., Korotin, S. A., Spite, F., Bonifacio, P., Cayrel, R., Hill, V., & François, P. 2008, A&A, 481, 481

Ashman, K. M. & Zepf, S. E. 1992, ApJ, 384, 50

Asplund, M., Grevesse, N., & Sauval, A. J. 2005, in Astronomical Society of the Pacific Conference Series, Vol. 336, Cosmic Abundances as Records of Stellar Evolution and Nucleosynthesis, ed. T. G. Barnes, III & F. N. Bash, 25–+

Barmby, P., Holland, S., & Huchra, J. P. 2002, AJ, 123, 1937

Barmby, P., Huchra, J. P., Brodie, J. P., Forbes, D. A., Schroder, L. L., & Grillmair, C. J. 2000, AJ, 119, 727

Barmby, P., McLaughlin, D. E., Harris, W. E., Harris, G. L. H., & Forbes, D. A. 2007, AJ, 133, 2764

Baumgardt, H. & Makino, J. 2003, MNRAS, 340, 227

Baumueller, D. & Gehren, T. 1997, A&A, 325, 1088

Beasley, M. A., Baugh, C. M., Forbes, D. A., Sharples, R. M., & Frenk, C. S. 2002a, MNRAS, 333, 383

Beasley, M. A., Brodie, J. P., Strader, J., Forbes, D. A., Proctor, R. N., Barmby, P., & Huchra, J. P. 2004, AJ, 128, 1623

Beasley, M. A., Brodie, J. P., Strader, J., Forbes, D. A., Proctor, R. N., Barmby, P., & Huchra, J. P. 2005, AJ, 129, 1412

Beasley, M. A., Hoyle, F., & Sharples, R. M. 2002b, MNRAS, 336, 168

Bensby, T., Feltzing, S., Lundström, I., & Ilyin, I. 2005, A&A, 433, 185

Bergemann, M. 2008, Physica Scripta Volume T, 133, 014013

Bernstein, R., Shectman, S. A., Gunnels, S. M., Mochnacki, S., & Athey, A. E. 2003, in Society of Photo-Optical Instrumentation Engineers (SPIE) Conference Series, Vol. 4841, Society of Photo-Optical Instrumentation Engineers (SPIE) Conference Series, ed. M. Iye & A. F. M. Moorwood, 1694–1704

Bernstein, R. A. & McWilliam, A. 2002, in IAU Symposium, Vol. 207, Extragalactic Star Clusters, ed. D. Geisler, E. K. Grebel, & D. Minniti, 739–+

Bernstein, R. A. & McWilliam, A. 2005, in Resolved Stellar Populations, ed. D. Valls-Gabaud & M. Chavez, Astronomical Society of the Pacific Conference Series

Bica, E., Claria, J. J., Dottori, H., Santos, J. F. C., & Piatti, A. E. 1996, ApJS, 102, 57

Brocato, E. & Castellani, V. 1993, ApJ, 410, 99

Brocato, E., Castellani, V., Di Carlo, E., Raimondo, G., & Walker, A. R. 2003, AJ, 125, 3111

Brocato, E., Castellani, V., Poli, F. M., & Raimondo, G. 2000, A&AS, 146, 91

Brocato, E., Castellani, V., Raimondo, G., & Romaniello, M. 1999, A&AS, 136, 65

Brodie, J. P. & Strader, J. 2006, ARA&A, 44, 193

Bruzual, G. & Charlot, S. 2003, MNRAS, 344, 1000

Burstein, D., Faber, S. M., Gaskell, C. M., & Krumm, N. 1984, ApJ, 287, 586

Busso, M., Gallino, R., & Wasserburg, G. J. 1999, ARA&A, 37, 239

Cameron, S., Bernstein, R. A., Colucci, J. E., & Mc William, A. 2010, in preparation

Cameron, S. A. 2009, PhD thesis, University of Michigan, Ann Arbor

Carrera, R., Gallart, C., Hardy, E., Aparicio, A., & Zinn, R. 2008, AJ, 135, 836

Carretta, E. 2006, AJ, 131, 1766

Carretta, E., Gratton, R. G., Bragaglia, A., Bonifacio, P., & Pasquini, L. 2004, A&A, 416, 925

Castelli, F. & Kurucz, R. L. 2004, ArXiv Astrophysics e-prints

Cescutti, G., Matteucci, F., Lanfranchi, G. A., & McWilliam, A. 2008, A&A, 491, 401

Chapman, S. C., Ibata, R., Lewis, G. F., Ferguson, A. M. N., Irwin, M., McConnachie, A., & Tanvir, N. 2006, ApJ, 653, 255

Chiosi, C., Bertelli, G., & Bressan, A. 1992, ARA&A, 30, 235

Cioni, M., Girardi, L., Marigo, P., & Habing, H. J. 2006, A&A, 448, 77

Cohen, J. G. 1978, ApJ, 223, 487

Cohen, J. G. 2004, AJ, 127, 1545

Cohen, J. G., Gratton, R. G., Behr, B. B., & Carretta, E. 1999, ApJ, 523, 739

Cole, A. A., Smecker-Hane, T. A., & Gallagher, J. S. 2000, AJ, 120, 1808

Colucci, J. E., Bernstein, R. A., Cameron, S., & Mc William, A. 2010, in preparation

Colucci, J. E., Bernstein, R. A., Cameron, S., Mc William, A., & Cohen, J. G. 2009, ApJ, 704, 385

Cordier, D., Pietrinferni, A., Cassisi, S., & Salaris, M. 2007, AJ, 133, 468

Cote, P., Marzke, R. O., & West, M. J. 1998, ApJ, 501, 554

de Freitas Pacheco, J. A. & Barbuy, B. 1995, A&A, 302, 718

Denisenkov, P. A. & Denisenkova, S. N. 1990, Soviet Astronomy Letters, 16, 275

Denissenkov, P. A., Da Costa, G. S., Norris, J. E., & Weiss, A. 1998, A&A, 333, 926

Dinescu, D. I., Majewski, S. R., Girard, T. M., & Cudworth, K. M. 2000, AJ, 120, 1892

Dirsch, B., Richtler, T., Gieren, W. P., & Hilker, M. 2000, A&A, 360, 133

Djorgovski, S. G., Gal, R. R., McCarthy, J. K., Cohen, J. G., de Carvalho, R. R., Meylan, G., Bendinelli, O., & Parmeggiani, G. 1997, ApJ, 474, L19+

Dubath, P. & Grillmair, C. J. 1997, A&A, 321, 379

Eggen, O. J., Lynden-Bell, D., & Sandage, A. R. 1962, ApJ, 136, 748

Elson, R. A. W. 1991, ApJS, 76, 185

Elson, R. A. W. & Freeman, K. C. 1985, ApJ, 288, 521

Faber, S. M., Friel, E. D., Burstein, D., & Gaskell, C. M. 1985, ApJS, 57, 711

Faber, S. M. & Jackson, R. E. 1976, ApJ, 204, 668

Fagiolini, M., Raimondo, G., & Degl'Innocenti, S. 2007, A&A, 462, 107

Fan, Z., Ma, J., de Grijs, R., & Zhou, X. 2008, MNRAS, 385, 1973

Fenner, Y., Campbell, S., Karakas, A. I., Lattanzio, J. C., & Gibson, B. K. 2004, MNRAS, 353, 789

Ferguson, J. W., Alexander, D. R., Allard, F., Barman, T., Bodnarik, J. G., Hauschildt, P. H., Heffner-Wong, A., & Tamanai, A. 2005, ApJ, 623, 585

Ferraro, F. R., Mucciarelli, A., Carretta, E., & Origlia, L. 2006, ApJ, 645, L33

Fischer, P., Welch, D. L., & Mateo, M. 1992, AJ, 104, 1086

Forbes, D. A., Brodie, J. P., & Grillmair, C. J. 1997, AJ, 113, 1652

Freeman, K. & Bland-Hawthorn, J. 2002, ARA&A, 40, 487

Fulbright, J. P., McWilliam, A., & Rich, R. M. 2006, ApJ, 636, 821

Gallart, C., Zoccali, M., & Aparicio, A. 2005, ARA&A, 43, 387

Galleti, S., Federici, L., Bellazzini, M., Fusi Pecci, F., & Macrina, S. 2004, A&A, 416, 917

Geha, M. C., et al. 1998, AJ, 115, 1045

Gehren, T., Shi, J. R., Zhang, H. W., Zhao, G., & Korn, A. J. 2006, A&A, 451, 1065

Geisler, D., Smith, V. V., Wallerstein, G., Gonzalez, G., & Charbonnel, C. 2005, AJ, 129, 1428

Geisler, D., Wallerstein, G., Smith, V. V., & Casetti-Dinescu, D. I. 2007, PASP, 119, 939

Girardi, L., Bressan, A., Bertelli, G., & Chiosi, C. 2000, A&AS, 141, 371

Gnedin, O. Y. & Prieto, J. L. 2009, Formation of Globular Clusters in Hierarchical Cosmology: ART and Science, ed. Richtler, T. & Larsen, S., 323–+

Gratton, R., Sneden, C., & Carretta, E. 2004, ARA&A, 42, 385

Gratton, R. G. 1989, A&A, 208, 171

Gratton, R. G., et al. 2001, A&A, 369, 87

Grocholski, A. J., Cole, A. A., Sarajedini, A., Geisler, D., & Smith, V. V. 2006, AJ, 132, 1630

Harris, W. E. 1991, ARA&A, 29, 543

Harris, W. E. 1996, AJ, 112, 1487

Hilker, M., Richtler, T., & Gieren, W. 1995, A&A, 294, 648

Hill, V., Andrievsky, S., & Spite, M. 1995, A&A, 293, 347

Hill, V., François, P., Spite, M., Primas, F., & Spite, F. 2000, A&A, 364, L19

Holland, S. 1998, AJ, 115, 1916

Huchra, J. P., Brodie, J. P., & Kent, S. M. 1991, ApJ, 370, 495

Hunter, I., Dufton, P. L., Smartt, S. J., Ryans, R. S. I., Evans, C. J., Lennon, D. J., Trundle, C., Hubeny, I., & Lanz, T. 2007, A&A, 466, 277

Huxor, A. P., Tanvir, N. R., Irwin, M. J., Ibata, R., Collett, J. L., Ferguson, A. M. N., Bridges, T., & Lewis, G. F. 2005, MNRAS, 360, 1007

Ivans, I. I., Kraft, R. P., Sneden, C., Smith, G. H., Rich, R. M., & Shetrone, M. 2001, AJ, 122, 1438

Ivans, I. I., Sneden, C., Kraft, R. P., Suntzeff, N. B., Smith, V. V., Langer, G. E., & Fulbright, J. P. 1999, AJ, 118, 1273

Iwamoto, K., Brachwitz, F., Nomoto, K., Kishimoto, N., Umeda, H., Hix, W. R., & Thielemann, F.-K. 1999, ApJS, 125, 439

Jasniewicz, G. & Thevenin, F. 1994, A&A, 282, 717

Johnson, J. A., Ivans, I. I., & Stetson, P. B. 2006, ApJ, 640, 801

Kalirai, J. S., Gilbert, K. M., Guhathakurta, P., Majewski, S. R., Ostheimer, J. C., Rich, R. M., Cooper, M. C., Reitzel, D. B., & Patterson, R. J. 2006, ApJ, 648, 389

Kerber, L. O., Santiago, B. X., & Brocato, E. 2007, A&A, 462, 139

Kirby, E. N., Guhathakurta, P., Bolte, M., Sneden, C., & Geha, M. C. 2009, ApJ, 705, 328

Kirby, E. N., Guhathakurta, P., & Sneden, C. 2008, ApJ, 682, 1217

Kraft, R. P. & Ivans, I. I. 2003, PASP, 115, 143

Kraft, R. P., Sneden, C., Langer, G. E., Shetrone, M. D., & Bolte, M. 1995, AJ, 109, 2586

Kroupa, P. 2001, MNRAS, 322, 231

Kroupa, P. 2002, Science, 295, 82

Kumar, B., Sagar, R., & Melnick, J. 2008, MNRAS, 386, 1380

Lederer, M. T., Lebzelter, T., Cristallo, S., Straniero, O., Hinkle, K. H., & Aringer, B. 2009, A&A, 502, 913

Lee, H.-c. & Worthey, G. 2005, ApJS, 160, 176

Lee, J.-W. & Carney, B. W. 2002, AJ, 124, 1511

Lee, J.-W., Carney, B. W., & Habgood, M. J. 2005, AJ, 129, 251

Lee, Y.-W., Demarque, P., & Zinn, R. 1994, ApJ, 423, 248

Letarte, B., Hill, V., Jablonka, P., Tolstoy, E., François, P., & Meylan, G. 2006, A&A, 453, 547

Luck, R. E. & Lambert, D. L. 1992, ApJS, 79, 303

Mackey, A. D. & Gilmore, G. F. 2003, MNRAS, 338, 85

Mackey, A. D., Huxor, A., Ferguson, A. M. N., Tanvir, N. R., Irwin, M., Ibata, R., Bridges, T., Johnson, R. A., & Lewis, G. 2006, ApJ, 653, L105

Mackey, A. D., Huxor, A., Ferguson, A. M. N., Tanvir, N. R., Irwin, M., Ibata, R., Bridges, T., Johnson, R. A., & Lewis, G. 2007, ApJ, 655, L85

Maraston, C., Greggio, L., Renzini, A., Ortolani, S., Saglia, R. P., Puzia, T. H., & Kissler-Patig, M. 2003, A&A, 400, 823

Martin, N. F., Ibata, R. A., Irwin, M. J., Chapman, S., Lewis, G. F., Ferguson, A. M. N., Tanvir, N., & McConnachie, A. W. 2006, MNRAS, 371, 1983

McLaughlin, D. E. & van der Marel, R. P. 2005, ApJS, 161, 304

McWilliam, A. 1997, ARA&A, 35, 503

McWilliam, A. 1998, AJ, 115, 1640

McWilliam, A. & Bernstein, R. A. 2008, ApJ, 684, 326

McWilliam, A., Preston, G. W., Sneden, C., & Searle, L. 1995a, AJ, 109, 2757

McWilliam, A., Preston, G. W., Sneden, C., & Shectman, S. 1995b, AJ, 109, 2736

McWilliam, A. & Rich, R. M. 1994, ApJS, 91, 749

McWilliam, A., Rich, R. M., & Smecker-Hane, T. A. 2003, ApJ, 592, L21

Meléndez, J. & Barbuy, B. 2009, A&A, 497, 611

Moehler, S. 2001, PASP, 113, 1162

Morrison, H. L., Harding, P., Perrett, K., & Hurley-Keller, D. 2004, ApJ, 603, 87

Mucciarelli, A., Carretta, E., Origlia, L., & Ferraro, F. R. 2008, AJ, 136, 375

Mucciarelli, A., Ferraro, F. R., Origlia, L., & Fusi Pecci, F. 2007, AJ, 133, 2053

Mucciarelli, A., Origlia, L., Ferraro, F. R., & Pancino, E. 2009, ApJ, 695, L134

Olsen, K. A. G., Hodge, P. W., Mateo, M., Olszewski, E. W., Schommer, R. A., Suntzeff, N. B., & Walker, A. R. 1998, MNRAS, 300, 665

Olszewski, E. W., Schommer, R. A., Suntzeff, N. B., & Harris, H. C. 1991, AJ, 101, 515

Olszewski, E. W., Suntzeff, N. B., & Mateo, M. 1996, ARA&A, 34, 511

Percival, S. M., Salaris, M., Cassisi, S., & Pietrinferni, A. 2009, ApJ, 690, 427

Perrett, K. M., Bridges, T. J., Hanes, D. A., Irwin, M. J., Brodie, J. P., Carter, D., Huchra, J. P., & Watson, F. G. 2002, AJ, 123, 2490

Pessev, P. M., Goudfrooij, P., Puzia, T. H., & Chandar, R. 2008, MNRAS, 385, 1535

Peterson, R. 1989, in Dynamics of Dense Stellar Systems, ed. D. Merritt, 161–166

Pietrinferni, A., Cassisi, S., Salaris, M., & Castelli, F. 2004, ApJ, 612, 168

Pietrinferni, A., Cassisi, S., Salaris, M., & Castelli, F. 2006, ApJ, 642, 797

Piotto, G., et al. 2002, A&A, 391, 945

Pompéia, L., Hill, V., Spite, M., Cole, A., Primas, F., Romaniello, M., Pasquini, L., Cioni, M., & Smecker Hane, T. 2008, A&A, 480, 379

Pritzl, B. J., Venn, K. A., & Irwin, M. 2005, AJ, 130, 2140

Pryor, C. & Meylan, G. 1993, in Astronomical Society of the Pacific Conference Series, Vol. 50, Structure and Dynamics of Globular Clusters, ed. S. G. Djorgovski & G. Meylan, 357–+

Puzia, T. H., Perrett, K. M., & Bridges, T. J. 2005, A&A, 434, 909

Puzia, T. H., Saglia, R. P., Kissler-Patig, M., Maraston, C., Greggio, L., Renzini, A., & Ortolani, S. 2002, A&A, 395, 45

Ramírez, S. V. & Cohen, J. G. 2002, AJ, 123, 3277

Recio-Blanco, A., Aparicio, A., Piotto, G., de Angeli, F., & Djorgovski, S. G. 2006, A&A, 452, 875

Rich, R. M., Corsi, C. E., Cacciari, C., Federici, L., Fusi Pecci, F., Djorgovski, S. G., & Freedman, W. L. 2005, AJ, 129, 2670

Rolleston, W. R. J., Trundle, C., & Dufton, P. L. 2002, A&A, 396, 53

Romanowsky, A. J., Strader, J., Spitler, L. R., Johnson, R., Brodie, J. P., Forbes, D. A., & Ponman, T. 2009, AJ, 137, 4956

Russell, S. C. & Bessell, M. S. 1989, ApJS, 70, 865

Sarajedini, A., et al. 2007, AJ, 133, 1658

Schiavon, R. P. 2007, ApJS, 171, 146

Schiavon, R. P., Rose, J. A., Courteau, S., & MacArthur, L. A. 2004, ApJ, 608, L33

Schlegel, D. J., Finkbeiner, D. P., & Davis, M. 1998, ApJ, 500, 525

Schweizer, F. 1987, in Nearly Normal Galaxies. From the Planck Time to the Present, ed. S. M. Faber, 18–25

Schweizer, F. & Seitzer, P. 1998, AJ, 116, 2206

Searle, L. & Zinn, R. 1978, ApJ, 225, 357

Shetrone, M., Venn, K. A., Tolstoy, E., Primas, F., Hill, V., & Kaufer, A. 2003, AJ, 125, 684

Shetrone, M. D., Côté, P., & Sargent, W. L. W. 2001, ApJ, 548, 592

Shetrone, M. D. & Keane, M. J. 2000, AJ, 119, 840

Smecker-Hane, T. A. & Wyse, R. F. G. 1992, AJ, 103, 1621

Smith, E. O., Rich, R. M., & Neill, J. D. 1998, AJ, 115, 2369

Smith, V. V., et al. 2002, AJ, 124, 3241

Sneden, C. 1973, ApJ, 184, 839

Sneden, C., Kraft, R. P., Guhathakurta, P., Peterson, R. C., & Fulbright, J. P. 2004, AJ, 127, 2162

Sneden, C., Kraft, R. P., Shetrone, M. D., Smith, G. H., Langer, G. E., & Prosser, C. F. 1997, AJ, 114, 1964

Spite, F., Barbuy, B., & Spite, M. 1993, A&A, 272, 116

Spitzer, L. 1987, Dynamical evolution of globular clusters (Princeton, NJ, Princeton University Press, 1987, 191 p)

Strader, J., Smith, G., Larsen, S., Brodie, J., & Huchra, J. 2009, ArXiv e-prints

Tautvaišienė, G., Wallerstein, G., Geisler, D., Gonzalez, G., & Charbonnel, C. 2004, AJ, 127, 373

Testa, V., Ferraro, F. R., Chieffi, A., Straniero, O., Limongi, M., & Fusi Pecci, F. 1999, AJ, 118, 2839

Thomas, D., Maraston, C., & Bender, R. 2003, MNRAS, 339, 897

Tinsley, B. M. 1979, ApJ, 229, 1046

Tolstoy, E., Hill, V., & Tosi, M. 2009, ARA&A, 47, 371

Tonry, J. & Davis, M. 1979, AJ, 84, 1511

Venn, K. A., Irwin, M., Shetrone, M. D., Tout, C. A., Hill, V., & Tolstoy, E. 2004, AJ, 128, 1177

Ventura, P. & D'Antona, F. 2008, A&A, 479, 805

Vesperini, E., McMillan, S. L. W., & Portegies Zwart, S. 2009, ApJ, 698, 615

Vogt, S. S., et al. 1994, in Society of Photo-Optical Instrumentation Engineers (SPIE) Conference Series, Vol. 2198, Society of Photo-Optical Instrumentation Engineers (SPIE) Conference Series, ed. D. L. Crawford & E. R. Craine, 362–+

Walker, A. R., Raimondo, G., Di Carlo, E., Brocato, E., Castellani, V., & Hill, V. 2001, ApJ, 560, L139

Whitmore, B. C. & Schweizer, F. 1995, AJ, 109, 960

Wolf, M. J., Drory, N., Gebhardt, K., & Hill, G. J. 2007, ApJ, 655, 179

Woosley, S. E. & Weaver, T. A. 1995, ApJS, 101, 181

Zinn, R. & West, M. J. 1984, ApJS, 55, 45